Development of a graphene-based electrochemical immuno-biosensor for the sepsis biomarker procalcitonin

Submitted by Laureline Sandra Anna Mahe to the University of Exeter

as a thesis for the degree of

Doctor of Philosophy in Physics

In June 2015

I certify that all material in this thesis which is not my own work has been identified and that no material has previously been submitted and approved for the award of a degree by this or any other University.

Abstract

Sepsis is a global health issue that is the primary source of death by infection. It is often deadly and being able to deliver an appropriate diagnosis as early as possible is crucial to ensuring a positive outcome of the patient. The currently lack of an adequate clinical diagnostic tool (speed, accuracy and so on) thus imposes a human and financial burden. Current research on providing the market with a quantitative and rapid (less than 40 minutes) point-of-care device focuses on the simultaneous detection of a range of biomarkers of sepsis whose concentration profiles in serum change over time in ways that have been clearly established in terms of indicating the severity of the condition. Among these, procalcitonin has been judged the most likely individual biomarker to indicate a sepsis condition of bacterial origin. The work of this thesis focuses on the development of a graphene-based sensor for procalcitonin, and a proof-of-concept was established for the electrochemical detection of procalcitonin in aqueous solution on a graphene platform. Electrochemical methods were chosen for their fast response, sensitivity, selectivity and low-cost, while graphene was chosen for its conductivity and transparency, which allows future combination of optical means of detection with electrochemistry. The difficulty of producing graphene electrodes with sufficient reproducibility for sensor development has been addressed, with partial success. Also, it has been shown that highly oriented pyrolytic graphite (HOPG) can be used as a model for biosensing on graphene. In terms of combining electrochemical and optical read outs, it was shown that graphene can support localised surface plasmon resonance (of gold nanostructures) and preliminary results suggest that this method could also be used for the detection of procalcitonin. Finally, another material that attracts particular attention in electrochemical biosensing is boron doped diamond (BDD) and this thesis also describes photo-electrochemistry at a BDD electrode as a possible future biosensing platform.

Table of content

Author's declaration

The SEM image in Figure 6.2 was taken by Dr D. K. Polyushkin.

Acknowledgment

I thank Dr S.J. Green, Prof C.P. Winlove, Dr T. Jenkins, A. Clowsley, Dr E. Green, M. Heath, Dr L. Shelford, Dr T.Bointon, Dr N. Meinzer, M. Vardaki, S. Zanjani Pour, Dr S. Hornett, Dr D. O'Hare, Dr D. Horsell, Dr F. Palombo, Dr A. Perry, Dr S. Nunez Sanchez, Dr J. Mansfield, Dr A. Lewandovska, R. Edington, L. Denton, Dr B. Sarri, Dr N. Garrett, Dr S. Garrett, Dr M. Smith, S. Eashwer-Singhraj, Dr V. Bhaskar, L. Bendhu, Dr N. Jayakrupakar, K. Kurtis, Dr I. Iping Petterson, Dr J. Dorney, L.Clark, Dr J, Corcoran, Dr B. Gardner, Dr D. Woods, M. Rouxel, A. Genat, F. Marticke, V. Sounthakith, D. Russell, the workshop, my family and the people from the Exeter Martial Art.

Major symbols and abbreviations

Symbol	Meaning
α	Transfer coefficient
	Absorption coefficient of a semiconductor for a monochromatic radiation
A	Area
a_O^s	Activity of the reduced species
a_R^s	Activity of the oxidised species
C_{dl}	Double layer capacitance
C_{O}^{∞}	Bulk concentration, oxidised species
C_{R}^{∞}	Bulk concentration, reduced species
C_s	Pseudo capacitance
D_{O}	Diffusion constant, oxidised species
D_{R}	Diffusion constant, reduced species
ε	Permittivity
ε_0	Permittivity of the vacuum
e	Electronic charge
$E_{1/2}$	Half wave potential in voltammetry
$E_{\mathrm{amplitude}}$	Amplitude of SWV potential signal
E_{eq}	Equilibrium potential of an electrode
$\mathrm{E_F}$	Fermi level
$E_{F,FC}$	Fermi level of the semiconductor
E_{fb}	Flat band potential
E_{pc}	Cathodic peak potential
E_{pa}	Anodic peak potential
E_{step}	Voltage increment in SWV
$E^{0'}$	Formal potential of an electrode
ΔE_p	$= E_{pc} - E_{pa}$
f	Frequency of sinusoidal excitation
F	Farady constant
i_{photo}	Photocurrent
i	Total current
i_a	Anodic current component
i_c	Cathodic current component
$\mathrm{I_{pc}}$	Cathodic current peak
$\mathrm{I_{pa}}$	Anodic current peak
I_0	Incident photon flux
i_0	Exchange current

Symbol	Meaning
Δi_{off}	Change in current at light switched off
Δi_{cath}	Difference between initial cathodic photocurrent and initial dark current
J_O	Anodic current density component
J_R	Cathodic current density component
K, K'	Location of Dirac cone in the reciprocal lattice of graphene
k	Wave vector
k_O	Heterogeneous rate constant, oxidation
k_R	Heterogeneous rate constant, reduction
k^0	Standard heterogeneous rate constant
L_m	Minority carriers diffusion length
μ	Mobility
η	Overpotential
n	Stoechimetric number of electrons involved in a reaction
	Electron density in a semiconductor
	Refractive index
N	Acceptor or donor density
O	Oxidised species
ω	Angular frequency
q	Momentum
R	Gas constant
R	Reduced species
R_s	Sheet resistance
	Series resistance
R_Ω	Electrolyte resistance
V_{bias}	Bias voltage
Vg	Gate voltage
v_F	Fermi velocity
R_u	Uncompensated resistance
ν	Scan rate
W	Width of the space charge layer
Z_f	Faradaic impedance
Z_w	Warburg impedance
Z'	Real impedance
Z''	Imaginary impedance

Abbreviation	Meaning
Ab1	Capture antibody
Ab1	Capture antibody
Ab2	Detection antibody
Ab2	Detection antibody
APS	Ammonium Persulfate
CE	Counter electrode
CoS	Co-substrate
CoSox	Oxidised co-substrate
CRP	C-reactive protein
CSPE	Screen printed electrode
CV	Cyclic voltammetry
CVD	Chemical vapor deposition
DPV	Differential pulse voltammetry
EIS	Electrochemical impedance spectroscopy
ELISA	Enzyme-linked immunosorbent assay
ethylmethylketone	Ethyl methyl ketone
FET	Field effect transistor
GNP	Gold nanoparticles
HNO_3	Nitric acid
HOPG	Highly oriented pyrolitic graphite
HRP	Horseradish peroxidase
HRP-Ab2	Detection antibody labelled with HRP
HSQ	Hydrogen silsesquioxane
IL-10	Interleukine 10
IL-6	Interleukine 6
IPA	Propan-2-ol
ITO	Indium Tin Oxide
LCAO	Linear Combination of Atomic Orbitals
LOD	Limit of detection
LSPR	Localised surface plasmon resonance
MIBK	4-methylpentane-2-one
OPD	*0* -phenylene diamine
PBS	Phosphate-buffered saline
PCT	Procalcitonin
PDMS	Poly (dimethylsiloxane)
PMMA	Poly (methyl methacrylate)
PSE	1-Pyrenebutanoic acid succinimidyl ester
RIE	Reactive ion etching
SDS	Sodium Dodecyl Sulfate
SEM	Scanning electron microscope
SHE	Standard hydrogen electrode
SPR	Surface plasmon resonance
SWV	Square wave voltammetry
TMB	Tetramethyl Benzidine
TMBox	Oxidised form of TMB
TNF-α	Tumor Necrosis Factor alpha
WE	Working electrode

Chapter 1

Introduction

'Every three heartbeats, someone dies of sepsis. In the developing world, sepsis accounts for 60-80% of childhood deaths. Those who survive, both adults and children, often struggle with life. It's our goal to reduce the incidence of sepsis by 20% by 2020'

UK sepsis trust

1.1 Sepsis

Sepsis is a life-threatening condition where the body's immune system damages the patient's organ in response to an infection. For every hour delay in the diagnosis, the risk of death of the patient increases by 6 to 10% and therefore there is a real and urgent need for rapid and quantitative diagnostic tools. The incidence of sepsis is on the rise and such tools would also help to reduce considerably the financial impact of sepsis on hospitals.

According to the ACCP/SCCM Consensus Conference of 1992, sepsis is a documented infection together with 2 or more of SIRS (Systemic Inflammation Response Syndrom) criteria such as [1] hypothermia, tachycardia, tachypnea and elevated white blood cell count (leucocytosis or leucopenia) . The different stages of sepsis, with increasing degree of severity, are: SIRS, sepsis, severe sepsis and septic shock. Severe sepsis is characterised by organ dysfunction and 25 to 50% of patients reaching septic shock die. The number of critical care admissions with severe sepsis and the mortality associated is increasing [2]. The mortality rate associated with sepsis is high. One third of patients suffering from sepsis die in the hospital and the number of children in the world that have died following severe sepsis has doubled in 20 years [3]. Children in intensive care following severe burns show higher infection rates than critically ill non-burnt patients [4] and are likely to suffer from complications/organ dysfunction if a treatment is not appropriate and quickly administered. Most important, the management of antibiotherapy is essential to avoid false diagnosis of sepsis and inappropriate administration of antibiotics. This would slow down the increasing bacterial resistance to antibiotics. This has led to a focus on biomarkers that have been reported to be valuable for the differentiation between viral and bacterial infection. This type of assay is quicker than blood cultures which can take 48 to 72 hours [3]. The possibility for misdiagnosis is high because the symptoms related to sepsis can also come from many other sources, which makes the diagnosis difficult. Current diagnostics of paediatric SIRS, sepsis, severe sepsis and septic shock have been published by Goldstein et al. Better definitions means an overall reduction in the delays occurring when treating burnt patients; that is, an improvement in the diagnosis and a reduction in the mortality in the emergency department (ED) due to severe sepsis. For example, antibiotic therapy for sepsis

saves more lives if the antibiotics are provided within 4 hours after admission to ED [5]. Tabrizian et al [6] stress on the necessity to have a multi-biomarkers test that would make a diagnosis at regular intervals and would be close to the patient ('point-of-care'). Current techniques like Enzyme-Linked Immunosorbent Assay (ELISA), Polymerase Chain Reaction (PRC) and DNA extraction are quicker than culture assay but remain too long (2-6 h) to monitor the changes occurring during the infection and following the treatment, thus failing to reduce the mishap therapies, the mortality and the healthcare related costs.

Point of care devices are close to the patient, that is, they take samples and analyse them on the spot, thereby removing the necessity to transport the samples to the laboratory. This limits the delay between the data collection, the diagnosis and the therapy decision. To reduce the delays further and increase the responsivity to a clinical change, systems now exist that communicate with hospitals' central units and send texts to a GP. The sepsis assay developed in this thesis could be integrated into a wireless body area network (WBAN), where different nodes measure different parameters (level of PCT, temperature, blood cell count, etc.) and communicate between themselves and with the hospital network, leading to better care for the patient.

Biomarkers are an important tool used to improve the diagnosis and prognosis of sepsis. However, the lack of sensitivity and specificity of current diagnostic tools for these biomarkers prevent their routine use in critical clinical care [7]. An ideal sensor would screen the data from several markers simultaneously, which would increase the accuracy of the diagnosis [7][8]. In the case of sepsis, the biomarkers that have been identified as being clinically useful are [7][9] Procalcitonin (PCT), C-reactive protein (CRP), tumor necrosis factor-alpha (TNF-alpha) and the interleukines 6 (IL-6) and 10 (IL-10). Their time-dependent concentration in plasma after an infection is shown in Figure 1.1.

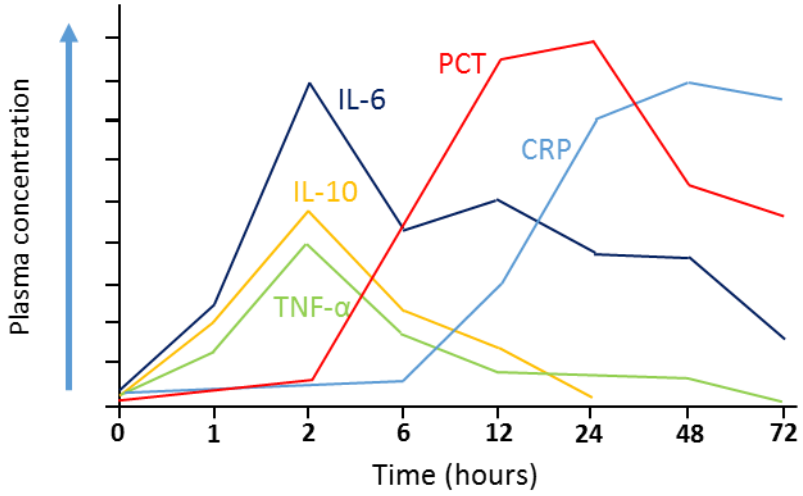

Figure 1.1: time-dependent concentration of the sepsis biomarkers procalcitonin (PCT), C-reactive protein (CRP), interleukine 6 (IL-6) and 10 (IL-10) and tumor necrosis factor-alpha (TNFα) in plasma after an infection. Adapted from [10].

Having a time-dependent fingerprint of the concentration in the serum of these biomarkers would help in monitoring the effect of the treatment given to the patient. The biomarker the most likely to provide a quick diagnostic of sepsis originating from a bacterial infection is PCT. Several articles discuss the clinical relevance [7][11] but it is generally agreed that it remains very likely to add value in paediatric care to early diagnostic, prognostic and therapeutic management of severe bacterial infection [4][12] .

Procalcitonin is a 116 amino acid that is considered to be the most specific [7][13] to bacterial infection. Its peptide sequence is composed of three parts: an N-terminal, calcitonin and katacalcin, as shown in figure 1.2.

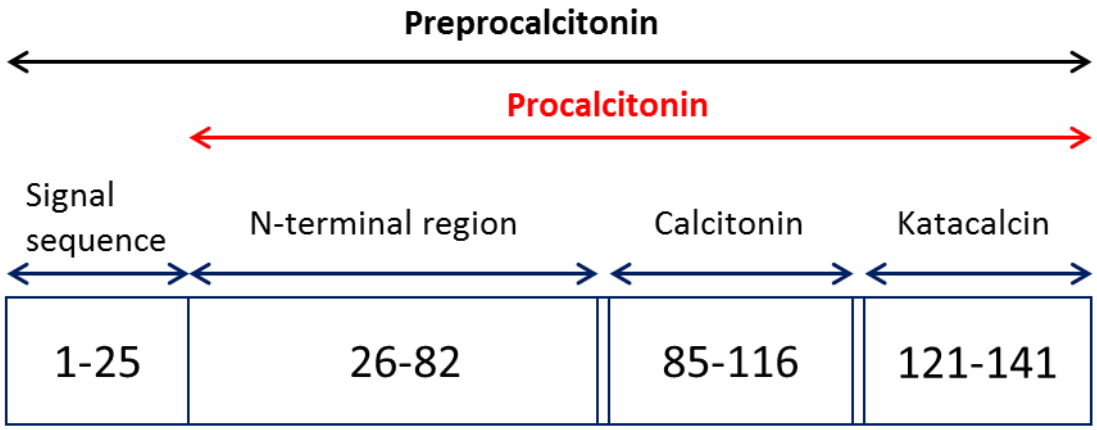

Figure 2: Breakdown peptide structure of preprocalcitonin.

It is a precursor of the hormone calcitonin which helps regulating the level of calcium in the blood. In healthy patients, PCT is produced by the C cells of the thyroid gland and its serum concentration is lower than 0.05 µg L^{-1}. The presence of a bacterial infection induces the release of PCT by nearly all tissues and cell types in the body (this phenomena is not yet understood) [14]. As a result, the concentration of PCT starts increasing sharply 4 hours after the beginning of the infection, in a way that correlates well with the severity of the bacterial infection. It can increase to over 100µg L^{-1}, and remains very low during viral infection [4][15][12][16][13], chronic inflammatory disorders and autoimmune processes. CRP is an acute phase protein (a protein whose plasma concentration increases following an infection) which is produced by the liver. Its production is stimulated by mediators called cytokines such as IL-1, IL-6, IL-8 and TNFα, and it has been identified as a good indicator of sepsis [17]. The concentrations of CRP in the serum are 10 mgL^{-1} in healthy patients and up to 50 mg L^{-1} after acute infection [13]. It is, however, much less specific to bacterial infection than PCT. Since the production of acute phase proteins is stimulated by the release of cytokines in the body, these have also raised an interest in the management of sepsis. TNFα is a cytokine of the inflammation reaction and its concentrations in serum lie between 0.004 to 0.5 ng L^{-1} [13]. TNFα causes the manifestation of several symptoms observed in a sepsis condition, including organ failure, and an anti TNFα therapy could help reduce the mortality associated with sepsis [18]. IL-10 and IL-6 are other cytokines involved in the inflammatory response and whose concentrations in plasma would be good indicators of the early development of a severe sepsis

condition [19][8]. IL-10 would help attenuating sepsis [20]and regulating the onset of irreversible sepstic shock [21]. The use of these biomarkers to assist a rapid sepsis diagnostic tool has been the subject of extensive research for the last 10 years. Shulte-Hostede et al [13] report on a proof of concept of a point of care test that simultaneously determines the concentration of PCT, TNFα and CRP with an optical immune sensor. Preininger et al [22] have developed a protein chip for the simultaneous detection of CRP, TNFα, PCT, IL-6, IL-10, IL-8 and neopterin. They optimised the chip printing, the microfluidic set up and the assay parameter to account for the different detection range and sizes of the biomarkers. Brandenburg et al [8] have developed a point of care automated fluorimetric immunosensor for the simultaneous detection of CRP, IL-6 and PCT. At the moment, a project called RAPPID is under development to produce a portable test that will provide a diagnosis in less than 15 min.

Existing commercial assays are based on a quantitative or semi-quantitative measure of PCT concentrations (plasma or serum). The tests are commercialised by Thermo Scientific, use various techniques (fluorescence, luminometric, immunochromatography), are quantitative or semi-quantitative and provide a result between 19 min and 1h. However, these tests do not offer the required conditions of rapidity, quantitative and point of care measurement of PCT [4].

Most of these techniques, and the assay developed in this thesis, use antibodies to capture the molecule of interest and therefore are called immunosensors.

1.2 Immunosensors

A biosensor is a device used to identify and/or quantify a biological molecule, converting the signal into data readily comprehensible by the end user. It is comprised of a recognition element, a transducer which translates the binding on a recognition element into a signal readable by the device, and a data processing element. Immunosensors are biosensors where the recognition element is an antibody which is specific to the antigen the sensor is meant to detect [23]. A commercial biosensor must have most of the following characteristics [24]: cheap, easy to use, long shelf life, low limit of detection, repeatability, reproducibility, selectivity, sensitivity, wide linear range, low cross reactivity, be non-invasive (i.e. low volume prelevements on patients) and biocompatible. Immunosensor

transducers are based on many different physical methods: optical, electrochemical, mass sensitive, thermoelectric, piezoelectric and field effect transistors . The detection is either labelled (the label can be an enzyme or a fluorescent molecule) or label-free (direct electrochemistry of the antigen, surface plasmon resonance, magnetic biosensor). Electrochemical immunosensors are divided into amperometric, potentiometric, capacitive sensors and photoelectrochemical [23][25][26]. Optical sensors use fluorescence, chemoluminescence, chromogenic, and surface plasmon resonance (SPR) techniques [23][26][24].

Antibodies are proteins (immunoglobulines) composed of two heavy and two light chains. The light chains contain variable regions (paratope) where the antigen binds. They contain three complementary determining regions (CDRs) that determine the topography of the binding sites, therefore the specificity for a particular region of an antigen (epitope)[27] (in addition to short distance effective forces like hydrogen bonding, Van der Waals, coulombic and hydrophobic interactions). Antibodies contain primary amine groups, sulfhydryl groups and carbohydrate residues that allow their labelling.

According to the way they are produced, antibodies are mono- or polyclonal. Monoclonal antibodies are produced from a single B cell and are therefore specific to an antigen [28]. They are more expensive than polyclonal antibodies which are produced by different B cells and are less specific. The amine offers the possibility to immobilise antibodies on substrates that, for example, contain an ester group.

Proteins can be immobilised on a surface by polymer/gel entrapment, surface adsorption, covalent binding, and electrostatic forces (via charged amino acids)[24]. The choice of immobilisation depends on how stable the enzyme needs to be on the surface, e.g. is it a disposable sensor? Covalent bonding occurs via function groups on the amino acids like NH_2, COOH, OH and SH [24].

The biosensor may or may not require a label to translate the detection of an element on its surface into a readable signal, and therefore the techniques used are divided into labelled and label-free assays.

1.3 Labelled assays

Some assays require a label to produce a measurable signal and this label is often an enzyme which catalyses a particular reaction. The product of the reaction is then read by one or several methods simultaneously such as electrochemical and optical [29]. The enzyme based immunoassay used in this thesis is called Enzyme linked ImmunoSorbent Assay (ELISA). There are different types of ELISA assays (direct, indirect, sandwich, competitive), the most popular being the sandwich ELISA, where the antigen is trapped between two specific antibodies. One is attached to the transducer of the biosensor, the other one is labelled with an enzyme.

Enzymes are proteins that catalyse a specific reaction [28]. They speed up the reaction by 10^6-10^{14} by reducing the activation energy of the same reaction without use of the enzyme. They are generally detected by fluorometry, luminometry, colorimetry and electrochemistry [29]. Very common enzymes used in biosciences are Horseradish peroxidase (HRP) [30][31][19][32][33] , and Alkaline Phosphatase (AP) [34][29][19].

Horseradish peroxidase catalyses the reduction of hydrogen peroxide to water via a two electron transfer from a mediator (substrate) according to the following equation:

$$H_2O_2 + donor \xrightarrow{HRP} 2H_2O + oxidised\ donor$$

The donor is a chromogenic substrate. Some common substrates for HRP are: 3,3',5,5'-Tetramethylbenzidine (TMB)[31][19], o-phenylene diamine (OPD) [35][31][19][36], and 2,2'-azino-bis(3-ethylbenzothiazoline-6-sulphonic acid) (ABTS) [34] [37], hydroquinone and ferrocene derivatives [38]. TMB is non carcinogenic contrary to other sensitive subtrates like ABTS or OPD [39] which often gives it the preference. Both TMB and OPD will be assessed in this thesis. Enzymes are unstable and very sensitive to the temperature, pH, ionic strength, and buffer composition interferences in the reactor. For each enzyme and co-substrate, these conditions can be optimised [38][40][24][41][36]. For example, HRP is more stable in the range of pH between 5 and 9 and has an optimum activity between pH 6 and 6.5 . In this thesis, the product of the reaction catalysed by HRP was analysed using electrochemical methods.

Electrochemical biosensors are attractive due to their low cost, sensitivity and their high bio-selectivity [24]. They are also rather portable, have a low limit of detection (they can detect as low as pM concentrations) and can be used to analyse small volume samples. In labelled techniques, one of the products of the reaction catalysed by the enzyme is reduced or oxidised, and the resulting current gives quantitative information about the antigen captured on the labelled sensor. Materials for transducers in electrochemical immunoassays include gold, platinum [30], glassy carbon [29][42], carbon screen printed electrodes [31][19], mercury electrode [32], diamond like carbon [33], boron doped diamond [43], carbon nanotubes [44], and graphene [45]. Commonly used methods for biosensors are amperometry [46], linear sweep voltammetry, differential pulse voltammetry (DPV), and square wave voltammetry (SWV). The Cyclic Voltammetry (CV) is often used for the characterisation of electrochemical systems. For example, the potential at which a redox active species is oxidised or reduced is easily determined by CV. Depending on the substrate used with HRP, it is not always possible to use methods like DPV that are more sensitive than amperometry. To overcome this issue, non-organic labels can be used instead or complementary to the enzyme label, such as gold nano-particles [47][48][49], and quantum dots [50][51][52]. However, the use of amplification labels may induce further costs and increase the diagnostic time. The sandwich ELISA also requires many steps and therefore non-labelled techniques might be preferred for the fabrication of a rapid assay for procalcitonin.

1.4 Label-free assays

Electrochemical Impedance Spectroscopy (EIS) is a powerful label-free electrochemical method to assess the modification of a conductive surface [53][54]. In this method, the binding of an antigen is seen as a resistance to the passage of an electric current that originates from the oxidation or reduction of a redox couple. It is this resistance that is measured as a function of the concentration of the analyte and provides the analytical information. Optical methods such as Surface Plasmon resonance (SPR) and Localised Surface Plasmon Resonance are widely used label-free methods in biosensing [55][6] . This technique has the advantage of having a fast response and being able to detect several analytes at the same time. Surface Plasmon Resonance is an optical

phenomenon based on the existence of a charge density oscillation at the interface between two materials of different dielectric constants, such as a dielectric and a metal. Resonance happens when an optical electromagnetic wave is incident on the interface (within the limits of the critical angle for total internal reflection) and its wavelength matches that of the surface plasmon wave. This can be recorded as a peak of intensity as a function of the wavelength of the incident light. When the light is incident on nanoparticles whose size is much smaller than the wavelength of the incident light, the surface plasmon oscillates around the nanoparticle and is no longer propagating. This method is called Localised Surface Plasmon Resonance (LSPR). Both SPR and LSPR are sensitive to a change in dielectric constant of their environment. As a result, antigen-antibody interactions can be monitored by a wavelength shift of the surface plasmon resonance peak (this is assuming that the metal was *a priori* modified with antibodies)[56]. Current detection limits are ~ 1-100 ng/ml of proteins [57]. In reference 6, Chung and et al suggest an amplification method based on HRP-catalysed precipitation to enlarge the dynamic range and increase the sensitivity of SPR based immunoassays. The thin gold layer can also be used as a working electrode and the dual device can collect optical and electrochemical data from the sample [23][24].

Graphene is also a good candidate for combined electrochemical and optical detection as it is conductive, and transparent.

1.5 Graphene-based biosensors

Graphene is a 2D honeycomb structure of carbon atoms. It is a very promising material for biosensing due to its unique combination of structural, electronic, physical and optical properties [58]. Importantly, it is conductive, transparent, has a low environment impact and is relatively cheap. Graphene is also easily modified via molecules containing a pyrene moiety (group of four benzene rings) that pi-stacks on the graphene surface without modifying its properties. It has been used in biosensors based on field effect transistors [59], electrochemical [60] and optical [61] biosensors.

A review [45] indicates that direct electron transfer between enzymes and electrodes would be facilitated on graphene. It also reports on an electrochemical HRP biosensor based on graphene that exhibits long term stability, high sensitivity

and low limit of detection. Banks et al [62] report on the use of graphene for the detection of biomolecules. They found that the electrochemical properties of graphene would be due to the electroactivity at the edges and on graphitic islands in the CVD graphene. Though a recent study [63] brings some evidence that freshly cleaved highly oriented pyrolytic graphite (HOPG) would support fast electron transfer. Gold nanoparticles (GNP) can be deposited on graphene in a controlled fashion to help the mediation of electron transfer to the attached proteins (proteins can be grafted on GNPs via the hydroxyl groups present on the GNPs). Nicolini et al [64] report on glucose electrochemical sensing on a GNP modified graphene double layer. The low capacity of graphene for electron transfer and the possibility to grow GNPS on it makes it also possible to detect targeted proteins by surface plasmon resonance.

1.6 This thesis

This thesis concerns the development of a graphene-based electrochemical and optical sensor for the sepsis biomarker procalcitonin.

Chapter 2: This chapter gives an introduction to graphene electrochemistry. Graphene and its properties are first introduced. Then, the electrochemical methods used in this thesis are described and the graphene electrodes made in-house are characterised electrochemically. The results show that the electrodes are suitable for electrochemical measurements.

Chapter 3: The first method used to detect procalcitonin was an ELISA where the biomarker is trapped between two of its specific antibodies and the detection is made via the enzyme horseradish peroxidase. Since the quantity of procalcitonin is directly related to the quantity of enzyme in solution, it was important to verify that the horseradish peroxidase can be detected by electrochemical methods. This is the concern of this chapter and it is shown that such detection of HRP is possible.

Chapter 4: This chapter concerns the proof-of-concept of the labelled detection of procalcitonin on a graphene platform by square wave voltammetry. Though the results show that such detection is possible, it was not possible to calibrate the graphene electrodes for the detection of procalcitonin due to the lack of reproducibility of the graphene electrodes. One strategy to overcome this issue

consisted in regenerating the surface of the electrodes using Sodium Dodecyl Sulfate (SDS) and was successful.

Chapter 5: Calibrating graphene for the electrochemical detection of procalcitonin has proven difficult. Highly Oriented Pyrolitic Graphite consists of a pile stack of graphene and therefore it was investigating as a model for biosensing on graphene. The method used was electrochemical impedance spectroscopy and HOPG was successfully calibrated for the detection of procalcitonin.

Chapter 6: In this chapter, optical methods such as Localised Surface Plasmon Resonance are explored as a complementary method to electrochemistry for the detection of procalcitonin.

Chapter 7: This chapter concerns the study of the potential and pH dependence of photocurrent transients for boron-doped diamond electrodes in aqueous electrolyte as a possible alternative to transparent graphene electrodes in immune sensing.

Bibliography

[1] B. Y. C. M. Limjoco, S. Whittier, and D. Abmm, "Improving Sepsis Diagnosis : Key to Better Patient Outcomes , Higher Reimbursement," *English J.*, 2000.

[2] D. a Harrison, C. a Welch, and J. M. Eddleston, "The epidemiology of severe sepsis in England, Wales and Northern Ireland, 1996 to 2004: secondary analysis of a high quality clinical database, the ICNARC Case Mix Programme Database.," *Crit. Care*, vol. 10, no. 2, p. R42, 2006.

[3] D. O. Acheampong and P. K. Feglo, "Empirical treatment of neonatal sepsis by Klebsiella : A Case study at Komfo Anokye Teaching Hospital (Kath), Ghana," vol. 1, no. 1, pp. 18–22, 2011.

[4] M. Chalumeau, S. Leroy, D. Gendrel, G. Bréart, F. Moulin, and F. Dubos, "Procalcitonin bedside testing in the pediatric emergency department," *Arch. Pediatr.*, vol. 14, no. 6, pp. 529–531, 2007.

[5] J. Homola, "Surface plasmon resonance sensors: review," *Sensors Actuators, B Chem.*, vol. 54, pp. 3–15, 1999.

[6] S. S. Yee, "Surface plasmon resonance sensors: review," *Sensors Actuators, B Chem.*, vol. 54, pp. 3–15, 1999.

[7] C. Pierrakos and J.-L. Vincent, "Sepsis biomarkers: a review.," *Crit. Care*, vol. 14, no. 1, p. R15, 2010.

[8] M. Kemmler, B. Koger, G. Sulz, U. Sauer, E. Schleicher, C. Preininger, and A. Brandenburg, "Compact point-of-care system for clinical diagnostics," *Sensors Actuators, B Chem.*, vol. 139, no. 1, pp. 44–51, 2009.

[9] M. Meisner, “Biomarkers of sepsis: clinically useful?,” *Curr. Opin. Crit. Care*, vol. 11, no. 5, 2005.

[10] M.Meisner, “Procalcitonin. Experience with a new diagnostic tool for bacterial infection and systemic inflammation,” *J. Lab. Med.*, vol. 23, pp. 253–272, 1999.

[11] B. M. P. Tang, G. D. Eslick, J. C. Craig, and A. S. McLean, “Accuracy of procalcitonin for sepsis diagnosis in critically ill patients: systematic review and meta-analysis.,” *Lancet Infect. Dis.*, vol. 7, no. 3, pp. 210–217, 2007.

[12] J. N. Deis, C. B. Creech, C. M. Estrada, and T. J. Abramo, “Procalcitonin as a Marker of Severe Bacterial Infection in Children in the Emergency Department,” *Pediatr. Emerg. Care*, vol. 26, no. 1, 2010.

[13] P. M. Krämer, M. Kess, E. Kremmer, and S. Schulte-Hostede, “Multi-parameter determination of TNFα, PCT and CRP for point-of-care testing.,” *Analyst*, vol. 136, no. 4, pp. 692–695, 2011.

[14] J. O. N. C. White, E. S. Nyle, R. H. Snider, K. L. Becker, and J. F. Habener, “Ubiquitous Expression of the Calcitonin-I Gene in Multiple Tissues in Response to Sepsis *,” *J. Clin. Endocrinol. Metab.*, vol. 86, no. 1, pp. 396–404, 2001.

[15] C. Wacker, A. Prkno, F. M. Brunkhorst, and P. Schlattmann, “Procalcitonin as a diagnostic marker for sepsis: A systematic review and meta-analysis,” *Lancet Infect. Dis.*, vol. 13, no. 5, pp. 426–435, 2013.

[16] A M. C. van Rossum, R. W. Wulkan, and A M. Oudesluys-Murphy, “PCT as an early marker of infection in neonates and children,” *Lancet Infect. Dis.*, vol. 4, no. October, pp. 620–630, 2004.

[17] E. Almeida, P. Moreira, A. Fernandes, R. Mealha, and A. Arag, “C-reactive protein as an indicator of sepsis,” *Intensive care Med.*, vol. 24, pp. 1052–1056, 1998.

[18] S. Lv, M. Han, R. Yi, S. Kwon, C. Dai, and R. Wang, “Anti-TNF- a therapy for patients with sepsis : a systematic meta-analysis,” *Int. J. Clin. Pract.*, vol. 68, no. 4, pp. 520–528, 2014.

[19] P. Fanjul-Bolado, M. B. González-García, and A. Costa-García, “Amperometric detection in TMB/HRP-based assays,” *Anal. Bioanal. Chem.*, vol. 382, no. 2, pp. 297–302, 2005.

[20] K.Nemeth, A. Leelahavanichku, P. S. . Yuen, B. Mayer, A. Parmelee, K. Doi, P. G. Robey, K. Leelahavanichkul, B. H. Koller, J. M. Brown, X. Hu, I. Jelinek, R. A. Star, and E. Mezey, “Bone marrow stromal cells attenuate sepsis via prostaglandin E2–dependent reprogramming of host macrophages to increase their interleukin-10 production,” *Nat. Med.*, vol. 15, pp. 42–49, 2009.

[21] S. Q. Latifi, M. A. O. Riordan, and A. D. Levine, “Interleukin-10 Controls the Onset of Irreversible Septic Shock,” *Infect. Immun.*, vol. 70, no. 8, pp. 4441–4446, 2002.

[22] U. Sauer, P. Domnanich, and C. Preininger, “Protein chip for the parallel quantification of high and low abundant biomarkers for sepsis,” *Anal. Biochem.*, vol. 419, no. 1, pp. 46–52, 2011.

[23] D. Grieshaber, R. MacKenzie, J. Vörös, and E. Reimhult, “Electrochemical Biosensors - Sensor Principles and Architectures,” *Sensors*, vol. 8, no. 3, pp. 1400–1458, 2008.

[24] D. . Thevenot, K. Toth, R. a. Durst, and G. S. Wilson, “Electrochemical biosensors : Recommended definitions and classification - (Technical Report),” *Pure Appl. Chem.*, vol. 71, no. 12, pp. 2333–2348, 1999.

[25] K. Soreng and H. R. Levy, “Procalcitonin: An Emerging Biomarker of Bacterial Sepsis,” *Clin. Microbiol. Newsl.*, vol. 33, no. 22, pp. 171–178, 2011.

[26] L. Su, W. Jia, C. Hou, and Y. Lei, “Microbial biosensors: A review,” *Biosens. Bioelectron.*, vol. 26, no. 5, pp. 1788–1799, 2011.

[27] K.Kramer; B.Hock, *Ultrathin Electrochemical Chemo- and Biosensors*. 2004.

[28] P. W. Bruce Alberts, Alexander Johnson, Julian Lewis, Martin Raff, Keith Roberts, *The cell*, Garland Sc. 2002.

[29] G. Volpe, R. Draisci, G. Palleschi, and D. Compagnone, "3,3′,5,5′-Tetramethylbenzidine as electrochemical substrate for horseradish peroxidase based enzyme immunoassays. A comparative study," *Analyst*, vol. 123, no. 6, pp. 1303–1307, 1998.

[30] J. C. Pyun, H. H. Lee, and C. S. Lee, "Application of an amperometric detector to the conventional enzyme-immunoassay (EIA)," *Sensors Actuators, B Chem.*, vol. 78, no. 1–3, pp. 232–236, 2001.

[31] A.-C. Lee, G. Liu, C.-K. Heng, S.-N. Tan, T.-M. Lim, and Y. Lin, "Sensitive electrochemical detection of horseradish peroxidase at disposable screen-printed carbon electrode," *Electroanalysis*, vol. 20, no. 18, p. 2040, Aug. 2008.

[32] W. Sun, K. Jiao, and S. Zhang, "Electrochemical ELISA for the detection of cucumber mosaic virus using o-pheneylenediamine as substrate," *Talanta*, vol. 55, no. 6, pp. 1211–1218, 2001.

[33] J. Kim, A. Bordeanu, and J. Pyun, "Biosensors and Bioelectronics Diamond-like carbon (DLC) microelectrode for electrochemical ELISA," vol. 24, pp. 1394–1398, 2009.

[34] K. A. H. Fujimoto, M. Isomura, "A comparison of chromogenic substrates for Horseradish Peroxidase as a label in Steroid enzyme immunoassay," *Biosci. Biotechnol. Biochem.*, vol. 34, no. 10, pp. 4177–4182, 1986.

[35] B. Jiang, M. Wang, Y. Chen, J. Xie, and Y. Xiang, "Highly sensitive electrochemical detection of cocaine on graphene/AuNP modified electrode via catalytic redox-recycling amplification," *Biosens. Bioelectron.*, vol. 32, no. 1, pp. 305–308, 2012.

[36] J. H. Bovaird, T. T. Ngo, and H. M. Lenhoff, "Optimizing the o-phenylenediamine assay for horseradish peroxidase: Effects of phosphate and pH, substrate and enzyme concentrations, and stopping reagents," *Clin. Chem.*, vol. 28, no. 12, pp. 2423–2426, 1982.

[37] J. E. M. J.Anderson, T. Byrne, K. J. Woelfel, "The Hydrolysis of pNitrophenyl Acetate: A Versatile Reaction To Study Enzyme Kinetics," *J. Chem. Educ.*, vol. 71, no. 8, pp. 715–718, 1994.

[38] E. M. Sheehy, "Pediatric burn care trends.," *AORN J.*, vol. 20, no. 5, pp. 831–832, 834, 1974.

[39] O. Thuemer, E. Hüttemann, and S. G. Sakka, "Procalcitonin as an early marker of sepsis," *Der Anaesthesist*, vol. 55, no. 6. pp. 650–654, 2006.

[40] R. L. Sheridan, "Sepsis in pediatric burn patients.," *Pediatr. Crit. Care Med.*, vol. 6, no. 3 Suppl, pp. S112–S119, 2005.

[41] S. V. Kergaravat, M. I. Pividori, and S. R. Hernandez, "Evaluation of seven cosubstrates in the quantification of horseradish peroxidase enzyme by square wave voltammetry," *Talanta*, vol. 88, pp. 468–476, 2012.

[42] M. Del Carlo and M. Mascini, "Enzyme immunoassay with amperometric flow-injection analysis using horseradish peroxidase as a label. Application to the determination of polychlorinated biphenyls," *Anal. Chim. Acta*, vol. 336, no. 1–3, pp. 167–174, 1996.

[43] A. Preechaworapun, T. a Ivandini, A. Suzuki, A. Fujishima, O. Chailapakul, and Y. Einaga, "Development of Amperometric Immunosensor Using Boron-Doped Diamond with Poly (o-aminobenzoic acid) been developed at boron-doped diamond (BDD) electrode," *Science (80-.).*, vol. 80, no. 6, pp. 2077–83, 2008.

[44] D. Tang, J. Tang, B. Su, and G. Chen, "Ultrasensitive electrochemical immunoassay of staphylococcal enterotoxin B in food using enzyme-nanosilica-doped carbon nanotubes for signal amplification," *J. Agric. Food Chem.*, vol. 58, no. 20, pp. 10824–10830, 2010.

[45] T. Kuila, S. Bose, P. Khanra, A. K. Mishra, N. H. Kim, and J. H. Lee, "Recent advances in graphene-based biosensors," *Biosens. Bioelectron.*, vol. 26, no. 12, pp. 4637–4648, 2011.

[46] I. S. Kucherenko, D. Y. Didukh, O. O. Soldatkin, and A. P. Soldatkin, “Amperometric biosensor system for simultaneous determination of adenosine-5???-triphosphate and glucose,” *Anal. Chem.*, vol. 86, no. 11, pp. 5455–5462, 2014.

[47] A. Ambrosi, M. T. Castañeda, A. J. Killard, M. R. Smyth, S. Alegret, and A. Merkoçi, “Double-codified gold nanolabels for enhanced immunoanalysis,” *Anal. Chem.*, vol. 79, no. 14, pp. 5232–5240, 2007.

[48] L. Wang, H. Zhu, H. Hou, Z. Zhang, X. Xiao, and Y. Song, “A novel hydrogen peroxide sensor based on Ag nanoparticles electrodeposited on chitosan-graphene oxide/cysteamine-modified gold electrode,” *J. Solid State Electrochem.*, vol. 16, no. 4, pp. 1693–1700, 2012.

[49] A. de la Escosura-Muñiz, M. Maltez-da Costa, C. Sánchez-Espinel, B. Díaz-Freitas, J. Fernández-Suarez, Á. González-Fernández, and A. Merkoçi, “Gold nanoparticle-based electrochemical magnetoimmunosensor for rapid detection of anti-hepatitis B virus antibodies in human serum,” *Biosens. Bioelectron.*, vol. 26, no. 4, pp. 1710–1714, 2010.

[50] H. W. Yu, J. Lee, S. Kim, G. H. Nguyen, and I. S. Kim, “Electrochemical immunoassay using quantum dot/antibody probe for identification of cyanobacterial hepatotoxin microcystin-LR,” *Anal. Bioanal. Chem.*, vol. 394, no. 8, pp. 2173–2181, 2009.

[51] H. Wang, J. Wang, C. Timchalk, and Y. Lin, “Magnetic electrochemical immunoassays with quantum dot labels for detection of phosphorylated acetylcholinesterase in plasma,” *Anal. Chem.*, vol. 80, no. 22, pp. 8477–8484, 2008.

[52] R. Malhotra, V. Patel, J. P. Vaqué, J. S. Gutkind, and J. F. Rusling, “Ultrasensitive electrochemical immunosensor for oral cancer biomarker IL-6 using carbon nanotube forest electrodes and multilabel amplification,” *Anal. Chem.*, vol. 82, no. 8, pp. 3118–3123, 2010.

[53] T. Xue, X. Cui, W. Guan, Q. Wang, C. Liu, H. Wang, K. Qi, D. J. Singh, and W. Zheng, “Surface plasmon resonance technique for directly probing the interaction

of DNA and graphene oxide and ultra-sensitive biosensing," *Biosens. Bioelectron.*, vol. 58, pp. 374–379, 2014.

[54] E. Katz and I. Willner, "Probing biomolecular interactions at conductive and semiconductive surfaces by impedance spectroscopy: Routes to impedimetric immunosensors, DNA-sensors, and enzyme biosensors," *Electroanalysis*, vol. 15, no. 11, pp. 913–947, 2003.

[55] Y. Yao, B. Yi, J. Xiao, and Z. Li, "Surface plasmon resonance biosensors and its application," *2007 1st Int. Conf. Bioinforma. Biomed. Eng. ICBBE*, pp. 1043–1046, 2007.

[56] J.-H. Lee, B.-C. Kim, B.-K. Oh, and J.-W. Choi, "Highly sensitive localized surface plasmon resonance immunosensor for label-free detection of HIV-1," *Nanomedicine Nanotechnology, Biol. Med.*, vol. 9, no. 7, pp. 1018–1026, May 2015.

[57] M. G. Kim, Y. B. Shin, J. M. Jung, H. S. Ro, and B. H. Chung, "Enhanced sensitivity of surface plasmon resonance (SPR) immunoassays using a peroxidase-catalyzed precipitation reaction and its application to a protein microarray," *J. Immunol. Methods*, vol. 297, no. 1–2, pp. 125–132, 2005.

[58] Y. Huang, X. Dong, Y. Liu, L.-J. Li, and P. Chen, "Graphene-based biosensors for detection of bacteria and their metabolic activities," *J. Mater. Chem.*, vol. 21, no. 33, pp. 12358–12362, 2011.

[59] K. Xu, X. Meshik, B. M. Nichols, E. Zakar, M. Dutta, and M. a Stroscio, "Graphene- and aptamer-based electrochemical biosensor," *Nanotechnology*, vol. 25, no. 20, p. 205501, 2014.

[60] Y. Shao, J. Wang, H. Wu, J. Liu, I. a. Aksay, and Y. Lin, "Graphene based electrochemical sensors and biosensors: A review," *Electroanalysis*, vol. 22, no. 10, pp. 1027–1036, 2010.

[61] H. Ma, D. Wu, Z. Cui, Y. Li, Y. Zhang, B. Du, and Q. Wei, "Graphene-Based Optical and Electrochemical Biosensors: A Review," *Anal. Lett.*, vol. 46, no. 1, pp. 1–17, 2013.

[62] D. A. C. Brownson, M. Gomez-Mingot, and C. E. Banks, “CVD graphene electrochemistry: biologically relevant molecules,” *Phys. Chem. Chem. Phys.*, vol. 13, no. 45, pp. 20284–20288, 2011.

[63] A. N. Patel, M. G. Collignon, M. a O. Connell, W. O. Y. Hung, K. Mckelvey, J. V Macpherson, and P. R. Unwin, “A New View of Electrochemistry at Highly Oriented Pyrolytic Graphite,” 2012.

[64] Y. Chen, Y. Li, D. Sun, D. Tian, J. Zhang, and J.-J. Zhu, “Fabrication of gold nanoparticles on bilayer graphene for glucose electrochemical biosensing,” *J. Mater. Chem.*, vol. 21, no. 21, p. 7604, 2011.

Chapter 2

Graphene as a substrate for electrochemistry

Abstract

Graphene is a 2 dimension material made of carbon atoms arranged in a honeycomb fashion. Theoretically known since 1947, it was isolated for the first time in 2004 by Andre Geim and Constantin Novoselov and since then has been the object of extensive research in very various fields owing to its exceptional set of physical properties. Such properties include transparency, high electrical and thermal conductivities and flexibility, which could lead to many innovations in fields such as energy (batteries and solar cells), optoelectronics,wearable electronics, biomedical. Because graphene has a high specific area and has shown to have excellent electrocatalytic properties, it is likely to have many application in electrochemistry, e.g. for biosensing purpose.

Here, graphene electrodes were fabricated by photolithography and their electrochemical behaviour was assessed in typical redox solutions. Cyclic voltammograms recorded in $Ru(NH_3)_6^{3+/2+}$ (outer-sphere) or $FeCN_6^{4-/3-}$ (inner-sphere) showed that the former has a semi-reversible behaviour on graphene and the latter an irreversible behaviour on graphene. The heterogeneous rate constant at a graphene electrode was measured in 1 M KCl containing 1 mM $Ru(NH_3)_6^{3+/2+}$ and was found to be 0.00183 cm s^{-1} (calculated using to Nicholson's method). Overall, the graphene electrodes fabricated for the purpose of this thesis were found to be suitable for the electrochemical experiments of this thesis.

2.1 Introduction

Graphene has been known theoretically since 1947, but was isolated for the first time in 2004 by Andre Geim and Constantin Novoselov [1], work for which they received the Nobel prize in in Physics in 2010. Its two dimensional honeycomb structure made of carbon atoms confers graphene unusual charge transport properties that made it one of the most exciting materials to study.

Besides its importance for understanding some fields in fundamental physics better, graphene also has triggered a wide research that aims at using it in commercial devices in fields such as energy storage [2], displays, nano-electronics, wearable devices [3], biosensors [4]. Indeed, monolayer graphene combines a plethora of physical properties such as flexibility [5], transparency [6] and high conductivity [7] that make it a good candidate for a wide range of low-cost, flexible, light-weight and portable applications. Graphene has a high surface area and has shown to have excellent electrocatalytic properties [6], and therefore triggered a lot of interest in the field of electrochemistry with applications in energy storage [8] and delivery, and sensing [9][10]. In terms of electrochemical biosensors, graphene opens up the prospect for the development of affordable and non-invasive point-of-care devices.

This chapter is concerned with showing that graphene electrodes are suitable to perform the electrochemical measurements undertaken in this thesis. Firstly, graphene and its physical properties are described. This is followed by a description and characterisation by Raman spectroscopy of the graphene electrodes produced in-house. Then, an introduction to electrochemistry and in particular the methods used in this thesis are given. Finally, the in-house produced graphene electrodes are characterised using cyclic voltammetry.

2.2 Introduction to graphene

2.2.1. Graphene properties and Graphene crystallographic and band structures

Graphene is a two dimensional material made of carbon atoms arranged in a honeycomb structure, which is shown on the left of Figure 2.1. The crystallographic structure is made of two triangular lattices (red and blue system on Figure 2.1) and the unit cells contain two atoms (A and B). The reciprocal lattice (on the right of Figure 2.1) also consists of a honeycomb structure where K and K' are two high symmetry points called Dirac points which will be explained later on in this section.

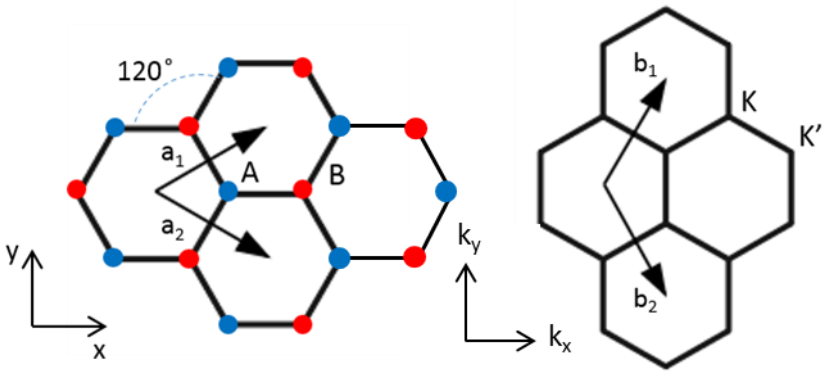

Figure 2.1: The graphene honeycomb crystallographic structure in the real (left) and reciprocal (right) spaces.

Amongst the four valence electrons of each carbon atom, three of them participate in the formation of strong covalent bonds (σ bonds) with neighbouring carbons (this is sp^2 hybridization) and one is delocalised within a π-bonding orbital created by the non-hybridized p atomic orbitals on two consecutive carbons overlapping. The energy band structure can be derived using a tight binding approach [11][12] that resembles the Linear Combination of Atomic Orbitals (LCAO) where electrons are considered tightly bonded to the atom they belong to and their wave function resembles that of isolated atoms. In this approach, the wave function of an electron is a linear combination of Bloch waves. These are created by multiplying a plane wave with a function describing the periodicity of the lattice and are of the form

$$\varphi(\boldsymbol{r}) = e^{i\boldsymbol{k}.\boldsymbol{r}}u(\boldsymbol{r}) \qquad (1)$$

where $u(\boldsymbol{r})$ is the periodic function, of the same period as the crystal.

The energy bands were first derived by Wallace in 1947 [23] and in the first and second nearest neighbour approximation are of the form [13]

$$E_{\pm}(k) = \pm t\sqrt{3 + f(k)} - t'f(k) \tag{2}$$

$$f(k) = 2\cos\left(\sqrt{3}\,k_y a\right) + 4\cos\left(\frac{\sqrt{3}}{2}\,k_y a\right)\cos\left(\frac{3}{2}\,k_x a\right) \tag{3}$$

where t and t' are the first and second nearest neighbour hopping energies and a ≈1.42 Å is the carbon-carbon distance . The plus and minus signs account for the π and π* bands respectively.

The dispersion energy $E(k)$ of the graphene lattice in the first and extended Brillouin zone (Figure 2.2) shows that the valence and conduction bands are degenerate at particular points, K and K', called Dirac points where the dispersion has a conical shape.

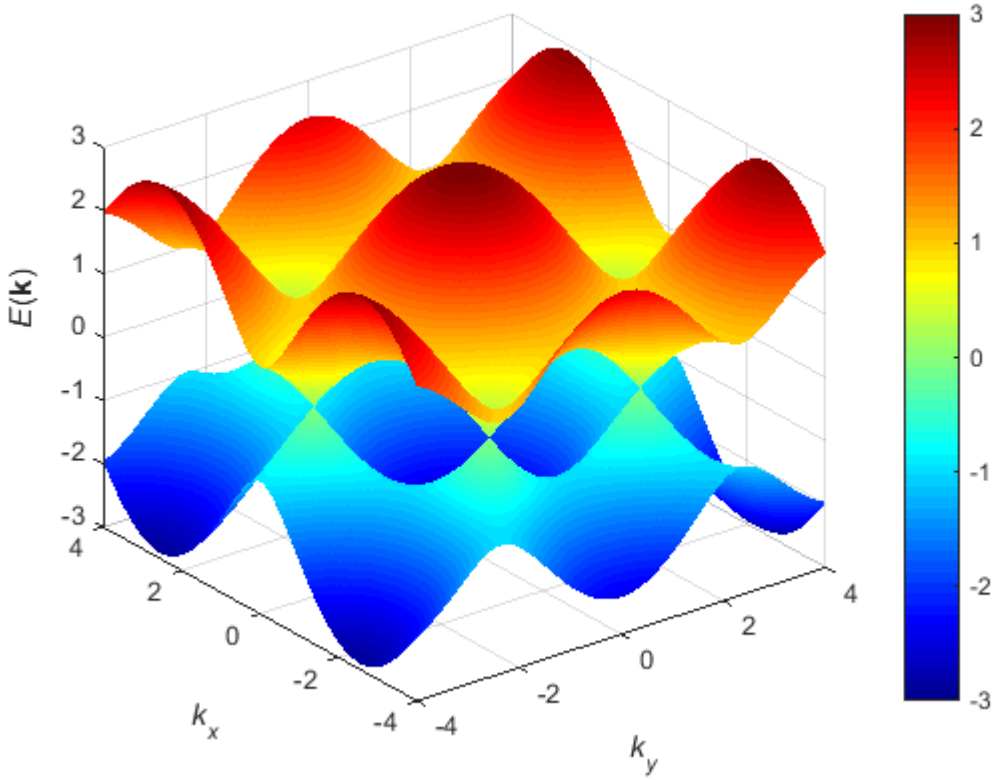

Figure 2.2: Energy dispersion of the graphene lattice in the first Brillouin zone considering the interaction between only first nearest neighbours. The colour scale reflects the value of E.

The dispersion energy at these points

$$E(q) \approx \pm v_f |\mathbf{q}| + O\left[\left(\frac{q}{K}\right)^2\right] \quad (4)$$

is derived from the full expression of the dispersion around K and K' with $\mathbf{k}$ (wave vector) being substituted by $\mathbf{k} = \mathbf{K} + \mathbf{q}$ with $|\mathbf{q}| \ll |\boldsymbol{K}|$[13]. v_f is the Fermi velocity and $\mathbf{q}$ is the momentum measured relatively to the Dirac points, K and K'.

As a consequence of the degeneracy and the linearity of the π and π* bands at the Dirac points, graphene is considered as a semi-conductor with zero band gap where at low energies the electrons behave like massless (in the sense that the

dispersion is linear around the Dirac point) Dirac fermions that travel at the Fermi velocity which is $\approx 10^6$ m s^{-1} [14]. As a result, electrons in graphene mimic the behaviour of relativistic particles, except that they travel at a much smaller speed (300 times less than the speed of light [14]). This behaviour opened the opportunity to use graphene as a bench-top experimental platform for the study of some quantum relativistic phenomena [14].

It is possible to control the electronic properties of graphene by doping it chemically or electronically. For instance, applying a negative or positive gate voltage to a graphene FET induces a p or n doping respectively, as represented on Figure 2.3.

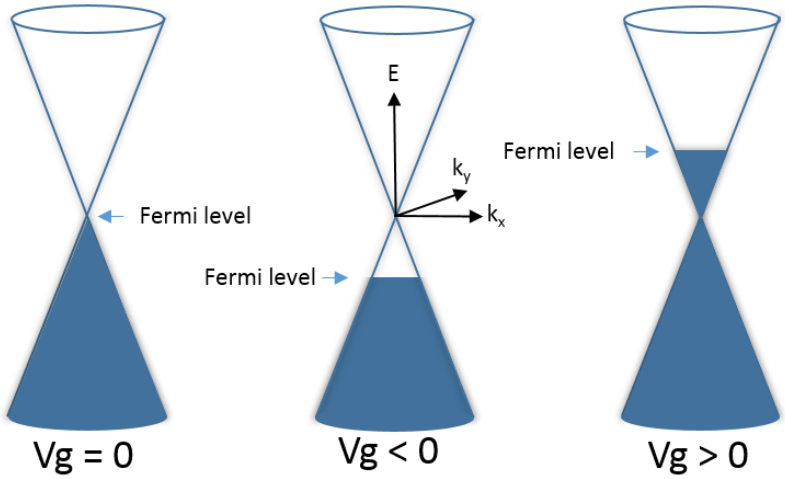

Figure 2.3: low energy dispersion spectrum (Dirac cones) of graphene at points K and K' of the first Brillouin zone indicating the position of the Fermi energy according to the gate voltage Vg applied to a graphene FET. Left: no voltage applied, the Fermi level lies at the cross point of the conduction and valence bands. Middle (right): negative (positive) Vg induces holes (electrons) at concentration $n = \alpha$ Vg where $\alpha = 7.2\ 10^{10}$ cm^{-2} V^{-1} for monolayer graphene devices with 300 nm SiO_2 used as a dielectric [1].

The possibility to control the physical properties of graphene is important in the sense that this material might replace silicon and indium tin oxide (ITO) in optoelectronics components in the future. ITO is the most widely used transparent conductor in fields such as displays, but indium is forecast to run out and therefore ITO is becoming increasingly expensive. It is also brittle and therefore cannot be

used in the fabrication of flexible displays, whose demand is increasing. As a result, the market for alternative transparent conductors is growing fast, with new actors such as metal meshes, graphene-based materials and silver nanowires.

2.2.2 Graphene physical properties

Aside from being one of the strongest known materials, electronic quality is one of the most interesting and useful properties of graphene where its charge carriers have high mobilities and ballistic transport over submicron distance. The mobility, μ, of the electrons and holes at a carrier density of $n = 10^{12}$ cm^{-2} can reach 10,000 cm^2 V^{-1} s^{-1} and shows a weak dependence on temperature [2].The mobility is then mostly affected by scattering by impurities or interaction with the substrate (e.g. ripples, fabrication residues, interfacial phonons [16]), and therefore it can be greatly enhanced by enhancing the quality of the transferred graphene samples (e.g. annealing the samples), finding a different substrate [17]or removing the substrate, increasing the number of graphene layers. Mobilities of 200,000 cm^2 cm^{-1} V^{-1} have been reported for suspended graphene for a carrier density of 10^{12} cm^{-2} [16], which is the highest found in any semi-conductor so far. For comparison, the mobility of electrons in silicon is 1500 cm^2 V^{-1}s^{-1} at an electron density $n = 10^{15}$ cm^{-2}, and replacing silicon by graphene would produce faster devices. The sheet resistance (in Ω/□) of few layer graphene, assuming no interaction between layers, is given by [18]

$$R_s = \frac{1}{\sigma_{2D} N} \tag{5}$$

where $\sigma_{2D} = n\mu e$, with e the unit electrical charge, is the 2D d.c. conductivity and N the number of layers. An interesting property of graphene is that it has a minimal conductivity of $\sigma_{2D} = \frac{4\,e^2}{h}$ when the carrier concentration approaches zero [18], with h the Plank constant, and n the density of charge carriers.

As well as being an excellent conductor, graphene has optical properties that makes it an excellent material for photonic and optoelectronic [18] (e.g. photovoltaic devices, touch screens, displays, light emitting devices) applications. Though only one atom thick, it is possible to identify and quantify the number of graphene layers by optical contrast. The transmittance of freestanding single layer graphene is given by the following equation [19]:

$$T = (1 + 0.5\pi\alpha)^{-2} \approx 97.7\ \% \quad (6)$$

where $\alpha \approx 1/137$ is the fine structure constant. Less than 0.1% of the light is reflected by graphene and each layer of graphene absorbs ≈ 2.3 % over the visible spectrum. As shown on Figure 2.4, CVD graphene has a higher optical transmittance between 200 nm and 900 nm than currently used transparent semi-conductors. Notably, it has the potential to replace ITO, which is currently the dominant material in optoelectronic applications but suffers a lot of constraints that are not suitable with some current technological expectations, such as flexibility of electronic devices, whose market is growing fast. Such constraints concern for example the increasing rarity of Indium which makes ITO increasingly more expensive, its sensitivity to acids and basic environments and its brittleness.

Commercial ITO has transmittance and sheet resistance values of 85 % and 10 Ω/□, respectively. Though the cost of graphene production is low, it has to at least match these values to potentially replace ITO. The actual research focuses on maintaining a high transmittance while reducing the sheet resistivity and Khrapach et al. [15] have recently reported a resistance $R_s = 8.8\ \Omega/\square$ for a transmittance $T = 85.5\ \%$ by intercalating few layer graphene with $FeCl_3$.

In the case of this thesis, it is sufficient to note that graphene is a good transparent conductor.

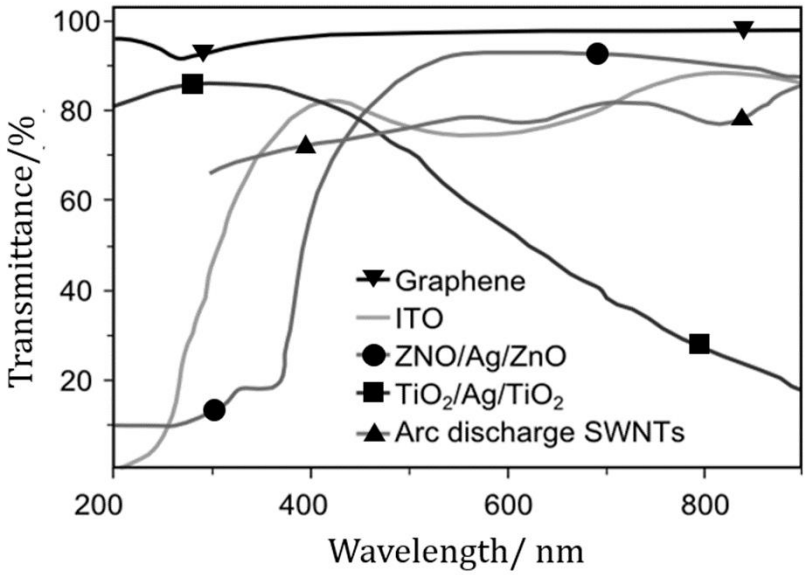

Figure 2.4: Transmittance for different transparent conductors : graphene, ITO, ZnO/Ag/ZnO, TiO_2/Ag/TiO_2, Arc discharge single wall nanotubes (SWNTs). Adapted from [18].

2.3 Fabrication of monolayer graphene electrodes and electrode array

2.3.1 Growth of graphene by chemical vapour deposition

Graphene was first produced by mechanical exfoliation of graphite and gave the samples with the best electronic and optical properties (i.e. closest to the theoretical values for intrinsic single layer graphene). However, the size of the flakes produced (small area of single and multilayer graphene ≈50 μm) is not suitable for large scale applications. On the other hand, graphene produced by chemical vapour deposition (CVD) on transition metals (Ni and Cu are used mostly) allows the production of large graphene area, up to 30 square inches [5]. The trade-off is that the quality is lesser because of the multiple nucleation sites on the catalyst metal, whose grains are not all oriented in the same direction, and the formation of grain boundaries. These boundaries play the role of scatterers and may influence the transport properties of graphene. CVD graphene growth is currently the focus of graphene growth research on Cu [20], Ni [21][22] and SiC [23] in order to provide better quality graphene. Growing CVD graphene on copper [24] consists of introducing a mixture of H_2/CH_4 in a furnace at around 1000 °C then cooling down to room temperature.

In most cases, graphene needs to be transferred from copper to an arbitrary non-conductive substrate**.** The main challenge in this process is to introduce as few defects (e.g. cracks, tears) and impurities as possible to avoid degrading the physical properties of graphene that are actively sought for such as high electrical conductivity and transparency. Both dry (etchant free) and wet techniques to transfer graphene from metal to solid (glass, quartz, Si/SiO_2) or flexible substrates (PDMS) have been reported in the literature [25][26][27][28][29]. The most commonly used wet method involves the use of a chemical etchant ($FeCl_3$, HNO_3, $(NH_4)_2S_2O_8$) that oxidises the metal to its oxide. Such techniques necessitate the use of a carrier polymer such as PMMA or PDMS to facilitate the transfer of graphene without mechanically damaging it during the rinsing and transferring steps. PMMA is mostly removed by its dissolution in acetone, but no technique has been found yet that allows its complete removal. Several improvements to the 'classical' wet transfer technique have been reported, such as reheating the transferred PMMA-coated graphene under the curing temperature of PMMA (180°C), re-curing a layer of PMMA after transfer, post annealing [30][31] the graphene under argon-nitrogen atmosphere, oxidative atmosphere or vacuum. Other strategies to circumvent this important issue have been established that are polymer-free or involve the doping of graphene by intercalation of dopant between few layers of graphene. Dry techniques mainly consist of peeling off graphene from the substrate it has been grown on, using, for example, heat-release tape. This has been used to transfer large areas (up to 16 mm^2) of epitaxial graphene grown on SiC [32].

2.3.2 Fabrication of monolayer graphene electrodes

2.3.2.1 Reagents

Graphene was purchased from Graphene Supermarket (monolayer, on copper foil). Quartz slide were purchased from UQG Optics (Fused quartz Vitrosil 077®, 1 mm thick). Acetone (99.98%), propan-2-ol (IPA, 99.96%), hydrochloric acid (HCl, 32%), 4-methylpentane-2-one (MIBK, 99.98%), ethylmethylketone (MEK, ≥99%) were purchased from Fisher Scientific. Iron Chloride ($FeCl_3$, anhydrous, ≥ 99.99%), Nitric Acid (HNO_3, >65%), ammonium persulfate (APS, ≥ 98%), were purchased from Sigma Aldrich. Polymethylmethacrylate (PMMA, 950K and 495K,

4% in anisol) was purchased from Microchem. MF-319 developer was purchased from Dow. All chemicals were used as received.

2.3.2.2 Substrate preparation

Glass and quartz samples were cut into squares of varying sizes using a MicroAce Series 3 stand-alone 6" semi-automatic dicing saw (LoadPoint). After dicing, samples were cleaned by first sonicating in ultra-pure water, then soaking in acetone (50 °C, 30 min) followed by sonication in fresh acetone (30 min) and rinsing in fresh acetone. Then, the substrates were soaked in propan-2-ol (70 C, 30 min) followed by sonicating in fresh propan-2-ol (30 min) and rinsing in fresh propan-2-ol. The samples were then blow dried with nitrogen and further cleaned by oxygen plasma etching with a Mini-Lab RIE 80 etching system (JLS).

2.3.2.3 Transfer

First, a solution of 495K MW PMMA was spin coated one side of the copper giving about a 100 nm layer of the polymer, and was then cured for 10 min at 180 ˚C on a hot plate before being allowed to cool down to room temperature. The other side of the copper was then etched with a Mini-Lab RIE 80 etching system (JLS), as graphene was grown on both sides of the metal foil. The PMMA-coated graphene on copper was then put to float on a solution of 0.1 M $FeCl_3$ in ultra-pure water (18.2 MΩ cm) and the copper was chemically etched till the copper was not visible anymore. Then, the floating PMMA/graphene film was rinsed by transferring four times consecutively onto fresh ultra-pure water then left overnight for further rinsing. Following that, the film was transferred onto a glass or quartz slide dipped into the water beneath it and dried in an oven at 40 ˚C for 45 min to flatten the transferred graphene/PMMA and remove the water trapped beneath it. Then, the glass (or quartz)-backed graphene film was heated on a hot plate at 160 ˚C for 15 min to ease the removal of the PMMA by immersion in acetone at 50 ˚C for 30 min then rinsed in propan-2-ol at 50 ˚C for 30 min and blown-dried with nitrogen. The transfer process is summarized in Figure 2.5.

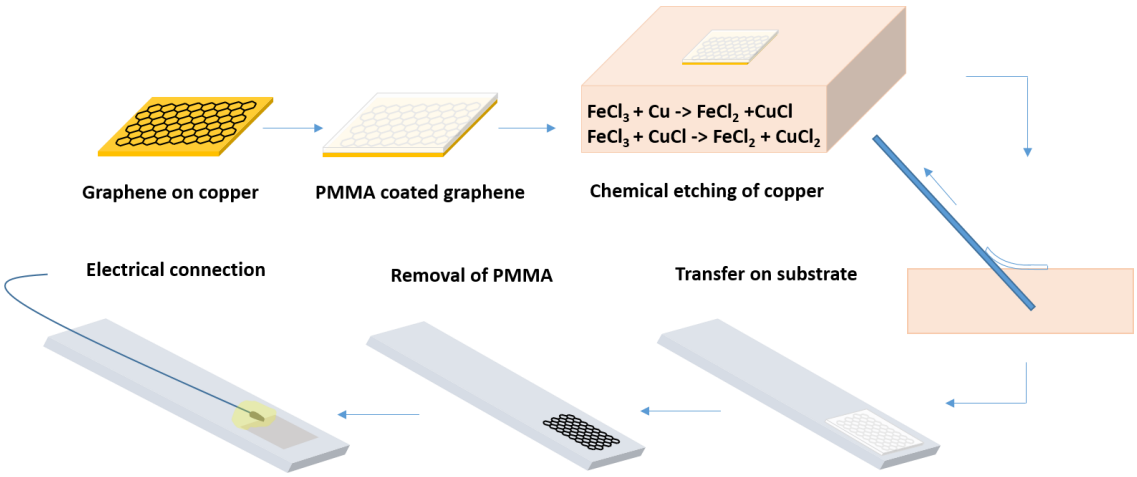

Figure 2.5: Graphene transfer method.

A typical image of the CVD graphene transferred on glass is shown in Figure 2.6 (left) where clean areas, holes and residues are visible. An SEM picture (Figure 2.6, right) of the surface (tilted at 30°) shows that the visible residues are located on the surface of the graphene and are likely to be PMMA. Strategies to remove the PMMA residues are discussed in section 4.4.

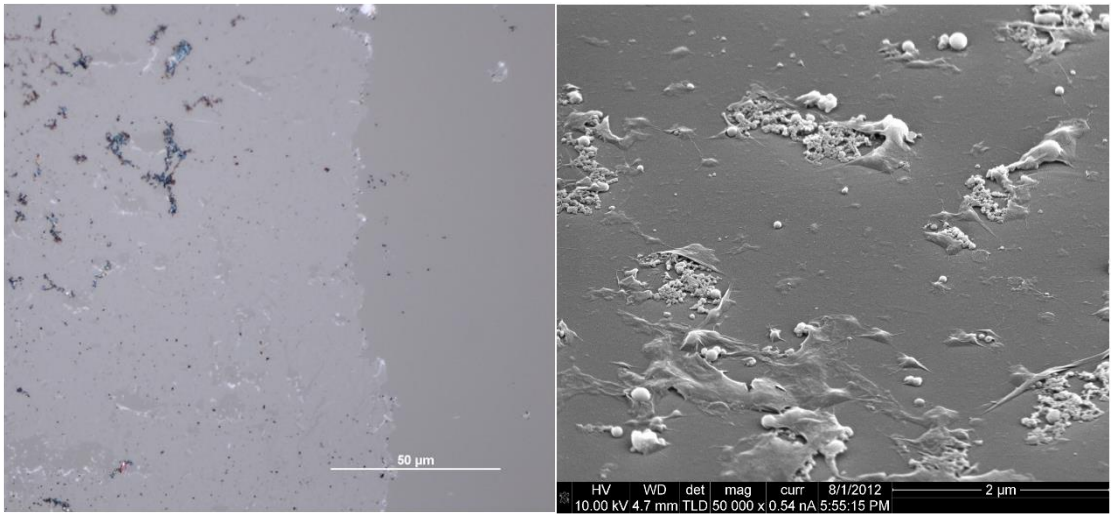

Figure 2.6: Optical image of CVD graphene after transfer on quartz (left) taken with a lens 50x and corresponding SEM picture showing residues on the surface (right). Parameters for the SEM picture: 10 kV, 0.54 nA.

A gold contact about 2 mm^2 was prepared by thermal evaporation onto the sample, by use of an appropriate mask. Then a tinned wire contact was made via silver epoxy, and the contact was electrically isolated with an epoxy resin.

2.3.2.4 Fabrication of graphene electrode arrays by electron beam lithography

First, a piece of graphene is transferred on a substrate as described in part 3.2.3. Then a 150 nm layer of PMMA 495K is spin-coated on the sample and cured for 10 min at 180 °C. After that, a 150 nm layer of HSQ is spin coated on top of the PMMA and cured for 3 min at 220 °C, HSQ is a negative resist that is used to protect the areas of graphene that will be the electrodes. If the substrate is not conductive, a 10 nm layer of aluminium is deposited on top of the HSQ layer by thermal evaporation to provide a path for electrons during the lithography. The sample is then introduced in the electron beam lithography machine and is exposed to an electron beam according to a pattern drawn with Autocad. Then, the unexposed area of HSQ are removed by soaking the sample 3 minutes in the developer MF-319 followed by rinsing in ultra-pure water. After that, the PMMA and graphene that are no longer protected by HSQ are etched by reactive ion etching using a Mini-Lab RIE 80 etching system (JLS). Finally, the remaining PMMA and HSQ is removed by immersing the sample in acetone at 50 °C for 30 minutes then rinsing in IPA at 50 °C for 30 minutes, and blow drying with nitrogen. Another lithography step is used to deposit gold electrical connections. This time, a positive resist, PMMA, is used in order to expose only wanted areas. A layer of 300 nm PMMA 495K is spin coated on the sample (if the pattern features are fine, a double layer of 495K then 950K is spin coated) and cured for 10 minutes at 180 °C. Then, a 10 nm layer of aluminium is deposited by thermal evaporation if the substrate is not conductive to provide a path for electrons from the beam to the substrate holder (silver paint is used to connect the Al and the holder), and the sample is exposed to an electron beam according to a pre-programmed pattern. Then, the aluminium was removed by immersing the sample for 3 minutes in MF-319 followed by rinsing for 3 minutes in ultra-pure water. A developer solution composed of IPA:MIBK:MEK (15:5:1) was used to remove exposed PMMA areas. The sample was left in the developer till the edges of the pattern created in the PMMA were sharp, then rinsed for 1 minute in IPA and blow dried with nitrogen. Then, 10 nm of Cr and 50 nm of gold are evaporated on the sample and the remaining PMMA

removed by immersing the sample in acetone at 50 °C for 30 minutes then rinsing in IPA at 50 °C for 30 minutes, and blow drying it with nitrogen. After placing the substrate in a chip carrier, electronic connections are made using a wire bonder.

2.3.3 Characterisation of graphene electrodes by optical methods

2.3.3.1 Characterisation by optical contrast

Though only 1 atom thick, it is possible to detect graphene on Si/SiO_2 and quartz substrates and quantify the number of graphene layers by optical contrast. With white light, the optical contrast on Si/SiO_2 increases by 5% per layer and it can be increased by filtering the white light with a green filter. The contrast between graphene and the quartz substrate is clearly visible in Figure 2.6, left, and holes and contamination can be observed that were created during the process of transfer of the graphene on the quartz. Figure 2.7 shows a picture of graphene flakes produced by exfoliating graphite, taken with white light and where graphene flakes with different numbers of graphene layers are visible.

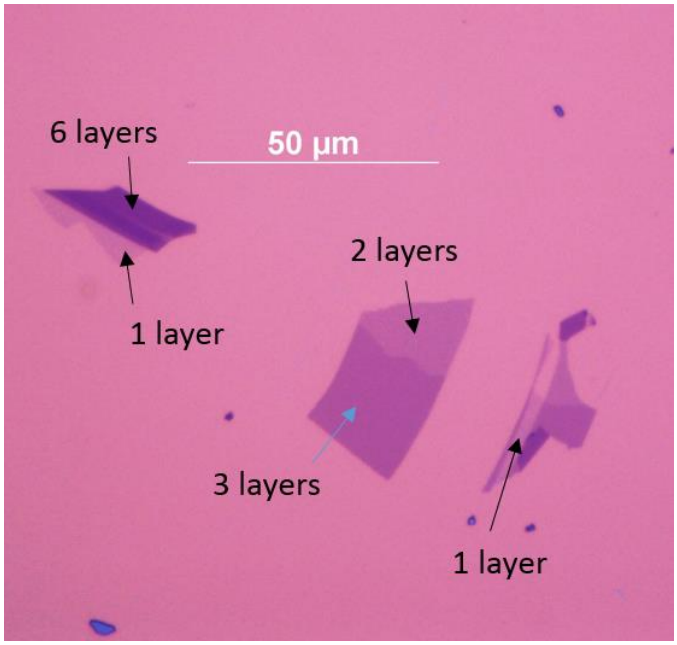

Figure 2.7: Optical image with white light of exfoliated graphene on 300 nm SiO_2 .

Raman spectroscopy is a powerful tool to determine the quality and electronic structure of graphene, and the number of layers in the sample [33][34][35] [36].

2.3.3.2 Characterisation by Raman spectroscopy

Raman spectroscopy is based on the Raman effect which relies on the observation that a small proportion of an incident electromagnetic wave is scattered inelastically when it interacts with matter. It means that after being excited to a virtual state, some molecules relax to a different vibrational state than their original one. As a consequence, while most photons conserve the same wavelength after interaction (Rayleigh scattering), a small fraction have a higher wavelength (Stokes scattering) or a lower wavelength (anti-Stokes scattering) than the incident light. The difference in frequency between the incident and scattered photons is called Raman shift and corresponds to the difference in energy between the original and new vibrational state of the molecule/atom irradiated. Raman spectra are recorded as intensity (in u.a.) with respect to the Raman shift or wavenumber (in cm^{-1}).

In the case of graphene, electrons that are photo excited by incident coherent light either relax by Rayleigh scattering to their original state (in the majority of cases) or lose energy by scattering on a phonon before relaxing to their original state. The latter process is called resonant Raman Stokes scattering. The Raman spectrum of graphene is very well known. The main features are the G and 2D peaks located respectively at 1580 cm^{-1} and 2670 cm^{-1}. When the sample contains defects, or when measurements are done on the edges of graphene, a D peak is visible at 1350 cm^{-1}. The G peak corresponds to the stretching of the sp_2 bonds. The D and 2D peaks are associated with a double resonance where after excitation, an electron with wavevector originating from one Dirac cone scatters first off an optical phonon to an adjacent Dirac cone, then scatters back off a defect (case of the D peak) or an optical phonon (case of the 2D peak), and relaxes back to its original state. The different scattering and relaxation processes leading to the Raman spectrum of graphene are described in Figure 2.8.

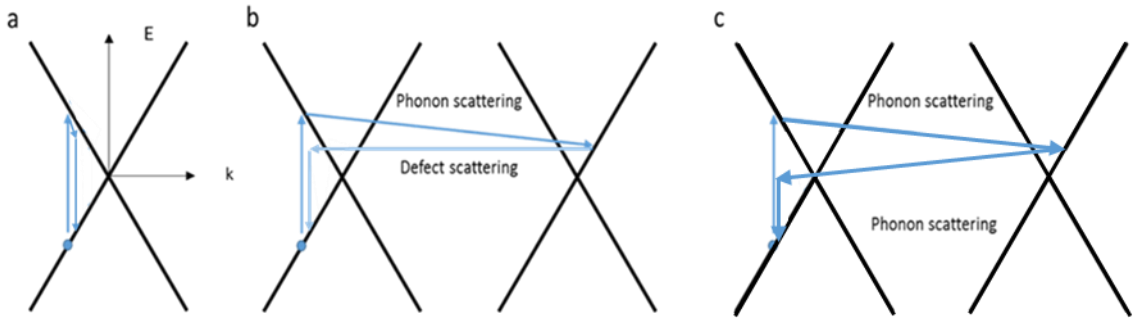

Figure 2.8: Raman spectral processes associated with the main features of the Raman spectrum of graphene: a) G peak, b) D peak, c) 2D peak.

The ratio of the intensity of the 2D and G peak should be equal to 2 for defect free single layer graphene. Raman measurements were recorded with a Renishaw RM 1000 microscope, at a laser wavelength excitation of 532 nm, 10 % power, recording 3 successive accumulations with 10 s acquisition time.

Figure 2.9 shows the Raman spectrum of CVD graphene transferred on a glass substrate. The spectrum shows a broad peak corresponding to the glass substrate at 1097 cm^{-1}, a D peak at 1344 cm^{-1}, a G peak at 1589 cm^{-1} and a 2D peak at 2678 cm^{-1}. Within the resolution of the Raman microscope, the values of the main peaks are similar to those of graphene on Si/SiO_2. The ratio of the 2D peak to the G peak is ~2 which is expected for monolayer graphene. The CVD graphene contains a certain amount of defects, as shown by the D peak. The ratio of the G peak to the D peak is proportional to the inter-defect distance and therefore may be interpreted as the more defects the graphene sheet contains, the higher the ratio of the D to the G peak. The shape of the 2D peak is indicative of the number of graphene layers. Here Raman spectroscopy is mostly used to get an indication of the number of defects in one sample and to assess the homogeneity of graphene used to prepare the samples.

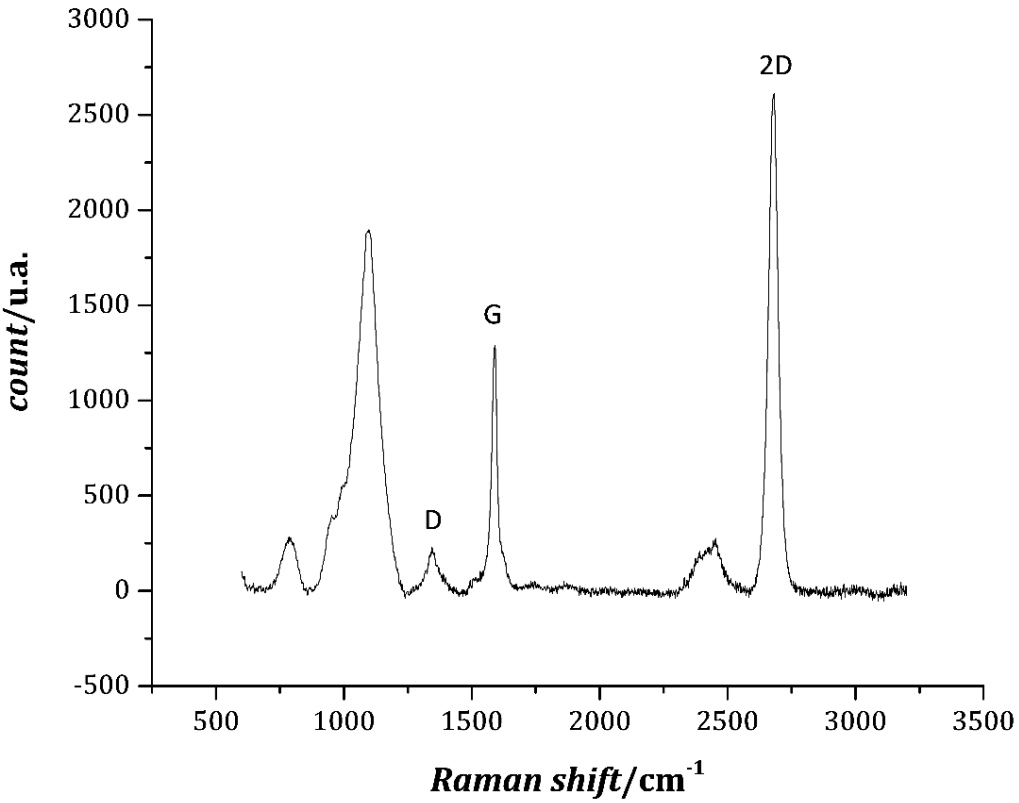

Figure 2.9: Raman spectrum of CVD graphene transferred onto a glass substrate. Laser: 532 nm.

2.4 Graphene for electrochemical biosensors

Electrochemistry is a very sensitive and inexpensive method that also allows the selective detection of electroactive analytes. As a transparent and conductive material, graphene is a very attractive material for bio-sensing devices utilising electrochemical and optical readout methods. Producing it is also low-cost and has a low environmental impact. The biocompatibility of graphene and graphene-based materials, however, has yet to be clearly established [37].

The surface of graphene is heterogeneous and electron transfer on graphene has been reported [37][38] to occur at the edges (ground boundaries) and at defects, where the density of electronic states (DOS) is higher. Graphitic islands were also observed [39] on commercially available CVD graphene and have been shown to dominate the electron transfer. A recent study [39] however shows some evidence of high activity on highly oriented pyrolytic graphite, and to the extent that

graphene can be considered a model for the base plane of graphite, faster electron transfer (higher heterogeneous rate constant) may not be restricted to the edge planes. Also, since CVD graphene electrodes are manually prepared, a certain variability in electroactivity is expected, and the reproducibility of the measurements depends on the ability to fabricate the electrodes in a reproducible manner. A first strategy to achieve this reproducibility consisted of producing electrodes from the same piece of transferred graphene and is the subject of section 4.4, and a second one consisted of reusing the same electrode by renewing the surface and is the object of Chapter 4 part 3.2 .

2.4.1 A simple model for electrochemical reactions

The ease with which electrons may transfer between a solution species and an electrode (the current is a direct measure of the rate of these processes) is affected by numerous factors, including the intrinsic properties of the solution species, its rate of diffusion through the electrolyte solution, and the presence of any other adsorbed species that may restrict the intimate contact with the surface of the electrode. This blocking effect, combined with the intrinsic characteristic electrode potential at which the electron transfer reaction may occur, offers a means of using the reaction to quantify the amount of the adsorbed species blocking its path to the electrode surface. As an example, the presence of a molecule on the surface of a metal electrode may prevent the passage of an electric current due to no reaction at that point, and therefore it may not be possible to quantify this adsorbed molecule. A typical electrochemical cell used to perform such measurements consists of three electrodes: the working (WE), the reference (Ref) and the counter (CE) electrodes. These are arranged in an electrolyte (ionic solution), as shown in Figure 2.10 . The redox reaction under study and being blocked by the adsorbed molecule, happens at the working electrode and the potential that drives the reaction is measured between the working and reference electrodes. The necessary second electrode reaction (to complete the circuit) occurs at the CE, but since this is arranged to be large relative to the working electrode, the current is limited by processes happening at the latter and so is proportional to the rate of reaction at the working electrode. For this reason, it is possible to quantify species at the working electrode.

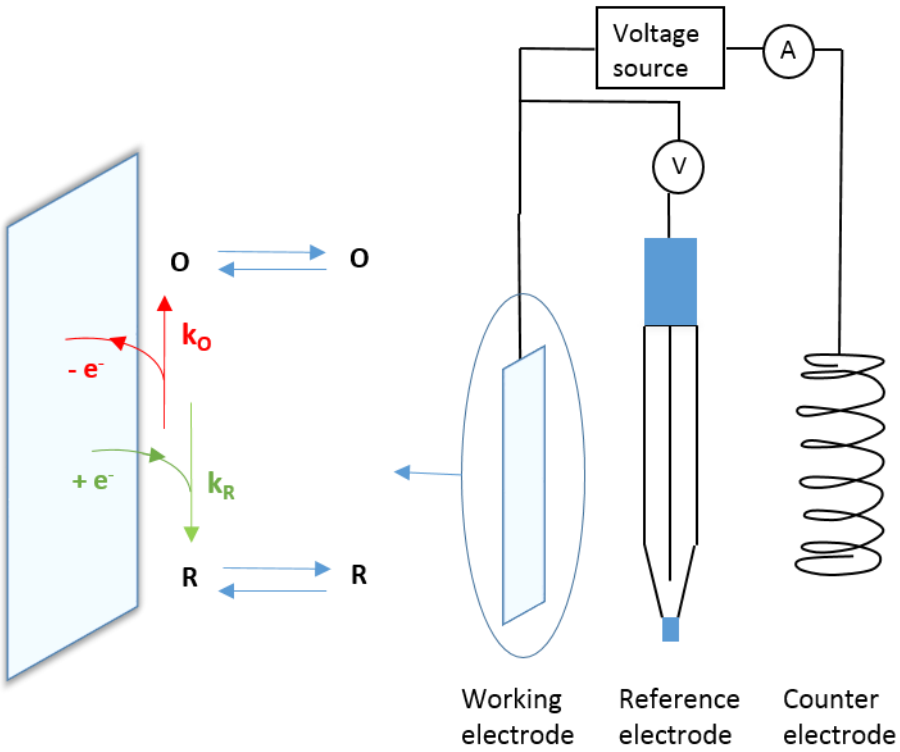

Figure 2.10: Three-electrode electrochemical cell (right) and zoom in of a simple redox reaction happening at the working electrode (left). O represents the oxidised species, R the reduced species, e^- represents a single electron, k_O is the oxidation reaction rate constant and k_R is the reduction reaction rate constant.

In Figure 2.10 (left) is shown a scheme of the simple redox reaction

$$O + ne \underset{k_O}{\overset{k_R}{\rightleftarrows}} R \tag{7}$$

where n is the number of electrons exchanged between the oxidised, O, and the reduced, R, forms of the O/R redox couple at the interface with the working electrode, and the two species are not involved in other chemical reactions.

2.4.1.1 General expression of the total current flowing at the electrode/electrolyte interface

The oxidation and reduction reactions have respective reaction rate constants k_O and k_R and the total current transferred at the working electrode is the difference of two partial currents, i_a (anodic current), and i_c (cathodic current) which are defined as followed:

$$i_a = nFAk_O C_O(0,t) \tag{8}$$

$$i_c = -nFAk_R C_R(0,t) \tag{9}$$

where $C_O(0,t)$ and $C_R(0,t)$ are the O and R concentrations at the interface (x=0) with the working electrode at any time t, F is the Faraday constant and A is the active surface area of the working electrode.

The combination of i_a ad i_c gives a total measured current as

$$i = i_a + i_c = nFA\,[k_O C_O(0,t) - k_R C_R(0,t)] \tag{10}$$

The overall sign of the total current is arbitrary, but the convention adopted in this thesis defines the overall anodic (oxidation) current as positive and the overall cathodic (reduction) current as negative.

The reaction rate constants are given by a simple transition-state-theory expression

$$k = k^0 e^{\frac{-E_a}{RT}} \tag{11}$$

where the activation energy, E_a, depends on the interfacial potential existing at the working electrode/electrolyte interface. The activation energy can then be written as a linear function of the overpotential η, defined as the difference between the applied potential (potentials are measured between working and reference electrodes) and the zero-current potential, E_{eq}, conveniently taken here to be the formal potential $E^{0'}$, but in general related to the formal potential by the Nernst equation written as

$$E_{eq} = E^{o\prime} + \frac{RT}{nF} ln \frac{C_{\mathrm{O}}^{\infty}}{C_{\mathrm{R}}^{\infty}} \tag{12}$$

Where C_{O}^{∞} and C_{R}^{∞} are the bulk concentrations in oxidised and reduced species. Taking $E_{\mathrm{eq}} = E^{0'}$ is convenient as this position corresponds to equal oxidation and reduction rates at equal concentrations of oxidised and reduced species, in which case $k_{\mathrm{R}} = k_0 = k^0$, which is called the standard rate constant and is an indication of

the intrinsic kinetic facility of the electrode reaction (a reaction with a large k^0 delivers a large current for a small overpotential). With $E_{eq} = E^{0'}$, the diagram in Figure 2.11 shows in terms of the standard Gibbs energy the effect of applying an overpotential on the activation barrier for oxidation and reduction.

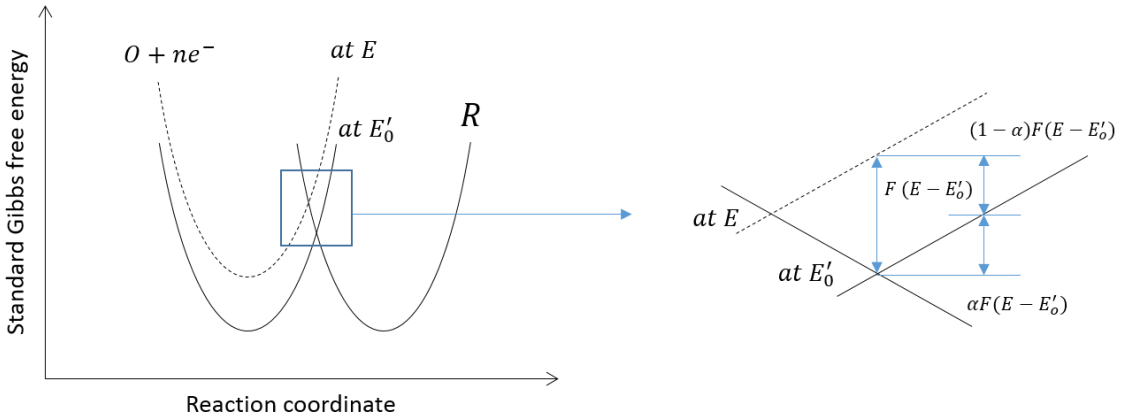

Figure 2.11: Effect of applying a potential E (dotted line) at an electrode-electrolyte interface containing both species of a redox couple (O and R) at equilibrium, $\boldsymbol{E^{0'}}$ (solid lines). The figure on the right is a magnification of the intersection of Gibbs energy profiles of the reduced and oxidised species, shown in the left figure.

2.4.1.2 The current-overpotential equation

It is usual to consider the intersection region of the parabola to be linear, to permit simple expression of the barrier symmetry in terms of a constant α, as shown in Figure 2.11 (right). This constant α, called the transfer coefficient, is interpreted as the fraction of the total energy change at the electrode-electrolyte interface (by application of an over potential) by which the activation energy barrier for a reduction reaction is lowered. The fraction becomes $1-\alpha$ for the oxidation. The expressions of the reaction rate constants thus written in terms of α and $E - E^{0'}$ as

$$k_O = k^0 e^{\left[\frac{(1-\alpha)nF}{RT}(E-E^{0'})\right]} \quad (13)$$

$$k_R = k^0 e^{\left[\frac{-\alpha nF}{RT}(E-E^{0'})\right]} \quad (14)$$

It is possible to express the total current as the sum of i_a and i_c, including the expressions for k_O and k_R, and the general expression for the overpotential, $\eta = E - E_{eq}$. The result is the current-overpotential equation.

$$i = i_O \left[\frac{C_R(0,t)}{C_R^{\infty}} e^{\left[\frac{(1-\alpha)nF}{RT}\eta\right]} - \frac{C_O(0,t)}{C_O^{\infty}} e^{\left[\frac{-\alpha nF}{RT}\eta\right]} \right] \quad , \tag{15}$$

where the current i_O is termed the exchange current, given by

$$i_O = nFAk^0 (C_O^{\infty})^{(1-\alpha)} (C_R^{\infty})^{\alpha} \quad , \tag{16}$$

and being equal to both i_c and i_a at equilibrium.

The parameters C_O^{∞} and C_R^{∞} are the oxidized and reduced species bulk concentrations. The ratios $\frac{C_R(0,t)}{C_R^{\infty}}$ and $\frac{C_O(0,t)}{C_O^{\infty}}$ are therefore an indication of the effects of mass transport on the current.

The left term of the current-overpotential equation represents the anodic contribution to the total current, and the right term represents the cathodic contribution. The total current is represent in plain line and the partial currents in dashed lines on Figure 2.12.

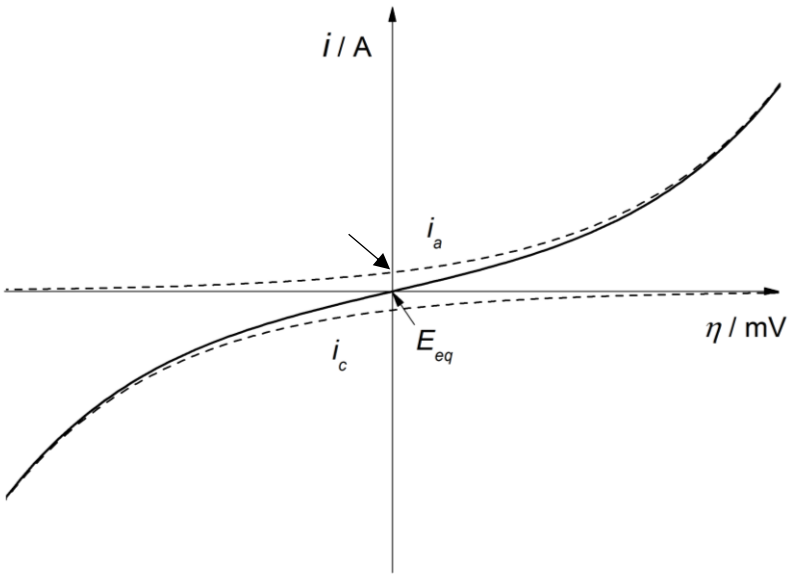

Figure 2.12: Total current as a function of applied potential at the electrode-electrolyte interface, as the sum of cathodic and anodic partial currents (see Equation 15).

2.4.1.3 Kinetics limitation and the Butler-Volmer equation

The electron transfer rate (current) at the electrode-electrolyte interface may be limited by the kinetics of the reaction or the diffusion of O and R to/from the electrode interface (or some intermediate position). In the case where the kinetics of the reaction are limiting, the surface reactant concentrations are approximately equal to their bulk concentrations and equation 15 simplifies to

$$i = i_O \left[e^{\left[\frac{(1-\alpha)nF}{RT}\eta\right]} - e^{\left[\frac{-\alpha nF}{RT}\eta\right]} \right] \tag{17}$$

called the Butler-Volmer equation, which is function of the exchange current i_O, the transfer coefficient α and the overpotential η upon which application the current increases steadily. This equation indicates that by application of high positive (negative) values of η, the left (right) term in the Butler-Volmer equation is dominant and the current is predominantly anodic (cathodic).

The exchange current, i_0, is a function of the standard rate constant k^0 of the O/R redox couple (as shown in equation 16) and therefore is representative of how quick a system is to deliver a desired current density without having to apply a

high overpotential. For instance, a system with a large exchange current will deliver high current within a few millivolts from the equilibrium potential. On the other hand, systems that have a small exchange current will not deliver a significant current unless a high overpotential, called the activation overpotential, is applied. For sufficiently large overpotentials, the kinetics of the heterogeneous process is so quick that the rate of charge transfer becomes limited by mass transfer to the electrode and the current levels off.

2.4.1.4. Diffusion limitation in potential sweeps

In this part, the oxidised and reduced species are considered to only migrate by diffusion (no migration or convection).

The concentration profile, $C(x,t)$, and the diffusion limited current, $i(t)$, are determined resolving Fick's first and second laws given respectively by the following equations (for an oxidised species):

$$J_{\mathrm{O}}(x,t) = -D_{\mathrm{O}} \frac{\partial C_{\mathrm{O}}(x,t)}{\partial x} \tag{18}$$

$$\frac{\partial C_{\mathrm{O}}(x,t)}{\partial t} = D_{\mathrm{O}} \frac{\partial^2 C_{\mathrm{O}}(x,t)}{\partial x^2} \tag{19}$$

where $J_{\mathrm{O}}(x,t)$ and $C_{\mathrm{O}}(x,t)$ are respectively the flux and concentration of oxidised species at position x and time t, and D_{O} is the diffusion coefficient of the oxidised species. The concentration profiles of the oxidised and reduced species are shown in Figure 2.13, considering that only O is present in the solution at $t = 0$.

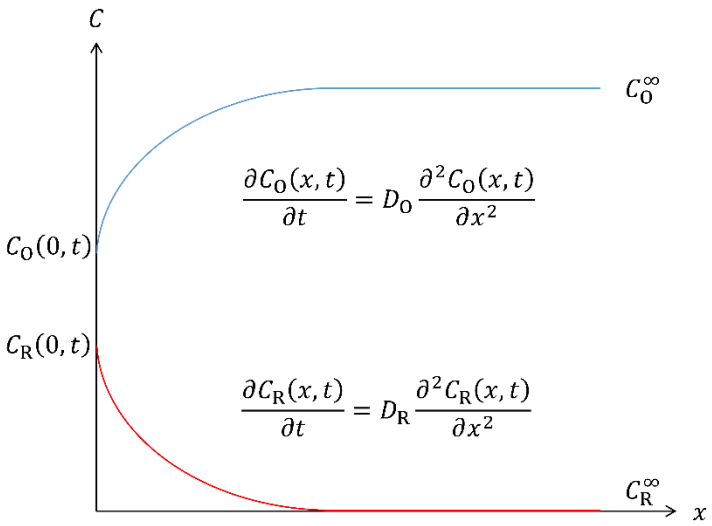

Figure 2.13: Concentration profiles of the oxidised, O and reduced, R, species of a redox couple at time t. The equations correspond to Fick's second law applied to O and R.

Considering that the quantity of electrons transferred per unit time must be proportional to the number of oxidised molecules reaching the surface of the electrode per unit time (a flux balance), it is always possible to relate the current and the concentration profile of the oxidised species at $x = 0$ by the following equation (case of an oxidation reaction)

$$\frac{i}{nFA} = -D_O \left[\frac{\partial C_O(x,t)}{\partial x}\right]_{x=0} = D_R \left[\frac{\partial C_R(x,t)}{\partial x}\right]_{x=0} . \qquad (20)$$

Equation 20 shows that the current is proportional to the slope of the concentration profile at the surface of the electrode. This relation is used to explain the evolution of the current when the potential is driven away from the equilibrium potential as in a typical voltammetry experiment and illustrated in the inset of Figure 2.14. When driven to more the positive potentials, the energy of the electrons in the metal decreases and the oxidation reaction is predominant. The consequent evolution of the concentration profile of the oxidised species and the corresponding evolution of the current are shown respectively in Figure 2.14 and Figure 2.15 (taking into account the diffusion limitation). When a negative potential sweep is applied at the electrode (inset of Figure 2.15), $C_O(x,t)$

decreases, and the slope $\left[\frac{\partial C_O(x,t)}{\partial x}\right]_{x=0}$ increases (regions 1, 2 and 3), as well as the current according to equation 20 till the surface is completely depleted in O (region 4). After this point, the slope of the concentration profile at the surface keeps decreasing, as a depletion region in O grows out from the electrode, till it reaches a limit set by natural convection. Hence the profile of the current in regions 5 and 6. A reduction peak is thus created as shown on Figure 2.15, and its height is proportional to C_O^∞.

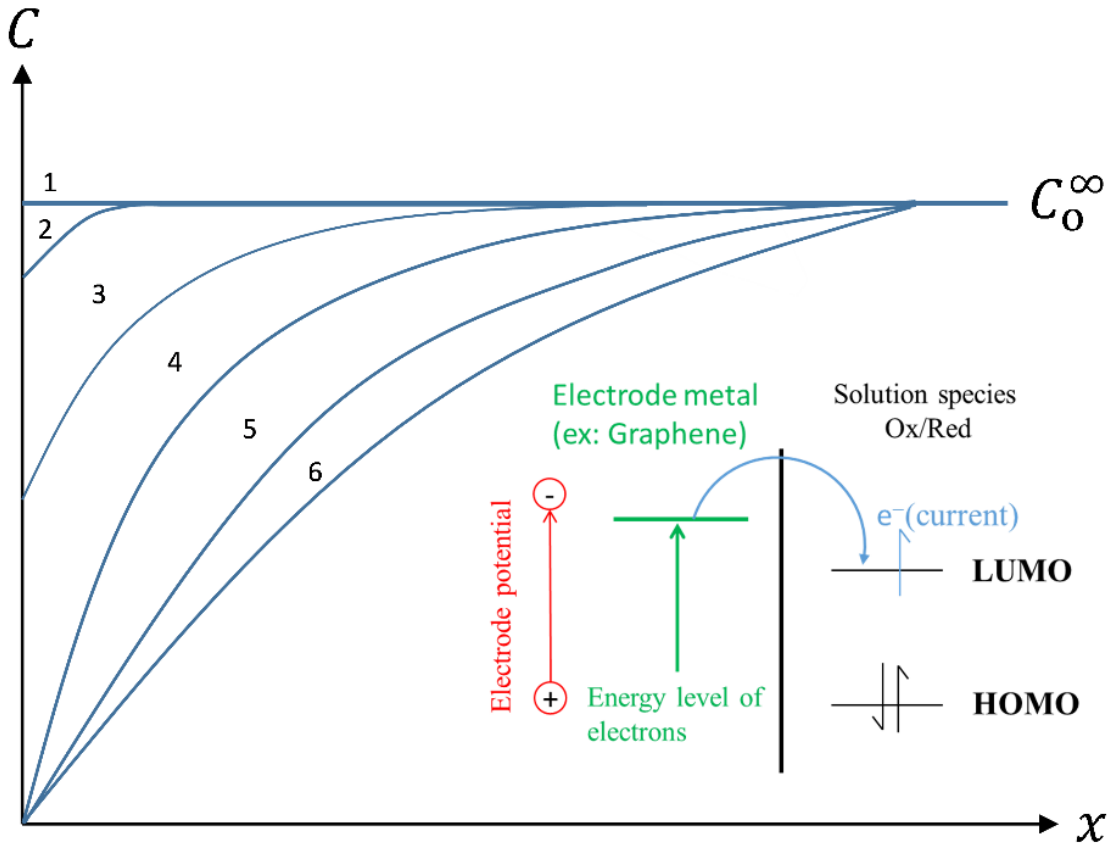

Figure 2.14: Time-dependant concentration profiles of the oxidised species of a redox couple. The numbers 1 to 6 correspond to increasing time and so increasingly negative E (reduction).

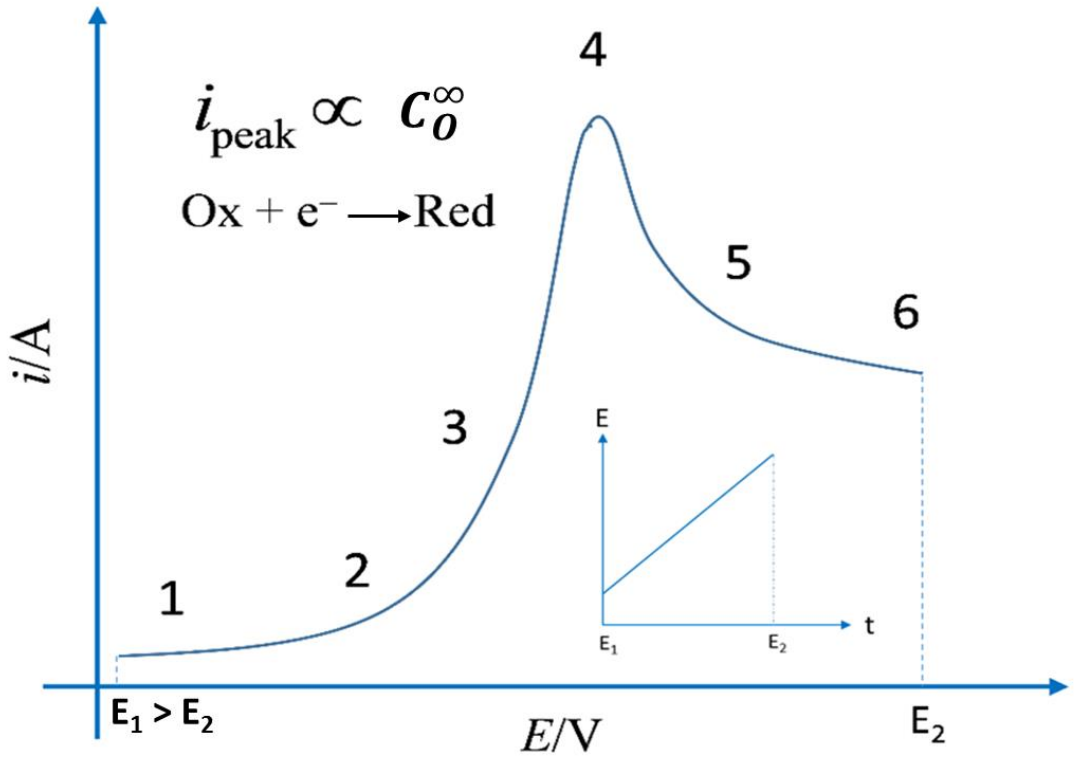

Figure 2.15: Current-potential profile of a redox couple when the potential at the working electrode is varied linearly from E_1 to E_2 (the applied potential profile is shown in the inset)

Similarly, when a negative potential slope is applied at the electrode and the system is diffusion limited, a reduction peak is created.

2.4.1.5 Kinetic limitation

As mentioned before, if a system is kinetically slow, it requires more energy than the diffusion limited case before any significant current is produced, and the oxidation and reduction peak appear further away from the equilibrium potential. Therefore, the current response of a system when driven far away from its equilibrium gives indications about its kinetics, the bulk concentrations of the oxidised and reduced species of a redox couple and the nature of the redox couple (as E_{eq} is function of $E^{0'}$ of the redox couple). This is used in voltammetry techniques like cyclic voltammetry (see section 4.2.1) and square-wave voltammetry (see section 4.2.3).

The diffusion rate increases with the sweep rate. Figure 2.16 shows the concentration profiles and corresponding *i*-*E* profiles at the working electrode of the oxidised species for three different sweep rates.

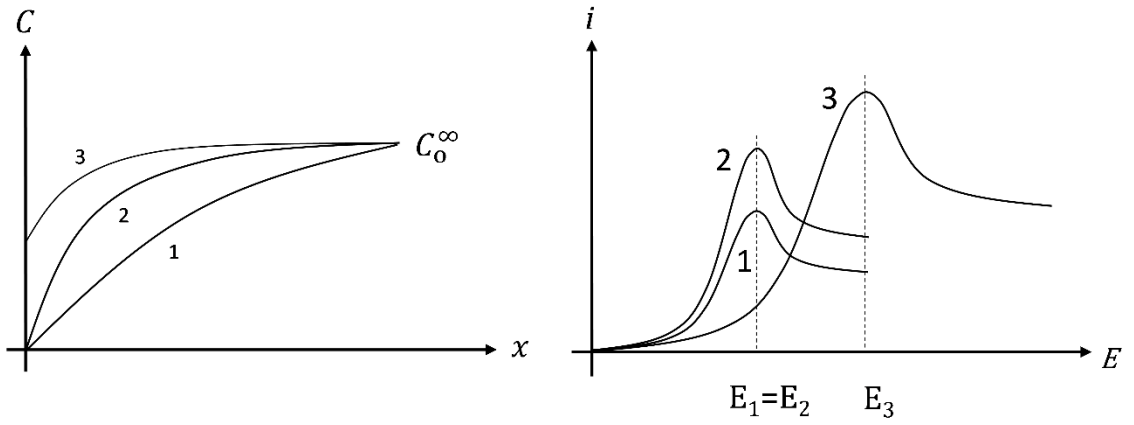

Figure 2.16: Influence of the scan rate ν (V s^{-1}) of the potential applied at the working electrode on the concentration profile at the working electrode of the oxidised species (left) and on the reduction current peak height. The numbers 1, 2 and 3 correspond to increasing scan rates.

Increasing the sweep rate (curve 1 to curve 2) increases the diffusion rate (because there is less time for a concentration profile to extend into solution, it is thus steeper) and therefore the height of the peak current. However, when the scan rate increases even more (curve 3), the kinetics becomes limiting and it requires more energy to reduce the oxidised species. Therefore, the current peak lies further away from the equilibrium potential ($E_3 > E_1 = E_2$).

Alternatively, the same behaviour should be expected for an AC signal applied at the working electrode and if the frequency of the signal is increased (analogous to increasing the potential sweep rate in voltammetry, although not linear).

2.4.1.6 Response to a small sinusoidal excitation

Sections 4.1.4 and 4.1.5 were concerned with the study of the transient response of a system brought far away from equilibrium. This part is concerned with the steady-state response of a simple redox system $O + ne \rightleftharpoons R$ stimulated from a position of equilibrium at the electrode surface by a small amplitude AC potential signal. The amplitude of the signal is small so that the system response to the AC

stimulation is linear and the response signal is also an AC signal of the same frequency (or harmonic thereof). A typical value for the amplitude is 10 mV. The AC voltage is superimposed on a DC potential that sets the mean surface concentrations of the O and R species.

The electrochemical cell is considered as an impedance to the passage of charges and a measurement of the faradaic impedance (impedance to the passage of the faradaic current) and gives indication of interfacial kinetic phenomena. One common method to treat the faradaic impedance theoretically in terms of electrochemical phenomena at the interface is to compare the electrochemical cell to an electrical circuit of resistances and capacitances. One commonly used circuit is called a Randles equivalent diagram, which is shown in Figure 2.17 (a) . The parallel branches correspond to the contributions of the faradaic current and of the charging of the double layer. In this circuit, R_Ω is the resistance of the electrolyte, C_{dl} is the capacitance of the double-layer, Z_f is the faradaic impedance. Figure 2.17 (b) shows the separation of Z_f into a series resistance R_s and a pseudo capacitance C_s. It will be shown later in this section that it can alternatively been described as a pure resistance (to charge transfer) R_{ct} and an impedance Z_w, the Warburg impedance, that represents the impedance to mass transfer by diffusion.

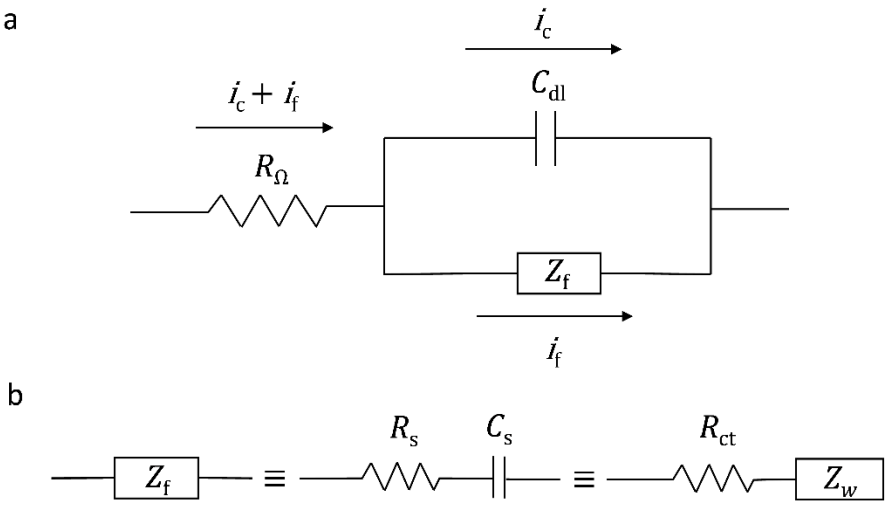

Figure 2.17: Randles equivalent circuit diagram (a) and subdivision of Z_f into $\boldsymbol{R_s}$ and $\boldsymbol{C_s}$, or R_{ct} and Z_w (b)

Upon passage of a current $i = Isin(\omega t)$ at the working electrode the voltage drop is

$$E[i, C_{\mathrm{O}}(0,t), C_{\mathrm{R}}(0,t)\,] = iR_{\mathrm{S}} + \frac{q}{C_{\mathrm{S}}} \quad . \tag{21}$$

Hence

$$\frac{dE}{dt} = R_{\mathrm{S}}\frac{di}{dt} + \frac{q}{C_{\mathrm{S}}}i = R_{\mathrm{S}}\omega I\cos\omega t + \frac{q}{C_{\mathrm{S}}}I\sin\omega t \quad . \tag{22}$$

As E is a function of $i, C_{\mathrm{O}}(0,t)$ and $C_{\mathrm{R}}(0,t)$, dE/dt can be written

$$\frac{dE}{dt} = \frac{\partial E}{\partial i}\frac{di}{dt} + \frac{\partial E}{\partial C_{\mathrm{O}}(0,t)}\frac{dC_{\mathrm{O}}(0,t)}{dt} + \frac{\partial E}{\partial C_{\mathrm{R}}(0,t)}\frac{dC_{\mathrm{R}}(0,t)}{dt} \quad , \tag{23}$$

with

$$R_{\mathrm{ct}} = \left(\frac{\partial E}{\partial i}\right)_{C_{\mathrm{O}}(0,t),C_{\mathrm{R}}(0,t)} \quad , \tag{24}$$

$$\beta_{\mathrm{O}} = \left[\frac{\partial E}{\partial C_{\mathrm{O}}(0,t)}\right]_{i,C_{\mathrm{R}}(0,t)} \quad , \tag{25}$$

$$\beta_{\mathrm{R}} = \left[\frac{\partial E}{\partial C_{\mathrm{R}}(0,t)}\right]_{i,C_{\mathrm{O}}(0,t)} \quad . \tag{26}$$

These three parameters depend on the kinetics of the redox reaction. The time derivatives of $C_{\mathrm{O}}(0,t)$ and $C_{\mathrm{R}}(0,t)$ are determined using mass transfer, assuming a semi-infinite linear diffusion and the initial conditions $C_{\mathrm{O}}(0,t) = C_{\mathrm{O}}^{\infty}$ and $C_{\mathrm{R}}(0,t) = C_{\mathrm{R}}^{\infty}$. Fick's law for both species gives:

$$\frac{\partial C_{\mathrm{O}}(0,t)}{\partial t} = -D_{\mathrm{O}}\frac{\partial^2 C_{\mathrm{O}}(0,t)}{\partial x^2} \quad , \tag{27}$$

$$\frac{\partial C_{\mathrm{R}}(0,t)}{\partial t} = -D_{\mathrm{R}}\frac{\partial^2 C_{\mathrm{R}}(0,t)}{\partial x^2} \quad . \tag{28}$$

From section 4.1.4

$$\frac{i}{nFA} = -D_{\mathrm{O}}\left(\frac{dC_{\mathrm{O}}(x,t)}{dx}\right)_{x=0} = D_{\mathrm{R}}\left(\frac{dC_{\mathrm{R}}(x,t)}{dx}\right)_{x=0} \quad . \tag{29}$$

Using Laplace transformations and Fresnel standard integrals, one can find

$$C_{\mathrm{O}}(0,t) = C_{\mathrm{O}}^{\infty} + \frac{i}{nFA(2D_{\mathrm{O}}\omega)^{1/2}}(\sin\omega t - \cos\omega t) \quad , \tag{30}$$

$$C_{\mathrm{R}}(0,t) = C_{\mathrm{R}}^{\infty} + \frac{i}{nFA(2D_{\mathrm{R}}\omega)^{1/2}}(\sin\omega t - \cos\omega t) \quad , \tag{31}$$

and the time derivatives of $C_{\mathrm{O}}(0,t)$ and $C_{\mathrm{R}}(0,t)$ are

$$\frac{\partial C_{\mathrm{O}}(0,t)}{\partial t} = \frac{i}{nFA}\left(\frac{\omega}{2D_{\mathrm{O}}}\right)^{1/2}(\cos\omega t + \sin\omega t) \quad , \tag{32}$$

$$\frac{\partial C_{\mathrm{R}}(0,t)}{\partial t} = \frac{i}{nFA}\left(\frac{\omega}{2D_{\mathrm{R}}}\right)^{1/2}(\cos\omega t + \sin\omega t) \quad . \tag{33}$$

After substitution in 23, dE/dt is obtained:

$$\frac{dE}{dt} = \left(R_{\mathrm{ct}} + \frac{\sigma}{\sqrt{\omega}}\right) I\omega\cos\omega t + I\sigma\sqrt{\omega}\sin\omega t \quad , \tag{34}$$

with

$$\sigma = \frac{1}{nFA\sqrt{2}}\left(\frac{\beta_{\mathrm{O}}}{\sqrt{D_{\mathrm{O}}}} - \frac{\beta_{\mathrm{R}}}{\sqrt{D_{\mathrm{R}}}}\right) \quad . \tag{35}$$

R_{s} and C_{s} are obtained by equalizing equations 34 and 22:

$$R_{\mathrm{s}} = R_{\mathrm{ct}} + \frac{\sigma}{\sqrt{\omega}} \quad , \tag{36}$$

$$C_{\mathrm{s}} = \frac{1}{\sigma\sqrt{\omega}} \quad . \tag{37}$$

Equations 36 and 37 show that the faradaic impedance Z_{f} can be redefined as a resistance that mainly depends on the heterogeneous charge transfer kinetics, R_{ct}, and an impedance Z_f, called the Warburg impedance, that comes from mass transport and is composed of a frequency dependent resistance $\frac{\sigma}{\sqrt{\omega}}$ and of a pseudo capacitance $\frac{1}{\sigma\sqrt{\omega}}$ in series (Figure 2.17 (b)).

The Warburg impedance is then defined as

$$Z_f = R_{\mathrm{ct}} - j\frac{1}{\omega C_{\mathrm{s}}} = R_{\mathrm{ct}} + \left[\frac{\sigma}{\sqrt{\omega}} - j\frac{\sigma}{\sqrt{\omega}}\right] \tag{38}$$

To completely evaluate R_{ct} and C_{s}, it is required to interpret R_{ct}, β_{O} and β_{R} in electrochemical terms.

As the amplitude of the excitation is small, that is, $\frac{\alpha nF}{RT}\eta << 1$, a Taylor expansion of equation 17 gives

$$\eta = \frac{RT}{nF}\left[\frac{i}{i_0} + \frac{C_{\mathrm{R}}(0,t)}{C_R^{\infty}} - \frac{C_{\mathrm{O}}(0,t)}{C_O^{\infty}}\right] \tag{39}$$

from which R_{ct}, β_{O}, β_{R} and σ are determined

$$R_{\mathrm{ct}} = \left(\frac{\partial E}{\partial i}\right)_{C_{\mathrm{R}}(0,t),C_{\mathrm{O}}(0,t)} = \frac{RT}{nFi_0} \tag{40}$$

$$\beta_{\mathrm{O}} = \left[\frac{\partial E}{\partial C_{\mathrm{O}}(0,t)}\right]_{i,C_{\mathrm{R}}(0,t)} = \frac{RT}{nFC_O^{\infty}} \tag{41}$$

$$\beta_{\mathrm{R}} = \left[\frac{\partial E}{\partial C_{\mathrm{R}}(0,t)}\right]_{i,C_{\mathrm{O}}(0,t)} = \frac{RT}{nFC_R^{\infty}} \tag{42}$$

$$\sigma = \frac{RT}{n^2F^2A\sqrt{2}}\left(\frac{1}{\sqrt{D_{\mathrm{O}}C_O^{\infty}}} - \frac{1}{\sqrt{D_{\mathrm{R}}C_R^{\infty}}}\right) \tag{43}$$

The key parameter for the work presented here is R_{ct}, which represents the resistance to charge transfer and so increases upon binding of a target molecule in

an electrochemical biosensor. This is clear from its relationship to the exchange current i_0.

2.4.2 Electrochemical methods

2.4.2.1 Cyclic voltammetry

In cyclic voltammetry, a triangular potential waveform (inset of Figure 2.19) is applied at the working electrode and the resulting current is plotted against the applied potential (this plot is called a cyclic voltammogram). A typical cyclic voltammogram is shown on Figure 2.19. The forward (here positive-going) waveform is explained by the theory discussed in section 4.1.4, while the reverse waveform is explained by much the same considerations.

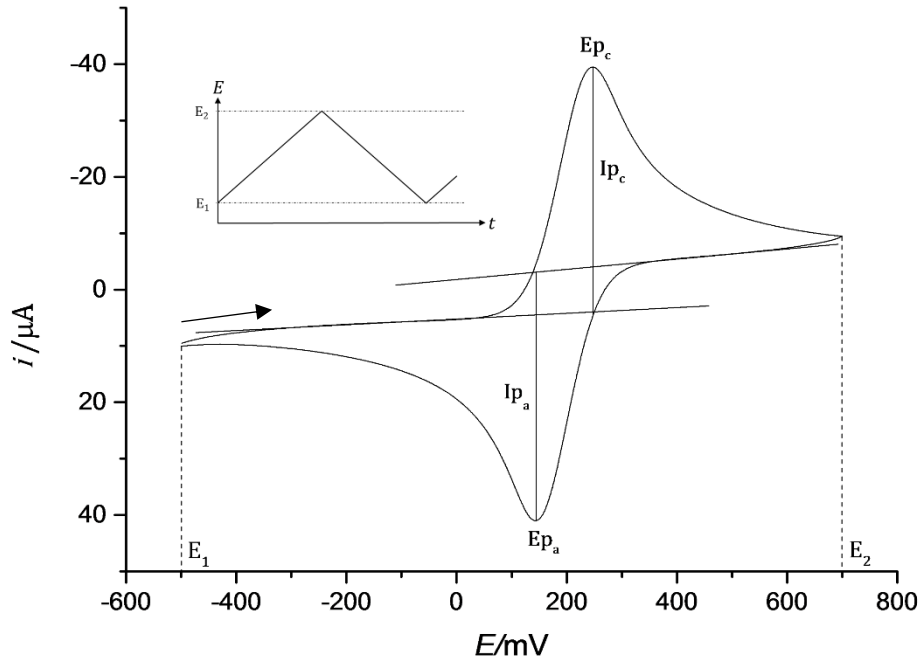

Figure 2.19: Cyclic voltammogram at a HOPG working electrode in 0.1 M ferrocyanide recorded at a scan rate of 0.05 mV s^{-1}, with an Ag/AgCl reference electrode and a Pt counter electrode. Ip_c and Ip_a are the cathodic and anodic current peaks. E_1 and E_2 are the potential limits of the cyclic voltammogram. E_{pc} and E_{pa} are the cathodic and anodic peak positions. The potential triangular waveform applied at the working electrode is shown in the inset.

Cyclic voltammetry is used to assess the reversibility of a redox reaction and as an analytical method to determine the potential at which a species gets oxidised or reduced and possibly to quantify the species.

In the first case, two measured parameters are of interest, the current peak ratio, $\frac{i_p}{i_a}$, and the current peak potential separation, $\Delta E_p = E_{pc} - E_{pa}$. For rapid, reversible (Nerntian) systems, the peaks ratio is equal to one and the peak potential separation is close to $\Delta E_p = 2.3\,\frac{RT}{nF}$, or $\frac{59}{n}$ mV at 25°C. A rapid system means that the concentrations of the oxidised and reduced species equilibrate instantly to those dictated by the Nernst equation. The potential of the peaks are also independent of ν and the peak current is proportional to $\nu^{1/2}$. For quasi-reversible systems, the shape of the CV and $\Delta E_p$are dependent on α, k^0 and ν. A method proposed by Nicholson [40] allows the determination of k^0 from ΔE_p, provided that the peak separation lies between 90mV and 250 mV. He suggested the introduction of a dimensionless parameter ψ that he tabulated for different values of ΔE_p (so for different values of ν) and which is defined as

$$\psi = \frac{\left(\frac{D_O}{D_R}\right)^{\alpha} k^0}{\sqrt{\pi a D_O}} \tag{44}$$

with $a = \frac{nF\nu}{RT}$ and from which $k_0$is extracted.

D_O and D_R are the diffusion coefficients of the oxidised and reduced forms of the redox couple, respectively, α is the transfer coefficient, $F$is the Faraday constant, ν is the potential scan rate, $R$is the gas constant and $T$is the temperature.

In the present work, it is assumed that the effect of α can be neglected and that $D_O \cong D_R$. Then the equation linking ψ to k^0 simplifies to

$$\psi = \frac{k^0}{\sqrt{\pi a D_O}} = k^0 \frac{1}{\sqrt{\pi \frac{nFD_O}{RT}}} \nu^{-1/2} \tag{45}$$

The heterogeneous rate constant is then extracted from the slope of the plot of

$\psi = f(\nu^{-1/2})$.

When extracting the measured information from potential sweep experiments, two effects have to be taken into account: the double layer capacitance and the

uncompensated resistance. The capacitive current is always flowing (since the potential is swept) and is defined as

$$|i_c| = AC_d v \tag{46}$$

The faradaic current have to be measured considering a capacitive current as a baseline.

The uncompensated resistance R_u corresponds to the voltage drop due to the solution resistance. The potential controlled at the working electrode is $E + iR_u$. As i depends on $v^{1/2}$, iR_u does as well, and effects dependent on the scan rate may be falsely interpreted as being due to the kinetics only. It is possible to minimise the effect of the uncompensated resistance by using a positive feedback compensation. One can also increase the concentration of the electrolyte, and minimise the separation between the working and the reference electrodes.

Matsuda and Ayabe [38] introduced a parameter ζ to sort out reversible, quasireversible and totally irreversible processes at a stationary electrode, and defined as

$$\zeta = \frac{k^0}{\sqrt{FDv/RT}} \tag{47}$$

A process is said reversible if $\zeta \geq 15$, quasireversible if $15 \geq \zeta \geq 10^{-3}$ and irreversible if $\zeta \leq 10^{-3}$.

2.4.2.2 Electrochemical Impedance spectroscopy

In electrochemical Impedance Spectroscopy (EIS), an AC signal of small amplitude is superimposed on a DC voltage at a working electrode. Following the theory discussed in section 4.1.6, the total impedance of the cell $Z = Z_{Re} - jZ_{Im}$ is measured for a range of frequencies ω, and R_Ω, C_{dl}, R_{s} and C_{s} can be extracted from the experimental data (by recording a Nyquist plot of the impedance).

The impedance of the circuit elements are given by
$Z_\Omega = R_\Omega, Z_{C_{\mathrm{dl}}} = \frac{1}{j\omega C_{\mathrm{dl}}}, Z_{R_{\mathrm{s}}} = R_{\mathrm{s}}$ and $Z_{C_{\mathrm{s}}} = \frac{1}{j\omega C_{\mathrm{s}}}$. It is usual to write R_{s} and C_{s} as
$R_{\mathrm{s}} = R_{\mathrm{ct}} + \frac{\sigma}{\sqrt{\omega}}$ and $C_{\mathrm{s}} = \frac{1}{\sigma\sqrt{\omega}}$, where R_{ct} is the charge transfer resistance.

A simple circuit analysis on Figure 2.17 **a** gives:

$$Z = Z_\Omega + Z_\mathrm{p} \tag{48}$$

With

$$\frac{1}{Z_\mathrm{p}} = \frac{1}{\frac{1}{j\omega C_\mathrm{dl}}} + \frac{1}{R_\mathrm{s} + \frac{1}{j\omega C_\mathrm{s}}} \tag{49}$$

After some simple manipulations and substitution of R_s and C_s, the real (Z') and imaginary (Z'') parts of the totat impedance are found:

$$Z' = Z_\Omega + \frac{R_{ct} + \frac{\sigma}{\sqrt{\omega}}}{\left(C_{dl}\sigma\sqrt{\omega} + 1\right)^2 + \omega^2 C_{dl}^2 \left(R_{ct} + \frac{\sigma}{\sqrt{\omega}}\right)^2} \tag{50}$$

$$-Z'' = \frac{\omega C_{dl}\left(R_{ct} + \frac{\sigma}{\sqrt{\omega}}\right)^2 + \frac{\sigma}{\sqrt{\omega}}(\sqrt{\omega}C_{dl}\sigma + 1)}{(\sqrt{\omega}C_{dl}\sigma + 1)^2 + \omega^2 {C_{dl}}^2 \left(R_{ct} + \frac{\sigma}{\sqrt{\omega}}\right)^2} \tag{51}$$

Behaviour at low frequencies

For very low frequencies, the impedance simplifies to

$$Z = R_\Omega + R_{ct} + \frac{\sigma}{\sqrt{\omega}} - j\left(\frac{\sigma}{\sqrt{\omega}} + 2\sigma^2 C_{dl}\right) \tag{52}$$

From which it is obvious that

$$Z'' = Z' - R_\Omega - R_{ct} - 2\sigma^2 C_{dl} \tag{53}$$

Therefore the Nyquist plot of the impedance at high frequencies is a straight line of slope 1. In this regime, only the Warburg impedance is frequency dependent and the redox reaction is diffusion limited.

Behaviour at high frequencies

At high frequencies, the Warburg impedance $Z_w = \frac{\sigma}{\sqrt{\omega}} - j\frac{\sigma}{\sqrt{\omega}}$ becomes negligable compared to the other impedances and Z simplifies to

$$Z = R_\Omega + \frac{R_{ct}}{1 + \omega^2 C_{dl}^2 R_{ct}^2} - j\frac{\omega C_{dl} R_{ct}^2}{1 + \omega^2 C_{dl}^2 R_{ct}^2} \tag{54}$$

from which it is deduced

$$\left(Z' - R_\Omega - \frac{R_{ct}}{2}\right)^2 + (Z'')^2 = \left(\frac{R_{ct}}{2}\right)^2 \tag{55}$$

This is the equation of a circle of centre $\left(R_\Omega + \frac{R_{ct}}{2}, 0\right)$ and radius $\frac{R_{ct}}{2}$. At high frequencies, the Nyquist plot of impedance is then a semi-circle, as shown in Figure 2.20.

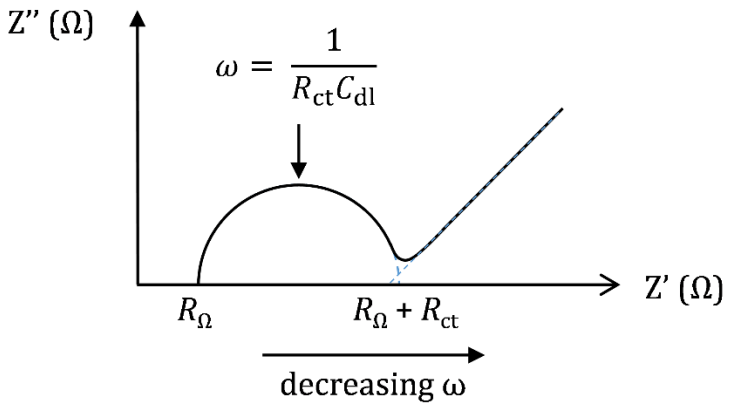

Figure 2.20: Nyquist plot of the interface impedance.

By plotting the Nyquist plot of the impedance, one can then fit a semicircle to the low frequencies data and deduce the charge transfer resistance, the capacitance of the double layer and the resistance of the electrolyte.

Impedance spectroscopy is used in chapter 4 to assess the attachment of 1-pyrene butanoic succinimidyl ester on graphene. It is also used in chapter 5 to detect different concentrations of procalcitonin on highly oriented pyrolytic graphite.

2.4.2.3 Square wave voltammetry

Square wave voltammetry is a technique based on pulse voltammetry and it is carried out at a stationary electrode. As said previously, the total measured current is the sum of the faradaic current provided by a redox reaction and a charging current provided by the double layer at the surface of the electrode. During a potential square pulse, the charging current decays as $e^{-\frac{t}{R_\Omega C_{dl}}}$ and the faradaic current as $t^{-\frac{1}{2}}$. Therefore, sampling the current at a time greater than a few time constants makes the charging current negligible and allows the detection of smaller concentrations than is possible in cyclic voltammetry, for instance.

The waveform involved in square wave voltammetry is presented in Figure 2.21. It consists of a square-wave signal superimposed on a staircase waveform and therefore each cycle is composed of a forward and a reverse pulse that have a height ΔE_p and a duration t_p. The potential shift of the staircase is ΔE_s and is usually significantly smaller than ΔE_p. Typically [41] $\Delta E_s = \frac{10}{n}$ and $\Delta E_p = \frac{50}{n}$ wih n the number of electrons exchanged during the redox process. The current is sampled twice per cycle, at the end of each pulse and the difference between the forward and reverse currents is plotted against the applied potential.

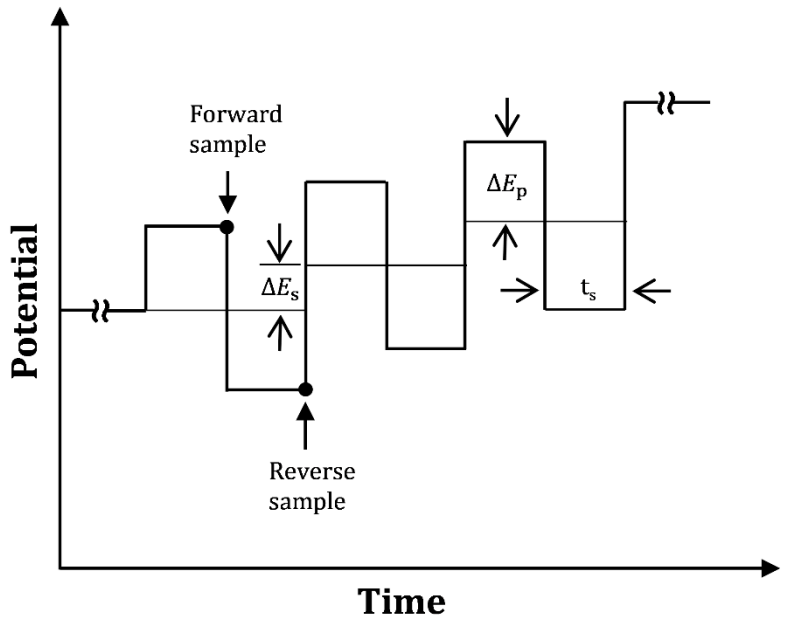

Figure 2.21: Potential waveform applied at the working electrode during a square wave voltammetry experiment.

The theory predicts that for a reversible redox reaction and in the semi-infinite linear diffusion approximation, the differential current is bell-shaped and is symmetrical about $E_{\frac{1}{2}}$, related to the formal potential as $E_{\frac{1}{2}} = E^{0'} + \frac{RT}{nF}\ln\left(\frac{D_O}{D_R}\right)^{\frac{1}{2}}$. In these conditions, and for a solution where only the oxidised species are present at $t = 0$, the current i_m for the mth half cycle is given by [41]

$$i_m = \frac{nFAD_O^{1/2}C_O^{\infty}}{\pi^{1/2}t_s^{1/2}}\psi_m \qquad (56)$$

Where n is the number moles of electrons per mole of reactant exchanged during the redox process, F is the Faraday constant, A is the surface area of the electrode, D_O is the diffusion constant of the oxidised species, C_O^{∞} is the bulk concentration of the oxidised species, t_s is the duration of the pulse and ψ_m is a dimensionless function of the potential waveform. The measured dimensionless differential current $\Delta\psi_m$ is given by $\Delta\psi_m = \psi_m - \psi_{m+1}$. The dimensionless current peak is symmetrical about

$E_{1/2} = E^{0'} + \frac{RT}{nF}\ln\left(\frac{D_O}{D_R}\right)^{\frac{1}{2}}$ and is a function of n, ΔE_p and ΔE_s.

Effect of the kinetics

An electron transfer process is said reversible when the half life of the electron transfer is small compared to the characteristic time of the experiment, here the pulse width. In this case, the concentrations of the oxidized and reduced species at the electrodes are determined thermodynamically and can be calculated using the Nernst equation. When the half life of the electron transfer is much longer than the characteristic time, the process is said to be totally irreversible. Osteryoung [42] introduced a dimensionless parameter $k\sqrt{\tau}$ where k is an effective rate constant with dimension $s^{-1/2}$ and τ is the period of the square wave. The electron transfer is reversible when $k\sqrt{\tau} \gg 1$ and totally irreversible when $k\sqrt{\tau} \ll 1$. When the parameter decreases, the square wave peak amplitude decreases and is shifted towards more negative potentials (for a reduction). The peak also broadens, which diminishes the sensitivity of the method analytically.

The advantages of this methods are [42][43] fast scanning while maintaining a good resolution, an excellent background rejection, a symmetrical current peak

shape (reversible reaction). Overall, this technique is a powerful analytical tool with improved sensitivity by several orders of magnitude compared to linear weep voltammetry and allows the detection of concentrations as low as 10^{-8} M.

This method was used in chapter 6 for the detection of 2,3-diaminophenazine at a graphene electrode.

2.4.2. Electrochemical characterisation of graphene electrodes

A typical way of assessing the electro-activity of a surface is to probe it with inner-sphere and outer-sphere redox couples such as $Ru(NH_3)_6Cl_3$ and $K_4Fe(CN)_6$ respectively. Outer-sphere probes are surface insensitive, i.e. the kinetics of their electron transfer is independent of the presence of chemical functionalities and impurities on the surface of the electrode. On the contrary, the reaction of inner-sphere redox couples involves the presence of surface sites and its heterogeneous charge transfer rate constant k^0 is thus sensitive to the state of the surface. For instance, the presence of oxygen functionalities can hinder or catalyse the redox reaction.

Figure 2.22 shows a comparison of the cyclic voltammogram of $Ru(NH_3)_6^{3+/2+}$ at a single monolayer graphene electrode and at a gold electrode. The peak separation $\Delta E_p = 159$ mV and the forward and reverse peak ratio $\frac{I_{pc}}{I_{pa}} = 1.20$ indicate that the reaction of this outer-sphere couple on graphene is quasi-reversible. A larger peak potential separation than that for the gold electrode, 66 mV, indicates more sluggish kinetics.

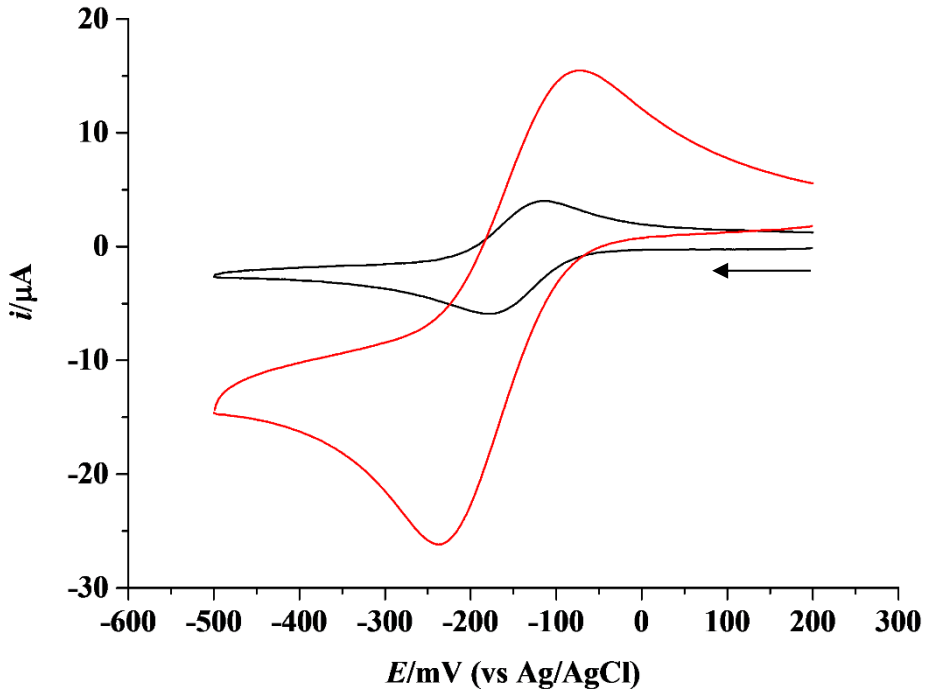

Figure 2.22: Cyclic voltammogram in 1 M KCl containing 1 mM $Ru(NH_3)_6^{3+/2+}$ at a potential sweep rate of 100 mV s^{-1} at a gold electrode (black curve) and at a graphene electrode (red curve)

Prior to measurements, the solution resistance, 1811 Ω as measured with the potentiostat BAS100, was compensated at 65 %. Then, the heterogeneous rate constant was calculated by Nicholson's method and was estimated to be 0.00183 cm s^{-1}, which is of the same order of magnitude but slightly smaller than the k^0reported in previous studies [10][12]. The graphene electrodes made for this thesis may have been less clean or have had fewer reaction-promoting surface defects than the ones used in these papers.

The influence of the uncompensated resistance is illustrated in Figure 2.23, where the CV of graphene in $Ru(NH_3)_6^{3+/2+}$is shown before (red curve) and after compensation (black curve) at 65%.

c

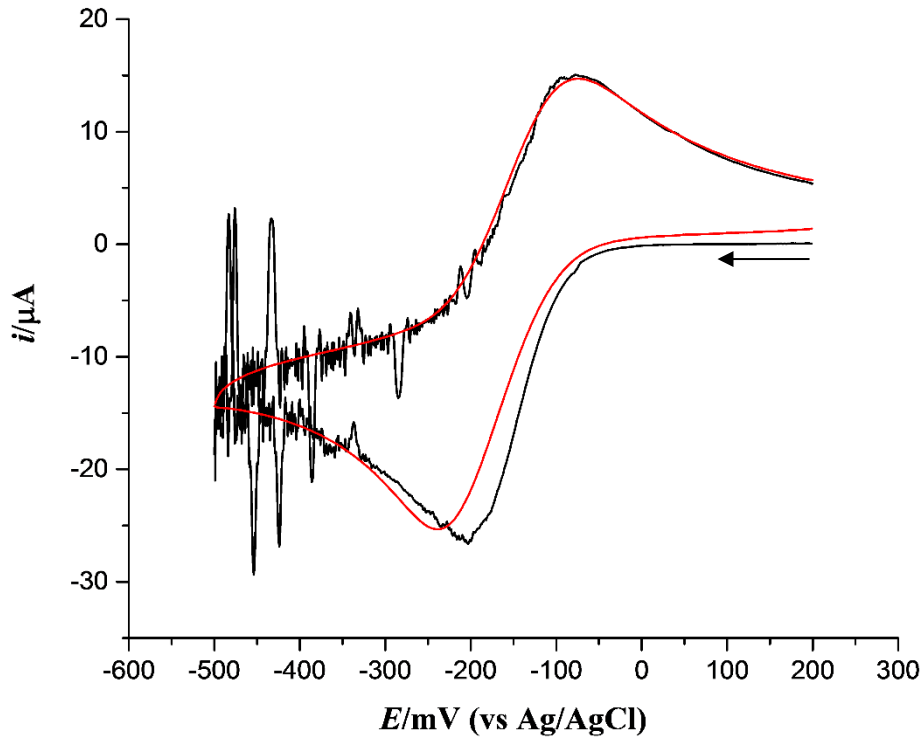

Figure 2.23: Effect of the uncompensated resistance on the calculation of the heterogeneous rate constant. Cyclic voltammogram in 1 M KCl of 1 mM $Ru(NH_3)_6^{3+/2+}$ at a potential sweep rate of 100 mV s^{-1} before (red curve) and after(black curve) 65% compensation of the solution resistance.

The heterogeneous rate was found to be 0.00178 cm s^{-1} before compensation of the solution resistance, which is 97% of its value after correction and shows that compensating the resistance has a minor effect (and probably within the experimental error- not estimated for this single data set). The signal disturbance on the curve corresponding to the measurement with compensation of the solution resistance is due to the instability of the feedback electronic circuit at this scan rate. The calculation of k^0 is shown on Figure 2.24 in the case of no resistance compensation.

CVs of $Ru(NH_3)_6^{3+/2+}$ were recorded at a graphene electrode for different scan rates and ψ was obtained for each corresponding potential peak separation from

working curves [40]. The inset is a plot of ψ against $v^{-1/2}$, from which $k^0$was extracted (see section 4.2.1).

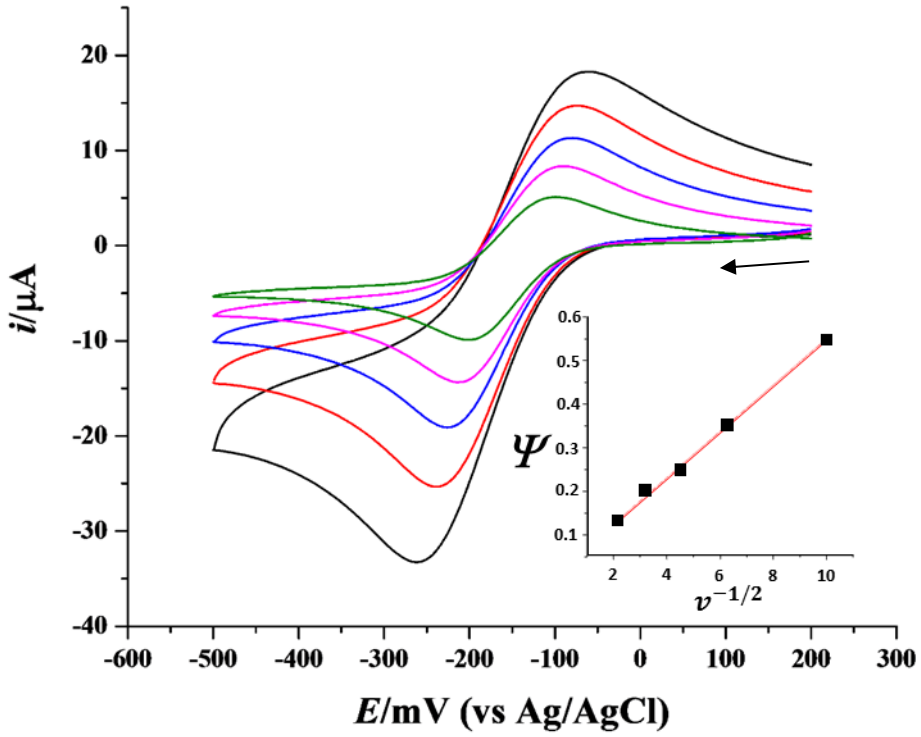

Figure 2.24: Cyclic voltammogram in 1 M KCl containing 1 mM Ru(NH3)6 $^{3+/2+}$ at scan rates of 10 mV s^{-1} (green curve), 25 mV s^{-1} (pink curve), 50 mV s^{-1} (blue curve), 100 mV s^{-1} (red curve), 200 mV s^{-1} (black curve). The variation of the dimensionless current ψ with the inverse of the square root of the scan rate is given in the inset

The cyclic voltammograms at a gold electrode and a graphene electrode for $FeCN_6^{4-/3-}$ are shown on Figure 2.25. It is evident that the reaction is irreversible on the graphene electrode, as $\Delta E_p = 523$ mV and $\frac{i_{pa}}{i_{pc}} \sim 0.33$. This is interpreted as the lack of kinetically active sites on the graphene surface, either because catalytic functionalities are absent or because the electrode surface is dirty.

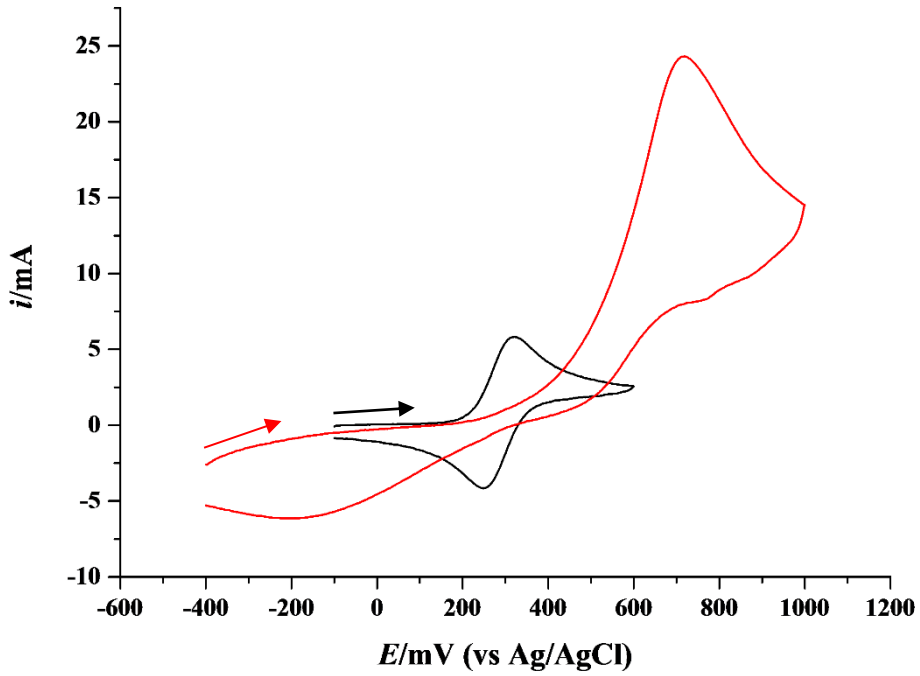

Figure 2.25: Cyclic voltammogram in 1 M KCl of 1 mM potassium ferrocyanide at a potential sweep rate of 50 mV s^{-1} at a gold electrode (black curve) and at a graphene electrode (red curve)

2.4.3 Methods to improve the cleanliness of the graphene electrodes

There are two sources of contamination in the process of making the graphene electrodes. One comes from the etching of the underlying layer of copper which leads to residues of metal oxides trapped between the substrate and the graphene. The other one comes from the polymer used during the transfer and e-beam lithography of graphene, such as PMMA. Contamination by it has been recognised as a major issue in the reproducibility of graphene devices [44] and several techniques have been used to remediate to this, such as post annealing [44][45]. However, it may not be possible to remove PMMA totally. A team from Korea [5] has set a roll-to-roll device to transfer graphene on large scales using a thermo-release polymer, but the transfer leads to residues from the tape. It may however lead to fewer defects and improved electronic properties. For electrochemical analysis, fewer defects may not bring benefits. A more promising method has been developed [46] that consists in accumulating charges on the desired substrate using an electrostatic generator, to attract the graphene.

The copper of the graphene samples was etched using solutions of $FeCl_3$ (iron chloride), $(NH_4)_2S_2O_8$ (ammonium persulfate), HNO_3 (nitric acid, 10%) (v/v in pure water). Iron chloride is the most widely used etchant for copper substrates [24], but leads to chemical residues trapped between the final substrate and the transferred graphene layer. Nitric acid was very effective but the etching of copper released bubbles that can produce defects in the graphene. Ammonium persulfate was found to give the best results and therefore was used as etchant for the copper. It was also found that changing the pure water used for rinsing increased the cleanliness of the samples. Further rinsing in acidic and alkaline solutions consecutively would improve the cleanliness further.

In this thesis, several conditions of temperature, duration and mixtures of H_2/Ar annealing were tested, though not extensively.

Figure 2.26 shows a comparison of a sample annealed under vacuum (10^{-5} mbar) for 10 min at 600°C (left) and under H_2/Ar (50% H_2, 50 sccm) for 1h at 400°C. The cleanliness was assessed optically and by Raman spectroscopy. Optically, fewer residues were observed compared to the pristine transferred graphene, equally good on either condition. A study reported that using H_2/Ar gives better results [35].

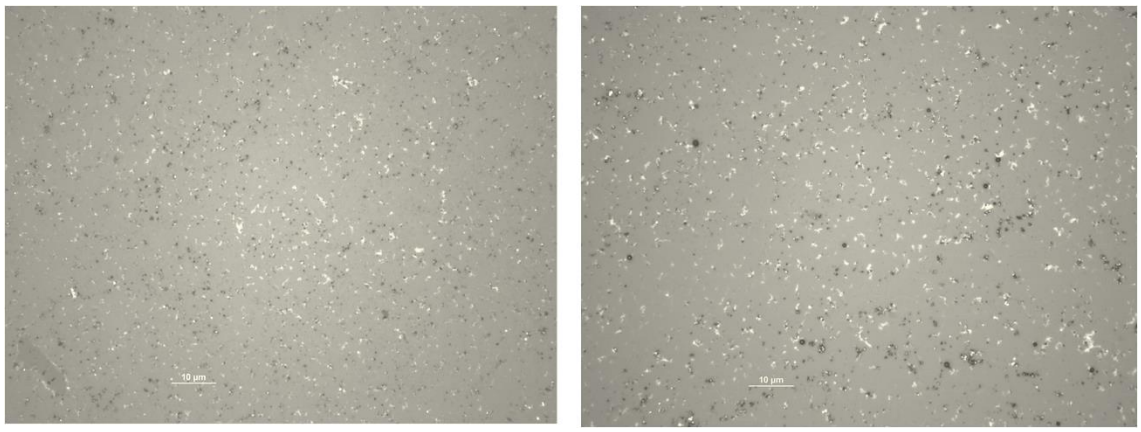

Figure 2.26: Effect of annealing on CVD graphene samples transferred on quartz. Left: after annealing under vacuum for 10 min at 600 °C, 10^{-5} mbar; Right: for 1h at 400 °C under H_2/Ar (50% H_2, 50 sccm).

The effect of annealing under 10 % H_2/Ar was then assessed by Raman spectroscopy and typical Raman spectra before and after annealing are shown in Figure 2.27. The ratio of the G peak to the 2D peak was 0.569 before the annealing

(red curve) and reduced slightly to 0.518 after annealing, and the ratio of the D peak to the G peak barely changed (0.569 before annealing and 0.518 after annealing), which may indicate that the graphene lattice was not much modified by the annealing step.

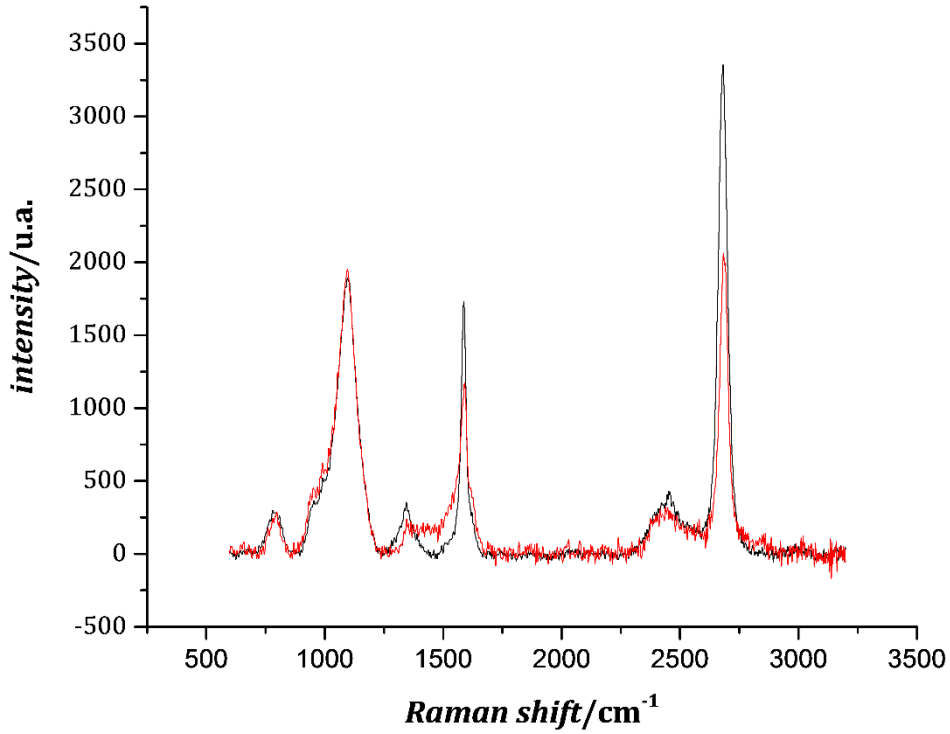

Figure 2.27: Typical Raman spectrum at 532 nm of CVD graphene transferred on glass before (black curve) and after (red curve) annealing for 1h at 400°C under H_2/Ar (10% H_2, 50 sccm). The Raman spectra were processed with an FFT low pass filter (cut-off frequency = 0.143124 Hz)

Cyclic voltammograms were recorded at graphene electrodes in 1 M KCl of 1 mM $Ru(NH_3)_6^{3+/2+}$, before and after annealing for 1h at 400°C under H_2/Ar (10% H_2, 50 sccm)

The peak separation after annealing was 162.5 $\pm$15 mV (n = 3) compared to 187.8 $\pm$72 mV (n = 28) before annealing. This result may suggest that annealing under H_2/Ar may improve the electron transfer kinetic, though more cyclic voltammograms need to be recorded after annealing to be statistically relevant.

Further study should include the effect of annealing on the heterogeneous transfer rate constant of the graphene electrodes.

Annealing is very time consuming. Owing to the lack of evidence that introducing such a step improves significantly the electrochemistry on the graphene electrode, no annealing step was introduced in the making of graphene electrodes.

Graphene array electrodes

Assuming that the cleanliness of the electrodes and the process of fabrication are mainly responsible for the lack of reproducibility of the graphene electrodes, the behaviour of graphene electrodes was tested when they are of the same size and fabricated by selecting clean graphene areas from a single piece of transferred graphene to create a multi-array micro electrode. The array could be used to either calibrate graphene for the detection of a biomolecule or for the simultaneous detection of several biomarkers of procalcitonin. For comparison, two arrays were made: one selecting only clean areas (Figure 2.28 (i), (ii) and (iii)) and one selecting random areas (Figure 2.28 (iv), (v), (vi)) from a single piece of transferred graphene. They were made using electron beam lithography and contain respectively four 200 μm^2 graphene electrodes and four 1 mm^2 graphene electrodes. Figure 2.28 (ii) contains an optical picture of the four clean selected graphene electrodes. It is visible that impurities have been introduced by the lift-off procedure. The corresponding cyclic voltammograms are shown on Figure 2.28 (iii). The responses of only two electrodes (a and b) are very similar. That of electrode d is shifted in potential and electrode c behaves like a pure resistance. Similarly, the electrodes of the array shown in figure 2.28 (iv) have a similar behaviour. They were recorded after depositing a drop of solution on the surface of the array. In order to insulate the electrodes electrically on this array, a layer of dielectric was deposited on its surface. The oxides CrO_3 and Al_2O_3 were tried first but without success, as CrO_3 was too brittle and it was difficult to create a thick enough layer of Al_20_3 from Al (a sputtering machine could be used). Then it was decided to use PMMA, which is already used in the process of making the array.

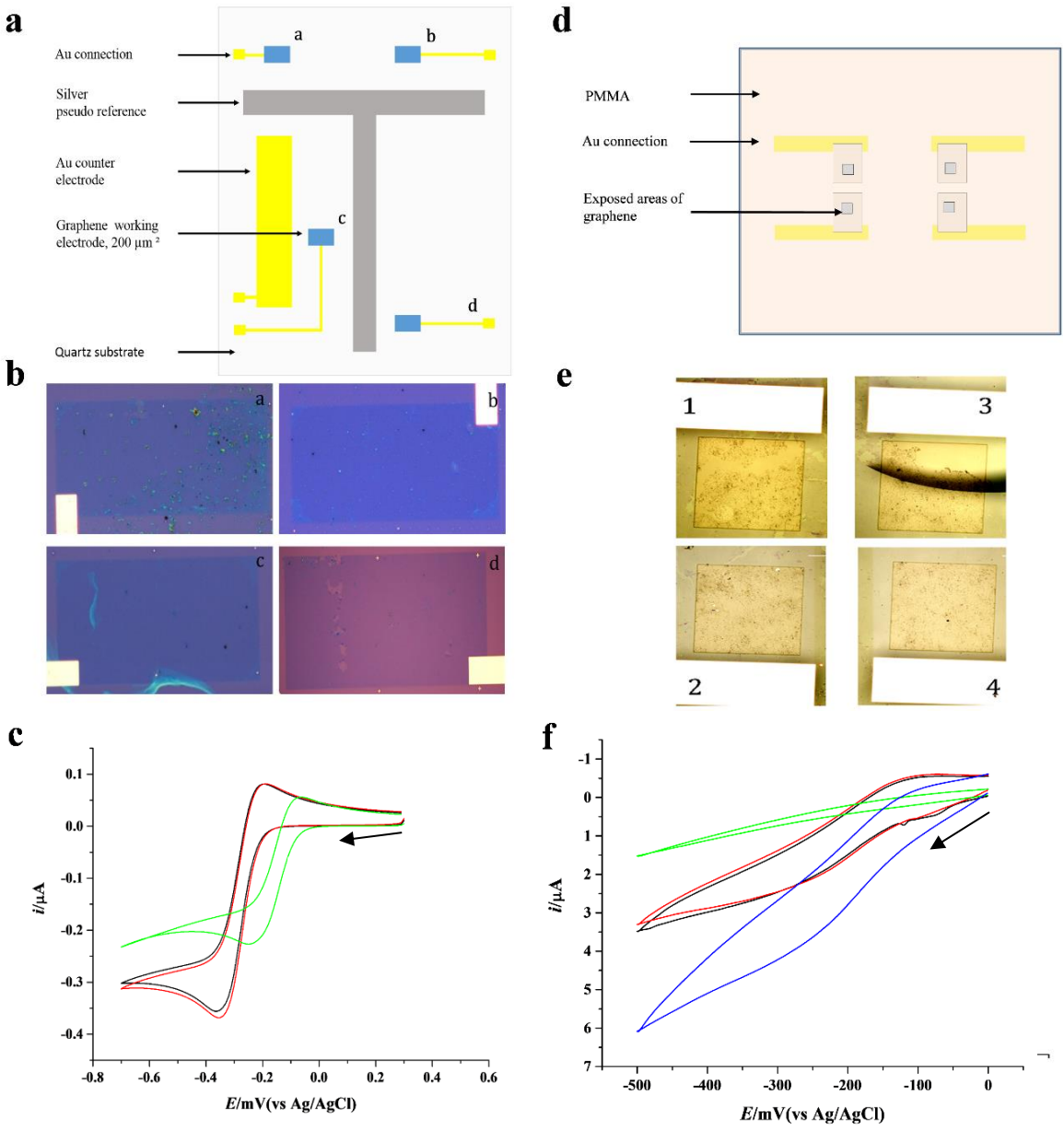

Figure 2.28: i, schematic of the graphene four electrode array whose optical pictures are shown in ii and corresponding cyclic voltammograms in iii; ii, optical pictures of the 100×200 µm² graphene electrodes a, b c and d (10×20 µm², lens 100x); iii, Cyclic voltammograms in 1 M KCl of 1 mM $Ru(NH_3)_6^{3+/2+}$ at a potential sweep rate of 50 mV s^{-1} at electrodes a (black curve), b (red curve), c (blue curve in inset) and d (green curve); iv, schematic of the graphene four electrode array whose optical pictures are shown in v and corresponding cyclic voltammograms in vi; v, optical image of graphene electrodes 1, 2, 3 and 4 (1 mm²); vi, Cyclic voltammograms in 1 M KCl of 1 mM $Ru(NH_3)_6^{3+/2+}$ at a potential sweep rate of 50 mVs^{-1} at electrodes 1 (black curve), 2 (red curve), 3 (green curve), 4 (blue curve)

2.5 Conclusion

Graphene was successfully transferred onto a transparent substrate (glass and quartz) and graphene electrodes were thus produced, with sufficiently good electrochemical behaviour to allow their use for electrochemical analysis. The heterogeneous rate constant at a graphene electrode was measured in 1 M KCl containing 1 mM $Ru(NH_3)_6^{3+/2+}$ and was found to be 0.00183 cm s^{-1} (calculated according to Nicholson's method). However, it was difficult to produce clean and reproducible graphene electrodes. In this chapter, attempts were described to overcome this difficulty by using a single sheet of CVD graphene to produce a multi-array electrode. Although the development of graphene arrays by this method needs investigating further, it seems possible to create reproducible electrodes this way. In chapter 5, a second approach is described, where the same graphene electrode was reused by renewing the surface using a regeneration buffer.

Bibliography

[1] A. K. Geim and K. S. Novoselov, "The rise of graphene," *Nat. Mater.*, vol. 6, no. 3, pp. 183–191, 2007.

[2] M. Pumera, "Graphene-based nanomaterials for energy storage," *Energy Environ. Sci.*, vol. 4, no. 3, p. 668, 2011.

[3] A. I. S. Neves, T. H. Bointon, L. V. Melo, S. Russo, I. de Schrijver, M. F. Craciun, and H. Alves, "Transparent conductive graphene textile fibers," *Sci. Rep.*, vol. 5, p. 9866, 2015.

[4] T. Kuila, S. Bose, P. Khanra, A. K. Mishra, N. H. Kim, and J. H. Lee, "Recent advances in graphene-based biosensors," *Biosens. Bioelectron.*, vol. 26, no. 12, pp. 4637–4648, 2011.

[5] S. Bae, H. Kim, Y. Lee, X. Xu, J.-S. Park, Y. Zheng, J. Balakrishnan, T. Lei, H. R. Kim, Y. Il Song, Y.-J. Kim, K. S. Kim, B. Ozyilmaz, J.-H. Ahn, B. H. Hong, and S. Iijima, "Roll-to-roll production of 30-inch graphene films for transparent electrodes," *Nat. Nanotechnol.*, vol. 5, no. 8, pp. 574–578, 2010.

[6] R. R. Nair, P. Blake, A. N. Grigorenko, K. S. Novoselov, T. J. Booth, T. Stauber, N. M. R. Peres, and A. K. Geim, "Fine structure constant defines visual transparency of graphene," *Science*, vol. 320, no. 5881, p. 1308, 2008.

[7] K. S. Novoselov, A. K. Geim, S. V. Morozov, D. Jiang, Y. Zhang, S. V. Dubonos, I. V. Grigorieva, "Electric Field Effect in Atomically Thin Carbon Films," *Science*, vol. 22, no. 306, pp. 666–669, 2004.

[8] B. Mendoza-Sánchez, B. Rasche, V. Nicolosi, and P. S. Grant, "Scaleable ultra-thin and high power density graphene electrochemical capacitor electrodes manufactured by aqueous exfoliation and spray deposition," *Carbon*, vol. 52, pp. 337–346, 2013.

[9] B. Jiang, M. Wang, Y. Chen, J. Xie, and Y. Xiang, "Highly sensitive electrochemical detection of cocaine on graphene/AuNP modified electrode via catalytic redox-recycling amplification," *Biosens. Bioelectron.*, vol. 32, no. 1, pp. 305–308, 2012.

[10] Y. Shao, J. Wang, H. Wu, J. Liu, I. a. Aksay, and Y. Lin, "Graphene based electrochemical sensors and biosensors: A review," *Electroanalysis*, vol. 22, no. 10, pp. 1027–1036, 2010.

[11] P.R.Wallace, "The band theory of graphite," *Phys.Rev.*, pp. 622–634, 1946.

[12] S. Reich, J. Maultzsch, C. Thomsen, and P. Ordejón, "Tight-binding description of graphene," *Phys. Rev. B*, vol. 66, no. 3, pp. 1–5, 2002.

[13] A. H. Castro Neto, F. Guinea, N. M. R. Peres, K. S. Novoselov, and A. K. Geim, "The electronic properties of graphene," *Rev. Mod. Phys.*, vol. 81, no. 1, pp. 109–162, 2009.

[14] K. S. Novoselov, A K. Geim, S. V Morozov, D. Jiang, M. I. Katsnelson, I. V Grigorieva, S. V Dubonos, and A A Firsov, "Two-dimensional gas of massless Dirac fermions in graphene.," *Nature*, vol. 438, no. 7065, pp. 197–200, 2005.

[15] I. Khrapach, F. Withers, T. H. Bointon, D. K. Polyushkin, W. L. Barnes, S. Russo, and M. F. Craciun, "Novel highly conductive and transparent graphene-based conductors," *Adv. Mater.*, vol. 24, no. 21, pp. 2844–2849, 2012.

[16] K. Bolotin, K. Sikes, and Z. Jiang, "Ultrahigh electron mobility in suspended graphene," *Solid State Commun.*, vol. 146, pp. 351–355, 2008.

[17] X. Hong, A. Posadas, K. Zou, C. H. Ahn, and J. Zhu, "High-Mobility Few-Layer Graphene Field Effect Transistors Fabricated on Epitaxial Ferroelectric Gate Oxides," *Phys.Rev.Lett.*, vol. 102, p. 136808, 2008.

[18] F. Bonaccorso, Z. Sun, T. Hasan, and A. C. Ferrari, "Graphene Photonics and Optoelectronics," vol. 4, no. August, pp. 611–622, 2010.

[19] A. B. Kuzmenko, E. Van Heumen, F. Carbone, and D. Van Der Marel, "Universal optical conductance of graphite," *Phys. Rev. Lett.*, vol. 100, no. 11, pp. 2–5, 2008.

[20] L. Gao, J. R. Guest, and N. P. Guisinger, "Epitaxial graphene on Cu(111)," *Nano Lett.*, vol. 10, no. 9, pp. 3512–3516, 2010.

[21] D. A. C. Brownson, M. Gomez-Mingot, and C. E. Banks, "CVD graphene electrochemistry: biologically relevant molecules," *Phys. Chem. Chem. Phys.*, vol. 13, no. 45, pp. 20284–20288, 2011.

[22] Z. Fogarassy, M. H. Rümmeli, S. Gorantla, A. Bachmatiuk, G. Dobrik, K. Kamarás, L. P. Biró, K. Havancsák, and J. L. Lábár, "Dominantly epitaxial growth of graphene on Ni (111) substrate," *Appl. Surf. Sci.*, vol. 314, pp. 490–499, 2014.

[23] C. Riedl, C. Coletti, and U. Starke, "Structural and electronic properties of epitaxial graphene on SiC(0 0 0 1): a review of growth, characterization, transfer doping and hydrogen intercalation," *J. Phys. D. Appl. Phys.*, vol. 43, no. 37, p. 374009, 2010.

[24] C. Mattevi, H. Kim, and M. Chhowalla, "A review of chemical vapour deposition of graphene on copper," *J. Mater. Chem.*, vol. 21, no. 10, p. 3324, 2011.

[25] J. W. Suk, A. Kitt, C. W. Magnuson, Y. Hao, S. Ahmed, J. An, A. K. Swan, B. B. Goldberg, and R. S. Ruoff, "Transfer of CVD-Grown Monolayer Graphene onto Arbitrary Substrates,"*ACS nano*, vol. 5, no. 9, pp. 6916–6924, 2011.

[26] P. J. Ko, H. Takahashi, S. Koide, H. Sakai, T. V Thu, H. Okada, and A. Sandhu, "Simple method to transfer graphene from metallic catalytic substrates to flexible surfaces without chemical etching," *J. Phys. Conf. Ser.*, vol. 433, no. 1, p. 012002, 2013.

[27] J. Song, F.-Y. Kam, R.-Q. Png, W.-L. Seah, J.-M. Zhuo, G.-K. Lim, P. K. H. Ho, and L.-L. Chua, "A general method for transferring graphene onto soft surfaces.," *Nat. Nanotechnol.*, vol. 8, no. 5, pp. 356–62, 2013.

[28] W. H. Lin, T. H. Chen, J. K. Chang, J. I. Taur, Y. Y. Lo, W. L. Lee, C. S. Chang, W. Bin Su, and C. I. Wu, "A direct and polymer-free method for transferring graphene grown by chemical vapor deposition to any substrate," *ACS Nano*, vol. 8, no. 2, pp. 1784–1791, 2014.

[29] X. Li, Y. Zhu, W. Cai, M. Borysiak, B. Han, D. Chen, R. D. Piner, L. Colomba, and R. S. Ruoff, "Transfer of large-area graphene films for high-performance transparent conductive electrodes," *Nano Lett.*, vol. 9, no. 12, pp. 4359–4363, 2009.

[30] P. Chiu, "Graphene Annealing : How Clean Can It Be ?," *Nano Lett.*, vol.12, no. 1, pp 414–419, 2012.

[31] C. Gong, H. C. Floresca, D. Hinojos, S. McDonnell, X. Qin, Y. Hao, S. Jandhyala, G. Mordi, J. Kim, L. Colombo, R. S. Ruoff, M. J. Kim, K. Cho, R. M. Wallace, and Y. J.

Chabal, “Rapid selective etching of PMMA residues from transferred graphene by carbon dioxide,” *J. Phys. Chem. C*, vol. 117, no. 44, pp. 23000–23008, 2013.

[32] J. D. Caldwell, T. J. Anderson, J. C. Culbertson, G. G. Jernigan, K. D. Hobart, F. J. Kub, M. J. Tadjer, J. L. Tedesco, J. K. Hite, M. A. Mastro, R. L. Myers-Ward, C. R. Eddy, P. M. Campbell, and D. K. Gaskill, “Technique for the dry transfer of epitaxial graphene onto arbitrary substrates,” in *ACS Nano*, 2010, vol. 4, no. 2, pp. 1108–1114.

[33] A. C. Ferrari and D. M. Basko, “Raman spectroscopy as a versatile tool for studying the properties of graphene,” *Nat. Nanotechnol.*, vol. 8, no. 4, pp. 235–46, 2013.

[34] A. C. Ferrari, “Raman spectroscopy of graphene and graphite: Disorder, electron-phonon coupling, doping and nonadiabatic effects,” *Solid State Commun.*, vol. 143, no. 1–2, pp. 47–57, 2007.

[35] A. C. Ferrari, J. C. Meyer, V. Scardaci, C. Casiraghi, M. Lazzeri, F. Mauri, S. Piscanec, D. Jiang, K. S. Novoselov, S. Roth, and A. K. Geim, “Raman spectrum of graphene and graphene layers,” *Phys. Rev. Lett.*, vol. 97, no. 18, 2006.

[36] L. M. Malard, M. A. Pimenta, G. Dresselhaus, and M. S. Dresselhaus, “Raman spectroscopy in graphene,” *Phys. Rep.*, vol. 473, no. 5–6, pp. 51–87, 2009.

[37] M. Pumera, “Graphene in biosensing,” *Mater. Today*, vol. 14, no. 7–8, pp. 308–315, 2011.

[38] D. A. C. Brownson, D. K. Kampouris, and C. E. Banks, "*Graphene electrochemistry: fundamental concepts through to prominent applications*," *Chem. Soc. Rev.*, vol. 41, no. 21, pp 6944-6976, 2012.

[39] D. A. C. Brownson and C. E. Banks, “CVD graphene electrochemistry: the role of graphitic islands,” *Phys. Chem. Chem. Phys.*, vol. 13, no. 35, pp. 15825–15828, 2011.

[40] R. Nicholson, “Theory and Application of Cyclic Voltammetry for Measurement of Electrode Reaction Kinetics,” *Anal. Chem.*, vol. 37, no. 11, pp. 1351–1355, 1965.

[41] L. R. F. Bard, Allen J., *Electrochemical Methods: Fundamentals and Applications*. (second edition), 2001, Wiley.

[42] J. G. Osteryoung and R. A. Osteryoung, "Square Wave Voltammetry," *Anal. Chem.*, vol. 57, no. 1, p. 101A–110A, 1985.

[43] L. Ramaley and M. S. Krause, "Theory of Square Wave Voltammetry," *Anal. Chem.*, vol. 41, no. 11, pp. 1361–1365, 1969.

[44] W. Li, C. Tan, M. A. Lowe, H. D. Habruna and D. C. Ralph, "Electrochemistry of Individual Monolayer Graphene Sheets," *ACS nano*, vol. 5, no. 3, pp. 2264–2270, 2011.

[45] X. Li, Y. Zhu, W. Cai, M. Borysiak, B. Han, D. Chen, R. D. Piner, L. Colomba, and R. S. Ruoff, "Transfer of large-area graphene films for high-performance transparent conductive electrodes," *Nano Lett.*, vol. 9, no. 12, pp. 4359–4363, 2009.

[46] D. Y. Wang, I. S. Huang, P. H. Ho, S. S. Li, Y. C. Yeh, D. W. Wang, W. L. Chen, Y. Y. Lee, Y. M. Chang, C. C. Chen, C. Te Liang, and C. W. Chen, "Clean-lifting transfer of large-area residual-free graphene films," *Adv. Mater.*, vol. 25, no. 32, pp. 4521–4526, 2013.

Chapter 3

Determination of 3,3',5,5'-tetramethylbenzidine diimine and 2,3 diaminophenazine by electrochemical and absorption spectroscopic methods for the indirect determination of horseradish peroxidase

Abstract

Horseradish peroxidase (HRP) is a very commonly used enzyme in biomedical tests. It specifically catalyses the reduction of hydrogen peroxide via the oxidation of a co-substrate, such as o-phenylene diamine (OPD) and tetramethylbenzidine (TMB). These substrates are chromogenic which means that their colour changes after oxidation and their concentrations can be measured by spectrophotometry. In the case when these substrates also have redox properties, it is possible to use electrochemical methods instead of spectrophotometry, by recording the current coming from the reduction of the substrates that have been oxidised by the enzyme. It is assumed that the quantity of oxidised co-substrate is proportional to the quantity of HRP in solution. Being able to measure the concentration of HRP in a sample is important as HRP is often tethered to a molecule of interest and their concentrations are therefore related to each other. This chapter explores different ways of quantifying the quantity of HRP in a sample using electrochemical methods such as amperometry. The absorbance spectroscopy assay for HRP was first verified. For both OPD and TMB, the relationship between concentration and absorbance was found to be linear, between 0 and 100 ng mL^{-1}. The limit of detection (LOD) for HRP was found to be respectively 1.43 ng mL^{-1} and 18.2 ng mL^{-1}. Then, an attempt was made to show that similar linearity could be achieved using electrochemical methods, with lower limits of detection than by spectrophotometry in order to be clinically useful. It was demonstrated that it is

possible to detect HRP indirectly using electrochemical methods such as amperometry (here at a Pt microelectrode and at a screen printed electrode). However, no linear relationship could be achieved within an acceptable error, between the concentration of HRP and the current of reduction of the oxidised form of TMB or OPD, indicating that more sensitive methods must be used, such as square wave voltammetry.

3.1 Introduction

Immunosensors are biosensors where the recognition element is an antibody specific to the analyte that needs to be detected [1]. The antibody is tethered on the recognition surface and the binding of the analyte forms a stable complex that can be detected directly (unlabelled) or indirectly (labelled) with high sensitivity [1] and selectivity [2]. Immunosensors divide into different categories according to how the antigen-antibody binding is transduced into a quantifiable electrical signal, mostly by electrochemical and optical methods. Electrochemical methods have advantages like being low cost, easy to set up and sensitive [3], improving the development of portable and affordable devices. Electrochemical immunoassays can be labelled [4] [5] [6] [7] or non-labelled [8] [9] [10]. A frequently used label is horseradish peroxidase (HRP) [11] and labelled electrochemical immunoassays often use an ELISA test [3] [12] (see Chapter 1 part 3). In this thesis, PCT was first detected using an ELISA sandwich test, in which HRP is used as the enzyme label. Since immunoassays are expensive and time consuming, preliminary research was conducted on the feasibility of detecting HRP in bulk analysis by electrochemical methods. To do so, the product of the homogenous reduction of H_2O_2 by HRP via the oxidation of a co-substrate (CoS) was analysed by amperometry (see Figure 3.1). Indeed, HRP is covalently linked to a specific antibody attached to PCT. Therefore, if the quantity of oxidised co-substrate (CoS_{ox}) relates linearly to the quantity of HRP present in solution , it is also expected to relate linearly to the quantity of PCT in the studied sample.

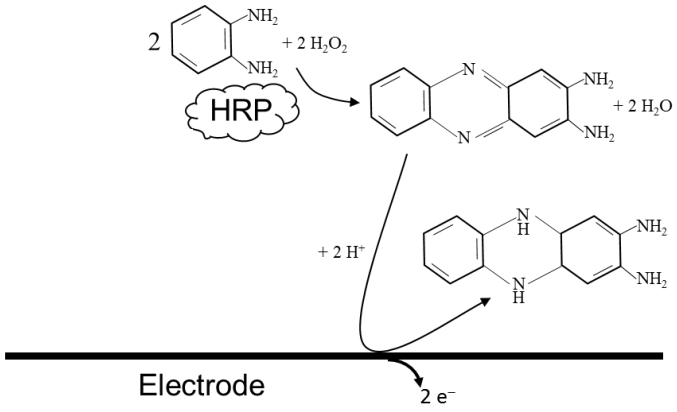

Figure 3.1: Schematic of the electrochemical detection of HRP using TMB as a cosubstrate

This chapter is concerned with the work undertaken on exploring different ways of quantifying HRP, such as the choice of co-substrate and analytical method. The results are a proof-of-concept for the detection and potential quantification of PCT by electrochemical methods.

3.2 Experimental

3.2.1 Reagents

Phosphate-citrate buffer (Sigma Aldrich, pH = 5) was used as electrolyte throughout, while all aqueous solutions were prepared using ultra-pure water (Milli-Q Millipore) with a resistivity of ca. 18.1 MΩ cm at 25 ˚C. Phosphate-buffered saline (PBS, pH = 7.4), Horseradish peroxidase (HRP, liophylised powder), hexaammineruthenium(III) chloride ($Ru(NH_3)_6Cl_3$, Fisher Scientific, 98%), *o*- phenylenediamine (OPD, tablet, ≥ 98%), tetramethylbenzidine (TMB, tablet, ≥ 98%), Tween20 (T20, viscous liquid, ≥ 97%) and bovine sulphate albumin (BSA, heat shock fraction, lyophilized powder, ≥98%, pH = 7), Corning® 96 well plate (round bottom) were all purchased from Sigma-Aldrich and used without further purification.

3.2.2 Horseradish peroxidase assay

The horseradish peroxidase (HRP) assay consists of quantifying the product of the HRP-catalysed oxidation of a substrate (e.g. TMB, OPD) by H_2O_2. The quantity of the reaction product is then expected to provide a quantifiable measure of the HRP, by spectrophotometry if it is coloured. An HRP solution of 5 μg mL^{-1} concentration was prepared by dissolution of HRP lyophilised powder in pH = 7.4 PBS, then diluted to different concentrations. The reactions of the HRP/H_2O_2/substrate system were carried out in a 96 well plate (Corning®, non treated round bottom 96 well plate). After dilution in pH = 7.4 PBS to the desired concentrations, HRP was adsorbed on the wells of the plate by incubating for 2 hours at room temperature and in the dark, then rinsing 3 times with a solution of pH = 7.4 PBS containing 0.05 % (v/v) Tween 20 (PBS-T20). A solution of 0.1 mM TMB or OPD in pH = 5 phosphate-citrate buffer solution containing 1 mM H_2O_2 was then introduced into the wells and the reaction was stopped by addition of 2 M H_2S0_4 after 10 minutes of reaction at room temperature and in the dark. The experiment was carried out in triplicate and it was then attempted to quantify the product of the reactions by spectrophotometric measurements and electrochemical measurements.

3.2.3 Spectrophotometric measurements

The HRP-catalysed oxidation of TMB by H_20_2 yields a blue product that changes to yellow upon addition of H_2SO_4 to stop the reaction. A study by Josephy et al. [13] suggested that the blue colour (absorbs at 620 nm) is due to a complex formed of the diamine parent and diimine oxidation product, in equilibrium with a radical cation. Increasing the acidity of the solution containing the equilibrium stabilises the diimine, which is yellow (absorbs at 450 nm), thus explaining the change of colour after addition of H_2SO_4. The mechanism of the reaction is shown in Figure 3.2. OPD is oxidised to 2,3-diaminophenazine, which is yellow (absorbs at 450 nm), according to the reaction scheme in Figure 3.3 . In acid media, such as after addition of H_2SO_4 to the reaction solution, the product of the oxidation is orange (absorbs at 490 nm).

Spectrophotometric data were recorded at 450 nm for TMB and 490 nm for OPD with a plate reader spectrophotometer. The pathlength of the cuvette in which the solutions were entroduced was 1cm.

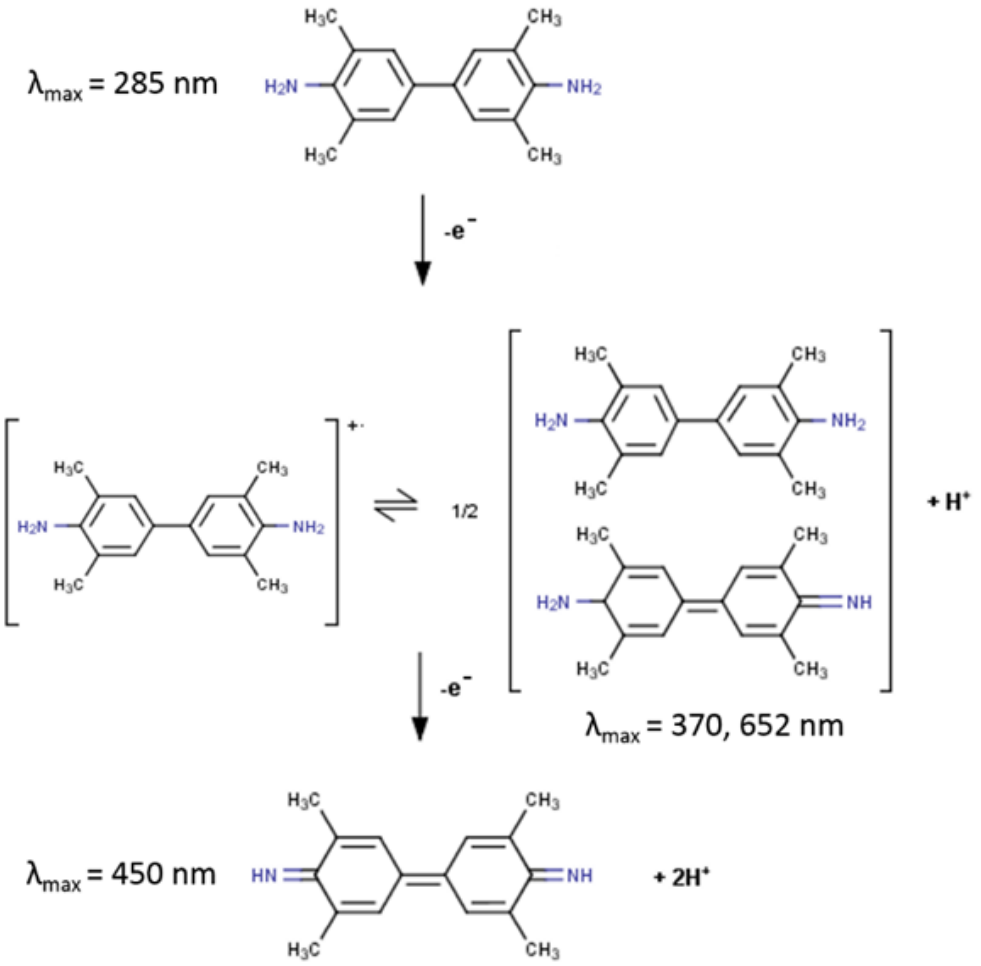

Figure 3.2: Reaction mechanism of the HRP-catalysed oxidation of 3,3',5,5'-tetramethylbenzidine by H_2O_2. λ_{max} corresponds to the maxima of the absorption spectrum of the chemical species.

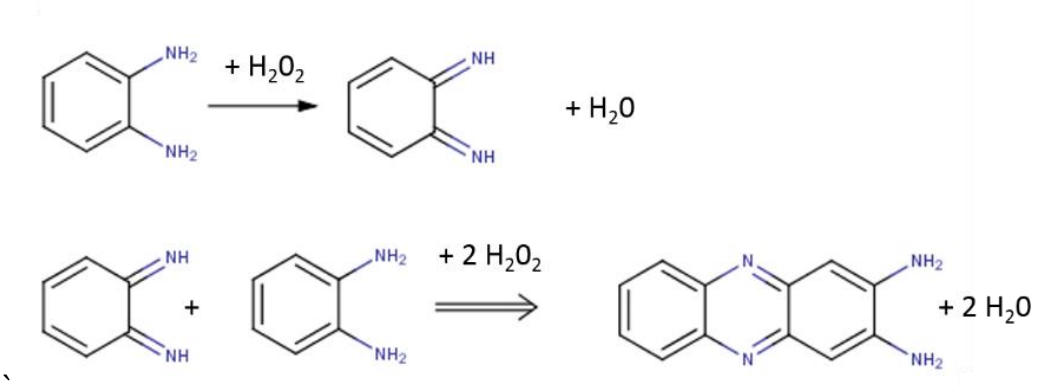

Figure 3.3: Reaction mechanism of the HRP-catalysed oxidation of o-phenylenediamine by H_2O_2.

3.2.4 Electrochemical measurements

The product of the oxidation reaction catalysed by HRP is determined by the signal produced when it is reduced back to its original form by electrochemical methods.

These electrochemical methods are described in chapter 2, part 4. In this chapter, two three-electrode systems were used: a Pt micro-electrode, Pt counter electrode, and Ag/ AgCl/ 3 M NaCl (BASi) system, and a carbon screen printed electrode (CSPE) containing a carbon working electrode, a carbon counter electrode and a silver pseudo reference electrode. All the potentials were recorded against a reference electrode. Open circuit measurements (OPC) were performed with a BAS 100B/W Electrochemical Analyser (BASi). Cyclic voltammetry was performed with a Compactstat electrochemical interface (Ivium Technologies) at a scan rate of 0.05 V s^{-1}. Amperometric measurements were performed with a Compactstat electrochemical interface (Ivium technologies), and the potential used for these measurements were chosen from the cyclic voltammograms. The times at which the values of the amperometric currents were recorded for analysis were chosen as a subjective judgement to when the isotherms i(t) were steady. All solutions were purged with nitrogen before measurement.

Amperometric measurements at the Pt micro-electrode

For 2,3-diaminophenazine (OPD_{ox}, oxidised form of OPD), anodic amperometric measurements were performed at 0.6 V vs Ag/AgCl/3 M NaCl and cathodic amperometric measurements were performed at -0.05 V vs Ag/AgCl/3 M NaCl.

For 3,3',5,5'-tetramethylbenzidine diimine (TMB_{ox}, oxidised form of TMB), cathodic amperometric measurements were performed at - 0.35 V vs Ag/AgCl/3 M NaCl. The experiment set up is illustrated in Figure 3.4.

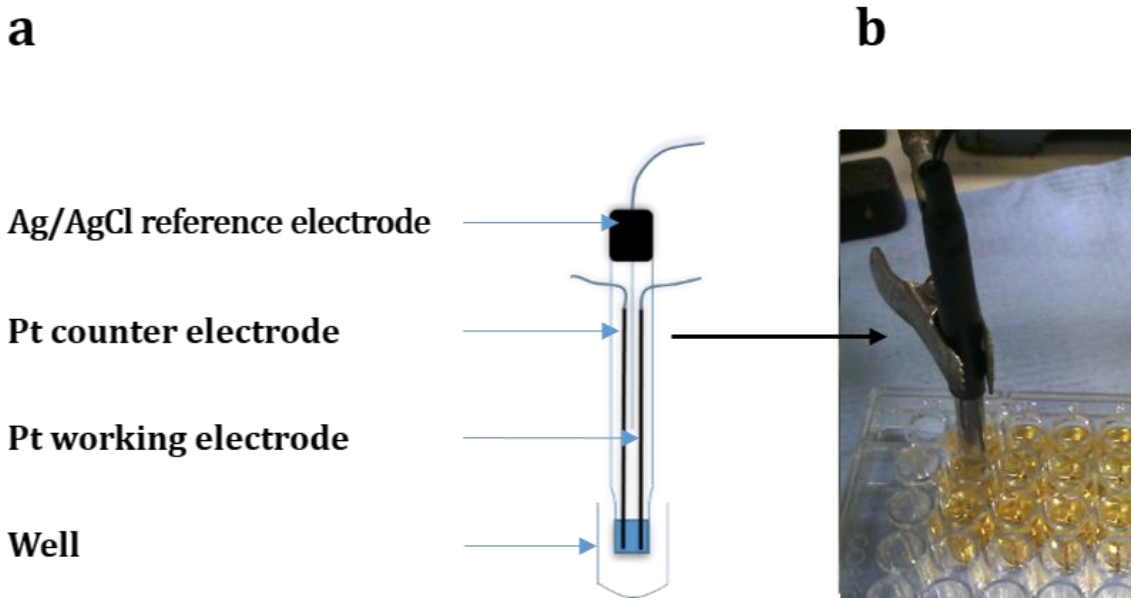

Figure 3.4: Schematic of the three electrode cell composed of an Ag/AgCl reference electrode, Pt working and counter electrode (a); picture of the electrochemical set up showing the three electrode system in one well of the 96 well plate where the HRP-catalysed oxidation of OPD has been stopped after 10 minutes of reaction (b)

Amperometric measurements at the CSPE

Measurements were performed by depositing a drop of solution from the vials of the 96 well plate on the CSPE. Cathodic amperometric measurements of 3,3',5,5'-tetramethylbenzidine diimine were performed at 0.1 V vs Ag. The CSPE is illustrated in Figure 3.5 (a) and the electrochemical set-up is shown in Figure 3.5 (b).

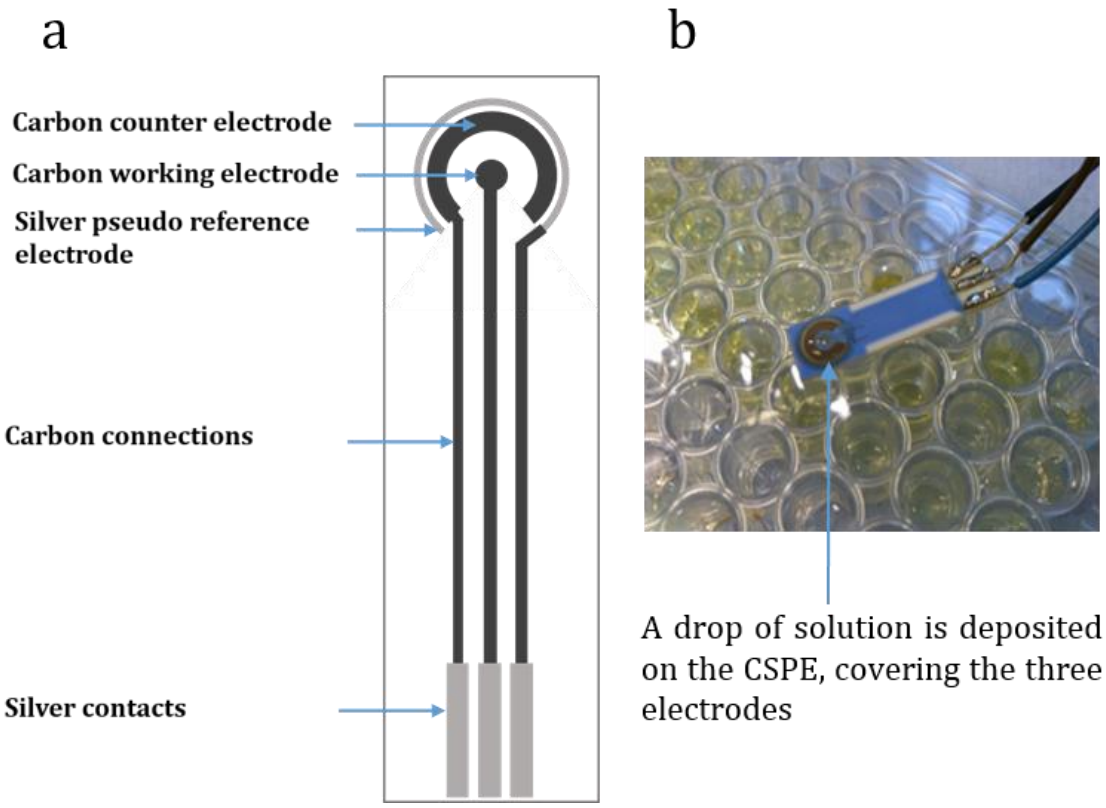

Figure 3.5: Schematic of the SPCE (a); picture of the electrochemical three electrode cell (b).

3.2.5 Determination of the limit of detection and limit of quantification for an analytical procedure

The limit of detection (LOD) and the limit of quantification (LOQ) are two key parameters for an analytical method [14]. The LOD indicates the smallest concentration of analyte that can be reliably detected by a method and the LOQ indicates the smallest concentration of analytes that can be quantified within an acceptable error stated by the conditions of the test. It means that the signal produced by the analyte must be distinguishable from the background noise, and it is generally accepted that this signal should be at least three times greater than the background noise [14]. When the signal measured is linearly related to the concentration of analytes producing this signal, the LOD is the concentration x that gives a response y three standard deviations above the y-intercept of the linear fit. The error bars were taken as one standard deviation calculated on a minimum of

three successive repeats of a measurement. Figure 3.6 shows an example of calculation of a LOD.

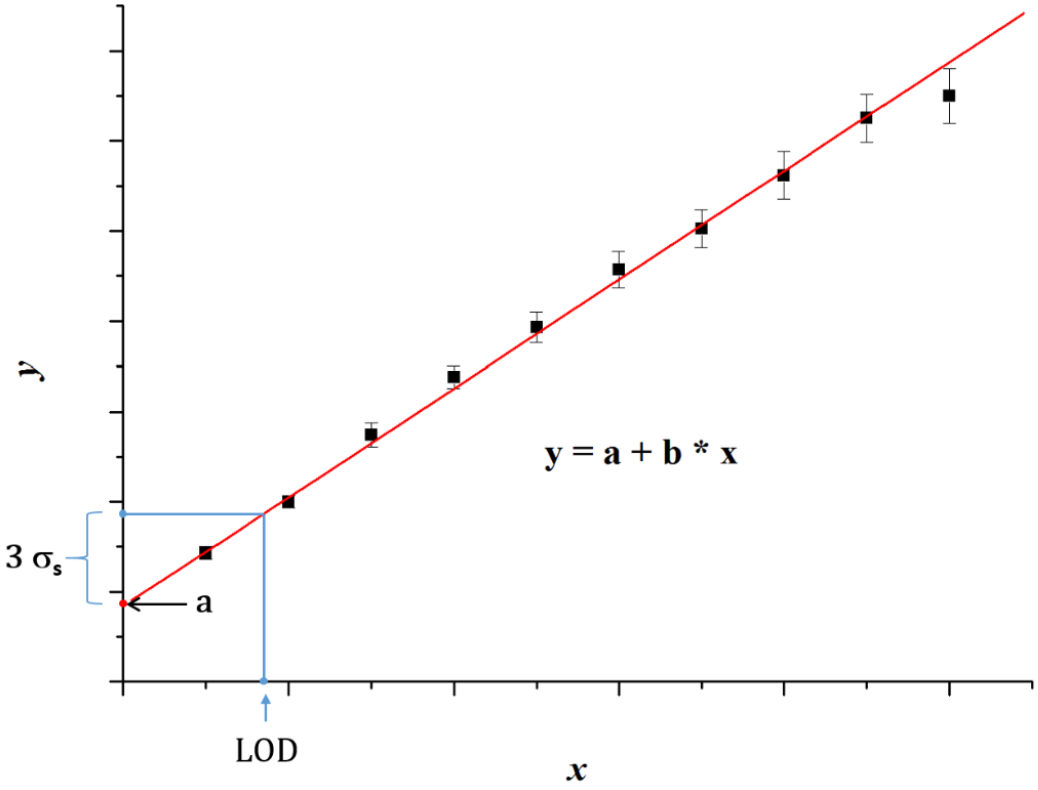

Figure 3.6: Example of calculation of a limit of detection (LOD).

3.3 Results and discussion

Tetramethylbenzidine (TMB) and *o*-phenylenediamine (OPD) are widely used chromogenic substrates for HRP- detection based systems because the products of their reaction with H_2O_2, catalysed by HRP, have high absorption coefficient and can be measured by spectrophotometry. TMB was chosen first as a co substrate, as it is not carcinogenic [15]. The range of HRP concentrations was chosen to correspond to the clinical range of PCT concentrations, as the purpose of studying the electrochemical detection of HRP is to use it as a label for the detection of PCT. In Chapter 4, HRP is attached to PCT via the associated specific anti-PCT antibody which binds on a particular area of PCT. It is then assumed that in the worse case, one molecule of HRP will be attached to a single molecule of PCT and [HRP] was then varied between 0 and 100 ng mL^{-1}. Figure 3.7 shows a picture of the 96 well

plate where the oxidation of 0.1 mM OPD by 1 mM H_2O_2 has been catalysed by increasing concentrations of HRP from 0 to 100 ng mL^{-1} and the reaction has been stopped after 10 minutes of reaction by addition of 2 M H_2SO_4. In each case, the three rows correspond to three repeats of the experiment. From left to right, each column corresponds to an increase in [HRP] of 10 ng mL^{-1}.

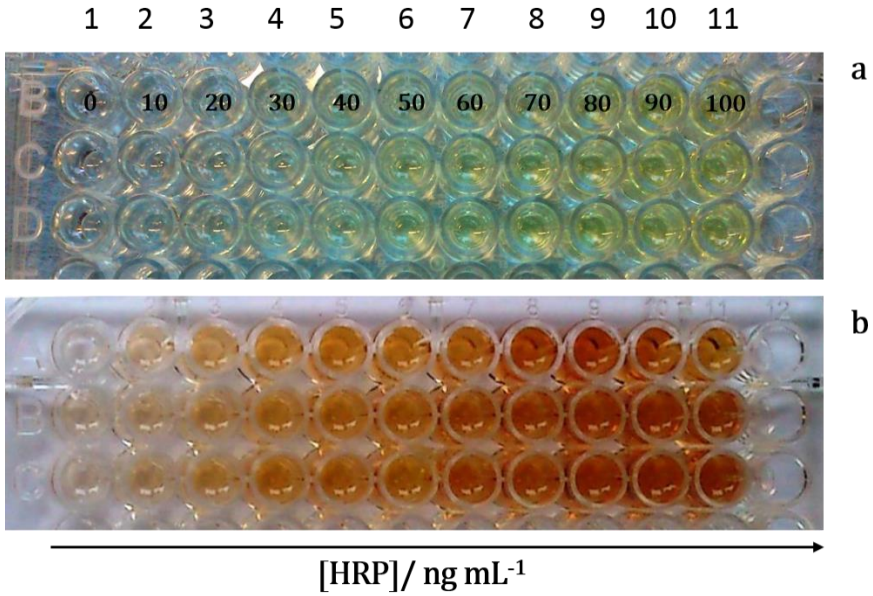

Figure 3.7: 96 well plates containing the reactions in pH = 5 phosphate-citrate buffer of 0.1 mM TMB (a) and 0.1 mM OPD (b) with 1mM H_2O_2, catalysed by concentrations of HRP. Between columns 1 and 11, [HRP] varies from 0 to 100 ng mL^{-1} by 10 ng mL^{-1} increment. The experiment was carried out in triplicate for OPD and TMB (three consecutive rows). The reaction has been stopped after 10 minutes of reaction by addition of 2 M H_2SO_4

The absorbance measurements corresponding to the experiments in Figure 3.7 are shown in Figure 3.8 (OPD is the substrate) and Figure 3.9 (TMB is the substrate). The data were fitted with a linear trend and indicate a linear relationship for both TMB and OPD substrates between 0 and 100 ng mL^{-1} (there are no error bars for TMB and the least mean square fit was done on the simple data points for reactions with TMB because of insufficient data to perform a statistical analysis).

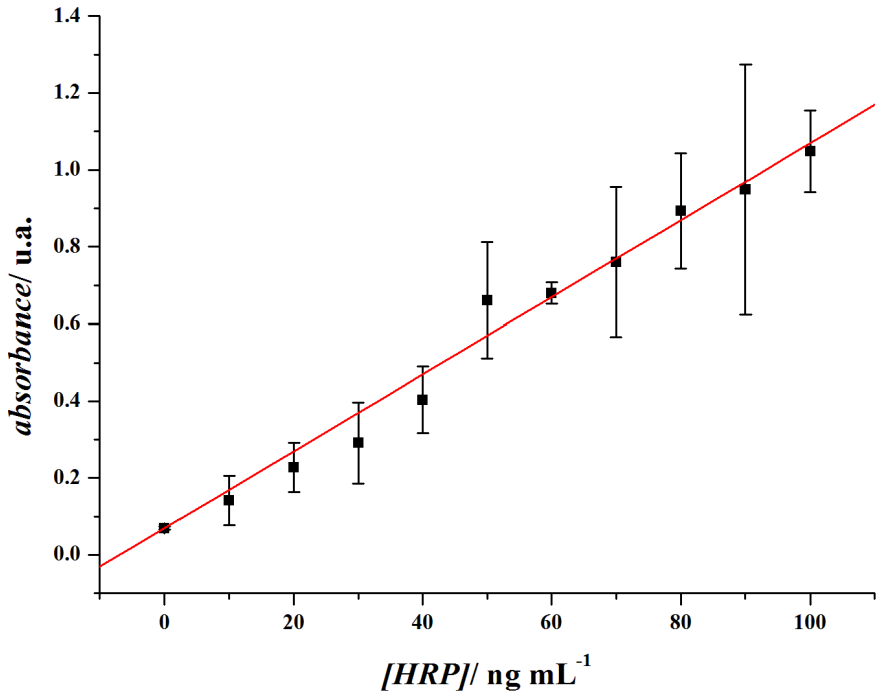

Figure 3.8: Absorbance spectrum at 490 nm of an HRP assay using OPD as a substrate. The error bars correspond to one standard deviation calculated for 3 repeats of the experiment. Red curve: linear fit.

The limit of detection for HRP was 1.43 ng mL^{-1} in the case of OPD, which is acceptable to indicate if the patient's condition is moderately likely to progress towards severe sepsis, but too low to distinguish a healthy condition from one which is septic. For comparison, recently developed biosensors have a limit of detection in the range of 10 pg mL^{-1} [16][17][18]. The LOD in the case of TMB is 18.2 ng mL^{-1} and is too high to be relevant for the determination of an early development of sepsis, but acceptable to confirm a suspected severe sepsis or septic shock condition (concentrations above 10 ng mL^{-1} are indicative of severe sepsis and septic shock).

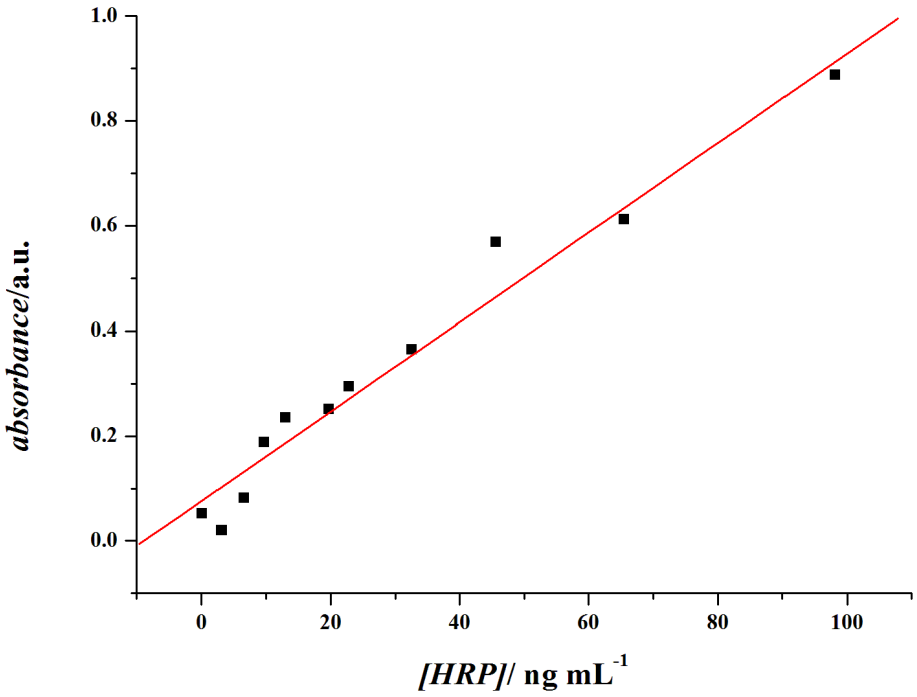

Figure 3.9: Absorbance spectrum at 450 nm of an HRP assay using TMB as a substrate. Red curve: linear fit.

3.3.1 Determination of 3,3',5,5'-tetramethylbenzidine diimine by amperometry at a Pt micro-electrode

Following absorbance spectroscopic measurements, we investigated the possibility of measuring the product of the oxidation of TMB by H_2O_2 using amperometry. It is possible to reduce the oxidation product and the reduction current recorded is assumed to be proportional to the product concentration. The three-electrode system made of the Pt working electrode, the Pt counter electrode and the Ag/AgCl/3 M NaCl reference electrode was inserted into each well containing a solution (Figure 3.5) and an electrochemical measurement was taken for each concentration of HRP. Figure 3.10 shows a cyclic voltammogram in pH = 5 phosphate citrate buffer containing 0.1 mM TMB and 1 mM H_2O_2, recorded after 10 minutes of reaction catalysed by 100 ng mL^{-1} HRP (in column 11 on the 96 well plates) and stopped by addition of 2 M H_2SO_4 (red curve). It shows a reduction peak at -0.32 V vs Ag/AgCl/3 M NaCl that is not visible in buffer only (black curve).

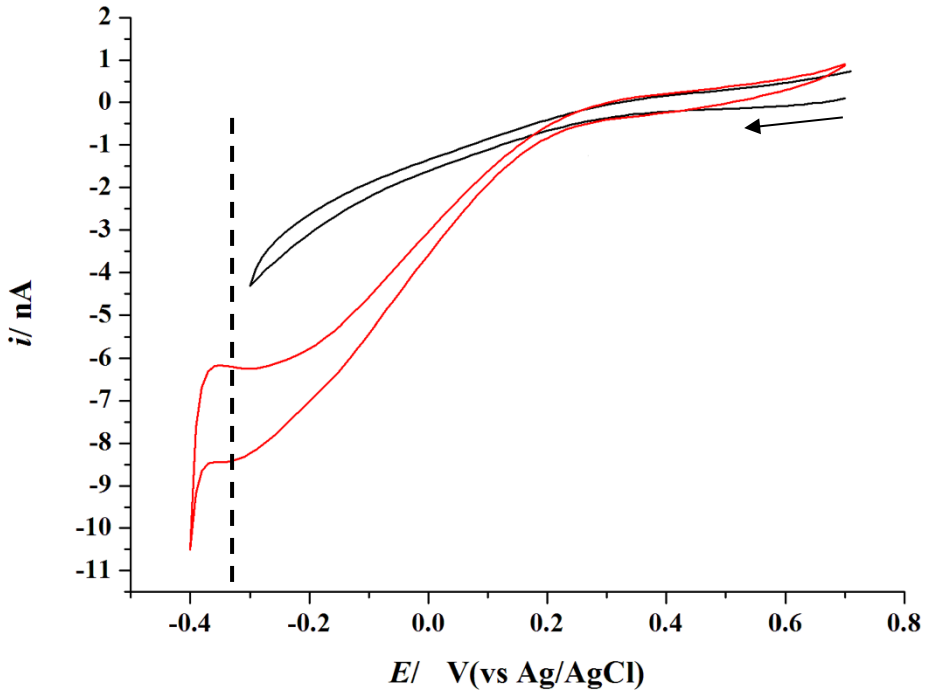

Figure 3.10: Cyclic voltammograms in pH = 5 citrate-phosphate buffer at a Pt micro-electrode: in buffer only (black curve); in buffer containing 0.1 mM TMB, 1 mM H_2O_2 and 100 ng mL^{-1} HRP, after 10 minutes of reaction stopped by addition of 2 M H_2SO_4 (red curve).

From these data, a DC voltage of -0.35 V vs Ag/AgCl/3 M NaCl could be seen to be needed to be applied at the Pt micro electrode to record amperometric measurements, which are shown in Figure 3.11. Values of the current have been taken at 180 s but are insufficiently linear to perform an analysis. The error associated which each value is also significant and the current transient is clearly levelling off at low concentrations, indicating that the LOD is too high to be clinically relevant .

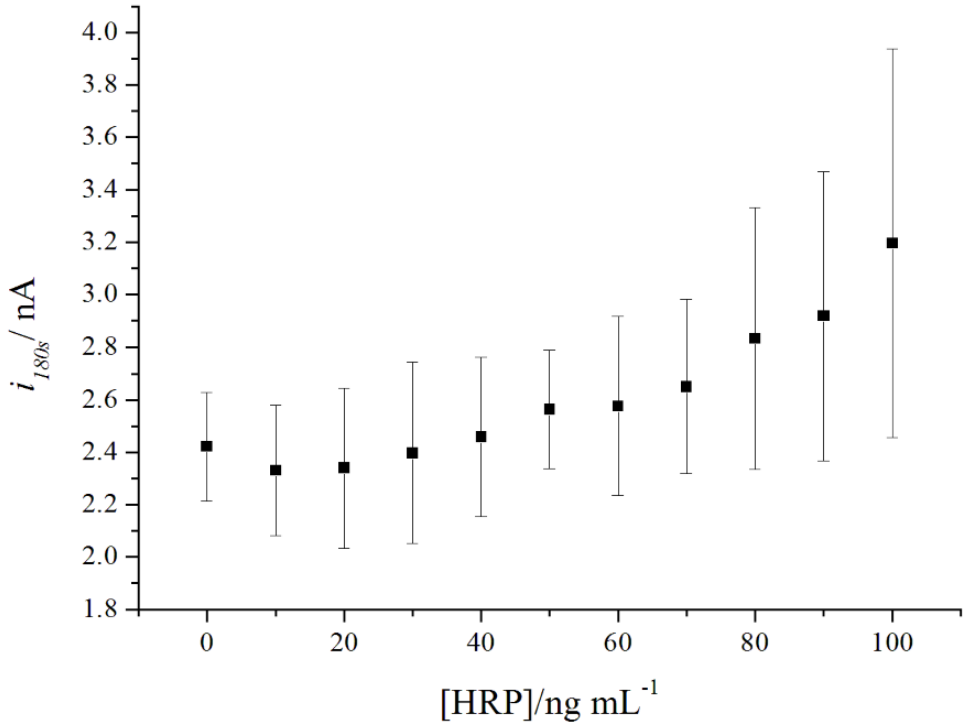

Figure 3.11: Values of the anodic current from the reduction of 0.1 mM TMB oxidised by 1 mM H_20_2 in the presence of HRP, whose concentration varies from 0 to 100 ng mL^{-1}. The error bars correspond to three repeats of the experiments.

3.3.2 Determination of 3,3',5,5'-tetramethylbenzidine diimine by measurement of the open circuit potential at a Pt micro-electrode

As both TMB and its oxidised form (3,3',5,5'-tetramethylbenzidine diimine) are present in solution in the presence of both HRP and H_20_2, we investigated the possibility of relating the concentration of HRP to the open circuit potential (OCP) of the solution. The OPC is the potential measured between the working electrode and the reference electrode when no potential is applied. It is related to the relative proportion of both oxidised (O) and reduced (R) species at the surface of the working electrode through the Nernst equation:

$$E = E^{0'} + \frac{0.059}{n} \log_{10} \frac{a_O^s}{a_R^s}$$

Where E is the open circuit potential, $E^{0'}$ is the formal redox potential of the electron transfer between O and R, n is the number of moles of electrons transferred in the cell reaction, and a_O^S is the activity of the oxidised species at the surface of the working electrode, a_R^S is the activity of the reduced species at the surface of the working electrode.

Figure 3.12 contains the values of OCP in pH = 5 phosphate-citrate buffer after 5 minutes of oxidation of 0.1 mM TMB by 1mM H_2O_2 catalysed by different concentrations of HRP. Two ranges of concentrations were investigated: between 0 and 100 ng mL^{-1} and between 0 and 1000 ng mL^{-1}. As shown from the data in Figure 3.12, within the error the OCP is independent of the concentration and the concentration range selected, and the method was not in later experiments.

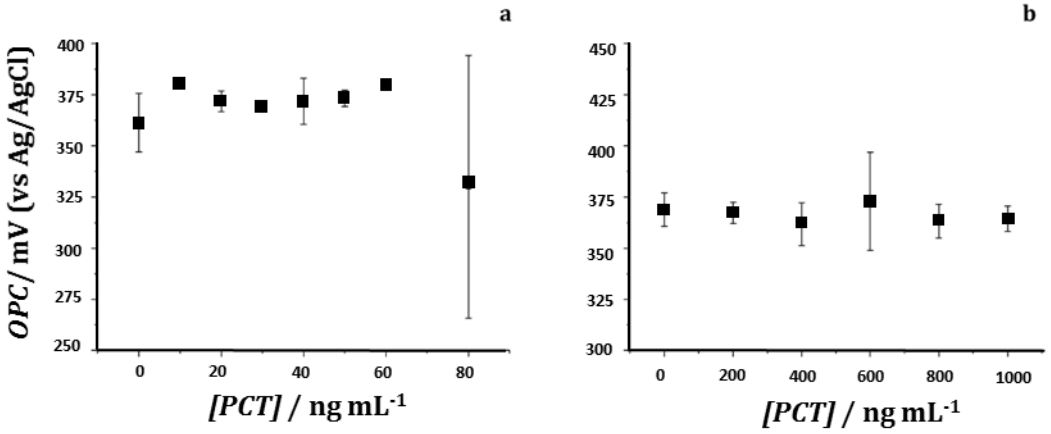

Figure 3.12: Open circuit potential values in pH = 5 phosphate-citrate buffer after 5 minutes of reaction between 0.1 mM TMB and 1mM H_2O_2 in the presence of PCT whose concentrations were varied from 0 to 100 ng mL^{-1} (a) and from 0 to 1000 ng mL^{-1} (b).

3.3.3 Determination of 2,3-diaminophenazine by amperometric measurements at a Pt micro-electrode

Another strategy to determine the concentration of HRP is to quantify the quantity of substrate that has not been oxidised by H_2O_2 after 5 minutes of reaction. Figure 3.13 shows a cyclic voltammogram in pH = 5 phosphate citrate buffer containing

0.1 mM OPD and 1 mM H_2O_2 but no HRP (column 1 on the 96 well plates in Figure 3.7), recorded after 5 minutes of reaction stopped by addition of 2 M H_2SO_4.

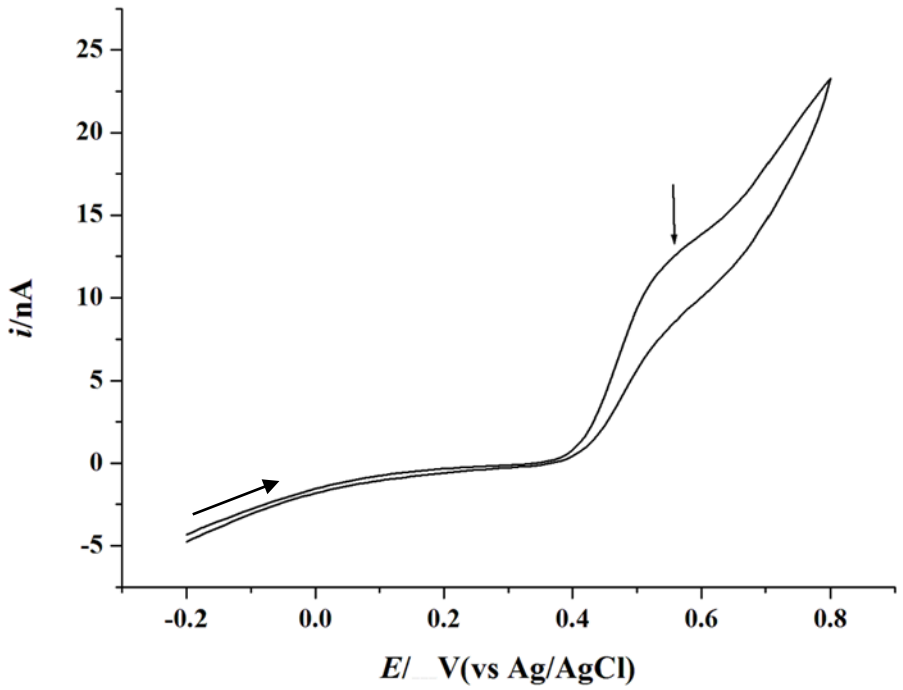

Figure 3.13: CV in pH = 5 phosphate-citrate buffer containing 0.2 mM OPD and 1 mM H_2O_2 at a Pt micro electrode. The reaction was stopped with 2 M H_2SO_4 after 5 min reaction.

Since the cyclic voltammogram shows an oxidation peak at 0.55 V vs Ag/AgCl/3 M NaCl, a DC voltage of 0.6 V vs Ag/AgCl/3 M NaCl was applied at the Pt micro electrode and anodic amperometric data were recorded for HRP concentrations between 0 and 100 ng mL^{-1}. The results for the electrochemical oxidation of the OPD remaining after 5 minutes reaction and addition of H_2SO_4 are presented in Figure 3.14 . The oxidation current was not found to be linearly related to [HRP] and the method was not used in later experiments.

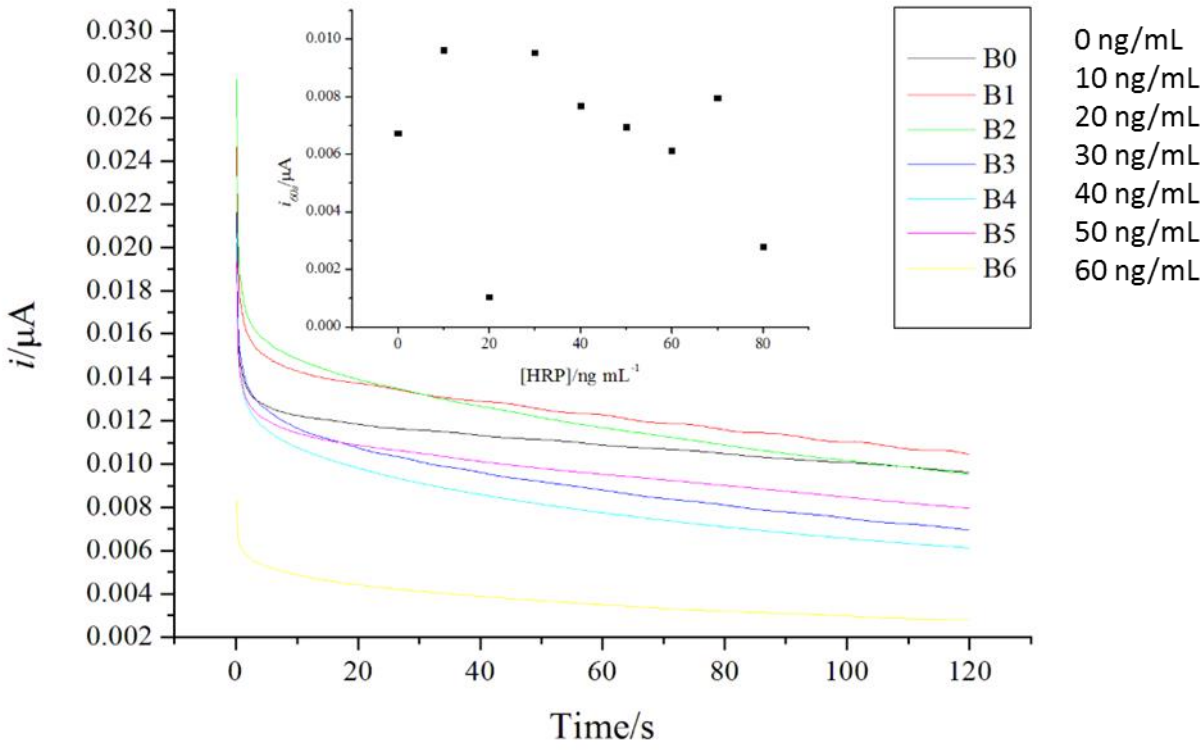

Figure 3.14: Amperometric measurements at E = 0.6 mV vs Ag/AgCl/3 M NaCl at a Pt microelectrode in a pH = 5 phosphate-citrate buffer after 5 minutes of reaction between 0.1 mM OPD and 1 mM H_20_2 catalysed by HRP whose concentration was varied between 0 ng mL^{-1} and 80 ng mL^{-1} by 10 ng mL^{-1} (B0 to B6). The inset shows a plot of current values taken at 60s after the beginning of the amperometric measurements.

3.3.4 Determination of 3,3',5,5'-tetramethylbenzidine diimine by amperometric measurements at a carbon screen printed electode

As experiments with a custom made three-electrode system were not conclusive, carbon screen printed electrodes (CSPE) were investigated as a substrate for the detection of TMB_{ox}. CSPE present a convenient inexpensive, reproducible and disposable three-electrode (carbon working and counter electrodes, silver pseudo reference electrode) platform for biosensing (see Figure 3.5 for a schematic of the CSPE used here). Figure 3.15 shows a cyclic voltammogram in pH = 5 phosphate-citrate buffer containing 0.1 mM TMB and 0.1 mM H_2O_2. An oxidation peak and a reduction peak are observed, respectively at 0.34 V vs Ag and 0.26 V vs

Ag. A DC voltage of 0.1 V vs Ag was then applied at the CSPE for the cathodic amperometric measurements.

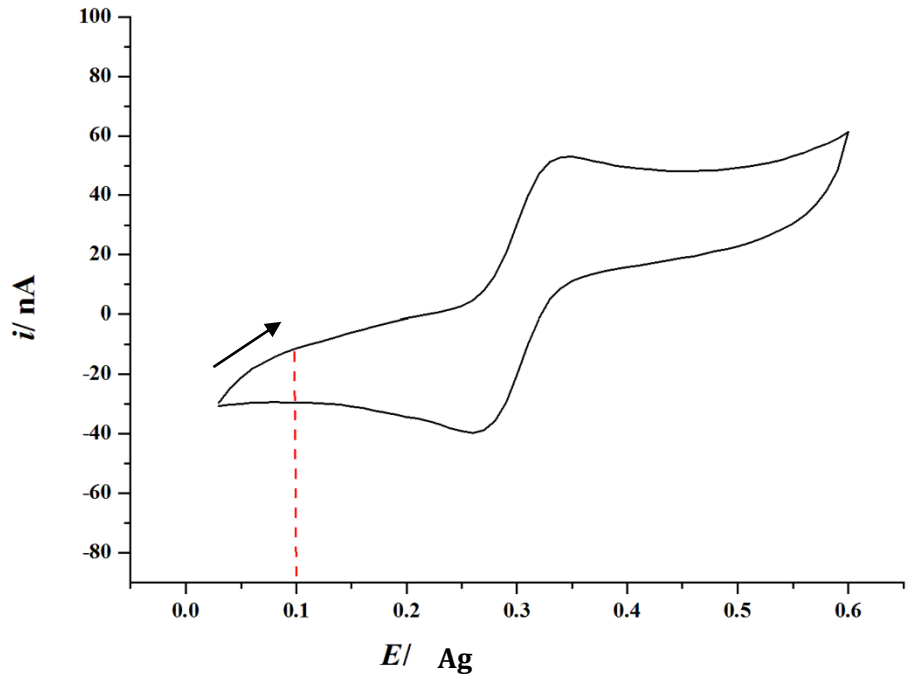

Figure 3.15: Cyclic voltammogram in pH = 5 phosphate-citrate buffer containing 0.1 mM OPD and 1 mM H_2O_2 at a carbon screen printed electrode and at a scan rate of 0.05 V s^{-1}. The potential selected for amperometric measurement is indicated by the dashed line.

Figure 3.16 shows that the value of the reduction current (taken at 20 s) is linearly related to the concentration of HRP between 10 and 70 ng mL^{-1}, with a limit of detection of 23.21 ng mL^{-1}. The limit of detection is too high and the error associated with the measurements to important for the test to be clinically relevant. More sensitive electrochemical methods must be explored to improve the diagnostic test.

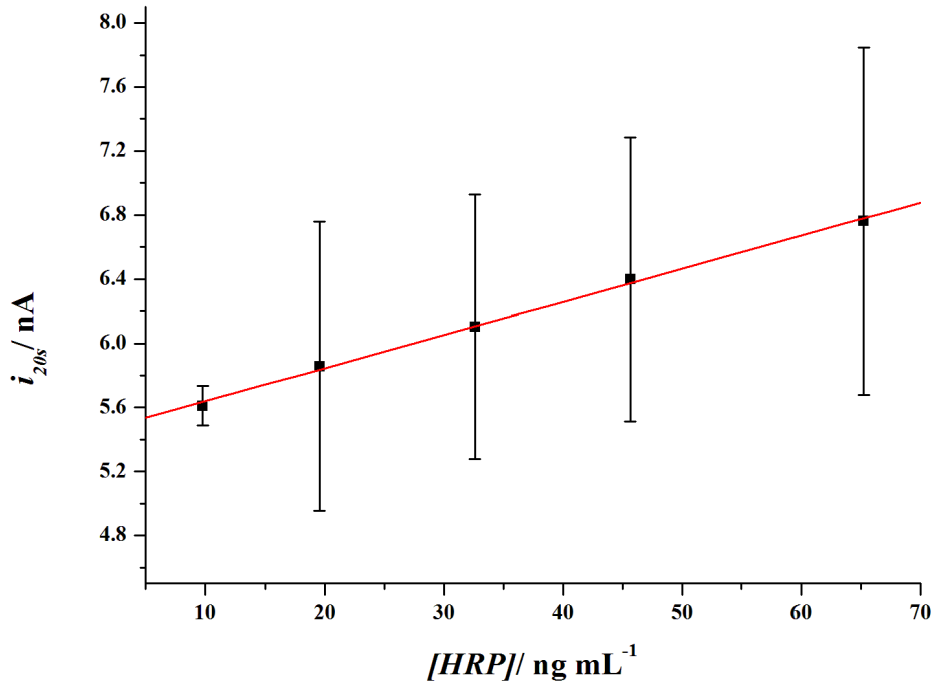

Figure 3.16: Reduction currents taken at 20s from amperometric measurements for concentrations of PCT between 10 and 70 ng mL^{-1}. The error bars correspond to one standard deviation calculated on 4 successive amperometric measurements at each concentration of PCT.

3.4 Conclusion

In this chapter, we first verified the absorbance spectroscopic assay for HRP. We then demonstrated that it is possible to detect HRP electrochemically, though a more sensitive method than amperometry have to be used to calibrate a working surface.

Bibliography

[1] P. B. Luppa, L. J. Sokoll, and D. W. Chan, "Immunosensors--principles and applications to clinical chemistry," *Clin. Chim. Acta.*, vol. 314, no. 1–2, pp. 1–26, 2001.

[2] W. R. Heineman and H. B. Halsall, "Strategies for electrochemical immunoassay," *Anal. Chem.*, vol. 57, no. 12, p. 1321A–1331A, 1985.

[3] F. Ricci, G. Adornetto, and G. Palleschi, "A review of experimental aspects of electrochemical immunosensors," *Electrochim. Acta*, vol. 84, pp. 74–83, 2012.

[4] X.-M. Li, X.-Y. Yang, and S.-S. Zhang, "Electrochemical enzyme immunoassay using model labels," *TrAC Trends Anal. Chem.*, vol. 27, no. 6, pp. 543–553, 2008.

[5] M. Y. Wei, S. D. Wen, X. Q. Yang, and L. H. Guo, "Development of redox-labeled electrochemical immunoassay for polycyclic aromatic hydrocarbons with controlled surface modification and catalytic voltammetric detection," *Biosens. Bioelectron.*, vol. 24, no. 9, pp. 2909–2914, 2009.

[6] J. Wu, J. Tang, Z. Dai, F. Yan, H. Ju, and N. El Murr, "A disposable electrochemical immunosensor for flow injection immunoassay of carcinoembryonic antigen," *Biosens. Bioelectron.*, vol. 22, no. 1, pp. 102–108, 2006.

[7] N. J. Ronkainen-Matsuno, J. H. Thomas, H. B. Halsall, and W. R. Heineman, "Electrochemical immunoassay moving into the fast lane," *TrAC - Trends Anal. Chem.*, vol. 21, no. 4, pp. 213–225, 2002.

[8] H. Tang, J. Chen, L. Nie, Y. Kuang, and S. Yao, "A label-free electrochemical immunoassay for carcinoembryonic antigen (CEA) based on gold nanoparticles (AuNPs) and nonconductive polymer film," *Biosens. Bioelectron.*, vol. 22, no. 6, pp. 1061–1067, 2007.

[9] K. Kerman, N. Nagatani, M. Chikae, T. Yuhi, Y. Takamura, and E. Tamiya, "Label-free electrochemical immunoassay for the detection of human chorionic gonadotropin hormone," *Anal. Chem.*, vol. 78, no. 15, pp. 5612–5616, 2006.

[10] K. Z. Liang, J. S. Qi, W. J. Mu, and Z. G. Chen, "Biomolecules/gold nanowires-doped sol-gel film for label-free electrochemical immunoassay of testosterone," *J. Biochem. Biophys. Methods*, vol. 70, no. 6, pp. 1156–1162, 2008.

[11] T. Porstmann and S. T. Kiessig, "Enzyme immunoassay techniques. An overview," *J. Immunol. Methods*, vol. 150, no. 1–2, pp. 5–21, 1992.

[12] A Bhimji, A. A. Zaragoza, L. S. Live, and S. O. Kelley, "Electrochemical Enzyme-Linked Immunosorbent Assay Featuring Proximal Reagent Generation: Detection of Human Immunodeficiency Virus Antibodies in Clinical Samples," *Anal. Chem.*, vol. 85, no. 14, pp. 6813–6819, 2013.

[13] P. D. Josephy, T. Eling, and R. P. Mason, "The Horseradish Peroxidase-catalyzed Oxidation of 3,5,3',5'- Tetramethylbenzidine," *J. Biol. Chem.*, vol. 257, no. 7, pp. 3669–3675, 1982.

[14] A. Shrivastava and V. Gupta, "Methods for the determination of limit of detection and limit of quantitation of the analytical methods," *Chronicles Young Sci.*, vol. 2, no. 1, p. 21, 2011.

[15] A. Frey, B. Meckelein, and M. A. Schmidt, "A stable and highly sensitive 3, 3', 5, 5'-tetramethylbenzidine-based substrate reagent for enzyme-linked immunosorbent assays," *J. Immunol. Methods.*, vol. 233, no. 1, pp. 47–56, 2000.

[16] Y. S. Fang, H. Y. Wang, L. S. Wang, and J. F. Wang, "Electrochemical immunoassay for procalcitonin antigen detection based on signal amplification strategy of multiple nanocomposites," *Biosens. Bioelectron.*, vol. 51, pp. 310–316, 2014.

[17] F. Baldini, L. Bolzoni, a. Giannetti, M. Kess, P. M. Krämer, E. Kremmer, G. Porro, F. Senesi, and C. Trono, "A new procalcitonin optical immunosensor for POCT applications," *Anal. Bioanal. Chem.*, vol. 393, no. 4, pp. 1183–1190, 2009.

[18] M. Kemmler, U. Sauer, E. Schleicher, C. Preininger, and A. Brandenburg, "Biochip point-of-care device for sepsis diagnostics," *Sensors Actuators, B Chem.*, vol. 192, pp. 205–215, 2014.

Chapter 4

Electrochemical labelled detection of 2,3-diaminophenazine on graphene for the indirect determination of procalcitonin

Abstract

A common way to detect a biomolecule is to use an enzyme-linked immunosorbent assay (ELISA) to sandwich it between two specific antibodies. One of the antibodies is often derivatized with an enzyme such as horseradish peroxidase (HRP) that catalyses a reaction whose product can be detected electrochemically. The other specific antibody is tethered to a surface that can support electrochemistry, such as graphene.

Here, a proof-of-concept is presented on the indirect detection of the sepsis biomarker procalcitonin by square wave voltammetry at a graphene electrode. The detection is based on the reduction of 2,3-diaminophenazine which is the product of the HRP catalysed oxidation of OPD by H_2O_2. A method is also described that was used to regenerate the graphene electrodes after use, in order to circumvent the issue of the lack of reproducibility of their fabrication method.

4.1 Introduction

Chapter 3 was concerned with investigating the possible detection of horseradish peroxidase (HRP) in bulk solution by electrochemical methods at various electrodes. The strategy used consisted of detecting the product of the HRP-catalysed oxidation of *o*-phenylenediamine (OPD) [1] or tetramethylbenzidine (TMB) [2] by H_2O_2. Success here was followed in the present chapter by the detection of HRP on graphene electrodes, both in homogenous solution and as an adsorbed species. The purpose of these experiments was to use HRP as a label on a graphene-based biosensor for the sepsis biomarker procalcitonin (PCT). The sensor is based on an electrochemical enzyme-linked immunosorbant assay (ELISA) which consists here of a sandwich of PCT (when present in the sample under study) between a specific antibody bound to the graphene electrode and a second specific antibody that has been labelled with HRP. The enzyme then catalyses the oxidation of OPD or TMB by H_20_2 and the product of the reaction is detected by electrochemical methods at the graphene electrode. The measured output signal is expected to provide a quantifiable measure of the amount of PCT in the sample of interest.

In this chapter a proof-of-concept sensor is described for the detection of PCT on graphene by square-wave voltammetry, based on the detection of 2,3-diaminophenazine which is the product of the HRP catalysed oxidation of OPD by H_2O_2 [3]. Square wave voltammetry was selected, as it is a very sensitive and fast technique [4][5]. Because the graphene electrodes could not be produced with sufficient reproducibility, different ways of increasing the reproducibility of the electrochemical measurements were investigated in order to be able to calibrate the graphene electrodes for PCT detection.

4.2 Experimental

4.2.1 Reagents

Graphene was purchased from Graphene Supermarket as a single layer grown on copper foil. Phosphate-citrate buffer (Sigma Aldrich, pH = 5) was used as

electrolyte throughout, while all aqueous solutions were prepared using ultra-pure water (Milli-Q Millipore) with a resistivity of ca. 18.1 MΩ cm at 25 ˚C. Methanol (CH_3OH, 99.99%), sodium carbonate (Na_2CO_3, ≥ 99%), sodium bicarbonate ($NaHCO_3$, ≥ 99%) were all purchased from Fisher Scientific and used without further purification. Ethanolamine ($H_2NC_2H_4OH$, ≥ 99.0%), ferrocenemethanol ($Fe(C_5H_5)_2$, 97%) phosphate-buffered saline (PBS, pH = 7.4), 1-pyrenebutanoic acid succinimidyl ester (PSE, 95%), hexaammineruthenium(III) chloride ($Ru(NH_3)_6Cl_3$, Fisher Scientific, 98%), *o*-phenylenediamine (OPD, tablet 20 mg), Tween 20 (T20, viscous liquid, ≥ 97%), tetrabutylammonium hexafluorophosphate (≥ 97%), sodium dodecyl sulfate (SDS, ≥ 99%) and bovine sulphate albumin (BSA, heat shock fraction, lyophilized powder, ≥ 98%, pH = 7) were all purchased from Sigma-Aldrich and used without further purification. Monoclonal anti-human procalcitonin capture antibody (clone 42) and HRP labelled monoclonal anti-human procalcitonin detection antibody (clone 16B5) were purchased from 2B Scientific. Human procalcitonin (PCT) was purchased from Prospec.

4.2.2 Fabrication of graphene electrodes

Single and multiple graphene electrodes were prepared according to the method described in Chapter 2.

4.2.3 Physisorption of 1-pyrenebutanoic acid succinimidyl ester on graphene

Graphene can be modified with proteins using the π-π stacking of pyrene-based linker molecules on its basal plane. One such linker molecule is 1-Pyrenebutanoic acid succinimidyl ester (PSE) [6]. PSE (Figure 4.1) contains a pyrene moiety (4 benzene ring structure) that π-stacks on graphene without disrupting its electronic structure as a covalent link would, and an active ester that reacts with an amine termination on proteins to create an amide bond.

The increasing surface coverage of PSE on a graphene electrode immersed in a methanol solution of PSE, at 1 mM, was monitored by electrochemical impedance spectroscopy (EIS) as a change in charge transfer resistance associated with

ferrocenemethanol 1 mM in the methanol solution, also containing 0.1 M tetrabutylammonium hexafluorophosphate.

This charge transfer resistance was related to the surface coverage of PSE according to the following equation:

$$\theta = \left[1 - \left(\frac{R_{ct}^{0}}{R_{ct}}\right)\right] * 100 \qquad (1)$$

θ is the surface coverage in % of the graphene electro-active surface, R_{ct}^{0} is the initial charge transfer resistance to bare graphene, R_{ct} is the charge transfer resistance to PSE modified graphene. This is considering that the increase in charge transfer resistance is due to the adsorption of pyrene on the graphene surface. EIS measurements were performed using a CompactStat Impedance Analyser controlled with the IviumSoft Electrochemistry software (Ivium), or with a Schlumberger/Solartron SI1260 Impedance/Gain-Phase Analyzer and SI1287 Electrochemical Interface, both under computer control using Z-Plot software (Scribner Associates Inc.).

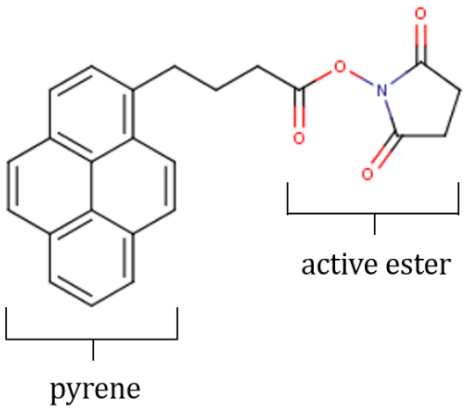

Figure 4.1: 1-Pyrene butanoic succinimidyl ester

4.2.4 Fabrication of the electrochemical ELISA graphene sensor for procalcitonin

The graphene electrode was incubated for 10 min in PSE then rinsed in methanol then ultrapure water. The others steps involved were all followed by rinsing in pH = 7.4 containing Tween20 (0.05 % v/v). The surface was then soaked in BSA

(1 % w/w in PBS) for 5 min. BSA, which is the major blood serum protein, was used as a standard commercial blocking buffer. This was in anticipation of future use of the sensor in biological media, where it would block nonspecific protein-surface interactions.

Attachment of HRP on the PSE modified graphene

The PSE modified graphene electrode surface was soaked for 1h at room temperature in a solution of HRP (5 μg mL^{-1} in pH = 9.2 carbonate-bicarbonate buffer).

Attachment of ELISA sandwich on the PSE modified graphene

The graphene sensor electrode surface was soaked for 1h at room temperature in a solution of capture anti-PCT antibody (Ab1, 5 μg mL^{-1} in pH = 9.2 carbonate-bicarbonate buffer). The antibody attaches to PSE by forming an amine bond, as illustrated in Figure 4.2.

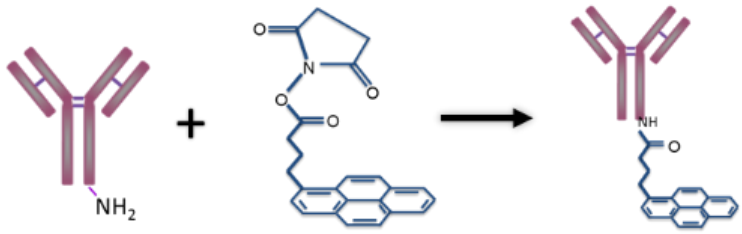

Figure 4.2: anti-procalcitonin antibodies attach o PSE via the formation of an amide bond between the ester group on PSE and an amine group on the antibody.

The surface was then left to soak in ethanolamine for 15 min to deactivate unreacted ester groups. The modified surface was then left to soak for 1 h at room temperature in a solution of PCT (500 ng mL^{-1} in pH = 7.4 PBS) to attach it by its specific antibodies on its antigen binding site. Finally, the sensor was soaked for 1h at room temperature in a solution of HRP-labelled anti-PCT antibody (Ab2, 40 μg mL^{-1} in pH = 7.4 PBS). Figure 4.3 illustrates the principles of the electrochemical ELISA PCT sensor.

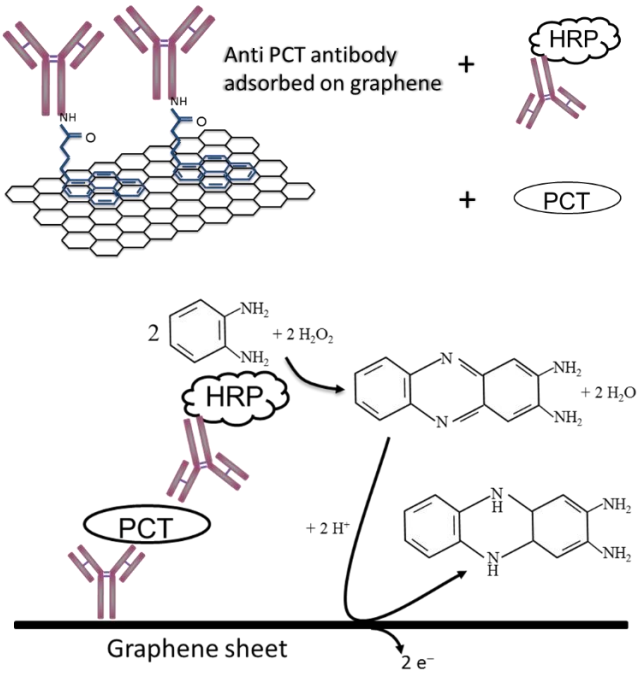

Figure 4.3: Configuration of the procalcitonin biosensor.

4.2.5 Electrochemical measurements

All potentials were recorded versus an Ag/ AgCl/ 3M NaCl (BASi) reference electrode. The counter electrode was a coiled platinum wire auxiliary electrode (23 cm, BASi). The electrochemical cell was operated in the normal, three-electrode mode for all the electrochemical measurements. Cyclic voltammetry was performed at a potential scan rate of 0.05 V s^{-1} using a CompactStat electrochemical interface (Ivium technologies) or a BAS 100B/W Electrochemical Analyser (BASi). Square-wave voltammetry measurements were performed at 15 Hz, with voltage pulses of 25 mV amplitude and staircase shift 1 mV at the beginning of each cycle. All solutions were purged with N_2 prior to electrochemical measurement.

4.2.6 Regeneration of the sensor surface

One strategy to circumvent the lack of reproducibility of graphene electrodes is to reuse them by renewing their surface, which means removing the attached ELISA sandwich with a chemical such as SDS.

SDS is a surfactant that denatures the ternary structure of proteins [7] and imparts a negative charge to them in proportion to their mass. After building the ELISA sensor as described in section and performing electrochemical measurements as described in section 2.5, the sensor was soaked in a solution of 1 mM SDS (in pH = 5 phosphate-citrate buffer) for 30 min and the removal of the ELISA sandwich was verified electrochemically. The sensor was then rebuilt according to the method described in section 2.4 and tested electrochemically. The process is shown schematically in Figure 4.4.

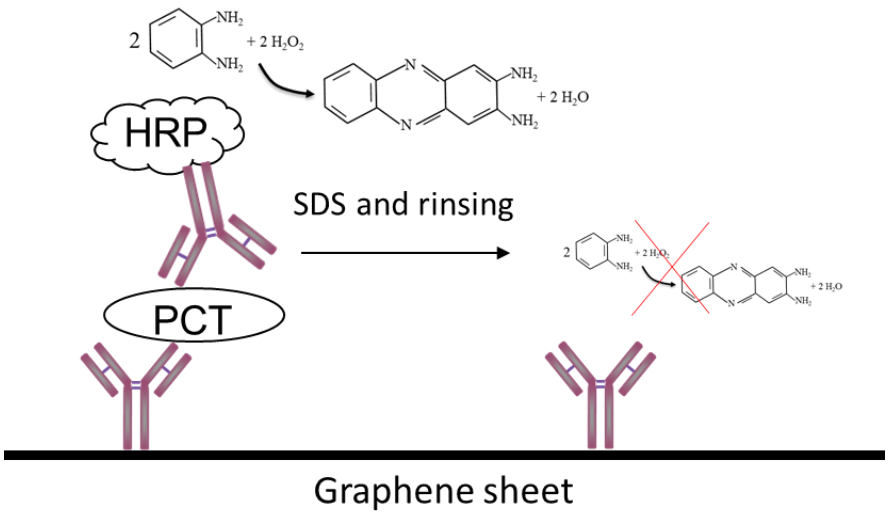

Figure 4.4 : Use of SDS as a regeneration buffer to renew the surface of the graphene electrodes.

4.3 Results and discussion

4.3.1 Proof-of concept of the detection of procalcitonin by square-wave voltammetry on a graphene electrode

In Chapter 3, it was shown that both TMB and OPD could be used to detect HRP electrochemically on a carbon screen printed electrode, using amperometry. Following this result, the detection of HRP was also attempted by amperometry on graphene single electrodes. However, the limit of detection achieved was too high to be clinically useful and the results were not reproducible. For these reasons, square wave voltammetry (see Chapter 2) was preferred as an electrochemical method for lower limits of detection. In adopting this method, it was necessary to

verify that no oxidised OPD was produced electrochemically at the start potential of the square wave voltammetry. This was done electrochemically. Figure 4.5 contains a cyclic voltammogram of TMB at a graphene electrode showing two oxidation peaks (0.35 V and 0.5 V vs Ag/AgCl/ 3M NaCl) and two reduction peaks (0.3 V and 0.45 V vs Ag/ AgCl/ 3M NaCl) which are very close to each other.

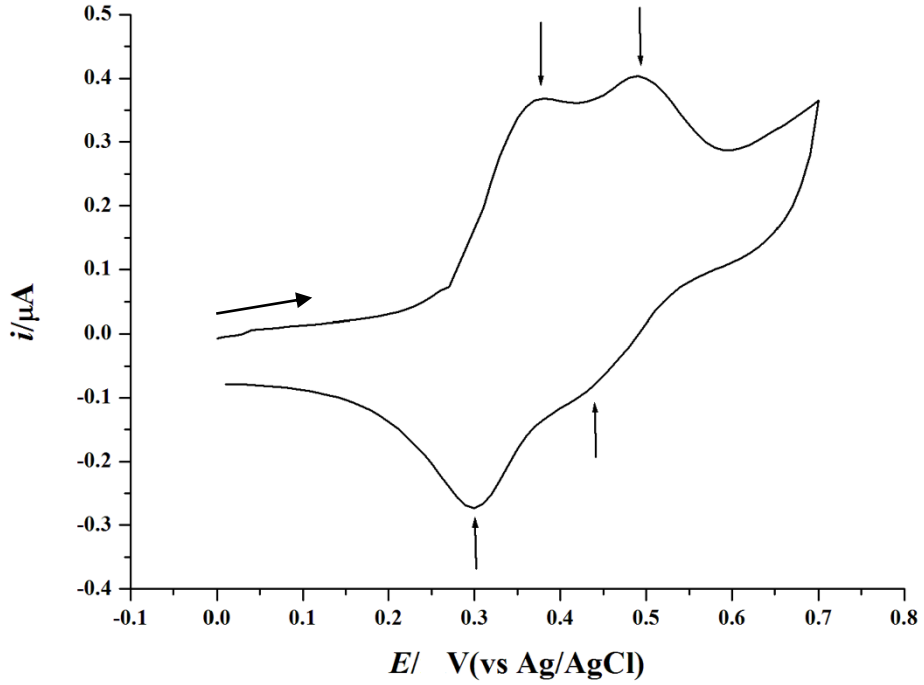

Figure 4.5: Cyclic voltammogram recorded at a graphene electrode in 0.1 mM TMB in pH = 5 phosphate-citrate buffer at a sweep rate of 0.05 V s^{-1}. The oxidation and reduction peaks positions are indicated by arrows.

To reduce the TMB oxidised by H_2O_2 and observe by square-wave voltammetry a peak that can be related to the quantity of HRP (therefore to PCT) attached to the graphene electrode, the potential sweep would have to start at around 0.4 V vs Ag/ AgCl/ 3M NaCl as a minimum positive value and then go to more negative potentials. It is clear from the voltammogram in Figure 4.4 that by beginning the square wave voltammetry at 0.4 V vs Ag/ AgCl/ 3M NaCl, it is very likely that some TMB would be oxidised electrochemically and contribute to the reduction peak.

As an alternative to TMB, the electrochemistry of OPD was investigated. The cyclic voltammogram of OPD, shown in Figure 4.6, contains only one oxidation peak (0.7 V vs Ag/ AgCl/ 3M NaCl) and one reduction peak (-0.5 V vs Ag/ AgCl/ 3M NaCl).

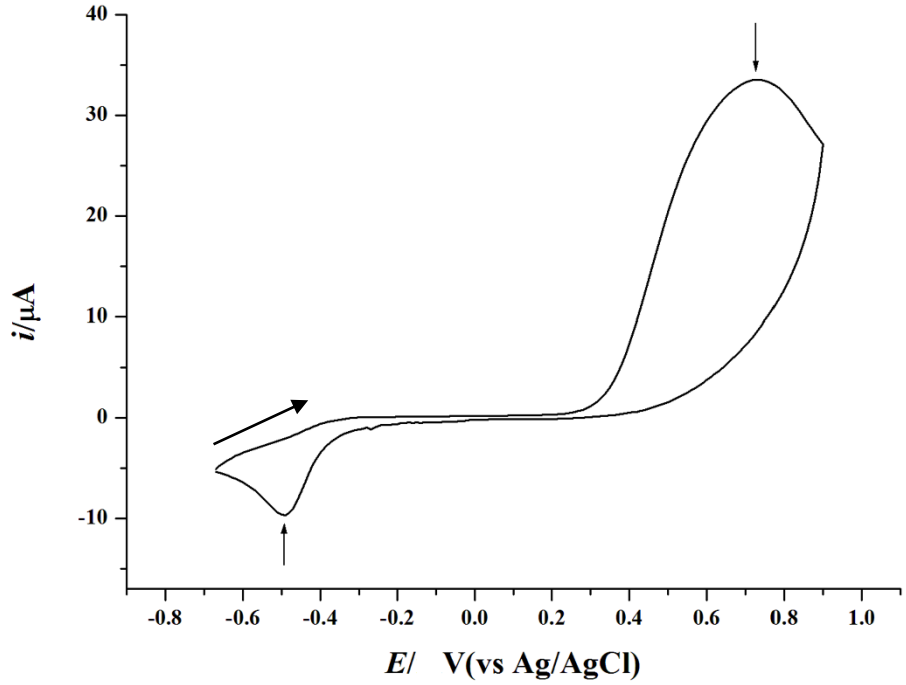

Figure 4.6: Cyclic voltammogram recorded at a graphene electrode in 0.1 mM OPD in pH = 5 phosphate-citrate buffer at a sweep rate of 0.05 V s^{-1}. The oxidation and reduction peaks positions are indicated by vertical arrows.

Starting the square wave voltammetry potential sweep at 0.1 V vs Ag/ AgCl/ 3M NaCl would therefore not produce oxidised OPD that is unrelated to the presence of HRP (and therefore of PCT). In order to verify this, successive cyclic voltammograms in OPD were recorded between -0.6 V and 0.1 V vs Ag/ AgCl/ 3M NaCl, starting at -0.6 V vs Ag/ AgCl/ 3M NaCl and going positively. These voltammograms are shown in Figure 4.7 and exhibit no oxidation or reduction peaks, which was interpreted as there being no OPD being electrochemically oxidised in this potential range. OPD was therefore preferred as a co-substrate in all subsequent experiments.

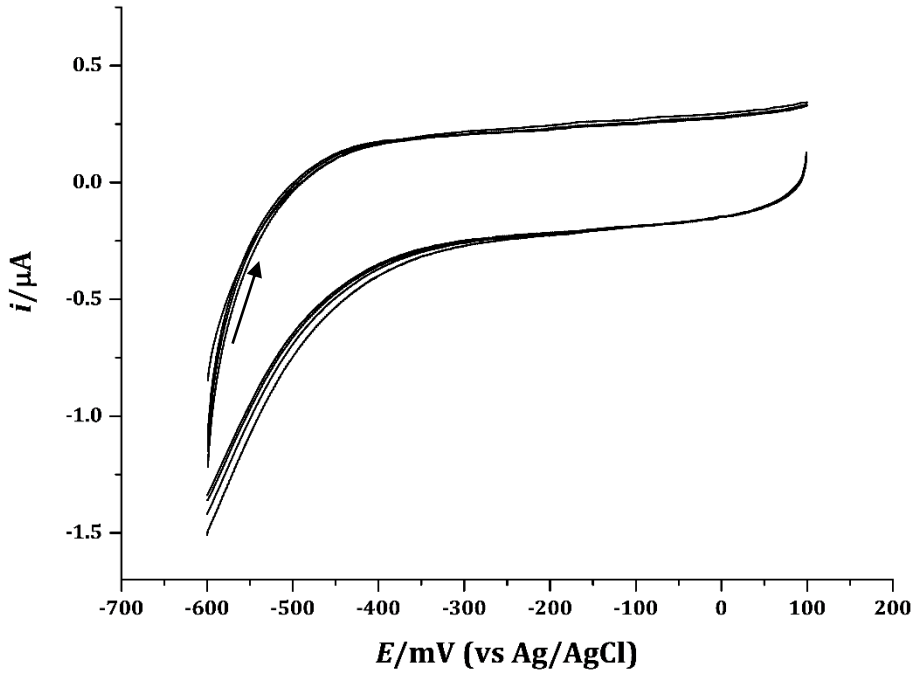

Figure 4.7: Cyclic voltammograms recorded at a graphene electrode between -0.6 V and 0.1 V vs Ag/ AgCl/ 3M NaCl in pH = 5 phosphate-citrate buffer containing 0.1 mM OPD and 2 M H_2SO_4, at a scan rate of 0.05 V s^{-1}.

Figure 4.8 shows further cyclic voltammograms of OPD 0.1 mM in phosphate-citrate buffer pH = 5 where the potential sweep range was extended to -0.8 V and 0.8 V vs Ag/ AgCl/ 3M NaCl. Two oxidation peaks are visible at 0.46 V and 0.7 V vs Ag/ AgCl/ 3M NaCl on the first segment (starting at -0.8 V vs Ag/ AgCl/ 3M NaCl), followed by three reduction peaks at 0.02 V, -0.26 V and -0.4 V vs Ag/ AgCl/ 3M NaCl on the second segment. That the third segment shows four successive oxidation peaks at -0.3 V, 0.11 V, 0.11 V and 0.51 V vs Ag/ AgCl/ 3M NaCl is likely to be due to the oxidative polymerisation of *o*-phenylenediamine. This behaviour has been observed elsewhere and used for various applications [8]. To avoid oxidising OPD electrochemically and to polymerise OPD on the electrode, it was decided to run square wave voltammetry measurements between 0.1 V to -0.6 V vs Ag/ AgCl/ 3M NaCl.

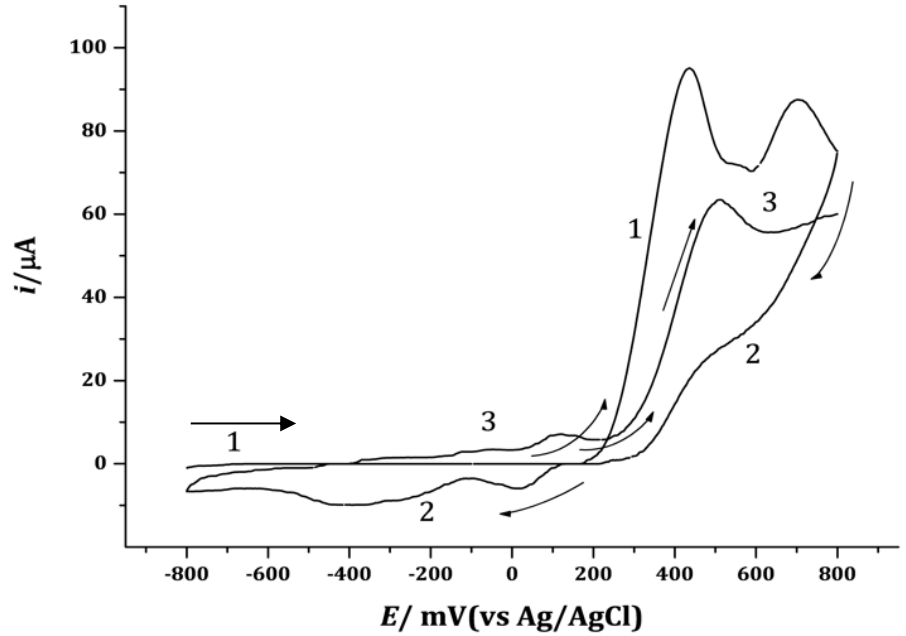

Figure 4.8: Cyclic voltammograms at a graphene electrode in pH = 5 phosphate-citrate buffer containing 0.1 mM OPD, at a scan rate of 0.05 V s^{-1} and between -0.8 V and 0.8 V vs Ag/ AgCl/ 3M NaCl (black curve). The numbers 1, 2 and 3 correspond to the first, second and third segments of the cyclic voltammogram.

Figure 4.9 contains a square wave voltammogram at a graphene electrode, recorded after 3 min of HRP catalysed homogeneous reaction (stopped by addition of 2M H_2SO_4) between OPD and H_2O_2. A definite reduction peak was observed at -0.17 V vs Ag/ AgCl/ 3M NaCl. The same experiment was performed with OPD only (dot line) and with OPD and H_2O_2 only (dash line), as control experiments. No peak was observed in the absence of HRP. Thus, the reduction peak at -0.17 V vs Ag/ AgCl/ 3M NaCl was attributed to the reduction of OPD oxidised by H_2O_2.

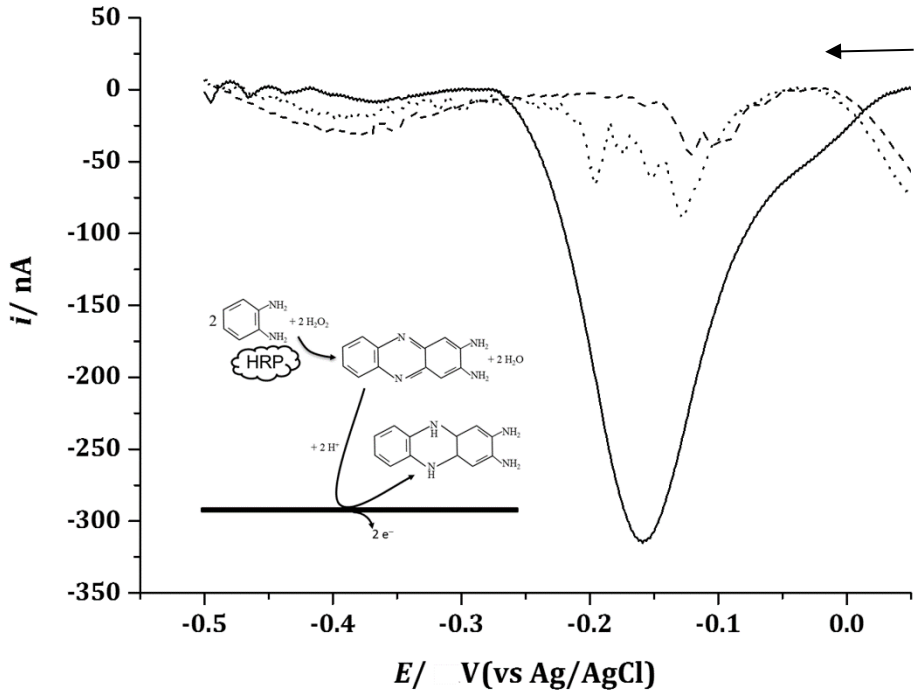

Figure 4.9: Square wave voltammograms recorded at a graphene electrode in phosphate-citrate buffer pH = 5 containing 0.1 mM OPD and 5 mM H_2O_2 30% (v/v) and 50 ng mL^{-1} HRP (solid line). Square wave voltammograms were also recorded at the same graphene electrode in the same phosphate-citrate buffer pH = 5 where H_20_2 and HRP were omitted (dotted line) or only HRP was omitted (dashed line). The data were recorded after 3 minutes and addition of 2 M H_2SO_4. Square wave voltammetry parameters: f = 15 Hz, E_{step} = 1 mV, $E_{\text{amplitude}}$ = 25 mV. Inset: Schematic of the HRP catalysed oxidation of OPD by H_2O_2 in a homogenous reaction at a graphene electrode

Figure 4.10 shows a comparison of square-wave voltammograms for a solution of OPD at graphene and glassy carbon electrodes, after the OPD had been oxidised by H_2O_2 for 3 minutes and the reaction stopped with 2 M H_2SO_4. Both voltammograms contain a reduction peak, at -0.14 V vs Ag/ AgCl/ 3M NaCl on glassy carbon and -0.15 V vs Ag/ AgCl/ 3M NaCl on graphene. Though very close in potential, the peak current recorded using graphene was about 12 times smaller for the same surface. This could indicate that only a small proportion of the graphene surface is

electrochemically active, possibly because of pinholes or defects (originally present and created during the transfer process).

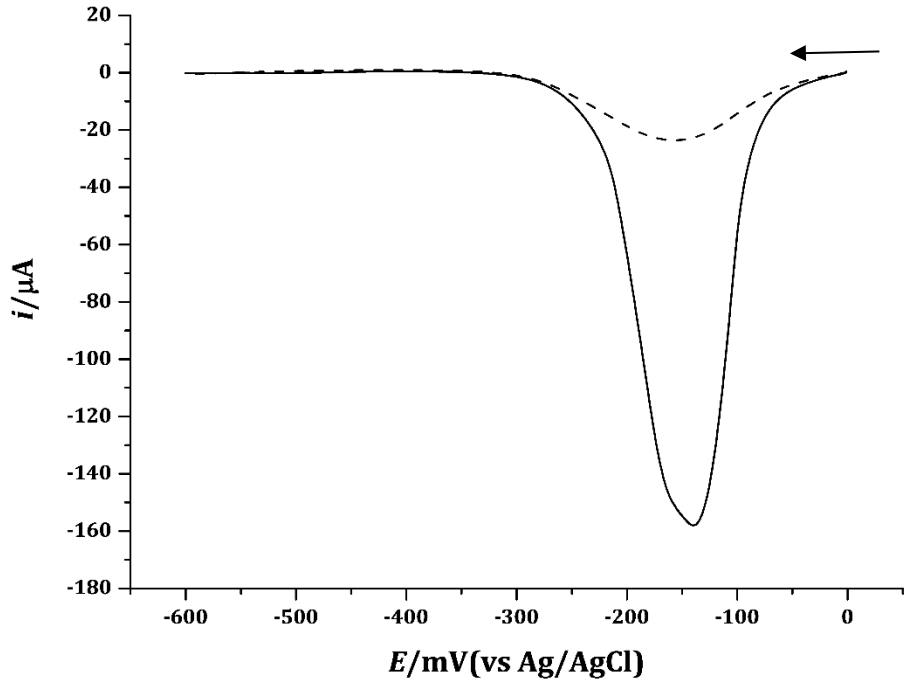

Figure 4.10: Square wave voltammograms of 0.1 mM OPD in pH = 5 phosphate-citrate buffer after 3 min of homogeneous reaction with 5 mM H_2O_2 catalysed by 50 ng mL^{-1} HRP, at a glassy carbon electrode (solid line) and a graphene electrode (dashed line). The reaction was stopped with 2 M H_2SO_4. Square wave voltammetry parameters: f = 15 Hz, E_{step} = 1 mV, $E_{amplitude}$ = 25 mV. A linear subtraction was applied to both curves and the surface area of the graphene electrode (0.5 cm^2) is ca. 1.8 times the surface area of the glassy carbon electrode (0.28 cm^2).

Following the successful detection of HRP in bulk solution by square-wave voltammetry, its detection as an adsorbed species attached to the graphene was attempted, as a prelude to making a proof-of-concept for the detection of PCT by both electrochemical and ELISA assays.

PSE was used to attach HRP onto the graphene electrode surface (see 2.3). The adsorption of PSE on graphene was achieved by immersing the graphene electrode in a solution of PSE in methanol. It is possible that this process might damage the

electrical insulation of the electrode wire contact. Therefore, an isotherm of the adsorption of PSE was constructed to determine the shortest time required for covering the graphene with PSE. This isotherm is shown in Figure 4.11 and it indicates that 60 % of the active surface is covered by PSE after 10 min, 70 % after 1 h, after which the adsorption rate levels off. Considering these data, graphene samples were incubated for 10 min in the PSE solution.

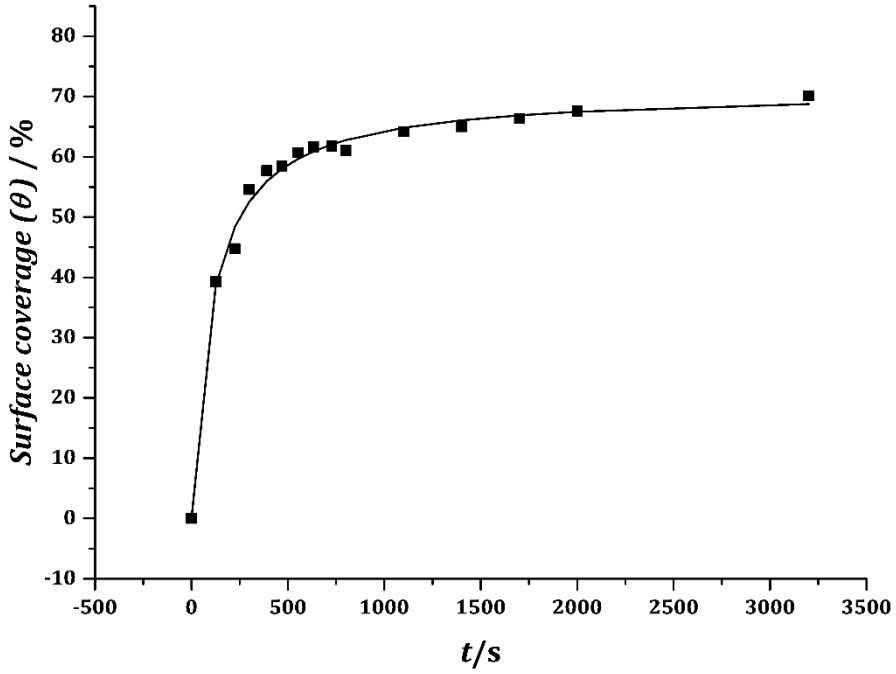

Figure 4.11: Adsorption isotherm of 1 mM 1-pyrenebutanoic acid succinimidyl ester in methanol on graphene. The surface coverage was calculated using equation 1. Plain line: fit of the data.

Figure 4.12 shows a picture of a single layer graphene sample transferred onto a glass substrate and modified with PSE and HRP according to the method described in section 2.4. The picture was taken after a few minutes of reaction between OPD and H_2O_2 and the spreading by diffusion of oxidised OPD (orange) from the graphene surface is apparent.

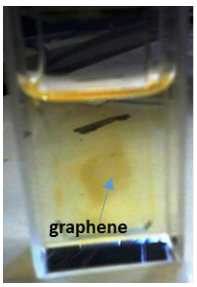

Figure 4.12: Picture of the diffusion of OPD oxidised (orange) after a few minutes of reaction in pH = 5 phosphate-citrate buffer between 0.1 mM OPD an 5 mM H_2O_2, catalysed by 50 ng mL $^{-1}$ HRP.

Figure 4.13 contains square wave voltammograms recorded using an HRP modified graphene electrode in phosphate-citrate buffer pH = 5 containing 0.1 mM OPD solution only, or 0.1 mM OPD and 5 mM H_2O_2. In both cases, the voltammograms were recorded after 3 minutes of reaction time and following addition of 2 M H_2SO_4. In the absence of H_2O_2, no peak is visible, while in the presence of H_2O_2, a reduction peak is visible at -0.2 V vs Ag/ AgCl/ 3M NaCl . This peak is therefore attributed to the reduction of the product of the oxidation of OPD by H_2O_2, catalysed by HRP immobilised on graphene.

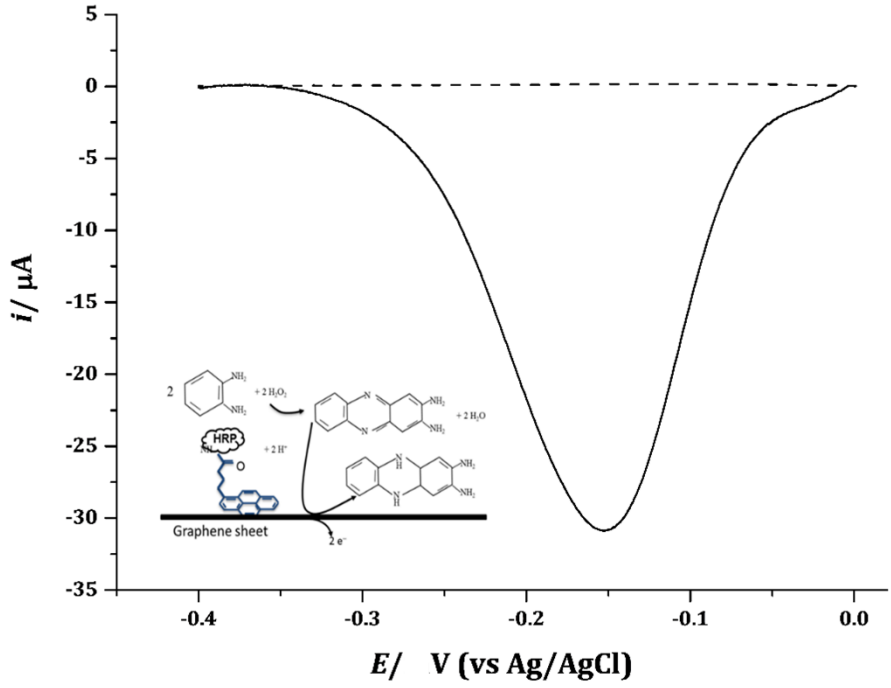

Figure 4.13: Square wave voltammograms in pH = 5 phosphate/citrate buffer containing 0.1 mM OPD and 5 mM H_2O_2 (30% v/v) at a HRP modified graphene

electrode: H_2O_2 omitted (dashed line) or not (plain line). Data were recorded after 3 minutes reaction stopped by addition of 2 M H_2SO_4. Square wave voltammetry parameters: $f = 15$ Hz, $E_{step} = 1$ mV, $E_{amplitude} = 25$ mV. A simple background subtraction was applied to both curves. Inset: diagram describing the reaction taking place at the HRP-modified graphene electrode

4.3.2 Regeneration of the sensor surface

Having shown that HRP could be detected by square-wave voltammetry when attached to graphene, it is then reasonable to assume that, if other molecules (e.g. PCT) were introduced between the PSE-modified graphene and the HRP, the latter can still be detected by square wave voltammetry. The signal so obtained would then be proportional to the amount of these molecules such as PCT. Here, an ELISA sandwich (see section 2.4) was formed on graphene and was composed successively of a specific anti-PCT antibody (Ab1), PCT, and a HRP-labelled specific anti PCT antibody (Ab2), as depicted in Figure 4.14.

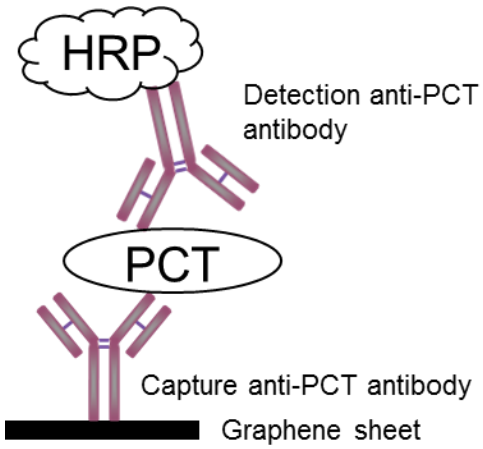

Figure 4.14: ELISA sandwich on graphene

Figure 4.15 shows square-wave voltammograms recorded at a graphene electrode modified with Ab1/PCT/HRP-Ab2, in pH = 5 phosphate-citrate buffer containing 0.1 mM OPD and in the presence and in the absence of PCT. A reduction peak was observed at -0.47 V vs Ag/AgCl/NaCl 3M only when PCT is present. This peak is thus attributed to the reduction of the oxidised OPD produced by reaction of OPD

with H_2O_2, catalysed by HRP immobilised by virtue of its attachment via the associated antibody, to PCT.

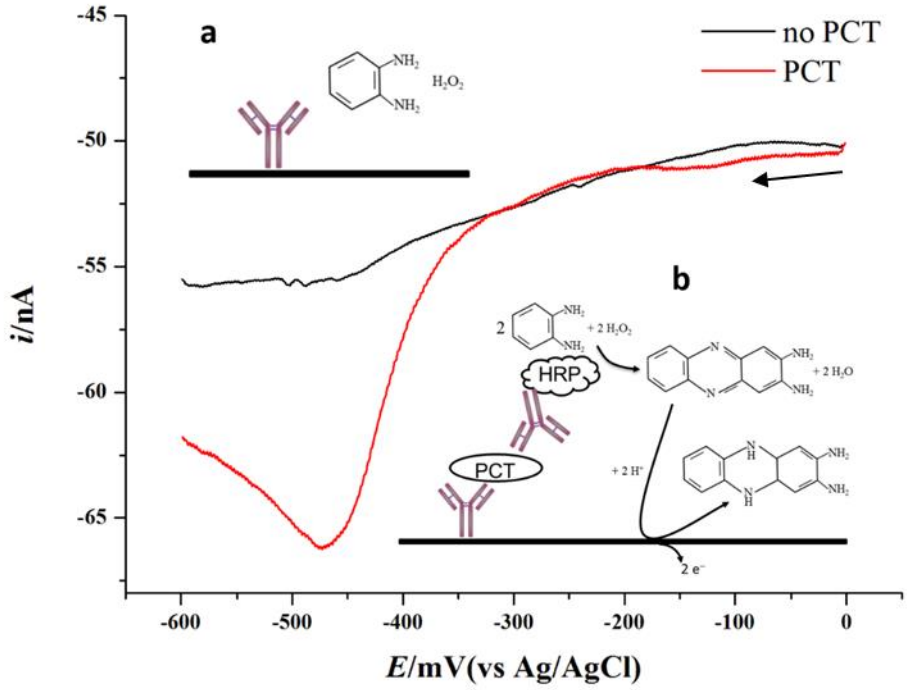

Figure 4.15: Square wave voltammograms in pH = 5 phosphate/citrate buffer, containing 0.1 mM OPD and 5 mM of H_2O_2 30% (v/v): PCT was omitted in the fabrication of the sensor in (a); not in (b). Square wave voltammetry parameters: f = 15 Hz, E_{step} = 1 mV, $E_{amplitude}$ = 25 mV. The data were recorded 3 min after inserting the Ab1/PCT/HRP-Ab2 modified graphene electrode into the solution. To compare the differently modified surfaces, the current in (b) has been attenuated by a factor 3.1. The data were smoothed by adjacent averaging on 15 points. Inset (a): schematic of the modified graphene electrode when PCT is omitted in the building of the ELISA sandwich; inset (b): schematic of the reaction taking place when PCT is not omitted in the construction of the ELISA sandwich.

After addition of 2 M H_2SO_4, decreasing the pH of the solution, the potential of the OPD reduction peak was shifted towards more positive potentials and the peak current decreased, as shown on Figure 4.16. The peak potential shift is explained by the Nernst equation but the diminished peak size has no obvious explanation.

The results presented in Figure 4.15 constitute a proof-of-concept for the detection of PCT by square-wave voltammetry at a graphene electrode, but are not yet

reproducible, mostly due to the intrinsic irreproducibility in the construction of the graphene electrodes. One solution that was tested in Chapter 2 consists of in selecting clean graphene surfaces from a single piece of transferred graphene, isolating them and creating a multi-array micro electrode. It was found that only half the electrodes on the array gave a similar response and therefore this technique is not yet suitable.

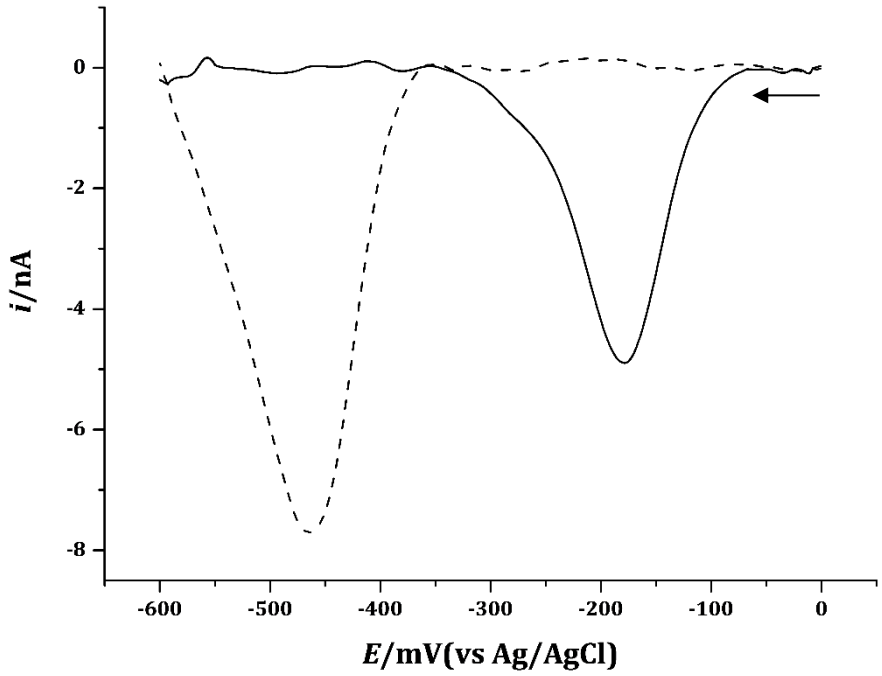

Figure 4.16: Square wave voltammograms at a graphene electrode in pH = 5 phosphate/citrate buffer containing 0.1 mM OPD and 5 mM of H_2O_2 30% (v/v), before (dash line) and after addition of 2 M H_2SO_4 (plain line). Square wave voltammetry parameters: $f =$ 15 Hz, $E_{step} = 1$ mV, $E_{amplitude} = 25$ mV.

Another way to circumvent the electrode consistency issue it to use a regeneration buffer. A regeneration buffer works by removing the proteins on the surface of the sensor they are attached to, thus making it reusable. The regeneration buffer used here was a solution of 1 mM sodium dodecyl sulfate (SDS) in pH = 5 phosphate-citrate buffer. SDS works by denaturing the ternary structure of proteins, which is expected to cause the removal of the PCT/ HRP-Ab2, to leave only Ab1 on the graphene.

Figure 4.17 shows square wave voltammograms recorded in pH = 5 phosphate-citrate buffer containing 0.1 mM OPD and 5 mM H_2O_2 30% (v/v) at a graphene electrode modified with Ab1/PCT/HRP-Ab2, showing the effect of SDS on the surface of the electrode. The data were recorded 3 minutes after the addition of H_2O_2 to the reaction mixture. After SDS treatment, the sensor surface was rebuilt starting from the step when PCT is attached to the Ab1 (i.e. omitting addition of Ab1 presumed to be still attached to the graphene).

A reduction peak is observed around -0.38 V vs Ag/ AgCl/ 3M NaCl before SDS treatment, after SDS treatment and after rebuilding the ELISA sandwich on the graphene electrodes, which is attributed to the presence of HRP attached to it (the square wave voltammogram performed without H_2O_2 has no reduction peak). The peak current was considerably diminished (from 950 nA to 55 nA) after SDS treatment, and fully recovers after rebuilding the ELISA sandwich (978 nA). From these results, it is concluded that SDS removes most of the PCT and HRP-Ab2 from the surface electrode, not the Ab1, and that the electrode can be reused. Regenerating the surface of the sensor is therefore potentially a good way to calibrate the graphene electrodes for PCT, eliminating the variability between different electrodes. However, more experiments need to be carried out to refine this method. For instance, the slight difference in the peak height when the ELISA sandwich is rebuilt (after SDS) and the original ELISA sandwich (28 nA) is likely to be important for the detection of very small concentrations of PCT. It would also be necessary to determine how many times the sensor can be reused.

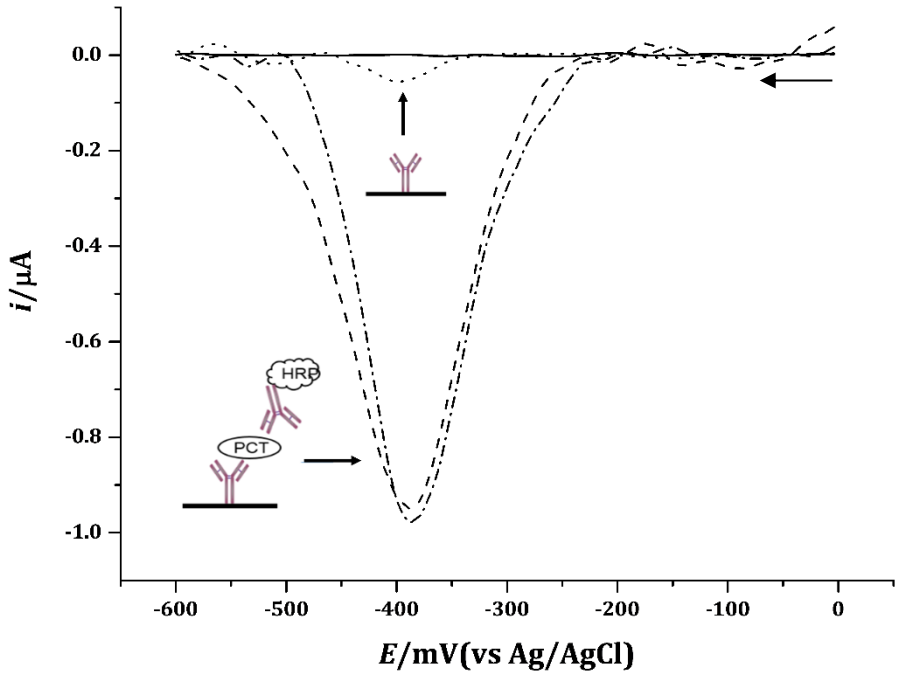

Figure 4.17: Square wave voltammograms in pH = 5 phosphate-citrate buffer containing 0.1 mM OPD and 5 mM H_2O_2 (30% v/v) at a graphene electrode modified with the Ab1/PCT/HRP-Ab2 ELISA sandwich: H_2O_2 omitted (plain line); H_2O_2 not omitted (dashed line); after soaking the modified electrode 30 min in SDS and rinsing (dotted line); after rebuilding the ELISA sandwich on the graphene electrode (dashed dot-line). Data were recorded after 3 min reaction between OPD and H_2O_2. A baseline subtraction was applied to all the data. Square wave voltammetry parameters: $f =$ 15 Hz, $E_{\text{step}} = 1$ mV, $E_{\text{amplitude}} = 25$ mV.

4.4 Conclusion

A proof-of-concept sensor has been built for the detection of PCT, with an electrochemical ELISA of Ab1/PCT/Ab2-HRP, and with square-wave voltammetry as the detection method. However, it was not possible to make the electrodes sufficiently reproducible for anticipated clinical application. Since graphene remains costly to buy and making graphene electrodes is very time-consuming, it was decided to use Highly Oriented Graphite Electrodes as a substrate for the detection and quantification of PCT. This is the subject of Chapter 5.

Bibliography

[1] K. JIAO, “Enzyme-catal yzed reaction of OPD-H_20_2 -HRP voltammetric enzyme-linked immunoassay system ,” no. 4, 1998.

[2] P. D. Josephy, T. Eling, and R. P. Mason, “The Horseradish Peroxidase-catalyzed Oxidation of 3,5,3’,5’- Tetramethylbenzidine,” *J. Biol. Chem.*, vol. 257, no. 7, pp. 3669–3675, 1982.

[3] P. J. Tarcha, V. P. Chu, and D. Whittern, “2,3-Diaminophenazine is the product from the horseradish peroxidase-catalyzed oxidation of o-phenylenediamine,” *Anal. Biochem.*, vol. 165, no. 1, pp. 230–233, 1987.

[4] X. Liu, P. A. Duckworth, and D. K. Y. Wong, “Square wave voltammetry versus electrochemical impedance spectroscopy as a rapid detection technique at electrochemical immunosensors,” *Biosens. Bioelectron.*, vol. 25, no. 6, pp. 1467–1473, 2010.

[5] L. Li, H. Zhao, Z. Chen, X. Mu, and L. Guo, “Aptamer biosensor for label-free square-wave voltammetry detection of angiogenin,” *Biosens. Bioelectron.*, vol. 30, no. 1, pp. 261–266, 2011.

[6] V. K. Kodali, J. Scrimgeour, S. Kim, J. H. Hankinson, K. M. Carroll, W. a. De Heer, C. Berger, and J. E. Curtis, “Nonperturbative chemical modification of graphene for protein micropatterning,” *Langmuir*, vol. 27, no. 3, pp. 863–865, 2011.

[7] A. K. Bhuyan, “On the mechanism of SDS-induced protein denaturation,” *Biopolymers*, vol. 93, no. 2, pp. 186–199, 2010.

[8] I. Losito, F. Palmisano, and P. G. Zambonin, “O-Phenylenediamine Electropolymerization By Cyclic Voltammetry Combined With Electrospray Ionization-Ion Trap Mass Spectrometry,” *Anal. Chem.*, vol. 75, no. 19, pp. 4988–4995, 2003.

Chapter 5

Pyrene-wired antibodies on highly-oriented pyrolytic graphite as a label-free impedance biosensor for the sepsis biomarker procalcitonin

An antibody-based, label-free impedance biosensor for the sepsis biomarker procalcitonin (PCT) has been produced using highly oriented pyrolytic graphite (HOPG) as the sensor electrode material and with attachment of the PCT capture antibody via coupling to 1-pyrenebutanoic acid succinimidyl ester (PSE) pre-immobilised on the electrode by π-π stacking. In an aqueous phosphate-buffered saline (PBS) at pH = 7.4, the charge-transfer resistance for the redox probe $Ru(NH_3)_6^{3+/2+}$ exhibited a linear dependence on the PCT concentration in the range 10 to 100 ng mL^{-1} and provided a detection limit for PCT of 3.70 ng mL^{-1}. Also, over the same PCT concentration range, the electrode capacitance showed a steady decrease, offering the prospect of a capacitive sensing mode for the label-free device, possibly removing the need to add a redox species to the sample under test. These results demonstrate the feasibility of using pyrene-modified HOPG as a simple platform for label-free impedance biosensors, here for the important sepsis biomarker PCT.

5.1 Introduction

Electrochemical impedance spectroscopy is an established probe of bioaffinity interactions at interfaces [1] and label-free electrochemical impedance biosensors represent a promising strategy for point-of-care monitoring of protein disease biomarkers [2]. The biosensor operation relies upon tethering a recognition element (often an antibody) to the sensor electrode surface, such that specific binding of the target biomarker changes the interfacial impedance. This is often recorded as an increase in the charge-transfer resistance associated with a redox couple in solution, or as a change in the electrode capacitance. One method that has been used to immobilise enzymes [3][4] and DNA [5] onto highly-oriented pyrolytic graphite (HOPG) is to use the π-π stacking interaction of the HOPG basal plane with pyrene-based linker molecules. Early work by Katz [6][7] demonstrated this method for attaching proteins in general to graphite surfaces but, to the best of our knowledge, this has not been used to immobilise antibodies directly onto HOPG for the purposes of biosensor fabrication, though it has been used to immobilise antibodies onto the related material graphene [8]. A recent investigation [9] of the electrochemistry of HOPG concluded that the basal plane supports fast and time-stable electron transfer for $Ru(NH_3)_6^{3+/2+}$.

In this chapter, the immobilisation of antibodies onto HOPG is demonstrated, using the pyrene-based linker molecule 1-pyrenebutanoic acid succinimidyl ester (PSE) as it provides a convenient route to the production of a label-free impedance biosensor with $Ru(NH_3)_6^{3+/2+}$ as a redox probe for read-out via the associated charge-transfer resistance, with the additional possibility of a capacitive sensing mode. In an aqueous phosphate buffer solution (PBS) at pH = 7.4 the charge-transfer resistance for the redox probe $Ru(NH_3)_6^{3+/2+}$ at the HOPG biosensor exhibited a linear dependence on the PCT concentration in the range 10 ng mL^{-1} to 100 ng mL^{-1} and provided a detection limit for PCT of 3.70 ng mL^{-1}. Also, over the same PCT concentration range, the electrode capacitance showed a steady decrease, offering the prospect of a capacitive sensing mode for the label-free device, possibly removing the need to add a redox species to the sample under test. These results demonstrate the feasibility of using pyrene-modified HOPG as a

simple platform for label-free impedance biosensors, here for the important sepsis biomarker PCT.

5.2 Experimental

5.2.1 Reagents

HOPG was purchased from NT-MDT Co. (ZYA grade, 10 mm × 10 mm × 1.2 mm). Phosphate-buffered saline (PBS, Sigma Aldrich, pH = 7.4 with [NaCl] = 0.137 M and [KCl] = 0.0027 M) was used as the electrolyte throughout, while all aqueous solutions were prepared using ultra-pure water (Milli-Q Millipore) with a resistivity of ca. 18.1 MΩ cm at 25 ^{o}C. Sodium carbonate (Na_2CO_3, ≥ 99.5%), sodium bicarbonate ($NaHCO_3$, ≥ 99.7%), methanol (CH_3OH, 99.99%) and hexaammineruthenium(III) chloride ($Ru(NH_3)_6Cl_3$, 98%) were all purchased from Fisher Scientific and used without further purification. Ethanolamine ($H_2NC_2H_4OH$, ≥ 99.0%), 1-pyrenebutanoic acid succinimidyl ester (PYSE, 95%), potassium chloride (KCl, ≥ 99.0%) and bovine sulphate albumin (BSA, heat shock fraction, lyophilized powder, ≥ 98%, pH = 7) were all purchased from Sigma-Aldrich and used without further purification. Monoclonal anti-human procalcitonin capture antibody (clone 42) was purchased from 2BScientific Ltd. Human procalcitonin (PCT) was purchased from ProSpec-Tany Technogene Ltd.

5.2.2 Sensor fabrication

The HOPG surface was renewed by cleaving with Sellotape, before being mounted in an electrochemical cell described in section 5.2.3. Surface modification (see Figure 5.1) was performed in the cell at room temperature, as follows. Firstly, the HOPG was soaked for 10 minutes in a solution of PYSE (1 mM in methanol), before being rinsed successively in methanol and then PBS. The surface was then soaked in BSA (1% w/w in PBS) for 5 minutes, before rinsing in PBS and then water. BSA, which is the major blood serum protein, was used as a standard commercial blocking buffer in anticipation of future use of the sensor in biological media, where it would block nonspecific protein-surface interactions. The surface was then soaked for 20 minutes in a solution of the PCT antibody (5 μg mL^{-1} in

carbonate-bicarbonate buffer pH = 9.2) to attach it to the surface via amide bond formation between an amine group on the antibody and the activated ester of the PYSE, before rinsing in PBS followed by water. Finally, the surface was soaked in ethanolamine for 15 minutes to deactivate any unreacted ester groups, before rinsing in PBS, then water.

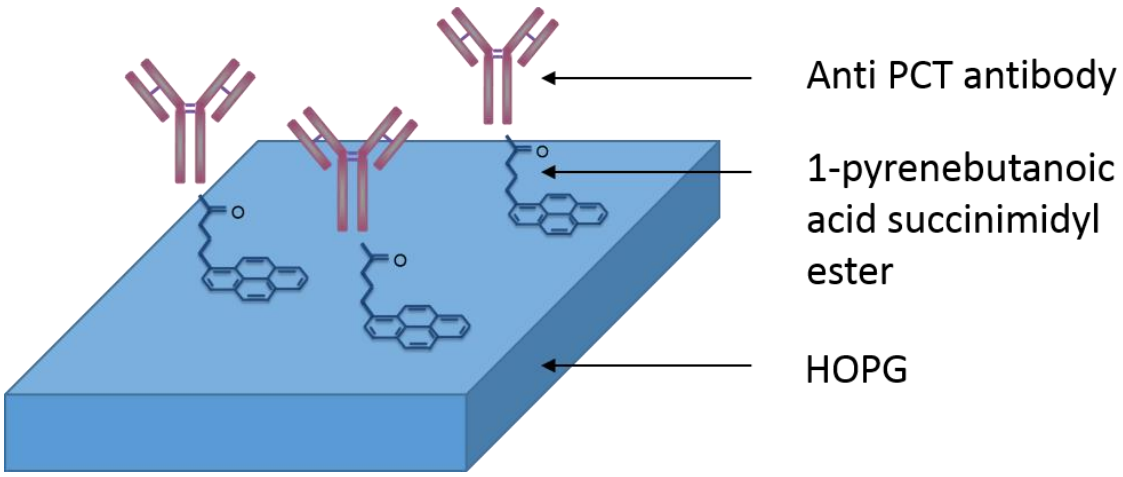

Figure 5.1: Configuration of the HOPG based PCT sensor.

5.2.3 Electrochemical Measurements

The electrochemical cell (Figure 5.2) consisted of a glass vial onto which was glued (using Araldite epoxy resin) a Perspex base. A rubber o-ring was glued (Araldite epoxy resin) to the outside of this base around the perimeter of a 6 mm diameter round hole such that the HOPG, backed by a polished aluminium plate to provide electrical contact, could be clamped to this o-ring to provide a well-defined, upward-facing electrode area at the bottom of the cell.

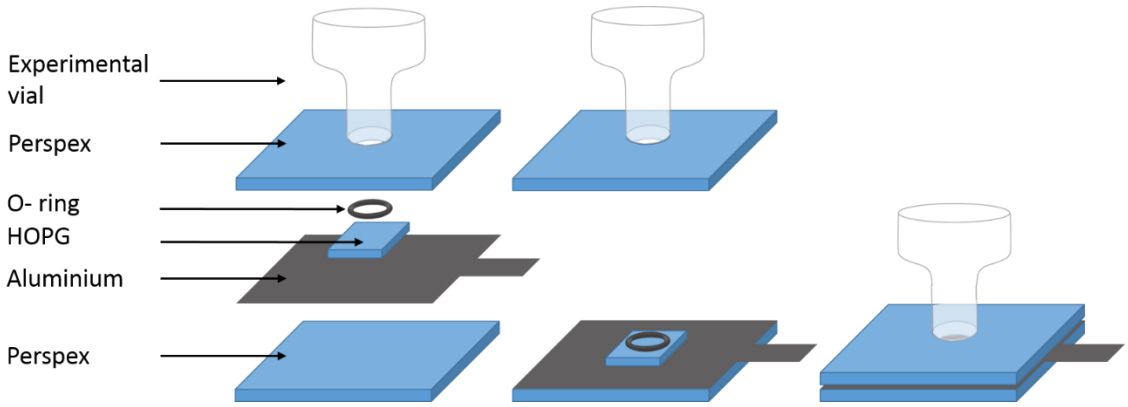

Figure 5.2: Electrochemical cell

The reference electrode was Ag/AgCl/3 M NaCl (BASi), contacting the cell solution via a salt bridge (MF 2030, BASi) containing 0.2 M KCl solution. The counter electrode was a Pt wire and the cell was operated in the normal, three-electrode mode for both voltammetry and impedance measurements. Cyclic voltammetry was performed using a BAS 100B/W Electrochemical Analyzer (BASi). Electrochemical impedance spectroscopy (EIS) experiments were performed using a Schlumberger/Solartron SI1260 Impedance/Gain-Phase Analyzer and SI1287 Electrochemical Interface, both under computer control using Z-Plot software (Scribner Associates Inc.) and with data analysis performed using Z-View software (Scribner Associates Inc.). All electrolyte solutions were purged with nitrogen prior to electrochemical measurements. The electrochemical methods used in this chapter are explained in Chapter 2, part 4.

5.3 Results and discussion

5.3.1 Modification of the HOPG with anti PCT capture antibodies

Figure 5.3 shows the cyclic voltammetry of 1 mM $Ru(NH_3)_6^{3+}$ in PBS (pH = 7.4) at the HOPG before and after surface modification with BSA and the PCT capture antibody. Reduction and oxidation peaks were observed for the $Ru(NH_3)_6^{3+/2+}$ redox couple, with the mid-peak potential of -0.2 V vs Ag/AgCl/3 M NaCl taken as the formal potential for the couple and used as the dc bias in all the EIS

measurements presented here. The peaks remained well defined after the surface modification, but were diminished in current and increased in their potential separation (to 167 mV vs Ag/AgCl/3 M NaCl from 118 mV vs Ag/AgCl/3 M NaCl at bare HOPG). The smaller current indicates a decrease in the active surface area of the modified electrode, while the increased potential separation shows that the antibody acts as a barrier slowing the electron transfer rate.

In the absence of data on the isoelectric point of the antibody, it is not possible to say whether it would have been positively or negatively charged at pH = 7.4 and so nothing can be speculated on the degree of electrostatic attraction or repulsion operating upon the positively-charged redox couple. The slowing of the electron transfer was confirmed using EIS as shown in the resulting complex-plane impedance plots in Figure 5.4 for the bare and BSA/antibody-modified HOPG surface.

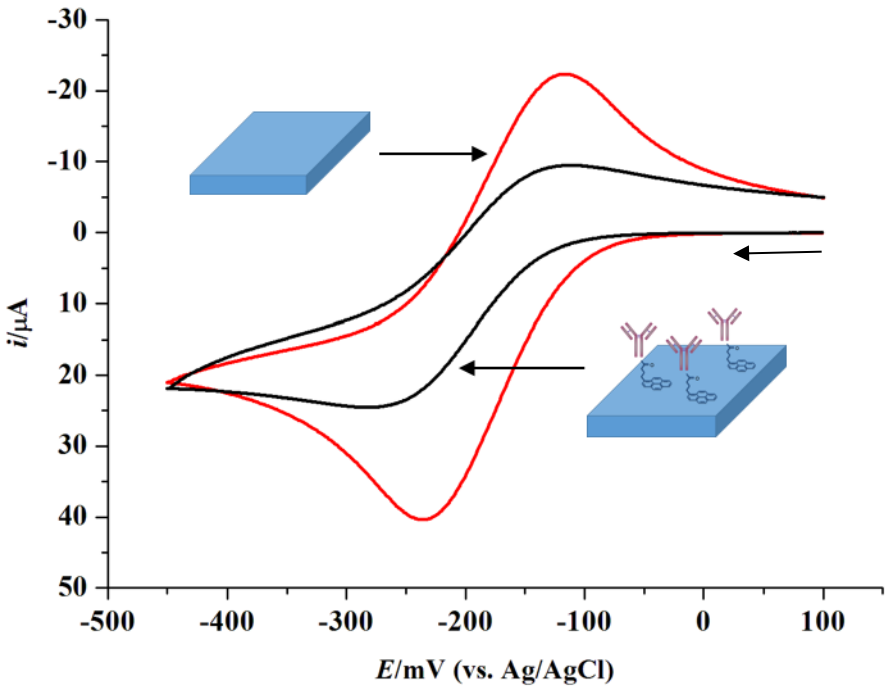

Figure 5.3: Cyclic voltammograms in pH = 7.4 PBS of 1 mM $Ru(NH_3)_6^{3+/2+}$ at a potential sweep rate of 20 mV s^{-1}, firstly at the bare HOPG electrode (red curve) and then following modification with the PCT capture antibody and BSA (black curve)

These data were fitted to the modified Randles circuit used throughout this work and shown in the figure inset, indicating that the charge-transfer resistance, R_{ct}, increased more than 6-fold (from 178 Ω to 1115 Ω) upon surface modification.

5.3.2 Calibration of the HOPG sensor for procalcitonin

Figure 5.5 shows the evolution of the complex-plane impedance plots for the sensor electrode as successive aliquots of PCT were added to a PBS solution (pH = 7.4) containing 1 mM $Ru(NH_3)_6^{3+}$, each time allowing twenty minutes for the electrode surface to reach equilibrium. Each successive aliquot increased the PCT concentration by 10 ng mL^{-1}.

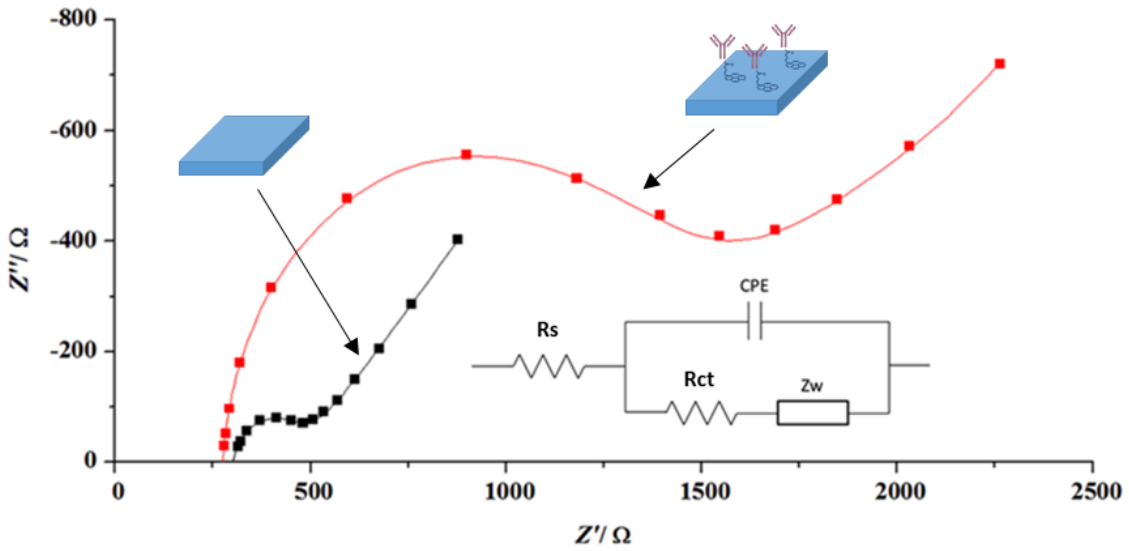

Figure 5.4: Complex-plane impedance plots obtained for $Ru(NH_3)_6^{3+/2+}$ (1 mM in PBS at pH = 7.4) at the bare HOPG (black curve) and then following modification with the PCT capture antibody and BSA (red curve) to form the sensor electrode. Data were recorded applying a dc bias potential of -0.2 V vs Ag/AgCl/3 M NaCl, overlaid with a voltage sinewave of 10 mV rms amplitude over the frequency range 1-20000 Hz. Solid lines are fits to the modified Randles circuit shown in the figure inset: R_s = uncompensated solution resistance; R_{ct} = charge-transfer resistance; CPE = constant phase element, and Z_w = Warburg impedance.

The impedance of the constant-phase element, Z_{CPE}, is represented by the following equation:

$$Z_{CPE} = \frac{1}{(j\omega)^{\alpha}T} \tag{57}$$

in which j is the imaginary coefficient, ω is the angular frequency of the ac voltage and T (and so Z_{CPE}) has different representations according to the value of the dimensionless parameter α. In particular, if $\alpha = 1$, then the CPE reduces to a simple capacitor for which T is then the capacitance. The values of α in this case (between 0.93 and 0.95) are considered sufficiently close to unity to regard T simply as the electrode capacitance.

Table 1 lists the fitted values of R_{ct} and also the CPE parameters T and α (defined below in association with equation 1) averaged over three EIS experiments for each PCT concentration. These EIS data provide two measures of the binding of PCT to the surface-bound capture antibody: the charge-transfer resistance and the electrode capacitance.

The bound PCT provides an additional barrier to the $Ru(NH_3)_6^{3+/2+}$ electron transfer, so increasing R_{ct}. Figure 5.6 shows that, within the calculated error bars, the increase in R_{ct} was linear with the concentration of PCT over the range 10 ng mL^{-1} to 100 ng mL^{-1}. The projected limit of detection (the R_{ct} intercept plus three times the standard deviation) was found to be 3.70 ng mL^{-1}.

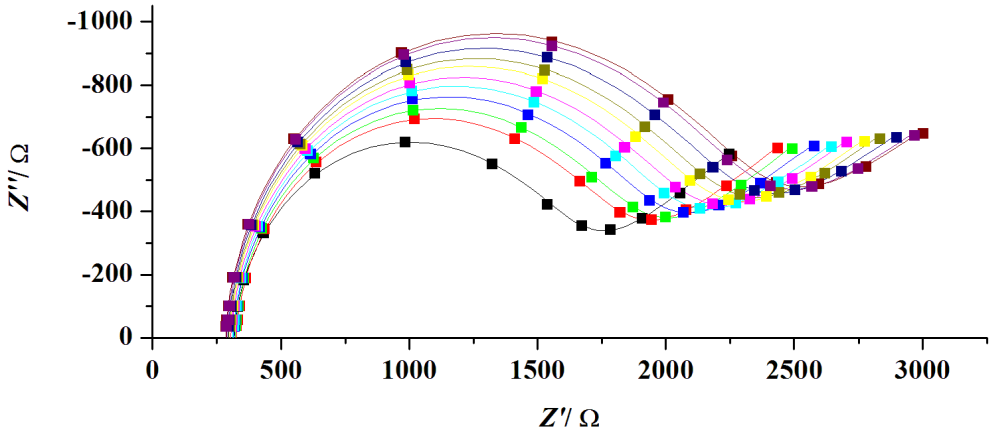

Figure 5.5: Evolution of the complex-plane impedance plots for the sensor electrode for successive additions of PCT (each increasing the solution concentration by 10 ng mL^{-1}), allowing 20 minutes post-addition for surface equilibration before measurement with conditions and fitting (solid lines) otherwise as detailed in Figure 5.4. The main near-semicircle arc expands with each successive addition of PCT.

Thus, in aqueous buffer solution, the sensor could be used to detect concentrations of PCT relevant to the diagnosis of sepsis. This is despite the fact that the charge-transfer resistance of 1203 Ω at zero PCT concentration presents a high baseline relative to the increases in this resistance over the range of PCT concentrations examined, for example an increase in resistance of 128 Ω (or 10.6%) for an increase in PCT concentration of 10 ng mL^{-1}.

Table 1: Average fitted values of Rct, T and α as a function of PCT.

[PCT]/ng mL^{-1}	R_{ct}/Ω	CPE-α	CPE-*T*/μF
0	1203	0.93	75.5
10	1331	0.93	71.4
20	1388	0.94	70.1
30	1456	0.94	69.3
40	1513	0.94	68.3
50	1561	0.94	68.3
60	1629	0.95	67.5
70	1668	0.95	67.5
80	1725	0.95	67.5
90	1785	0.95	67.0

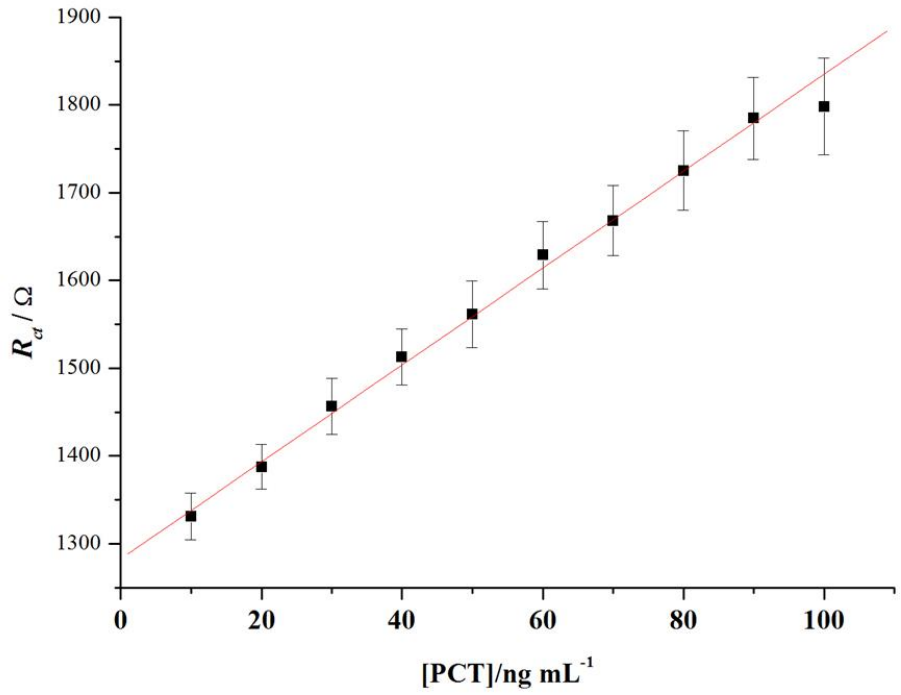

Figure 5.6: A plot of R_{ct} as a function of PCT concentration for the sensor electrode. The error bars correspond to one standard deviation calculated for three successive EIS measurements at each PCT concentration.

This high baseline influences the dynamic range and ultimately the limit of detection of the device and, although it may be attempted to diminish it by for example changing the surface coverage of the antibodies, it is to some extent inevitable because it reflects the antibody itself as a barrier to electron transfer relative to the additional barrier presented by the PCT.

5.3.3 A possible capacitive sensor

Figure 5.7 shows that the capacitance of the graphene electrode decreased smoothly (error bars shown are the corrected sample standard deviations) with increasing PCT concentration, dropping from 71 µF to 67 µF as the PCT concentration was increased from 10 ng mL^{-1} to 100 ng mL^{-1}. Figure 5.8 shows that the decrease of the capacitance follow a power law and that this power is 0.03.

This offers the prospect of a future capacitive sensing mode for the label-free device, possibly removing the need to add a redox species to the sample under test.

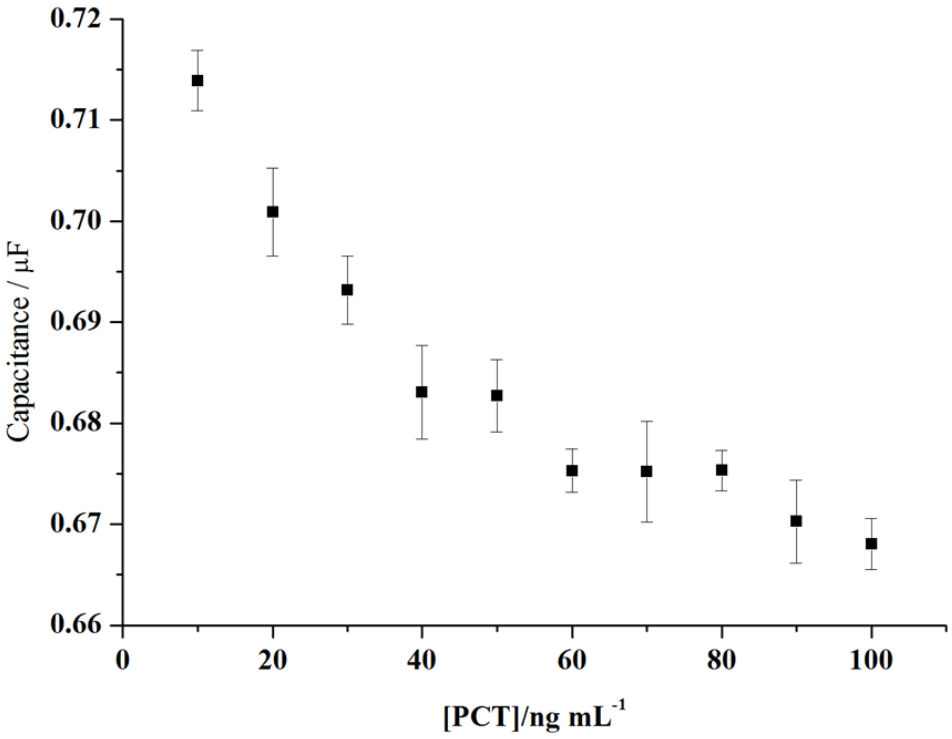

Figure 5.7: A plot of the electrode capacitance as a function of PCT concentration for the sensor electrode. The error bars correspond to one standard deviation calculated for three successive EIS measurements at each PCT concentration.

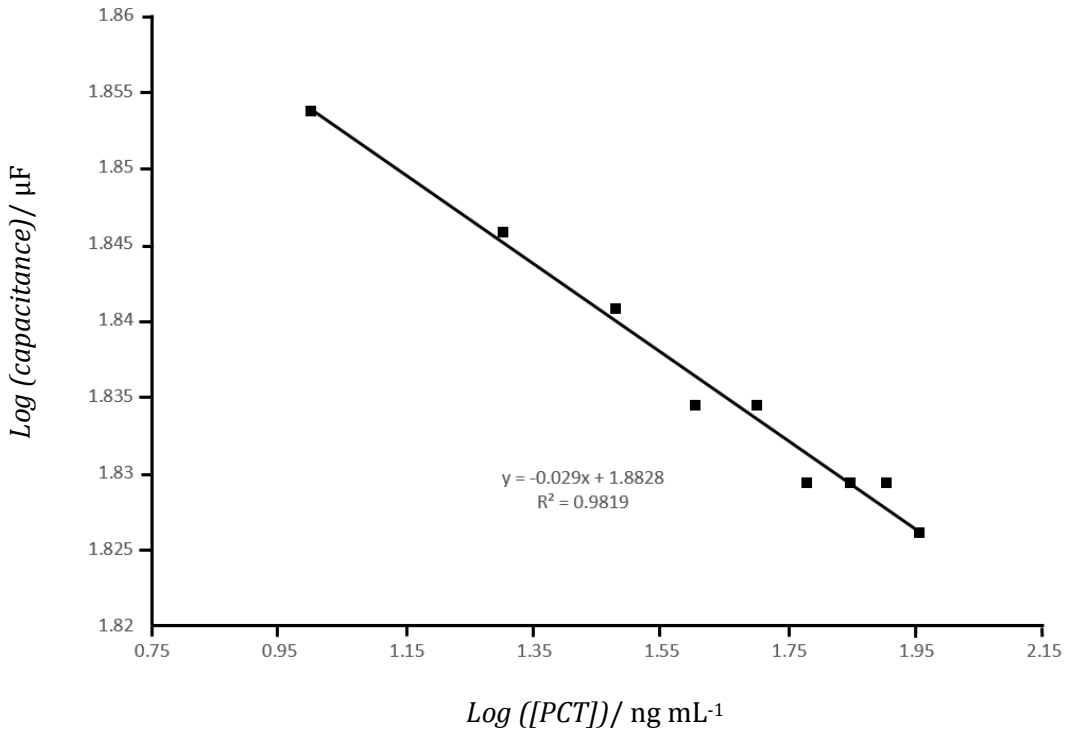

Figure 5.8: Determination of the power of the relationship between the concentration of PCT and the measured capacitance at the graphene electrode. The plain line is a least mean square fit of the data.

5.4 Conclusion

In this chapter, the immobilisation of capture antibodies onto an HOPG electrode using the π -π stacked, pyrene-based linker molecule 1-pyrenebutanoic acid succinimidyl ester (PYSE) has been shown to produce an effective, label-free impedance biosensor for the sepsis biomarker procalcitonin (PCT) in an aqueous buffer solution containing $Ru(NH_3)_6^{3+/2+}$ at physiological pH. Both the charge-transfer resistance and the electrode capacitance respond to PCT concentration, with the former giving a clinically relevant linear concentration range (10 ng mL^{-1} to 100 ng mL^{-1}) and limit of detection (3.70 ng mL^{-1}). These results demonstrate the feasibility of using pyrene-modified HOPG as a simple platform for label-free impedance biosensors, in particular the important sepsis biomarker PCT. Work is ongoing to test the sensor in more complex pseudo-physiological media and ultimately in blood serum.

Bibliography

[1] E. Katz and I. Willner, "Probing biomolecular interactions at conductive and semiconductive surfaces by impedance spectroscopy: Routes to impedimetric immunosensors, DNA-sensors, and enzyme biosensors," *Electroanalysis*, vol. 15, no. 11, pp. 913–947, 2003.

[2] X. Luo and J. J. Davis, "Electrical biosensors and the label free detection of protein disease biomarkers," *Chem. Soc. Rev.*, vol. 42, pp. 5944–5962, 2013.

[3] A. K. Udit, M. G. Hill, V. G. Bittner, F. H. Arnold, and H. B. Gray, "Reduction of Dioxygen Catalyzed by Pyrene-Wired Heme Domain Cytochrome P450 BM3 Electrodes," *J. Am. Chem. Soc.*, vol. 126, no. 33, pp. 10218–10219, 2004.

[4] C. Van Der Felt, K. Hindoyan, K. Choi, N. Javdan, P. Goldman, R. Bustos, A. G. Star, B. M. Hunter, M. G. Hill, A. Nersissian, and A. K. Udit, "Electron-transfer rates govern product distribution in electrochemically-driven P450-catalyzed dioxygen reduction," *J. Inorg. Biochem.*, vol. 105, no. 10, pp. 1350–1353, 2011.

[5] A. A. Gorodetsky and J. K. Barton, "Electrochemistry Using Self-Assembled DNA Monolayers on Highly Oriented Pyrolytic Graphite," *Langmuir*, vol. 22, no. 12, pp. 7917–7922, 2006.

[6] E. Katz, "Application of bifunctional reagents for selective immobilization of amino and thiol compounds on a carbon electrode surface," *J. Electroanal. Chem.*, vol. 361, pp. 109–114, 1993.

[7] E. Katz, "Application of bifunctional reagents for immobilization of proteins on a carbon electrode surface: Oriented immobilization of photosynthetic reaction centers," *J. Electroanal. Chem.*, vol. 365, no. 1, pp. 157–164, 1994.

[8] Y. Huang, X. Dong, Y. Liu, L.-J. Li, and P. Chen, "Graphene-based biosensors for detection of bacteria and their metabolic activities," *J. Mater. Chem*, vol. 21, pp. 12358–12362, 2011.

[9] A. N. Patel, M. G. Collignon, M. A. O. Connell, W. O. Y. Hung, K. Mckelvey, J. V Macpherson, and P. R. Unwin, "A New View of Electrochemistry at Highly Oriented Pyrolytic Graphite," *J. Am. Chem. Soc.*, vol. 134, no. 49, pp. 20117–20130, 2012.

Chapter 6

Localised Surface Plasmon Resonance (LSPR) for the detection of Procalcitonin

Abstract

Localised surface plasmon resonance (LSPR) is a promising route for the development of very sensitive label-free biosensors. This chapter introduces first the basis of LSPR biosensing. Then, work is described in which metallic nanoparticles were deposited on graphene using electrochemistry or electron beam lithography, and it is shown that both can support LSPR and form the basis of a biosensor platform. In particular, it is shown that it is possible to combine the LSPR signal from nanoparticles made of different metals, such as Ag and Au, where one is used as a reference. The results also indicate that the capture of the analyte may needs to happen in the very close vicinity of the nanoparticles to produce an obvious signal.

6.1 Introduction

Surface Plasmon Resonance (SPR) is an optical phenomenon that is used as a fast, real time and label-free analytical technique to detect several bioanalytes simultaneously [1]. A Surface Plasmon Wave (SPW) is an electromagnetic wave at the interface between a metal thin film (usually gold or silver) and a dielectric (the field of dielectric constants of opposite signs creates an oscillating electron plasma). The metal film is usually situated at the surface of a prism as in Figure 6.1 and the oscillating plasma is an evanescent wave that can be excited by an incident monochromatic p-polarised light within the limits of the critical angle where it is totally reflected within the prism. The angle at which the intensity of the reflected wave is least is termed the resonant angle. In these conditions, the excitation is called Surface Plasmon Resonance and the excited modes are called Surface Plasmons (SPs). For a given metal, the propagation of the SPs is dependent on the refractive index of the sensing environment, as shown in the following equation [1][2], which means that it will be dependent on any changes of the dielectric constant near the metal-dielectric interface:

$$\beta = k\sqrt{\frac{\varepsilon_m n_s^2}{\varepsilon_m + n_s^2}} \tag{1}$$

where β is the propagation constant of the surface plasmon at the interface between a semi-infinite dielectric and a metal, k is a free-space wavenumber, ε_m the dielectric constant of the metal and n_s the refractive index of the dielectric. Consequently, it is possible to study any interaction (protein-protein, antigen-antibody, drug-protein, etc.) occurring near the interface by measuring the change in resonance angles or, equivalently, in a wavelength shift [4] (the critical angle is wavelength dependant).

The LSPR peak wavelength shift, denoted $\Delta_{\lambda max}$, induced by the change of dielectric around the nanoparticles is given by [3] :

$$\Delta_{\lambda max} = m\Delta n\,(1 - e^{-\frac{2d}{l_d}}) \tag{2}$$

where m is the bulk refractive index of the nanoparticle, Δn is the change of refractive index caused by adsorption of a molecule, d is the thickness of the adsorbate and l_d is the electromagnetic decay length.

Gold and Silver are the most commonly used noble metals and the most common configuration using SPR for bioanalysis uses optical prism couplers, as shown in Figure 6.1.

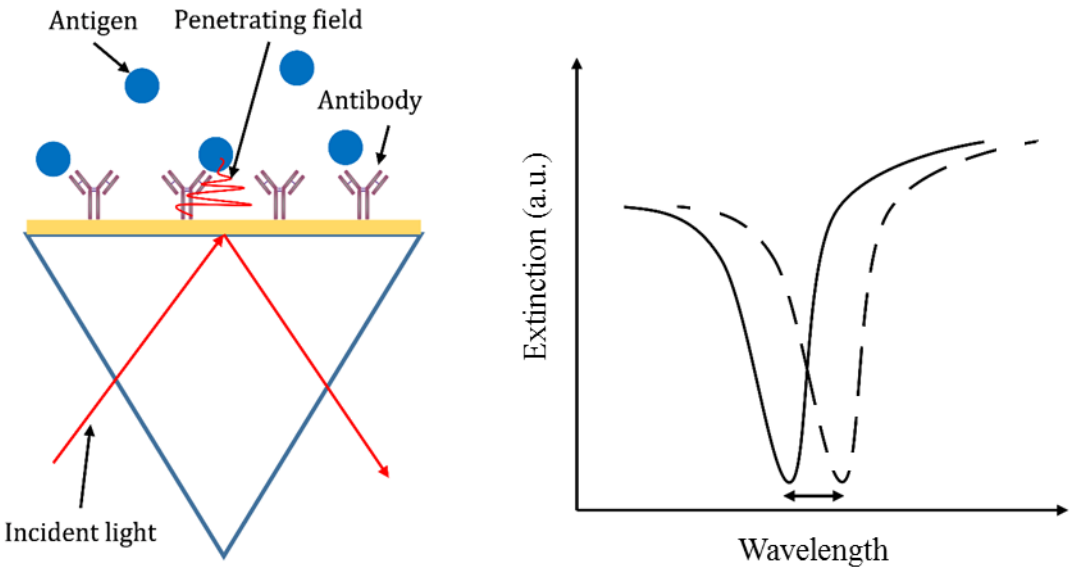

Figure 6.1: Typical LSPR biosensor. Left, schematic of the experiment; right, wavelength position of the LSPR resonance peak before (plain line) and after (dashed line) the attachment of antigens onto their specific antibody.

In this configuration (Kretschmann geometry), a SP is excited at the outer face of the metal layer (of thickness ~50 nm) by an incident laser totally reflected at the interface between the inner face of the metal and a prism coupler [2]. Other configurations use optical waveguides, optical fibers and grating couplers [1][2], which may be preferred for their simplicity. Approaches measuring the momentum of the optical wave rather than its intensity prevail since they allow better S/N ratios. Texas Instruments, BIAcore and others (Quantech, Xantec Analysensystem, EBI Sensor …) commercialise SPR analytical devices based on the different optical and measurement approaches. Current detection limits are ~ 1-100 ng/ml of proteins [4]. Chung et al [4] suggest an amplification method based on HRP-catalysed precipitation to enlarge the dynamic range and increase the sensitivity of SPR based immunoassays. The thin gold layer can also be used as a

working electrode and the dual device can collect optical and electrochemical data from the sample [5][6].

When the SP is confined to nanostructures (i.e. it is not propagating) whose lateral size is much smaller than the wavelength of the incident light, the method is called Localised Surface Plasmon Resonance (LSPR) [7][3]. This has been was shown to be useful for biosensing [8]. As for SPR sensors, LSPR sensors are sensitive to a change of refractive index of their environment. They also have the advantage over SPR sensors that they are more portable and they are tuneable by choosing the metal, shape, size and height of the deposited nanoparticles [3][9]. Van Duyne et al [10] found that triangular silver nanoparticles based biosensors are very sensitive to small changes to the refractive index next to the particles and could detect streptavidin down to the pM range. The strong localised electromagnetic field occurring in the vicinity of the nanoparticles [11] could improve the detection of very low concentrations of analytes, for example when they bind to surface bound ligands. When the analyte is too far away from the surface of the nanoparticle the sensor may lose sensitivity, as the strength of the electrical field decays rapidly (40-50 times shorter decay length than a SPR sensor [3]). To overcome this issue, nanoparticle labels can be used to enhance the resonance peak shift [12]. This strategy was reported to allow the detection of proteins down to the picomolar range [7]. Van Duyne et al [10] reported that the wavelength shift caused by the binding of streptavidin onto biotinylated silver nanoparticles was amplified 300 times by using biotinylated gold nanoparticles. Gold is preferentially used for SPR compared to other noble metals, because it is optically and chemically stable. However, biomolecules do not adsorb very well on gold. Silver substrates make more sensitive SPR sensors than gold thin films [13][14]in the visible range of wavelengths, but are susceptible to oxidation which damages their sensitivity. One strategy to overcome this issue consists of using a bimetallic gold silver layer [15] or using a small oxide layer on top of the silver thin film [14]. Alternatively, graphene could be used as a coating for gold and silver. Indeed, the high surface-to-volume ratio and the possibility to derivatise graphene via π interaction with its benzene ring structure could enhance the adsorption of molecules at the surface of the sensor and increase its sensitivity [14], while graphene also prevents the passivation of the metal [13].

Graphene has been shown to be a suitable substrate to support the LSPR properties of gold and silver nanoparticles [16][17][18]. It has already been decorated with arrays of nanoparticles using electrochemistry [19][20][21][22]. No LSPR biosensor so far has been made by depositing highly ordered arrays of gold nanoparticles (as can be achieved by electron beam lithography) onto graphene. Graphene and gold nanoparticles combined have also been shown to improve the sensitivity of SPR sensors [23][24][25], suggesting an inherent enhancement of plasmon - based sensing is possible, in addition to the benefits afforded by the transparency of the graphene. The transparency of graphene can be exploited here to make transmission-based LSPR biosensors. Lee et al [26] reported on the LSPR behaviour of gold nanoparticles deposited on graphene on a transparent flexible substrate (PEN). It can also support electrochemistry and it is reasonable to assume that a combined LSPR and electrochemical biosensor is possible. Several studies report on sensors combining LSPR (or SPR) and electrochemistry [27][28][29]. Zhu et al [30] reported on a sensitive biosensor combining LSPR and impedance spectroscopy to detect the protein α-thrombin. Apart from modifying the shape of nanoparticles on graphene for tuning the resonance wavelength of the sensor, an intermediate layer of variable thickness can be introduced between the graphene and the nanoparticle [31].

In this chapter, work is described in which metallic nanoparticles were deposited on graphene using electrochemistry or electron beam lithography, and it is shown that both can support LSPR and form the basis of a biosensor platform.

The results presented in parts 2.2, 2.3 and 3.1 are published in reference [17].

6.2 Material and methods

6.2.1 Reagents

Graphene was purchased from Graphene Supermarket (single layer, on copper foil). All rinsing steps in water were done using ultra-pure water (Milli-Q Millipore) with a resistivity of ca. 18.1 MΩ cm at 25 ˚C. Quartz slides were purchased from UQG Optics (Fused quartz Vitrosil 077®, 1mm thick). Acetone

(CH_3COCH_3, 99.98%), propan-2-ol (IPA, 99.96%), 4-methylpentane-2-one (MIBK, 99.8%), methyl ethyl ketone (MEK, $>$ 99%) were purchased from Fisher Scientific and used as received. Ammonium persulfate (APS, $\geq$ 98%) was purchased from Sigma Aldrich and used as received. Poly(methyl methacrylate) (PMMA, 495K and 950K, 4% v/v in anisole) was purchased from Microchem and used as received. MF-319 was purchased from Dow and used as received. Silver nitrate ($AgNO_3$) (Fluka, 99.0%) and sulfuric acid (H_2SO_4) (Sigma-Aldrich, 95–98%, reagent grade) were used as received. Hydrogen tetrachloroaurate ($HAuCl_4$) was prepared by a standard literature procedure. The Pt and Ag/AgCl /3M/NaCl electrodes were purchased from BASi. Monoclonal anti-human procalcitonin capture antibody (clone 42) was purchased from 2B Scientific.

6.2.2 Preparation of the graphene/Au/graphene/Ag structures

Graphene on glass electrodes were prepared as explained in Chapter 2 part 3.2. Then gold nanoparticles were electrodeposited as described in 2.3 and a second layer of graphene was deposited onto the nanoparticle layer. Prior to depositing a layer of silver nanoparticles onto the second layer of graphene, the edges of the bilayer structure were sealed using epoxy to avoid any liquid penetration in the structure. Finally, silver nanoparticles were electrodeposited as described in 2.3 and the whole structure was characterised as described in 2.5.

6.2.3 Electrodeposition of gold and silver nanoparticles

Electrodeposition of nanoparticles was done in a three-electrode electrochemical cell configuration (see chapter 2 section 2.4) controlled via a BASi 100 W electrochemical potentiostat. Graphene (surface area ca 0.5 cm^2) was used as the working electrode, Pt as a counter electrode and an Ag-wire as a pseudo reference or a Ag/AgCl /3 M/NaCl reference electrode. Gold nanoparticles were deposited onto graphene through four consecutive cyclic voltammograms in a nitrogen-purged solution of 1.3 mM $HAuCl_4$ in 0.5 M H_2SO_4. The cyclic voltammograms were recorded at a scan rate of 0.1 Vs^{-1}, between 0 V and 2 V relative to the Ag/AgCl /3 M/NaCl reference. Silver nanoparticles were electrodeposited onto graphene at a constant potential from a nitrogen-purged solution of 2.0 mM $AgNO_3$ in 0.5 M

H_2SO_4. The chosen potential was -2 V relative to the pseudo reference electrode and it was held for 60 s.

6.2.4 Deposition of gold nano-array by electron beam lithography

Gold nano-arrays were deposited on a quartz substrate. The substrates were first cleaned in acetone and then IPA for 10 min each, then further cleaned by exposure to an oxygen plasma for 5 min. Then a bilayer of PMMA was spin coated onto them. The first layer consisted of 150 nm of 495 K molecular weight PMMA and the second of 150 nm of 950 K molecular weight PMMA. The substrate was then baked for 10 min at 180 °C. After that, a 10 nm thick layer was deposited by thermal evaporation and the sample placed in the electron beam evaporator. The arrays produced were 3 mm^2 and contained 100 nm diameter nanoparticles separated by 300 nm. After patterning of the array, the aluminium layer was first removed by plunging the sample in MF-319 for 30 s followed by 3 min rinsing in ultrapure water. Then the exposed PMMA was removed by dipping the sample into a developing solution consisting of MIBK till the pattern was well defined (about 40 s) and rinsed immediately in IPA for 1 min and blown dry with Argon. After deposition of a 10/90 nm bilayer of chrome/gold, the remaining PMMA was removed in near boiling acetone, rinsed in near boiling IPA and blown dry with argon.

6.2.5 Characterisation of the nanoparticles deposited onto graphene

Scanning Electron Microscopy (SEM) was used in order to determine the size of the nanoparticles and their consistency over the graphene. Scanning was performed at 10 keV and 0.13 nA. Surface plasmon resonance measurements were performed using a EvolutionTM ArrayTM UV-visible spectrophotometer from Thermo Fisher Scientific Inc. .

6.3 Results and discussion

6.3.1 Optical characterisation of electrodeposited nanoparticles

The size of the electrodeposited nanoparticles was estimated to be 30-60 nm from SEM. A typical SEM picture is shown in Figure 6.2. The particles are distributed quite homogeneously over the surface and very close to each other. Figure 6.4 shows UV-vis spectra recorded at different steps of the graphene/Au/graphene/Ag (Ag on top) hetero-structure fabrication. The spectrum recorded for Au on graphene and in air shows a broad peak around 650 nm. After transfer of a graphene layer on top of the nanoparticles, the spectrum barely changed, indicating that the graphene did not significantly affect the plasmonic properties of the particles.

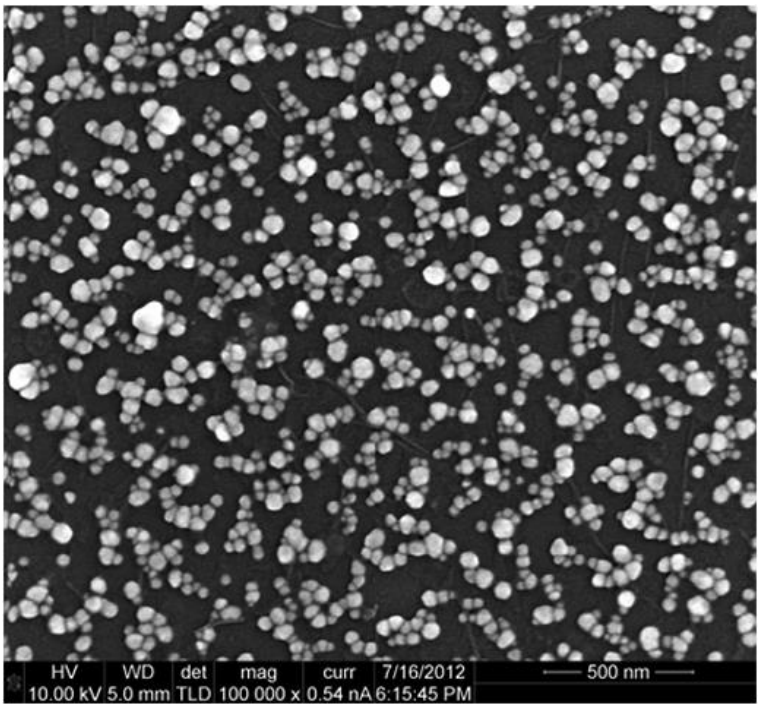

Figure 6.2: A typical SEM image of a graphene/gold electrode. The gold nanoparticles were electrodeposited according to the method described in 2.3.

As the graphene layer is extremely thin, its intimate contact with the nanoparticles would be expected to mean that a change from air to water (therefore a change of dielectric environment) on top of the graphene/gold nanoparticles/graphene hetero-structure would produce a change in the plasmonic response. However, the

spectrum taken in water shows very little change of peak shape and position compared to the one taken in air. This suggests firstly that the epoxy seal on the edges of the graphene is efficient, and also that the second graphene sheet only makes point contacts with the biggest underlying particles, as illustrated in Figure 6.3 (a), and therefore is relatively insensitive to the change in dielectric of its immediate environment. This may in future be resolved by annealing the sample so the graphene becomes more conformal to the gold nanoparticles (Figure 6.3 (b)). Such an annealing technique has been shown to promote a surface enhanced Raman response [32].

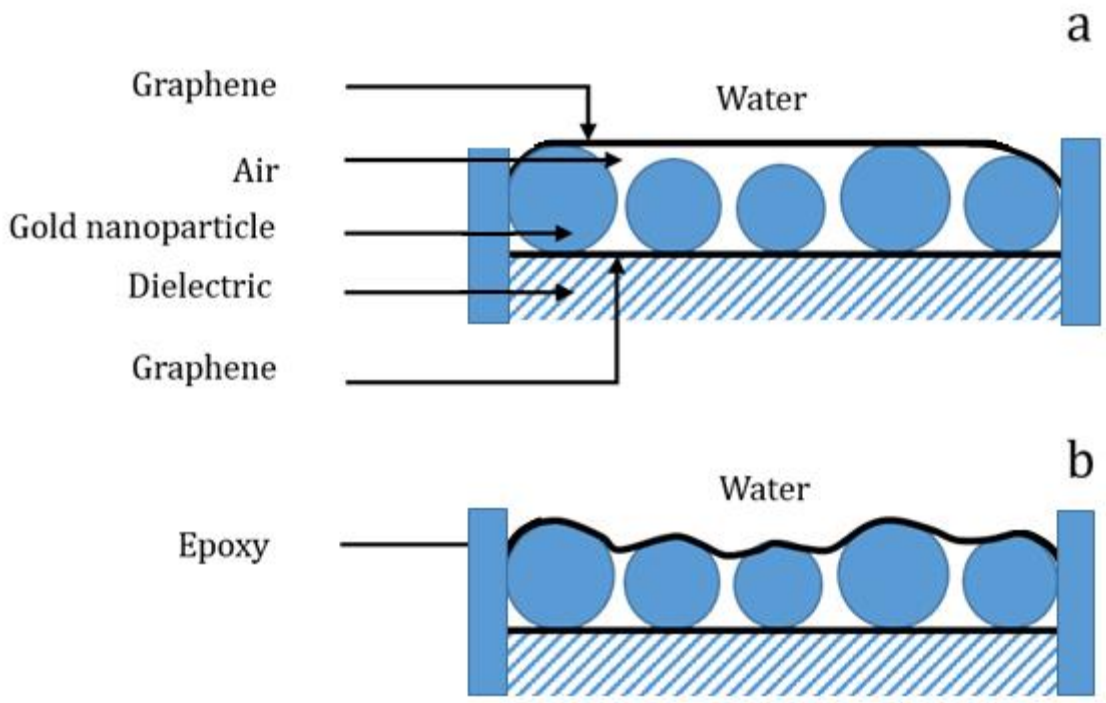

Figure 6.3: Graphene/Au nanoparticles/graphene heterostructure before (a) and after (b) annealing.

Noting the fact that the resonance peak of the gold nanoparticles does not shift in this result suggests that this could be used as a reference signal in a multi-plasmon sensor. In this context, the gold layer would be kept remote from the changing surface dielectric, by an interposing (see Figure 6.5) silver nanoparticles/graphene layer, which would provide the sensing signal for which the gold plasmon is the reference.

After deposition of the silver nanoparticles, the corresponding spectrum shows two peaks of resonance: one around 405 nm corresponding to the silver nanoparticles (as shown by the spectrum of silver nanoparticles on graphene) and one around 585 nm, corresponding to the gold.

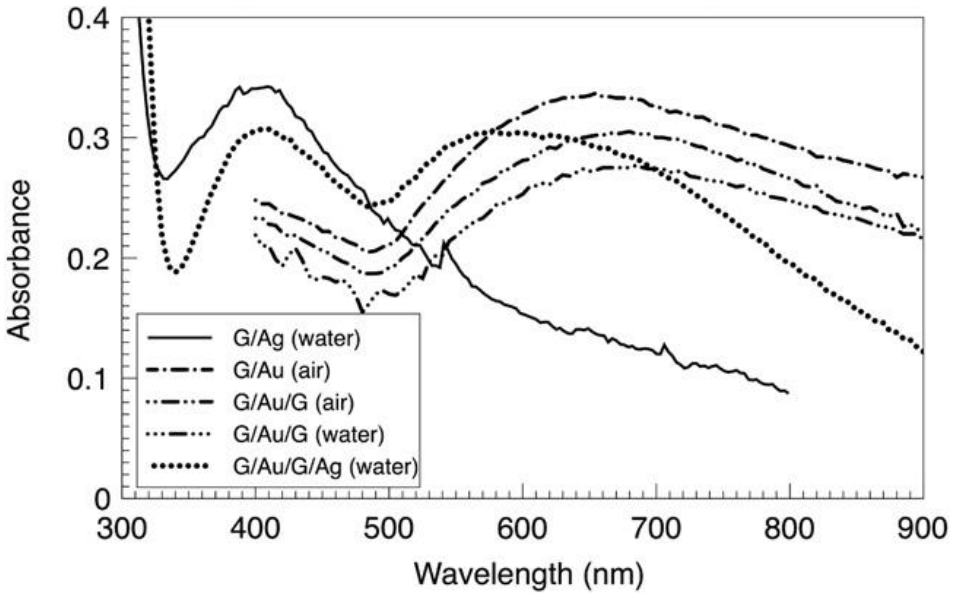

Figure 6.4: UV- visible absorption spectra recorded for the graphene/Au/graphene/Ag layered structure at the different steps of its construction.

In summary, this kind of hetero-structure could be used as a LSPR sensor, with the bottom layer being used as a peak reference and the top layer as the sensor. In this sensor, a third layer of graphene would be deposited on the silver particles, annealed, then modified with antibodies (Figure 6.5).

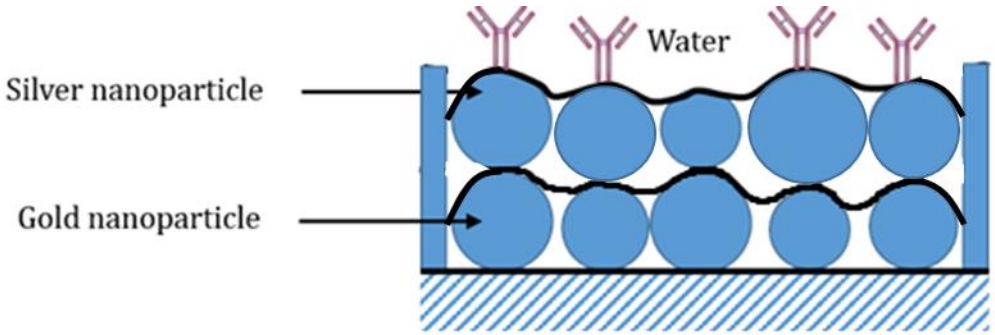

Figure 6.5: LSPR sensor using the plasmonic reponse of the gold nanoparticles as a reference and the plasmonic response of the silver nanoparticles as the sensing part

The attachment of antigen on the antibodies would change the dielectric environment of the particle and would be expected to change their plasmonic response.

It was shown in chapters 2, 4 and 5 that graphene can be used for the electrochemical detection of biomolecules (here procalcitonin). Therefore, one can imagine performing combined LSPR and electrochemical measurements on graphene. An example of such a sensor is presented in Figure 6.6. This sensor consists of a monolayer sheet of graphene modified with gold nanoparticles, graphene, silver nanoparticles and eventually graphene on the top. The last graphene layer could be modified with the same antibodies according to a method described in chapter 4. The attachment of the biomolecule onto their specific antibody would result in a change of the plasmonic response of the silver nanoparticles and a change of resistance to electron transfer from a typical redox couple present in the water phase (here Ruthenium hexamine, see chapter 2 part 4.2.2) to the graphene.

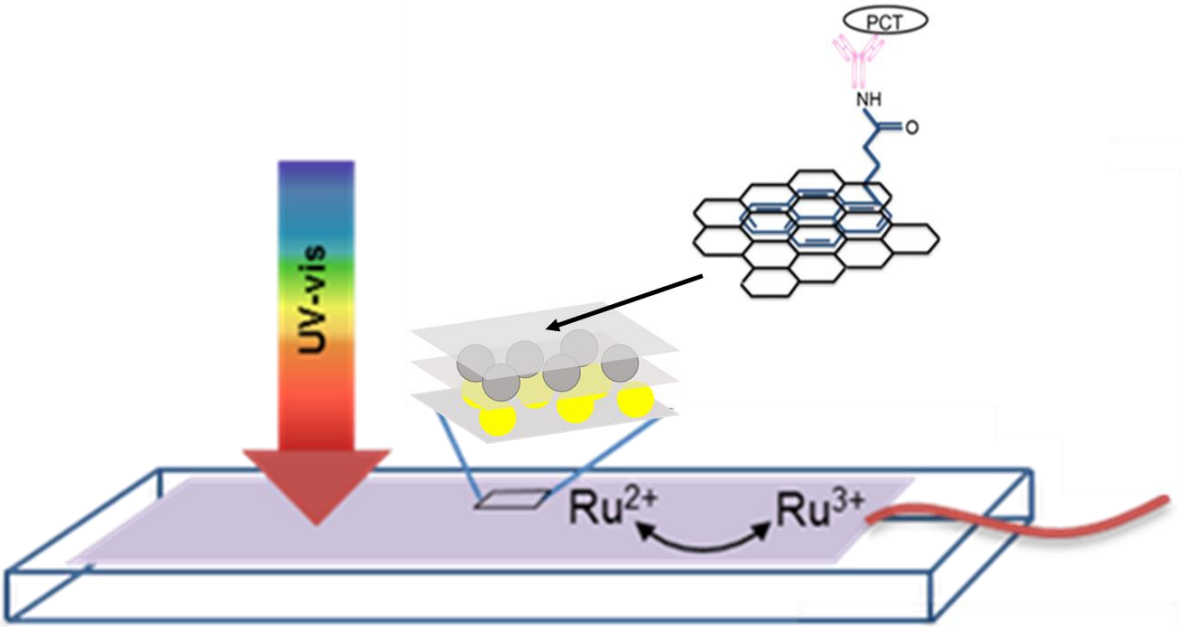

Figure 6.6: Combined LSPR and electrochemical sensor.

Depositing metal arrays on graphene by electron beam lithography would produce an evenly dispersed layer of same size nanoparticles, which could reduce the FWHM of the resonance peaks and allow better visibility in resonance peak shift. Progress toward this goal is described in the next section, concerned with the deposition and plasmonic response of gold arrays on graphene.

6.3.2 Optical characterisation of nanoparticles deposited by e-beam lithography

Figure 6.7 shows typical SEM images of the gold arrays produced by electron beam lithography. Images **a** and **b** show an array on glass while **c** and **d** show an array on graphene. Both show evenly distributed particles that are separated by 300 nm and are about 100 nm in diameter, even though the graphene substrate show some contamination. The tilted view indicates that the particles are also of the same height and that their shape is pear-like (their circumference is larger at the base than at the top).

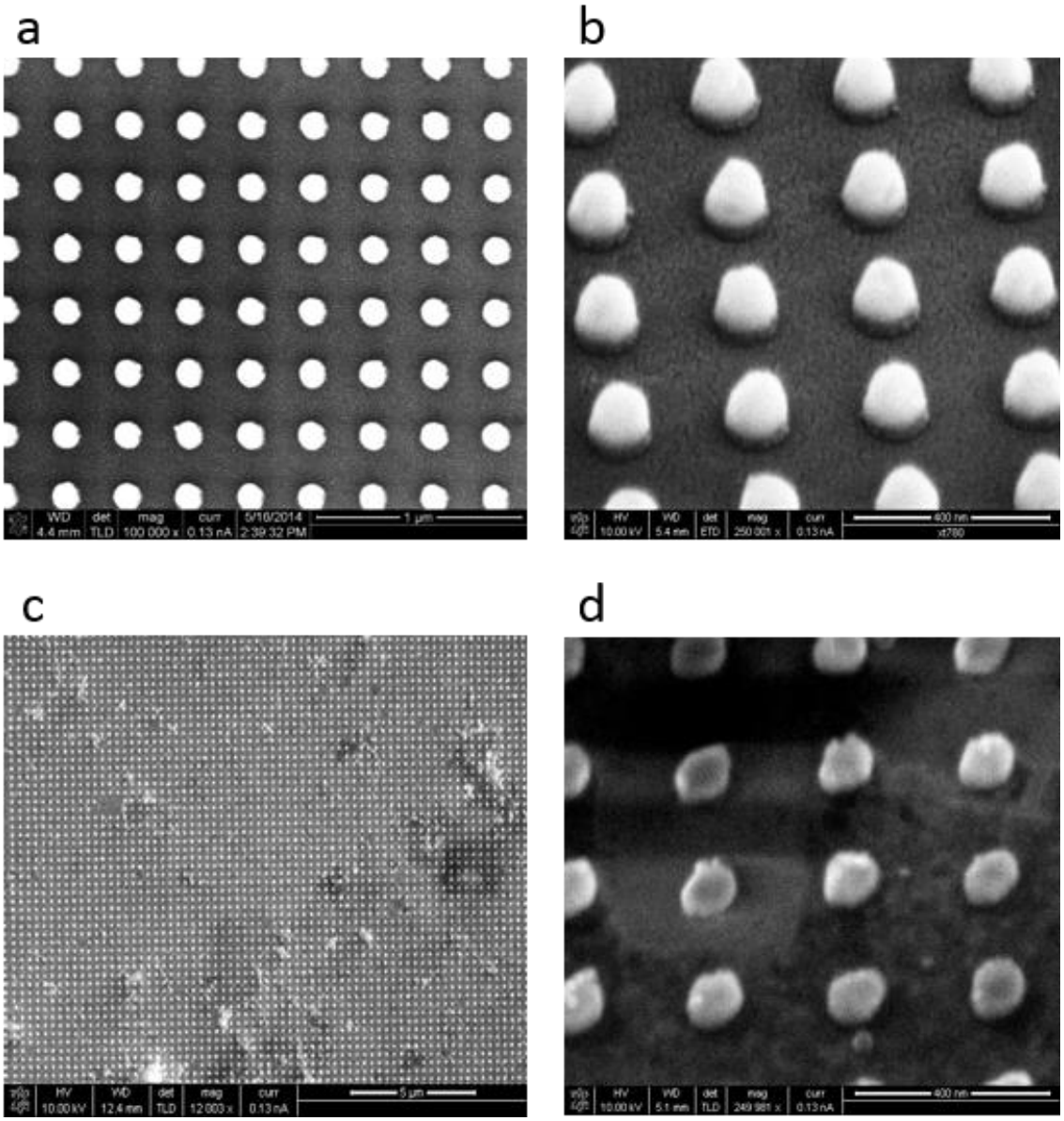

Figure 6.7: SEM pictures of gold nanoarrays (100 nm wide, separated by 300 nm) on glass (**a** and **b**) and on graphene (**c** and **d**).

Figure 6.8 shows UV-visible spectra recorded for two gold nanoarrays where the nanoparticles have different sizes and are separated by different distances. One array has nanoparticles of diameter 50 nm that are separated by 100 nm, and gives a LSPR peak an 619 nm. The other array has nanoparticles of diameter 100 nm that are separated by 300 nm, and gives a LSPR peak at 626 nm which is better defined than the previous array. It is also easier to fabricate and therefore these dimensions were selected for the rest of the experiments.

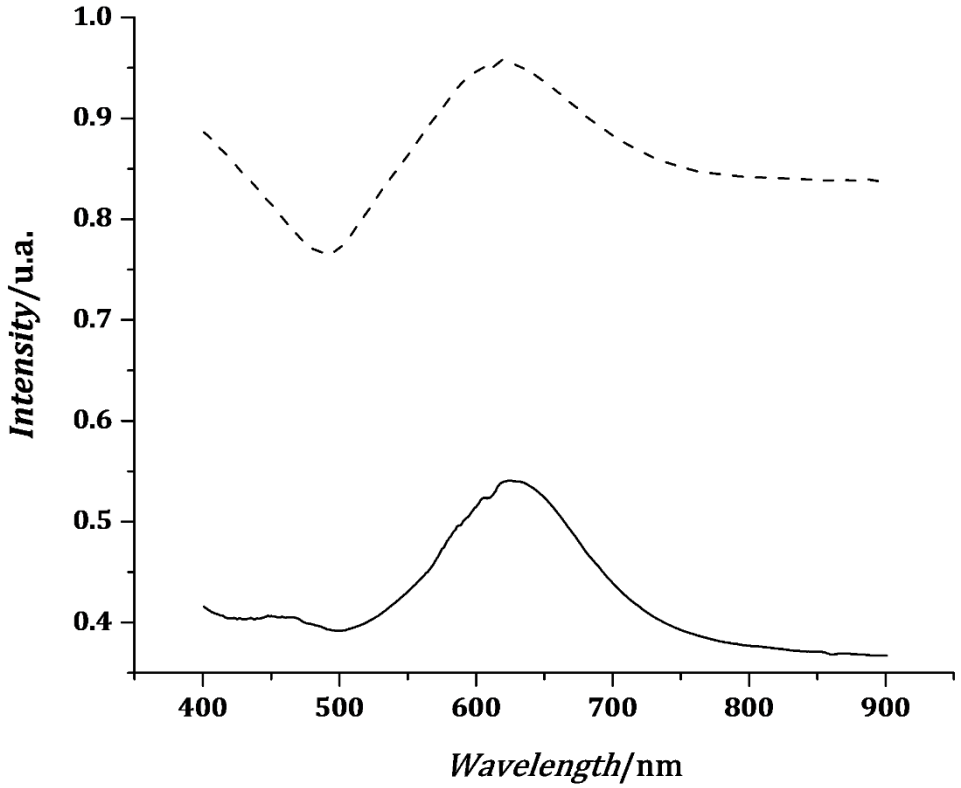

Figure 6.8: UV-visible spectrum recorded for gold nanoarrays where the nanoparticles are 50 nm in diameter and separated by 100 nm (dashed line) and 100 nm in diameter and separated by 300 nm (solid line).

Figure 6.9 shows UV-visible spectra recorded in air at two gold arrays on graphene (100 nm diameter and separated by 300 nm). Each show a well-defined LSPR peak around 640 nm. Figure 6.10 shows that the LSPR peak shifts when air is changed for ultra-pure water in Phosphate Buffered Saline (PBS). The array was blown dried with nitrogen before being exposed to each environment. After recording UV-visible spectra in water and PBS, another spectrum was recorded in air to verify that there is no memory effect when the array is subjected to environments with different dielectric constants. The second spectrum in air was found to have the same LSPR response as the first one.

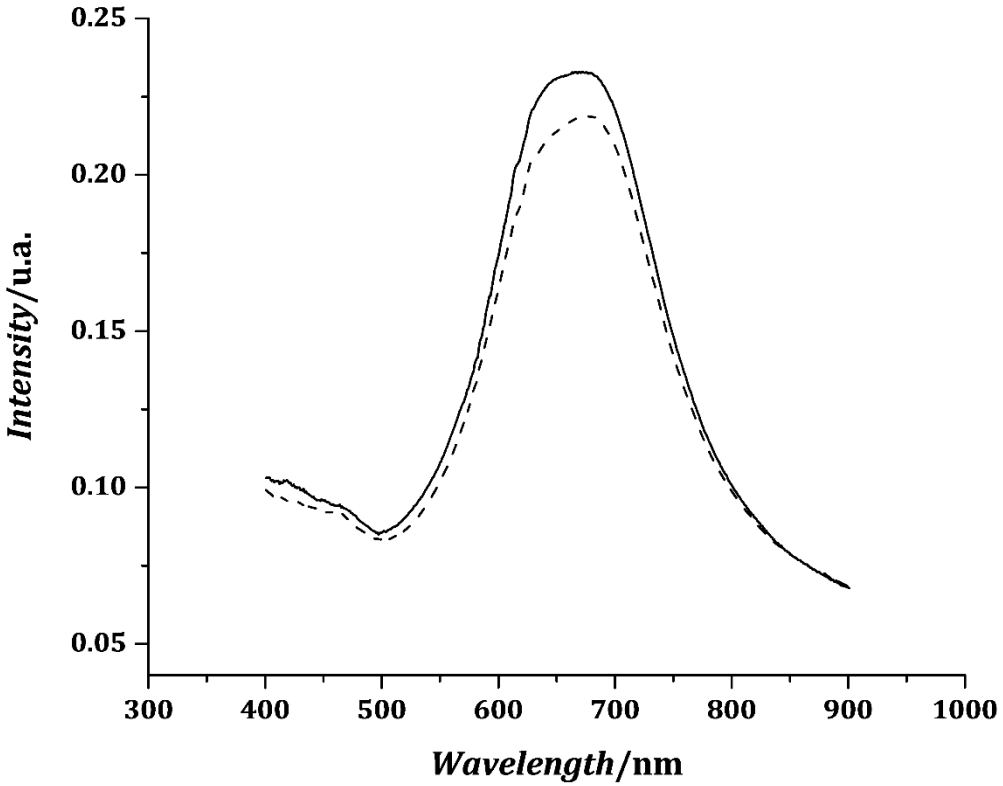

Figure 6.9: UV-visible absorption spectra recorded in PBS for a gold array on graphene.

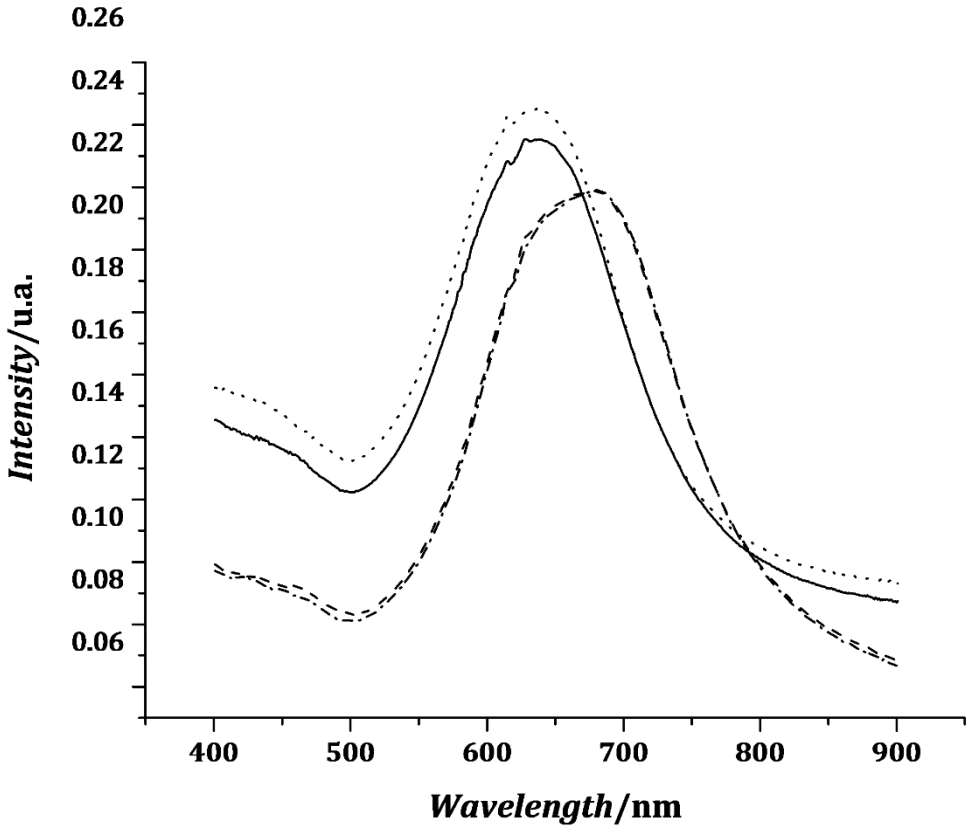

Figure 6.10: UV-visible spectra recorded at a gold array on graphene consecutively in air (plain line), in ultra-pure water (dash line), in PBS (dashed dot line) and in air again (dotted line). The array was blown dried with nitrogen between each recording.

The graphene between the nanoparticles was then modified with an ELISA sandwich used for the capture and detection of procalcitonin (this is explained in chapter 4) and a UV-visible spectrum was recorded. This spectrum is shown in Figure 6.11 and no noticeable peak shift was detected. This could be due to the lack of proximity of the proteins with the gold nanoparticles when they bind to the derivatised graphene.

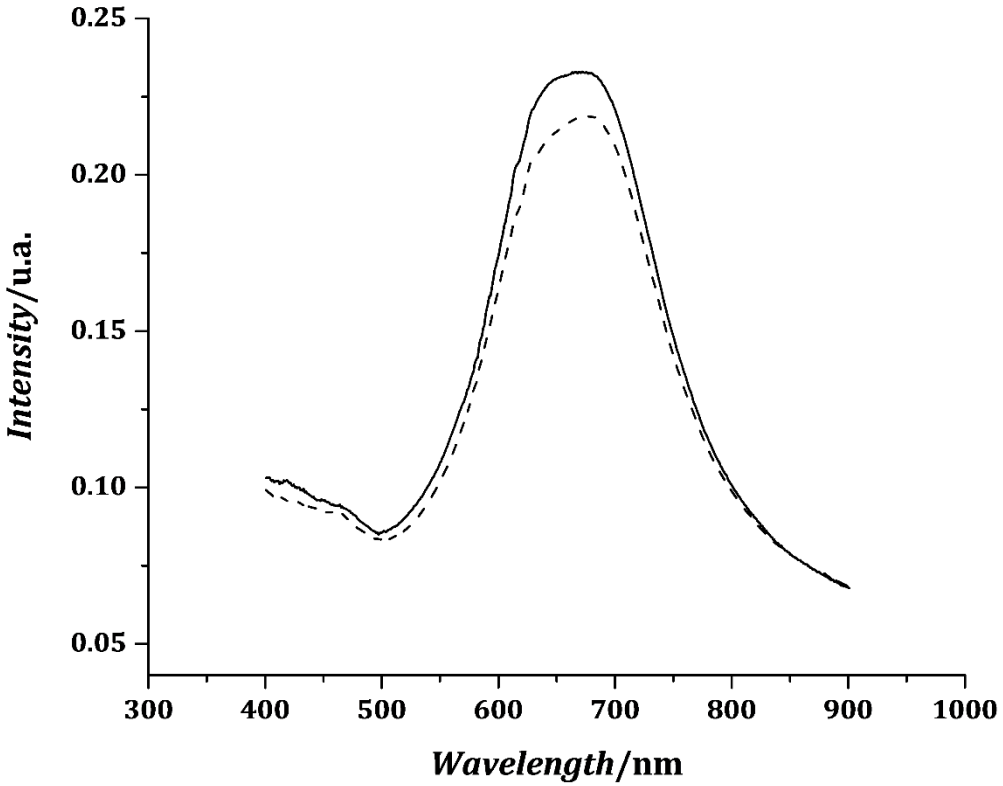

Figure 6.11: UV-visible spectra recorded for a gold nanoarray on graphene before (plain line) and after (dotted line) modification with an ELISA sandwich.

Figure 6.12 shows UV-visible spectra recorded for a gold nanoarray on graphene before and after being exposed for 5 days to a solution containing pyrene butanoic succinimidyl ester. After exposure, the LSPR peak shifted by 23 nm. Further study is required to investigate if an obvious peak shift could be observed on a much smaller time scale.

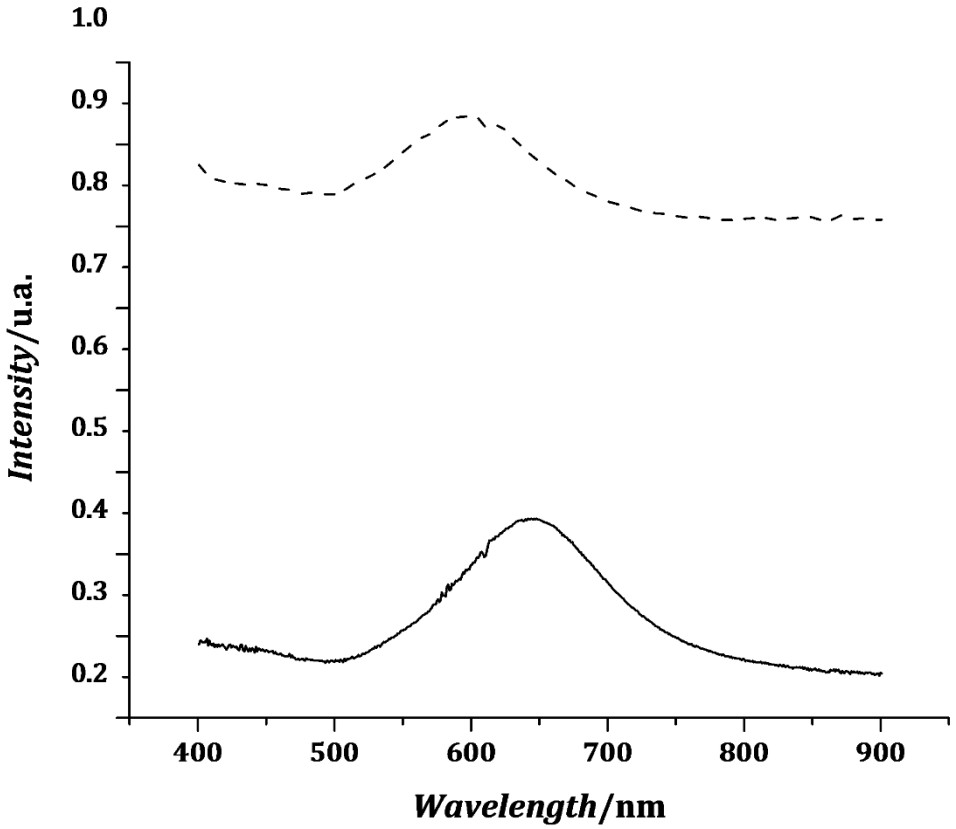

Figure 6.12: UV-visible spectra for a gold nanoarray on graphene before (dash curve), and after (plain line) exposure to the cross-linker pyrene butanoic succinimidyl ester and anti-procalcitonin antibody for 5 days.

In order increase the sensitivity of the LSPR device, one could think of adding a second layer of graphene on top of the gold nanoarray and annealing to make the graphene more conformal to the gold and then adsorbing antibodies to this intimately-contacting graphene.

6.4 Conclusion

In this chapter, results have shown that graphene can support LSPR when metal nanoparticules are either electrodeposited on graphene or metal nanoarrays are created on graphene using electron beam lithography. Electrodeposition has the advantage of being simple and cost effective, while arrays deposited by electron beam lithography allows control of the size and shape of the nanoparticles. Both

techniques offer the prospect of developing affordable and sensitive transmission LSPR biosensors, with the possibility of making them flexible if graphene is used as a substrate for the nanoparticles.

Bibliography

[1] Y. Yao, B. Yi, J. Xiao, and Z. Li, "Surface plasmon resonance biosensors and its application," *2007 1st Int. Conf. Bioinforma. Biomed. Eng. ICBBE*, pp. 1043–1046, 2007.

[2] J. Homola, "Surface plasmon resonance sensors: review," *Sensors Actuators, B Chem.*, vol. 54, pp. 3–15, 1999.

[3] K. A. Willets and R. P. Van Duyne, "Localized surface plasmon resonance spectroscopy and sensing," *Annu. Rev. Phys. Chem.*, vol. 58, pp. 267–297, 2007.

[4] M. G. Kim, Y. B. Shin, J. M. Jung, H. S. Ro, and B. H. Chung, "Enhanced sensitivity of surface plasmon resonance (SPR) immunoassays using a peroxidase-catalyzed precipitation reaction and its application to a protein microarray," *J. Immunol. Methods*, vol. 297, no. 1–2, pp. 125–132, 2005.

[5] D. Grieshaber, R. MacKenzie, J. Vörös, and E. Reimhult, "Electrochemical Biosensors - Sensor Principles and Architectures," *Sensors*, vol. 8, no. 3, pp. 1400–1458, 2008.

[6] D. . Thevenot, K. Toth, R. A. Durst, and G. S. Wilson, "Electrochemical biosensors : Recommended definitions and classification," *Pure Appl. Chem.*, vol. 71, no. 12, pp. 2333–2348, 1999.

[7] E. Hutter and J. H. Fendler, "Exploitation of localized surface plasmon resonance," *Adv. Mater.*, vol. 16, no. 19, pp. 1685–1706, 2004.

[8] A. J. Haes, W. P. Hall, L. Chang, W. L. Klein, and R. P. Van Duyne, "A Localized Surface Plasmon Resonance Biosensor : First Steps toward an Assay for Alzheimer ' s Disease," *Nano Lett.*, vol. 4, no. 6, pp. 1029–1034, 2004.

[9] K. M. Mayer, J. H. Hafner, and A. À. Antigen, "Localized Surface Plasmon Resonance Sensors," *Chem. Rev.*, vol. 111, no. 6, pp. 3828–3857, 2011.

[10] A. J. Haes and R. P. Van Duyne, “A nanoscale optical blosensor: Sensitivity and selectivity of an approach based on the localized surface plasmon resonance spectroscopy of triangular silver nanoparticles,” *J. Am. Chem. Soc.*, vol. 124, no. 35, pp. 10596–10604, 2002.

[11] T. Klar, M. Perner, S. Grosse, G. von Plessen, W. Spirkl, and J. Feldmann, “Surface-Plasmon Resonances in Single Metallic Nanoparticles,” *Phys. Rev. Lett.*, vol. 80, no. 19, pp. 4249–4252, 1998.

[12] W. P. Hall, S. N. Ngatia, and R. P. Van Duyne, “LSPR Biosensor Signal Enhancement Using Nanoparticle - Antibody Conjugates,” *J. Phys. Chem.*, vol. 115, pp. 1410–1414, 2011.

[13] S. H. Choi, Y. L. Kim, and K. M. Byun, “Graphene-on-silver substrates for sensitive surface plasmon resonance imaging biosensors.,” *Opt. Express*, vol. 19, no. 2, pp. 458–466, 2011.

[14] S. Szunerits, N. Maalouli, E. Wijaya, J. P. Vilcot, and R. Boukherroub, “Recent advances in the development of graphene-based surface plasmon resonance (SPR) interfaces,” *Anal. Bioanal. Chem.*, vol. 405, no. 5, pp. 1435–1443, 2013.

[15] L. Wang, Y. Sun, J. Wang, X. Zhu, F. Jia, Y. Cao, X. Wang, H. Zhang, and D. Song, “Sensitivity enhancement of SPR biosensor with silver mirror reaction on the Ag/Au film,” *Talanta*, vol. 78, no. 1, pp. 265–269, 2009.

[16] W. P. Hall, S. N. Ngatia, and R. P. Van Duyne, “LSPR Biosensor Signal Enhancement Using Nanoparticle - Antibody Conjugates,” pp. 1410–1414, 2011.

[17] D. K. Polyushkin, J. Milton, S. Santandrea, S. Russo, M. F. Craciun, S. J. Green, L. Mahe, C. P. Winolve, and W. L. Barnes, “Graphene as a substrate for plasmonic nanoparticles,” *J. Opt.*, vol. 15, no. 11, p. 114001, 2013.

[18] K. S. N. A. N. Grigorenko , M. Polini, “Graphene plasmonics,” *Nat. Photonics*, vol. 6, no. 11, pp. 749 – 758, 2012.

[19] J. Zhang, Y. Sun, Q. Wu, Y. Gao, H. Zhang, Y. Bai, and D. Song, “Preparation of graphene oxide-based surface plasmon resonance biosensor with Au bipyramid nanoparticles as sensitivity enhancer,” *Colloids Surfaces B Biointerfaces*, vol. 116, pp. 211–218, 2014.

[20] L. Wang, H. Zhu, H. Hou, Z. Zhang, X. Xiao, and Y. Song, “A novel hydrogen peroxide sensor based on Ag nanoparticles electrodeposited on chitosan-graphene oxide/cysteamine-modified gold electrode,” *J. Solid State Electrochem.*, vol. 16, no. 4, pp. 1693–1700, 2012.

[21] C. Liu, K. Wang, S. Luo, Y. Tang, and L. Chen, “Direct electrodeposition of graphene enabling the one-step synthesis of graphene-metal nanocomposite films,” *Small*, vol. 7, no. 9, pp. 1203–1206, 2011.

[22] B. Jiang, M. Wang, Y. Chen, J. Xie, and Y. Xiang, “Highly sensitive electrochemical detection of cocaine on graphene/AuNP modified electrode via catalytic redox-recycling amplification,” *Biosens. Bioelectron.*, vol. 32, no. 1, pp. 305–308, 2012.

[23] J. Zhang, Y. Sun, B. Xu, H. Zhang, Y. Gao, H. Zhang, and D. Song, “A novel surface plasmon resonance biosensor based on graphene oxide decorated with gold nanorod-antibody conjugates for determination of transferrin,” *Biosens. Bioelectron.*, vol. 45, no. 1, pp. 230–236, 2013.

[24] T. Xue, X. Cui, W. Guan, Q. Wang, C. Liu, H. Wang, K. Qi, D. J. Singh, and W. Zheng, “Surface plasmon resonance technique for directly probing the interaction of DNA and graphene oxide and ultra-sensitive biosensing,” *Biosens. Bioelectron.*, vol. 58, pp. 374–379, 2014.

[25] H. Zhang, D. Song, S. Gao, J. Zhang, H. Zhang, and Y. Sun, “Novel SPR biosensors based on metal nanoparticles decorated with graphene for immunoassay,” *Sensors Actuators, B Chem.*, vol. 188, pp. 548–554, 2013.

[26] S. Lee, M. H. Lee, H. Shin, and D. Choi, “Control of density and LSPR of Au nanoparticles on graphene.,” *Nanotechnology*, vol. 24, no. 27, p. 275702, 2013.

[27] T. Sannomiya, H. Dermutz, C. Hafner, J. Vörös, and A. B. Dahlin, "Electrochemistry on a localized surface plasmon resonance sensor," *Langmuir*, vol. 26, no. 10, pp. 7619–7626, 2010.

[28] K. Nakamoto, R. Kurita, and O. Niwa, "Electrochemical surface plasmon resonance measurement based on gold nanohole array fabricated by nanoimprinting technique," *Anal. Chem.*, vol. 84, no. 7, pp. 3187–3191, 2012.

[29] C. N. Tharamani, K. a. Mahmoud, G. R. Vasanthakumar, and H. B. Kraatz, "Studies into the interaction of a ferrocene-conjugates of Gly-Gly-Arg-Tyr with papain: AC voltammetry, impedance spectroscopy and surface plasmon resonance studies," *Sensors Actuators, B Chem.*, vol. 137, no. 1, pp. 253–258, 2009.

[30] L. Wang, C. Zhu, L. Han, L. Jin, M. Zhou, and S. Dong, "Label-free, regenerative and sensitive surface plasmon resonance and electrochemical aptasensors based on graphene," *Chem. Commun.*, vol. 47, no. 27, pp. 7794–7796, 2011.

[31] J. Niu, Y. Jun Shin, Y. Lee, J. H. Ahn, and H. Yang, "Graphene induced tunability of the surface plasmon resonance," *Appl. Phys. Lett.*, vol. 100, no. 6, p. 061116 2012.

[32] W. Xu, J. Xiao, Y. Chen, Y. Chen, X. Ling, and J. Zhang, "Graphene-veiled gold substrate for surface-enhanced raman spectroscopy," *Adv. Mater.*, vol. 25, no. 6, pp. 928–933, 2013.

Chapter 7

Potential and pH Dependence of Photocurrent Transients for Boron-Doped Diamond Electrodes in Aqueous Electrolyte

Abstract

Using illumination at energies below the intrinsic diamond energy gap, photocurrent transients have been recorded for boron-doped diamond (BDD) as an electrode in an aqueous electrolyte of 0.1 M KH_2PO_4. The commercially-supplied BDD was in the form of a free-standing, polycrystalline film grown by chemical vapour deposition (CVD), with a boron acceptor concentration of $\geq 10^{20}$ cm^{-3}. The effects of mechanical polishing of the BDD, of electrochemical hydrogen evolution and of electrochemical oxygen evolution (in 0.1 M KH_2PO_4), on the potential dependence of the photocurrent transients have been examined. Measurements of the cathodic photocurrent at light switch-on have been used to determine the photocurrent onset potential as a measure of the flatband potential. Comparison with and between related literature observations has shown broad agreement across considerably varying BDD/electrolyte systems. The flatband potential shifted positively following electrochemical oxygen evolution, indicating the formation of oxygen-containing groups on the diamond surface, these increasing the potential drop across the Helmholtz layer. For the electrochemically oxidised electrode, the cathodic photocurrent transient at a fixed potential changed reproducibly with changing solution pH, owing to the participation of the oxygen-containing surface groups in acid–base equilibrium with the solution. This clear demonstration of BDD as a photoelectrochemical pH sensor is in principle extendable to mapping the spatial variation in pH across a BDD surface by use of a focussed light spot.

7.1 Introduction

Photoelectrochemistry relates to the generation of a current at a semiconductor/electrolyte interface upon exposure to an electromagnetic excitation.

The electronic properties of semiconductors are understood in terms of energy bands. This arises from the overlap of atomic orbitals from the infinite number of atoms composing the material. The lowest occupied band is called the valence band and the highest unoccupied is called the conduction band. The gap between the two is called the band gap and allows to understand the difference between metals, semiconductors and dielectrics (see Figure 7.1).

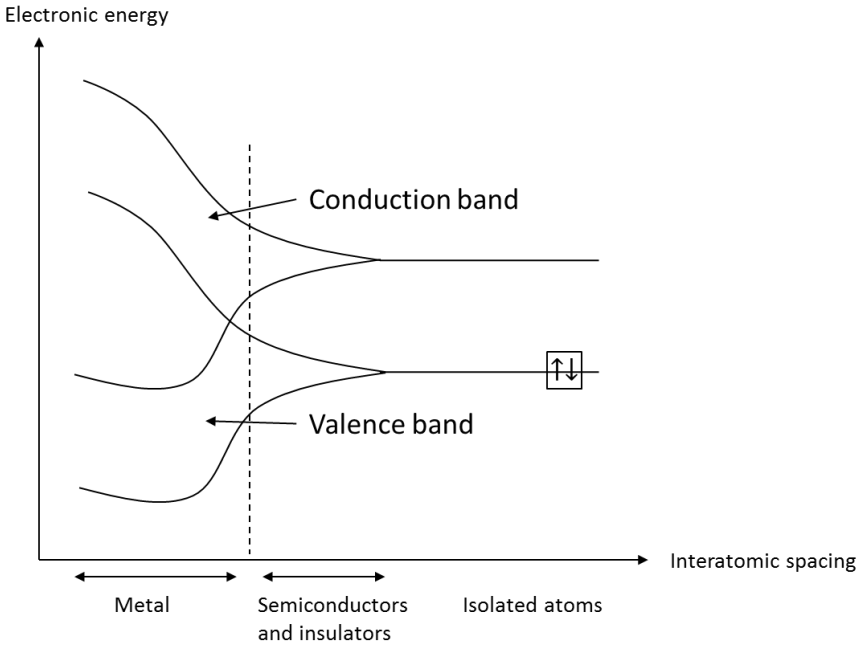

Figure 7.1: Generation of bands in semiconductors and metals from the atomic orbitals of isolated atoms. Adapted from [1]

Electrical conduction occurs when the conduction band is partially occupied. In metals, the two bands overlap and electrons can always be promoted to the conduction band. In insulators, the gap is too important to allow this promotion. For example, diamond has a band gap of 5eV and is an insulator. In semiconductors, electrons can be promoted to the conduction band upon excitation such as light and heat. Another way of introducing new charge carriers consists in doping the material by introducing a new element in the material. This

introduces an energy level either close to the conduction or valence band, thereby facilitating the promotion of electrons or holes (see Figure 7.2).

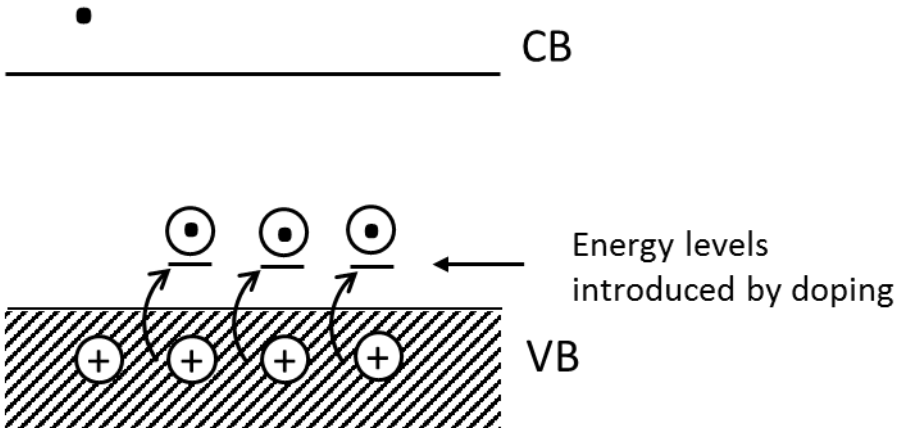

Figure 7.2: Promotion by excitation of electrons from the valence band to energy states introduced by doping. Case of a p semiconductor. Adapted from [1].

The semiconductor is said to be doped p (n) if the resulting majority carriers are holes (electrons). For example, doping diamond with boron (p doping) makes it electrically conductive. Another important concept for the understanding of photoelectrochemistry is the Fermi level, which is the energy level for which the probability of occupation by an electron is half. For an intrinsic semiconductor (not doped), the Fermi level lies in the middle of the band gap. P (n) doping moves the Fermi level closer to the valence (conduction) band.

At equilibrium, the electrochemical potential in the semiconductor (the Fermi level) and the electrolyte (the redox potential) must be the same. In the case of a p doped semiconductor like BBD, this results in a downwards band bending (see Figure 7.3) and an accumulation of electron at the interface over region called the space charge region (with an associated built-in electric field). This region is depleted in majority carriers, holes, and therefore is called a depletion region. Applying a potential (for example with a potentiostat) at a BDD electrode shifts the Fermi level, and therefore the band banding. Only the energy of the bands at the interface with the electrolyte is not changed. At equilibrium ($E = E_{eq}$), the total current exchange is null. At $E > E_{eq}$ (accumulation region), the bands are bent upward and holes accumulate in the space charge region. These holes then participate into an oxidation current. At $E < E_{eq}$ (depletion region), the bands bend upward and the region is depleted in majority carriers. There is very few

charge carriers available for transfer and the any reaction would be slow. The irradiation of the semiconductor with light of sufficient energy promotes an electron from the valence band to the conduction band. When this happens in the space charge region, the electron migrates towards the interface with the electrolyte due to the electrical field. There, it can participate into a reaction of reduction. A p doped semiconductor like BDD is a photoanode and a dark cathode.

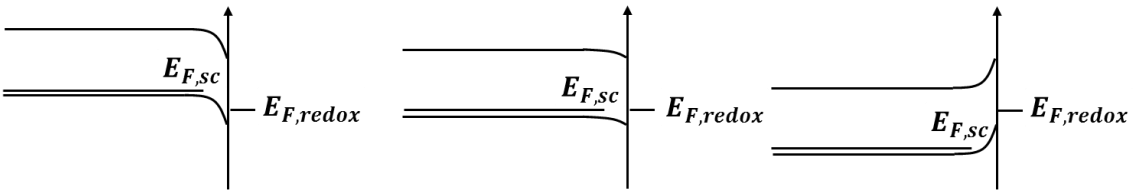

Figure 7.3: Effect of applying a bias voltage $V_{bias} = E_{F,FC} - E_{F,redox}$ on the band structure of a p doped semiconductor; middle: $V_{bias} = O$ (equilibrium); left: $V_{bias} < 0$; right: $V_{bias} > 0$. $E_{F,SC}$ is the Fermi level of the semiconductor; $E_{F,redox}$ is the redox potential of the electrolyte.

Used as an electrode in aqueous electrolyte, polycrystalline boron-doped diamond (BDD) grown by chemical vapour deposition (CVD) has been reported to give cathodic [2][3][4] and anodic [2][3] photocurrents upon illumination with light of energy below that of the bandgap of intrinsic diamond, 5.45 eV. The observation of such sub-bandgap photocurrents indicates that states within the energy gap can facilitate electron transfer to and from solution. These states may originate from sp^2 carbon impurities, [2][4] though states relating to the incorporation of boron into the diamond lattice may also be involved[1][3]. Cathodic photocurrents at BDD have been shown, by direct detection of hydrogen gas, to be due to the hydrogen evolution reaction[4], while the origin of the anodic photocurrents remains uncertain [5].

Pleskov *et al*. [5] reported the photoelectrochemical determination of the flatband potential for both polycrystalline and single-crystal BDD electrodes in 0.1 M H_2SO_4, using deuterium lamp illumination (200 - 400 nm) to provide a range of energies above the intrinsic diamond energy gap, or "supra-bandgap". Those authors suggested [5] that, for heavily-doped BDD (boron concentration exceeding 10^{19} cm^{-3}), the photocurrent onset potential provided a more reliable measure of the flatband potential than that achieved (following Gärtner's model [6] of the

reverse-biased *p*-*n* junction as often applied to the semiconductor/electrolyte interface [7]) by extrapolating to zero photocurrent the potential dependence of the photocurrent squared. Also using deuterium lamp illumination, Rao *et al*. [8] measured photocurrent onset potentials in agreement with flatband potentials determined by Mott-Schottky analysis [7] of capacitance data for polycrystalline BDD in 0.1 M KH_2PO_4. They reported [8] that electrochemical oxidation of BDD, initially hydrogen terminated by exposure to hydrogen plasma, shifted the flatband and photocurrent onset potentials positively in 0.1 M KH_2PO_4, attributing this to the oxidation producing C-OH, C-O-C and >C=O surface groups (detected using x-ray photoelectron spectroscopy) which increased the potential drop across the Helmholtz layer. They also reported [8] that the flatband potential of the electrochemically oxidised BDD showed a near-Nernstian (59 mV/pH) dependence on the solution pH between pH = 4.5 and pH = 12 in 0.1 M KCl, concluding that this was due to the oxygen containing groups on the BDD surface participating in acid-base equilibrium with the solution. Similar observations [2] have been made for sub-bandgap illumination of polycrystalline BDD where electrochemical oxidation caused a positive shift in the cathodic photocurrent onset potential and a pH-dependent positive shift in the Mott-Schottky determined flatband potential in 0.1 M KCl.

In the present study, sub-bandgap illumination (250-600 nm) of a polycrystalline BDD electrode, commercially supplied as a free-standing, CVD-grown film with a boron acceptor concentration of ≥ 10^{20} cm^{-3}, was used in recording both anodic and cathodic photocurrent transients as a function of applied potential in aqueous 0.1 M KH_2PO_4. Comparison with and between related literature observations has shown broad agreement across considerably varying BDD/electrolyte systems. In accordance with other authors,[5] but here for exclusively sub-bandgap illumination, the cathodic photocurrent onset potential was used as a measure of the flatband potential, in preference to an analysis based on the Gärtner model. Photocurrent transients were recorded using the BDD after simple mechanical polishing of the surface, then after a cathodic pre-treatment involving hydrogen evolution to promote surface hydrogenation, and finally after an anodic pre-treatment involving oxygen evolution to promote the removal of surface and sub-surface hydrogen and the formation of oxygen-containing groups on the diamond surface. For the anodically-treated BDD, the flatband potential was found to shift

positively relative to the values recorded for the material as-polished or cathodically-treated. Also, the cathodic photocurrent transient for the anodically-treated BDD was shown to be pH dependent in a reproducible manner, allowing a simple demonstration of the viability of BDD as a photoelectrochemical pH sensor. This, the first use of BDD as a pH sensor based on its photocurrent response, is in principle extendable to mapping the spatial variation in pH across the BDD surface by use of a focussed light spot in a manner similar to a light-addressable potentiometric sensor, [9]but here measuring a photocurrent due to the hydrogen evolution reaction.

7.2 Experimental

7.2.1 The photoelectrochemical cell

CVD-grown polycrystalline BDD of boron acceptor concentration ≥ 10^{20} cm^{-3} was supplied by Diamond Detectors Ltd (Poole, UK) as a free-standing disc, 3.8 cm in diameter, with one surface industrially ground to a nanometre-scale finish. Prior cleaning of the BDD involved "polishing" the ground surface with 0.3 μm and 0.05 μm Al_2O_3 pastes, followed by subjection to ultrasound for 2 minutes each time in water (of nominal resistivity 18.2 MΩ cm), then in 2-propanol and then in water again, before rinsing in water and drying in a nitrogen stream. Backed by a polished steel plate to provide electrical contact, the BDD disc was clamped via a rubber o-ring to cover a 6 mm diameter round hole in the base of an electrochemical cell, thus providing a defined area of the polished BDD as a working electrode contacting the electrolyte (0.1 M KH_2PO_4, Fluka, >99.0 %) in an upwards-facing orientation. A Pt counter electrode and Ag/AgCl/3 M NaCl reference electrode (BASi), cited below as "reference", completed the cell, controlled by a CV-50W Voltammetric Analyzer (BASi). For photoelectrochemical measurements, an EFOS Novacure Model N2001-A1 UV-curing lamp (spectral range 250-600 nm) was used to illuminate the BDD through the electrolyte of depth approximately 1 cm.

7.2.2 Measurement of photocurrent transients

A cyclic voltammogram was recorded at the polished BDD electrode to determine the potential range over which the faradaic current in the absence of UV illumination was sufficiently low to permit reasonable determination of subsequent photocurrents. Then, at 0.1 V intervals within this range and starting at the most positive potential, the current at constant potential was recorded for 60 s, with a 10 s pulse of the UV illumination begun at 30 s to elicit a photocurrent transient. This procedure of recording photocurrent transients over a suitable potential range was repeated after cathodic treatment (15 minutes of hydrogen evolution at -3.2 V (vs Ag/AgCl/3 M NaCl)) and then again after anodic treatment (15 minutes of oxygen evolution at +3.2 V (vs Ag/AgCl/3 M NaCl)) of the BDD electrode, which remained in the cell throughout. Before each measurement, the electrolyte was purged with nitrogen gas and then kept under nitrogen.

7.2.3 Raman characterisation of the BDD

Following the photoelectrochemical measurements described in 2.2., the BDD surface in its final, electrochemically-oxidised state was rinsed in water and then dried in a stream of nitrogen gas, before recording its Raman spectrum using a Renishaw RM1000 Spectrometer, with a 50× objective and a laser excitation wavelength of 532 nm.

7.2.4 Demonstration of the pH-dependence of the photocurrent

The BDD electrode was re-polished as described in 2.1., before being electrochemically oxidised, in nitrogen-purged 0.1 M KH_2PO_4, at +2.5 V (vs Ag/AgCl/3 M NaCl) for 5 minutes. Following the section 2.2 procedure, but using only a single potential of 0.6 V (vs Ag/AgCl/3 M NaCl), a photocurrent transient was then recorded in the 0.1 M KH_2PO_4 solution, which was of pH = 4.5. A series of such photocurrent transients at 0.6 V (vs Ag/AgCl/3 M NaCl) were then recorded, each following replacement of the cell contents with fresh, nitrogen-purged 0.1 M KH_2PO_4, alternating between one solution at pH = 4.5 and a second solution adjusted to pH = 10 by the addition of 0.5 M NaOH.

7.3 Results and Discussion

Figure 7.4 shows the initial photocathodic current and also the "dark" current recorded immediately prior to UV-illumination, as functions of potential for the as-polished BDD surface. The measurement of these currents, together with the definition of the initial cathodic photocurrent, Δi_{cath}, as the difference between them, is illustrated by the example in the figure inset. Figure 7.4 sub-insets show examples of the complete photocurrent transients, demonstrating their variation with the applied potentials noted within the diagrams. Figures 7.5 and 7.6 are as Figure 7.4, but for the BDD surface following its cathodic and then its anodic treatments, respectively, and including within the figure insets a magnified view of the difference between the dark current and the initial photocurrent for selected potential ranges.

7.3.1 Origin of the photocurrent

The spectral range of the radiation used in this work was 250 – 600 nm (4.96 eV to 2.07 eV) encompassing a wide range of energies for possible states within the bandgap that may have facilitated photocurrent generation. One possibility is that any sp^2 carbon in grain boundaries may have provided impurity states in the bandgap,[2][4] while another is the involvement of states relating to the incorporation of boron acceptors in the diamond lattice [3][4].

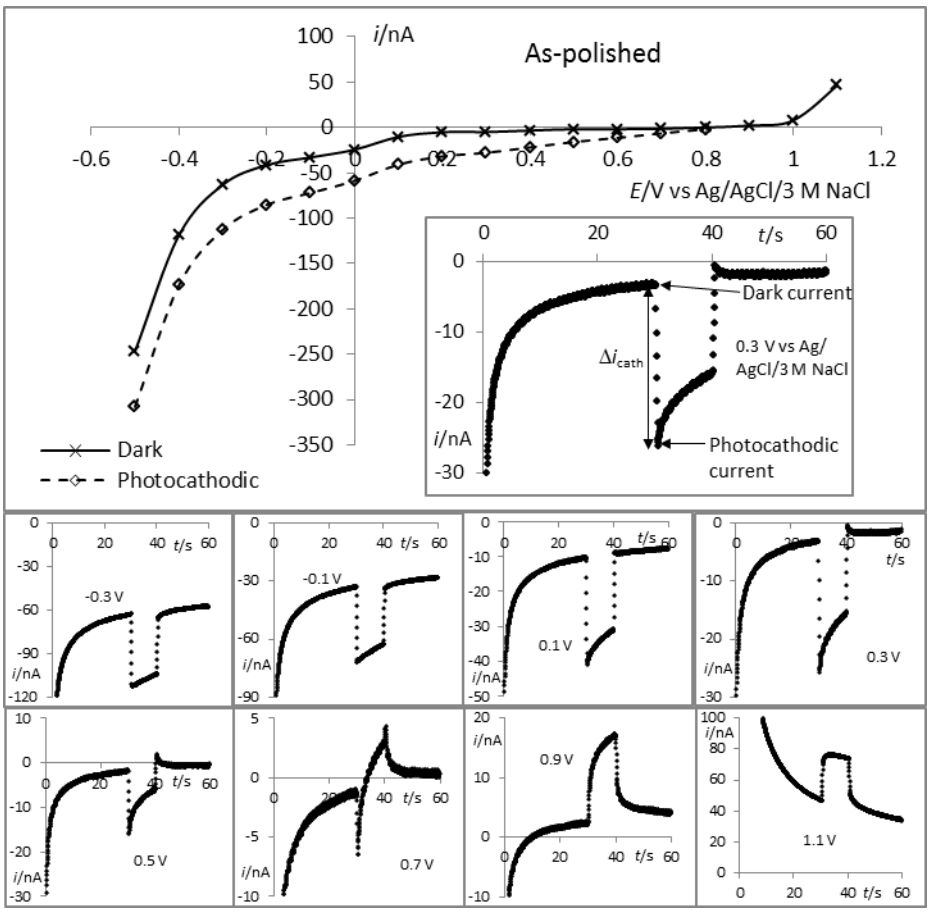

Figure 7.4: Potential dependence of dark current and initial photocathodic current, Δi_{cath}, measured as in the figure inset from photocurrent transients (example transients shown beneath graph) for as-polished BDD in 0.1 M KH_2PO_4

For polycrystalline BDD with <1% sp^2 carbon impurity, Boonma *et al*. [4] recorded cathodic photocurrents at an applied voltage of -1 V vs saturated calomel reference in aqueous 0.1 M KH_2PO_4. Under sub-bandgap illumination at 248 nm (5.0 eV), these currents decreased ca. 36-fold relative to those for band-to-band excitation at 193 nm (6.4 eV), while negligible photocurrent was recorded for illumination at 351 nm (3.53 eV). Those authors concluded that photocurrent generation for their BDD was via a nonzero density of states lying either just beneath the conduction band or (possibly related to the boron acceptor level) just above the valence band, rather than significant involvement of sp^2 carbon. Although the BDD used in the present study had a higher boron doping level (≥ 10^{20} cm^{-3}) than that used by Boonma *et al*.[4] (their doping level was 6.5 × 10^{18} cm^{-3} and so the band structure may have been more metal-like in the present case [10]), the highest energy used here (4.96 eV) was sufficient to suggest, as Boonma *et al*. [4], the involvement of states possibly relating to the boron acceptors in photocurrent generation. The

involvement of boron in photocurrent generation under sub-bandgap illumination has also been proposed by Sakharova *et al*.[3] for polycrystalline BDD in 0.5 M H_2SO_4. The authors suggested the possible involvement of lattice defects relating to the incorporation of boron into the diamond lattice.

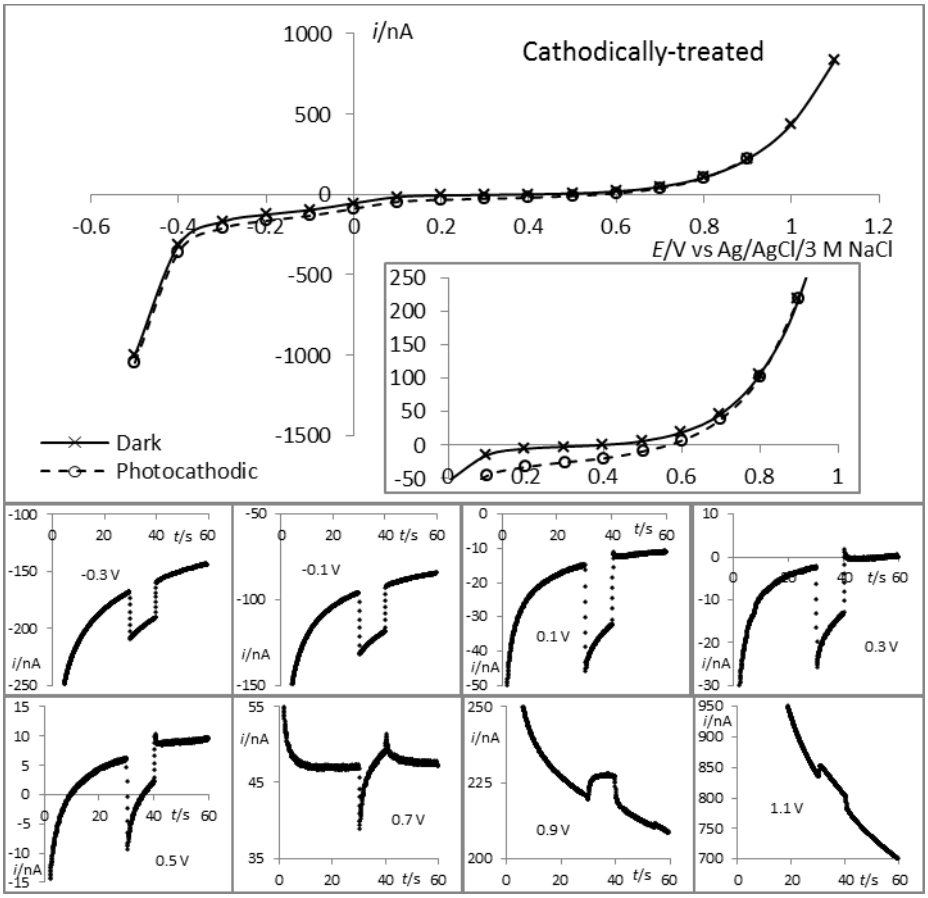

Figure 7.5: Potential dependence of dark current and initial photocathodic current for cathodically-treated BDD in 0.1 M KH_2PO_4 (zoom in inset); example photocurrent transients shown beneath graphs.

Figure 7.7 shows the Raman spectrum of the BDD disc used in the measurements presented here and contains features around 1500 cm^{-1} and 1200 cm^{-1} attributable to sp^2 carbon impurities (presumably at grain boundaries) and disordered diamond, respectively [11]. Noting the intrinsic Raman scattering for diamond is around 50-fold less than for sp^2 carbon [12], the latter was clearly a very minor component of the BDD. However, given the known prominent role of sp^2 carbon in grain boundaries in determining the optical properties of BDD [11], and given that the use here of a broad spectrum of illumination did not enable any more detailed inference regarding the energies involved, other than they must have been below

4.96 eV, it is not possible to rule out a role for sp^2 carbon in facilitating the photocurrent transients reported here.

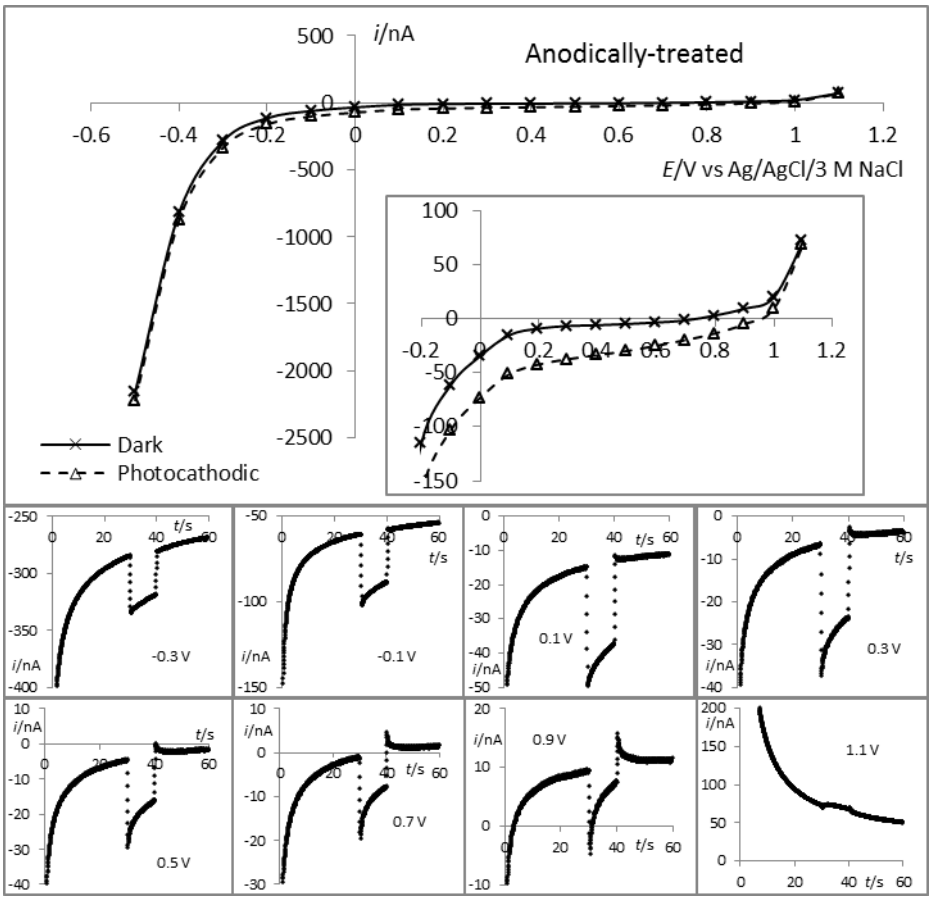

Figure 7.6: Potential dependence of dark current and initial photocathodic current for anodically-treated BDD in 0.1 M KH_2PO_4 (zoom in inset); example photocurrent transients shown beneath graphs.

7.3.2 Analysis of the photocurrent transient shapes

Following each of the BDD surface treatments, a series of photocurrent transients were recorded. The first transient in each case was recorded at 1.1 V (vs Ag/AgCl/3 M NaCl), with subsequent transients recorded at intervals of 0.1 V, shifting the potential negatively to a final value of -0.5 V (vs Ag/AgCl/3 M NaCl). Figures 7.4-7.6 show representative examples of these transients for the BDD surface as-polished, following its cathodic treatment and finally following its anodic treatment, respectively. The transients at 0.5 V (vs Ag/AgCl/3 M NaCl) for the surface as-polished and also following cathodic treatment show, as does that at 0.9 V (vs Ag/AgCl/3 M NaCl) for the anodically-treated surface, a decaying cathodic

photocurrent overshooting zero to give a similarly decaying but now anodic current at light switch-off. The decay of the initial cathodic photocurrent became less pronounced as the potential was made more negative. Irrespective of the particular surface treatment, the cathodic photocurrent transients recorded at the most negative potential essentially followed the square-wave pulse of illumination, with little decay of the photocurrent relative to the background dark current. This behaviour suggests that at all but the most negative potentials electron-hole recombination caused the initial cathodic photocurrent to decay towards a steady-state value determined by the relative rates of recombination and electron transfer (as $2\ H^+ + 2\ e^- \rightarrow H_2$) [4] to the electrolyte, with the effect of recombination (and so the current decay, plus the emergence of a current overshoot) most pronounced at potentials close to the flatband potential [7]. This standard model does not explain, however, the form of the transients at potentials positive of around 0.7 V (vs Ag/AgCl/3 M NaCl) for the as-polished and the cathodically-treated BDD surface and positive of around 1.0 V (vs Ag/AgCl/3 M NaCl) for the anodically-treated surface. At these potentials, the decaying cathodic photocurrent changed sign to anodic before light switch-off. At the most positive potentials examined for the as-polished and the cathodically-treated surfaces, entirely anodic photocurrent transients were recorded. The origin of anodic photocurrents for BDD electrodes in aqueous electrolytes is uncertain [5], though it seems tenable that the electrode reaction involves the solvent as $2\ H_2O + 4\ h^+ \rightarrow O_2 + 4\ H^+$ (h^+ = hole). That the onset potential for anodic photocurrents was shifted around 0.3 V positive by anodic treatment of the BDD (relative to the surface either as-polished or cathodically-treated) indicates that the flatband potential was shifted positively by the electrochemical oxidation.

The photocurrent transients reported here, particularly for the BDD surface as-polished and then following its cathodic treatment, broadly resembled those reported by Sakharova *et al* [3]. for sub-bandgap illumination, in 0.5 M H_2SO_4, of polycrystalline BDD that had been post-growth annealed (and so surface oxidised) in air at 420 ^oC for 30 minutes. This suggests that the cathodic treatment used in the present work did not result in stable hydrogenation of the BDD surface and that this, since the BDD supplied by Diamond Detectors had been washing with strong acid to remove non-diamond impurities [13], was oxidised to some extent

[14] even before anodic treatment. In keeping with the present study, Sakharova *et al*. [3] reported cathodic photocurrent transients with little or no current overshoot at sufficiently negative potentials and/or sufficiently short wavelengths. The case of no overshoot for illumination at 280 nm and at 450 nm was contrasted with that of overshoot at 750 nm at the same negative potential, with substantially diminishing photocurrent as the wavelength was increased (as noted also by Boonma *et al*. [4]). At sufficiently positive potentials, they recorded entirely anodic photocurrents using illumination at 280 nm, but negligible photocurrent for illumination at 450 nm or 550 nm. As in the present work, it was noted [3] that the anodic photocurrent transients showed no decay to a steady-state value after the initial rise at light switch-on and that this rise was slower than for the corresponding cathodic case.

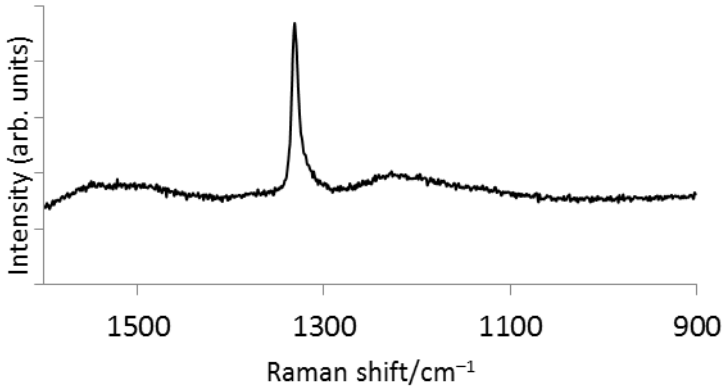

Figure 7.7: Raman spectrum of the BDD disc.

7.3.3 Applicability of the Gärtner model to the BDD-electrolyte interface

Figures 7.8, 7.9 and 7.10 show Δi_{cath} and (figure insets) $(\Delta i_{cath})^2$ plotted as functions of potential for the as-polished, the cathodically-treated and the anodically-treated surface, respectively. The observed cathodic photoelectrochemistry of the BDD/electrolyte interface is here analysed in terms of the model developed by Gärtner [6]. This was originally developed to explain the potential dependence of the photocurrent for a *p*-*n* junction under reverse bias, but is often adapted to interpret the steady-state photoelectrochemical behaviour of the semiconductor/electrolyte interface [7]. In the photoelectrochemical case, every incident photon absorbed by the semiconductor is assumed to produce a photo-

excited electron-hole pair. The minority carriers (electrons for BDD) are then accelerated through the electric field existing across the space charge region in the semiconductor first to, and then (via an electrochemical reaction presumed not to limit the photocurrent) across the semiconductor/electrolyte interface. The minority carriers crossing the interface may be photo-generated directly in the space charge region, or reach it following generation in the bulk of the semiconductor. The underlying assumptions are [7]: no electron-hole recombination occurs in the space charge layer or at the interface; no contribution is made to the photocurrent by photo-generated majority carriers (holes for BDD) crossing the interface; the incident radiation is monochromatic.

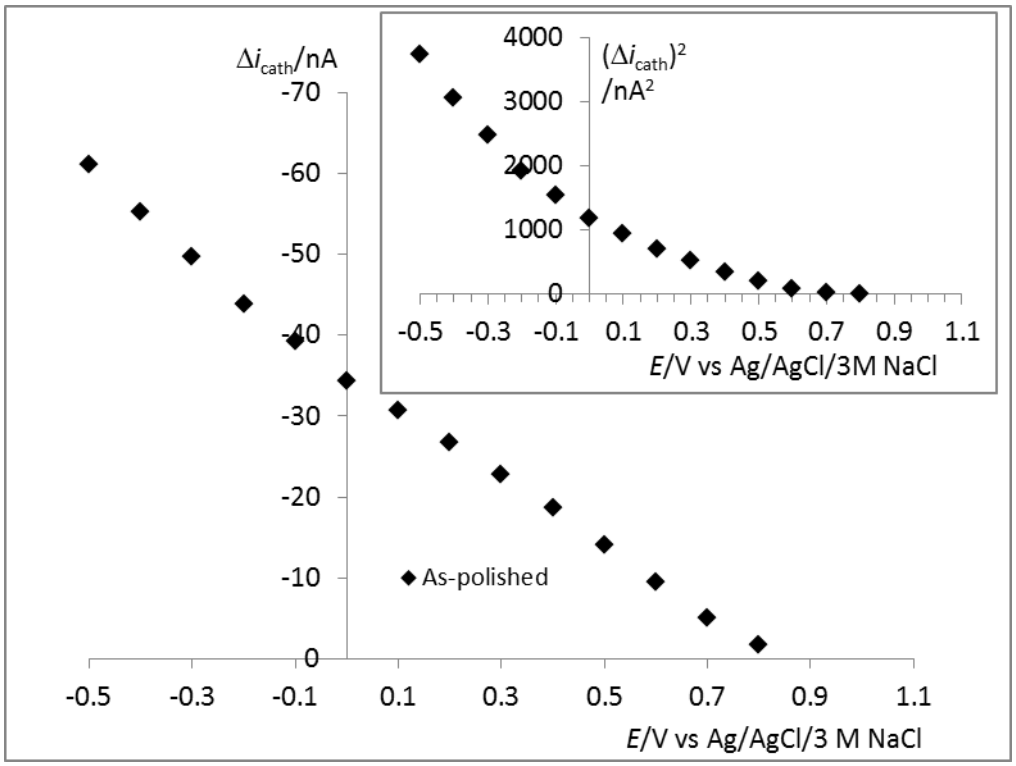

Figure 7.8: Plots of initial cathodic photocurrent, Δicath, and (figure inset) $(\Delta icath)^2$ against potential for as-polished BDD in 0.1 M KH_2PO_4.

These conditions give photocurrent, i_{photo}, at the semiconductor/electrolyte interface as [7]

$$i\text{photo} = -qI_0\{1 - [\exp(-\alpha W)/(1 + \alpha L_m)]\} \quad (1)$$

where q is the electronic charge, I_0 the (reflection-corrected) incident photon flux,

α the absorption coefficient of the semiconductor for the monochromatic radiation, W is the width of the space charge layer in the semiconductor and L_m is the minority carrier diffusion length. Here, W is given by [7]

$$W = (2\Delta\phi\varepsilon\varepsilon_0/qN)^{½} \quad (2)$$

where $\Delta\phi$ is the potential difference across the space charge region, ε and ε_0 are the relative permittivities of the semiconductor and of vacuum, respectively, and N is the acceptor or donor density. Assuming that α is small enough to make $\exp(-\alpha W) \approx 1 - \alpha W$ and also that $\alpha L_m << 1$, and replacing $\Delta\phi$ with $E - E_{fb}$ (where E and E_{fb} are the electrode potential and the flatband potential, respectively), equation 1 becomes

$$i_{photo} = -qI_0\alpha W_0(E - E_{fb})^{½} \quad (3)$$

where W_0 is the value of W given by equation 2 when $E - E_{fb} = 1$ V.

With these assumptions and simplifications, a plot of $(i_{photo})^2$ as a function of potential should be linear following equation 3 and allow determination of the flatband potential as the intercept with the potential axis at $(i_{photo})^2 = 0$.

In the present work, the marked decay of the cathodic photocurrent in transients at all but the most negative electrode potentials is taken to indicate electron-hole recombination as a factor in determining the steady-state current. In view of this (and notwithstanding that the illumination was not monochromatic), the Gärtner model in the form described by equation 3 was applied here taking the initial values of the cathodic photocurrent, Δi_{cath}. This approach was used successfully by Salvador [15] to analyse decaying photocurrent transients for the sub-bandgap illumination of of n-TiO_2 electrodes.

The plot of $(\Delta i_{cath})^2$ against potential for the cathodically-treated surface (Figure 7.9 inset) has a linear region between approximately -0.5 V vs Ag/AgCl/3 M NaCl and 0.5 V vs reference, extrapolation of which to zero photocurrent gives a flatband potential of 0.6 V vs Ag/AgCl/3 M NaCl. The plot of $(\Delta i_{cath})^2$ against

potential for the anodically-treated surface (Figure 7.10 inset) has a more limited linear region, between approximately -0.1 V and 0.7 V vs Ag/AgCl/3 M NaCl. Extrapolation to zero photocurrent in this case gives a flatband potential of 0.85 V vs Ag/AgCl/3 M NaCl. The plot of $(\Delta i_{cath})^2$ against potential for the as-polished surface (Figure 7.8 inset is curved over the entire potential range and no estimate of flatband potential could be made.

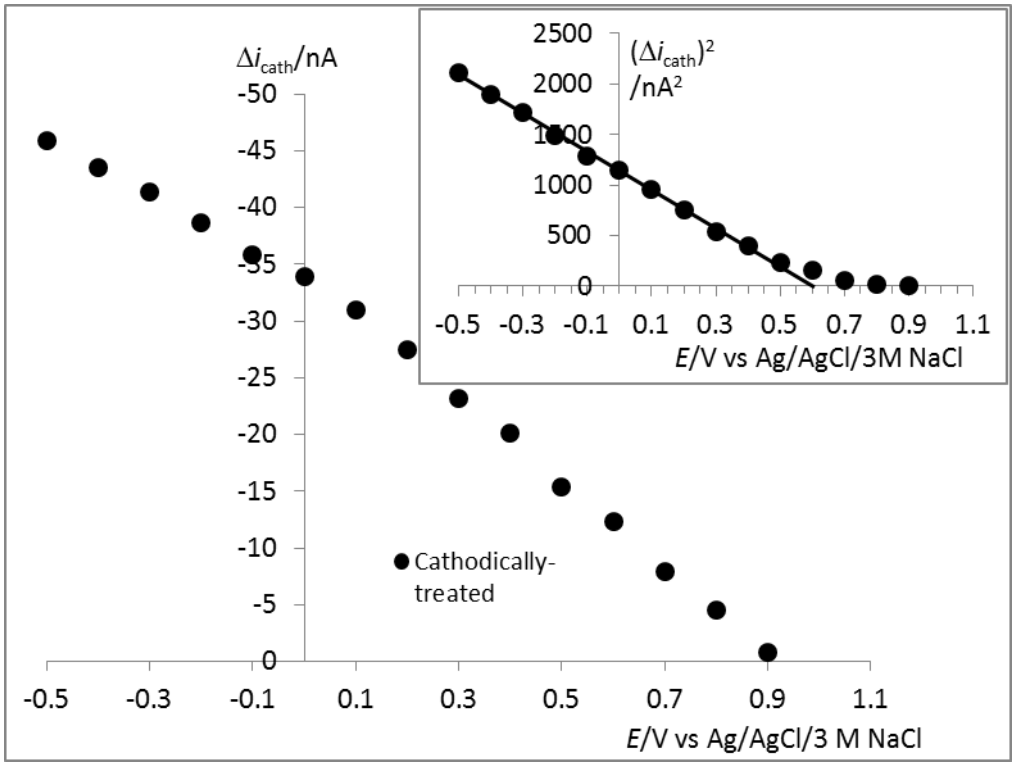

Figure 7.9: Plots of initial cathodic photocurrent, Δicath, and (figure inset) $(\Delta icath)^2$ against potential for cathodically-treated BDD in 0.1 M KH_2PO_4

The flatband potential of 0.6 V vs Ag/AgCl/3 M NaCl determined here for the cathodically-treated BDD is reasonable in comparison with the range of values, 0.44 V to 0.75 V relative to a Ag/AgCl (1 M) reference electrode, reported for a similar analysis of the potential dependence of the photocurrent squared by Pleskov *et al*. [5] However, in their study, which involved recording photocurrent vs potential curves for BDD electrodes in 0.1 M H_2SO_4 under supra-bandgap, deuterium-lamp illumination, those authors used CVD-grown materials (both single-crystal and polycrystalline, with acceptor concentrations in the range 10^{19} to 10^{21} cm^{-3}) that had been oxidised to some extent by annealing in air at 520 ^oC

for 20 minutes. The agreement of their Gärtner-Model-derived flatband potentials with the similarly-obtained value reported here for the cathodically-treated BDD thus reinforces the suggestion made in 3.2 (elaborated upon in section 3.4) that the cathodic treatment did not produce stable hydrogenation of the initially oxidised BDD surface. That the value of flatband potential determined here for the anodically-treated BDD was shifted positively relative to that for the cathodically-treated surface, to 0.85 V vs Ag/AgCl/3 M NaCl, indicates the formation of new oxygen containing groups on the diamond surface [8].

Sample-to-sample, Pleskov *et al*. [5] did not consistently observe linearity of photocurrent squared with potential for their BDD, while those plots with a linear range deviated from this such that extrapolation to zero photocurrent gave the flatband potential as negative of the photocurrent onset potential. Such deviation from linearity close to zero photocurrent was also seen in the present work in the plots of $(\Delta i_{cath})^2$ against potential for the cathodically-treated and the anodically treated surface (insets to Figures 7.9 and 7.10, respectively). These observations are tentatively ascribed here to a narrow space charge region for the heavily-doped BDD (equation (2) with a $N = 10^{20}$ cm^{-3} and $\varepsilon = 5.5$ as is typical for diamond [2] gives a value of $W_0 = 2.5$ nm) leading to an appreciable drop of the applied potential across the Helmholtz layer, particularly close to the flatband potential. The potential at zero photocurrent thus exceeded (was more positive than) that predicted by extrapolation of the linear portion of the plot of the photocurrent squared vs potential, this extrapolation neglecting the effects of the potential drop across the Helmholtz layer. Thus, although the shifts in Gärtner-model-derived flatband potential determined here for the change from the cathodically-treated to the anodically-treated surface may be regarded as valid, the suggestion, as also made by Pleskov *et al*.[5] (see also section 3.4), is that the photocurrent onset potential should provide the more reliable absolute measure of the flatband potential.

7.3.4 Effect of the surface treatment on the photocurrent onset potential interpreted as the flatband potential

Values of flatband potential, here assumed coincident with the photocurrent onset potential[4] [7], were estimated from those data used in constructing the plots of

dark current and cathodic photocurrent as functions of potential shown in Figures 7.4-7.6. The values obtained were 0.8 V, 0.9 V and 1.1 V vs Ag/AgCl/3 M NaCl (or 1.0 V, 1.1 V and 1.3 V adjusted to standard hydrogen electrode reference, SHE), respectively, for the surface as-polished, then after cathodic treatment and finally after anodic treatment. The BDD was supplied having been washed in strong acid,[13] which (as noted in section 3.2) is assumed to have produced a state of oxidation [14] that was retained for the "as-polished" surface.

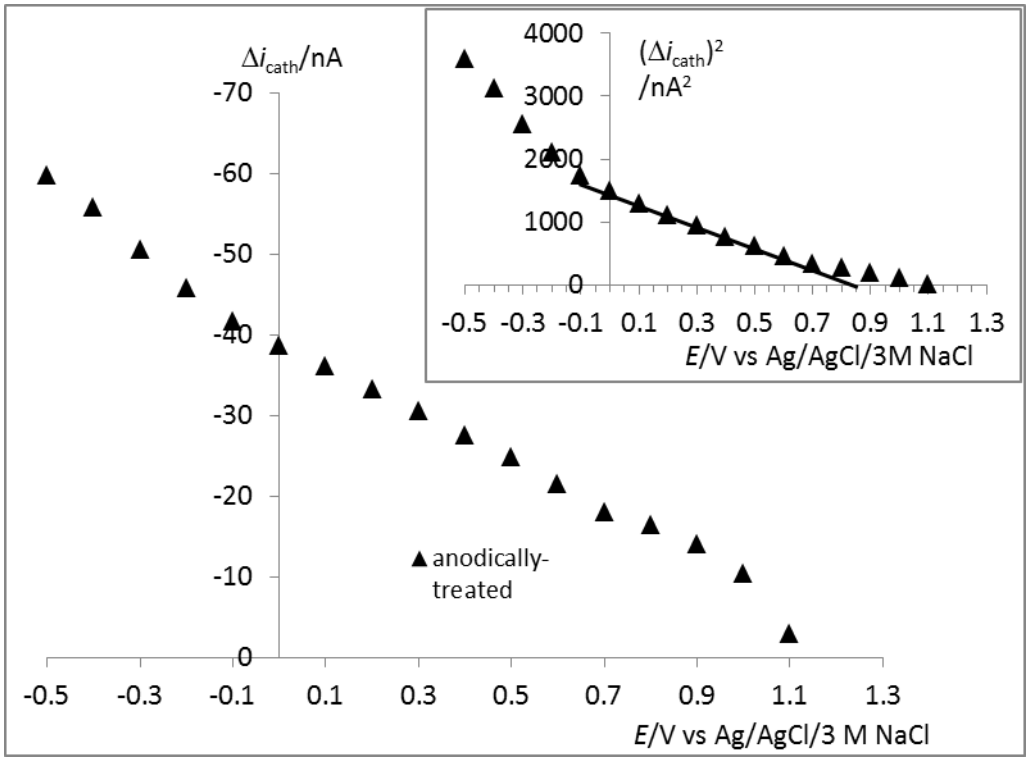

Figure 7.10: Plots of initial cathodic photocurrent, Δicath, and (figure inset) $(\Delta icath)^2$ against potential for anodically-treated BDD in 0.1 M KH_2PO_4.

The flatband potentials for the surface as-polished and also after cathodic treatment are in good agreement with the photocurrent onset potential of 1.09 V (adjusted to vs SHE) reported as the flatband potential by Pleskov *et al*. [5] for a polycrystalline BDD electrode under supra-bandgap, deuterium lamp illumination in 0.1 M H_2SO_4. (The comparison made here is valid, despite the less acidic solution of 0.1 M KH_2PO_4 (pH = 4.5) used in the present work, because no pH dependence of the flatband potential is anticipated below pH = 4.5. [2][8]) For a second, similar BDD electrode, Pleskov *et al*. [5] reported a photocurrent onset potential of 0.8 V (adjusted to vs SHE) and a value of 1.2-1.3 V on the same scale for the flatband potential determined by Mott-Schottky analysis. Attributing their

sample-to-sample variation to insufficient control of the state of oxidation of the BDD surface, those authors suggested that photocurrent onset potential was the more reliable measure of flatband potential for their heavily doped BDD (acceptor concentration 10^{20} cm^{-3}). This, they argued, was because a measurement of the photocurrent onset potential is, effectively, a measurement of a single potential and so not subject to the errors possible in extrapolating a Mott-Schottky plot. These errors arise when variations in the potential drop across the Helmholtz layer (neglected in the Mott-Schottky model) occur over a range of electrode potentials, particularly for heavily-doped BDD and close to flatband. Such variations in interfacial potential drop also appeared problematic in the analysis here (section 3.3) of photocurrents according to the Gärtner model, leading to the use here of photocurrent onset potential as the measure of flatband potential for the heavily-doped BDD.

Polycrystalline BDD (acceptor concentration ca. 10^{18} cm^{-3}) that had been hydrogen terminated by exposure to hydrogen plasma, was reported by Rao *et al*. [8] to have a Mott-Schottky-determined flatband potential of 0.2 V in 0. 1 M KH_2PO_4 and, seen by those authors as validating their Mott-Schottky analysis, a reasonably close value of photocurrent onset potential of 0.5 V under deuterium lamp illumination in the same electrolyte (both potentials adjusted to vs SHE). Both potential values are considerably more positive than the flatband potential of 1.1 V (adjusted to vs SHE) determined in the present work for the cathodically-treated BDD surface in 0.1 M KH_2PO_4. This indicates (see also sections 3.2 and 3.3) that the cathodic treatment did not significantly increase the hydrogenation of the as-polished BDD, or possibly that any increased hydrogenation was removed in recording initial photocurrent transients at positive electrode potentials; evidently, the hydrogen plasma treatment used by Rao *et al*. [8] was more effective in producing stable hydrogenation of BDD than was the electrochemical hydrogen evolution used here. A tentative explanation for why the flatband potential here was 0.1 V more positive for the cathodically-treated surface than for the as-polished surface, would be that possible loss of any cathodically-manufactured hydrogenation (by virtue of recording initial photocurrent transients at positive potentials) may not simply have reproduced the original oxygenated surface. Rather, it may have given different relative coverages of the different possible oxygen-containing groups, and

so a different flatband potential. This question is open to further investigation.

Rao *et al*. [8] electrochemically oxidised their initially hydrogenated BDD electrode at +1.5 V relative to saturated calomel electrode reference (SCE), either fixed for 10 minutes or as the anodic limit in 100 potential cycles with -1.3 V vs SCE as the cathodic limit. For this electrochemically oxidised material, they then measured, in 0.1 M KH_2PO_4, a flatband potential of 1.3 V by Mott-Schottky analysis and, in good agreement, a photocurrent onset potential of 1.2 V under deuterium lamp illumination (both potentials adjusted to vs SHE). These values are in good agreement with the value of 1.3 V (adjusted to vs SHE) determined as the flatband potential in the present work for the anodically-treated BDD surface in 0.1 M KH_2PO_4. Rao *et al*. [8] attributed the large positive shifts in Mott-Shottky-determined flatband potential (by 1.1 V) and photocurrent onset potential (by 0.7 V) upon electrochemical oxidation to the removal of surface and sub-surface hydrogen and the production of oxygen-containing functional groups (C-OH, C-O-C and >C=O, determined by x-ray photoelectron spectroscopy) on the diamond surface, these causing an increased potential drop across the Helmholtz layer and so shifting the flatband potential positively. In the present work, the effect of electrochemical oxidation was to cause 0.2 V and 0.3 V positive shifts in flatband potential for the anodically-treated surface relative to the values for the cathodically-treated and the as-polished surface, respectively. These potential shifts are ascribed to an increased degree of oxidation of the BDD surface and/or a change in the nature and relative coverage of the oxygen-containing groups. This conclusion is supported by the fact that water used to rinse the BDD disc, vertically aligned following its removal from the cell post-experiment, was visibly retained only in the anodically treated area; such enhanced hydrophilicity suggests the presence of >C=O and -C-O-C- groups [16].

For a polycrystalline BDD electrode (post growth annealed/oxidised in air at 420 $^{\circ}$C for 30 minutes) in 0.5 M H_2SO_4, Sakharova *et al*. [3] used Mott-Schottky analysis to determine an acceptor concentration of 3×10^{18} cm^{-3} and a flatband potential of 0.6 V vs SHE, while the photocurrent onset potential obtained under sub-bandgap illumination was 0.4 - 0.5V more positive. Thus, the flatband potentials reported in the present work both for the surface as-polished and then after being

cathodically-treated are in good agreement with the photocurrent onset potentials reported by Sakharova *et al*. [3] but not with their reported flatband potential determined by Mott-Schottky analysis.

In a study using sub-bandgap illumination (high-pressure xenon lamp) Patel *et al*. [2] reported a photocurrent onset potential of 0.8 V and, in reasonable agreement, a Mott-Schottky-determined flatband potential of 0.9 V (both potentials adjusted to vs SHE) for a polycrystalline BDD electrode of undetermined acceptor concentration in 1.0 M KCl (pH = 4.5). These potential values are not unreasonable (slightly less positive) relative to the flatband potentials determined in the present study for the as-polished and the cathodically-treated surface. The BDD used by Patel *et al*.[2] had been dipped into an oxidising solution of HNO_3:HF (3:1) to remove surface impurities and so was presumably in an initial state of surface oxidation comparable to the initial state of the material used in the present work. Also in keeping with the results reported in the present work, Patel *et al*. [2] noted a positive shift of 0.15 V in the photocurrent onset potential upon electrochemical oxidation of their BDD (1.0 V vs saturated calomel reference for 20 min in aqueous 0.1 M KCl) and a pH dependence (see also section 3.5) of the Mott-Schottky-determined flatband potential for the electrochemically oxidised surface. Patel *et al*.[1] considered retrospectively [4] that their BDD may have contained a substantial amount of sp^2 carbon impurity, but the later results of Rao *et al*. [8] confirm that positive shifts and pH-dependence of the flatband potential remain a feature of electrochemical oxidation of BDD with < 1% sp^2 carbon.

The values of flatband potential measured in the present work as the cathodic photocurrent onset potential are thus consistent with the majority of the literature concerning BDD photoelectrochemistry. Comparisons of the present work with these literature reports indicate that the as-polished surface was to some extent oxidised and that this state was not significantly influenced by the cathodic treatment, or at least that any cathodically-manufactured hydrogenation was not sufficiently stable to remain at the positive potentials used in recording initial photocurrent transients. Also, subsequent anodic treatment generated additional and/or different oxygen containing groups on the BDD surface causing an increased drop of the interfacial potential across the Helmholtz layer.

7.3.5 pH-dependence of the photocurrent

The Mott-Schottky-determined flatband potential for electrochemically-oxidised BDD electrodes is known to depend upon the solution pH [5][8] .This has been attributed [5][8] to the oxidation process producing oxygen-containing surface groups, which participate in acid-base equilibrium with the solution, influencing what fraction of the applied potential is dropped across the Helmholtz layer, rather than the space charge layer. If, for a given applied potential, the potential drop across the space charge layer is a function of pH, then the photocurrent at that applied potential should also be a function of pH. Figure 7.11 shows that this was so in the present study for the cathodic photocurrent transient recorded at 0.6 V vs Ag/AgCl/3 M NaCl in 0.1 M KH_2PO_4 for BDD that had been electrochemically oxidised (details in section 2.4).

Measured as shown in panel **a**, the cathodic photocurrent at light switch-on, Δi_{cath}, and the change in current at light switch-off, Δi_{off}, are plotted in panel **b** for repeated measurements of photocurrent transients at 0.6 vs Ag/AgCl/3 M NaCl, alternating the cell contents between two solutions of 0.1 M KH_2PO_4, one at pH = 4.5, the other adjusted to pH = 10 by adding 0.1 M NaOH. That the values of Δi_{cath} and Δi_{off} for the first of these measurements, at pH = 4.5, were somewhat larger than those recorded subsequently is assumed to have been due to the first measurement being followed by the first exposure of the electrochemically oxidised BDD surface to air (in changing solution). The subsequent measurements followed a reproducible pattern as the solution was repeatedly replaced to alternate the value of pH. Panel **d** of Figure 7.11 shows that the ratio $|\Delta i_{off}/\Delta i_{cath}|$ was effectively independent of pH. However, panel **c** shows that the difference Δi_{cath} - Δi_{off} provides a convenient and reproducible pH-responsive parameter and demonstrates the suitability of BDD as a photoelectrochemical pH sensor material. This opens up the possibility of achieving spatial resolution of the pH across a BDD surface, using either a focussed, chopped light source or an array of intensity-modulated light-emitting diodes in the manner of a light-addressable potentiometric device [9], but here recording the current due to the hydrogen evolution reaction. Such a device may, for example, be of interest in examining the pH variation around biological samples placed on the BDD surface. Work is presently under way to develop such a device.

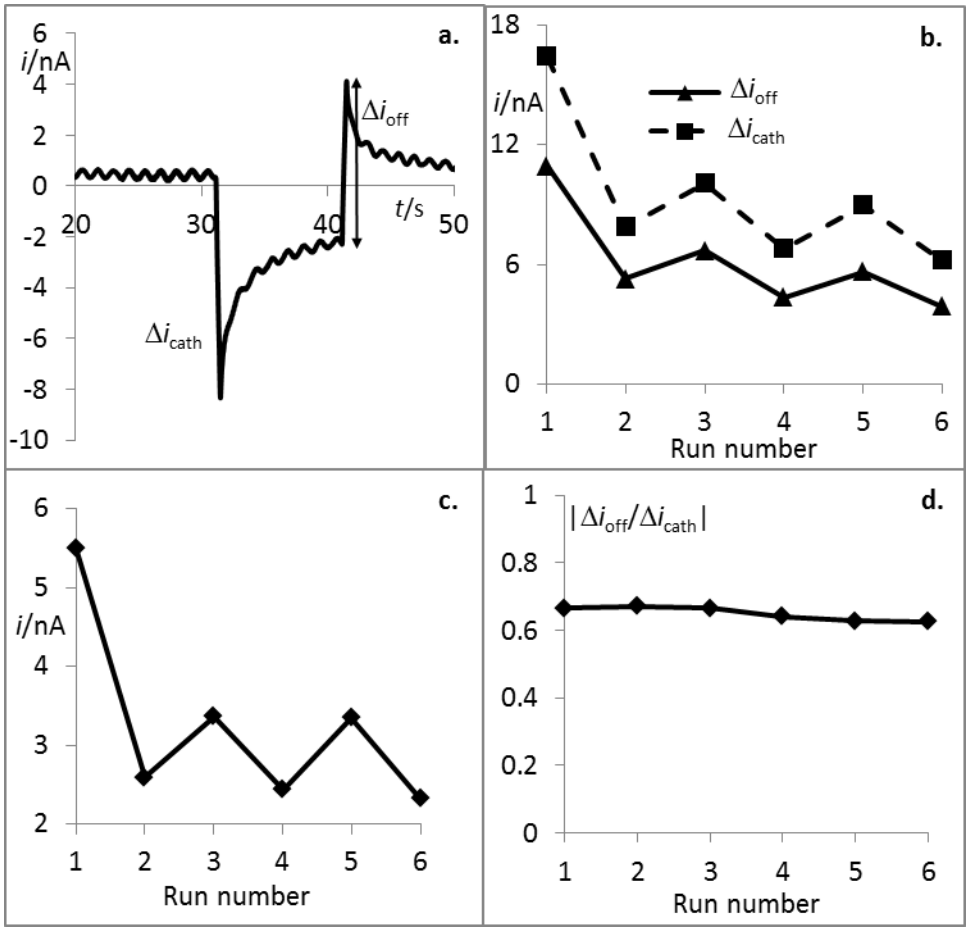

Figure 7.11: pH-dependence of the cathodic photocurrent transient at 0.6 V vs Ag/AgCl/3 M NaCl for electrochemically oxidised BDD in 0.1 M KH_2PO_4. Panel a. shows the measurement of the cathodic photocurrent at light switch on, Δi_{cath}, and the change in current at light switch off, Δi_{off}; panel b. shows Δi_{cath} and Δi_{off} plotted for measurements alternating between solutions of 0.1 M KH_2PO_4 at pH = 4.5 (odd run numbers) and pH = 10 (even run numbers); panel c. shows the equivalent plot for Δi_{cath} - Δi_{off}; panel d. shows the equivalent plot for the ratio $|\Delta i_{off}/\Delta i_{cath}|$.

7.3 Conclusion

Sub-bandgap photocurrent transients have been recorded for commercially-supplied, heavily-doped polycrystalline BDD in as-polished, cathodically-treated and anodically-treated states. The cathodic photocurrent as a function of electrode potential has been used to determine the photocurrent onset potential for the BDD in these differently treated states, as a measure of the flatband potential. This is

the first time that sub-bandgap measurements of photocurrent onset potential have been used to determine the flatband potential for BDD. A positive shift in the flatband potential upon electrochemical oxidation has been observed and attributed to the formation of oxygen-containing functional groups on the BDD surface. This explains the subsequently observed pH dependence of the cathodic photocurrent response for the electrochemically oxidised diamond, as the oxygen-containing groups participate in acid-base equilibrium with the solution, altering their influence on the partition of the applied potential between the Helmholtz layer and the space charge layer in the electrode. The consequent change in the cathodic photocurrent with pH has been shown to be reproducible in a simple demonstration of using a BDD electrode as a photoelectrochemical pH sensor.

Bibliography

[1] A. W. Bott and D. Ph, “Electrochemistry of Semiconductors,” *Sol. Energy*, vol. 8, no. 4, p. 136, 1964.

[2] K. Patel, K. Hashimoto, and A. Fujishima, “Photoelectrochemical investigations on boron-doped chemically vapour-deposited diamond electrodes,” *J. Photochem. Photobiol. A Chem.*, vol. 65, no. 3, pp. 419–429, 1992.

[3] V. P. V. A. Ya. Sakharova, Yu. V. Pleskov, F. Di Quarto, S. Piazza, C. Sunseri, I. G. Teremetskaya, “Synthetic Diamond Electrodes: Photoelectrochemical Investigation of Undoped and Boron-Doped Polycrystalline Thin Films,” *J. Electrochem. Soc.*, vol. 142, no. 8, pp. 2704–2709, 1995.

[4] L. Boonma, T. Yano, D. A. Tryk, K. Hashimoto, and A. Fujishima, “Observation of Photocurrent from Band-to-Band Excitation of Semiconducting p-Type Diamond Thin Film Electrodes,” *J. Electrochem. Soc.* , vol. 144 , no. 6 , pp. L142–L145, Jun. 1997.

[5] Y. V Pleskov, V. M. Mazin, Y. E. Evstefeeva, V. P. Varnin, I. G. Teremetskaya, and V. A. Laptev, “Photoelectrochemical Determination of the Flatband Potential of Boron-Doped Diamond,” *Electrochem. Solid-State Lett.* , vol. 3 , no. 3 , pp. 141–143, Mar. 2000.

[6] W. W. Gärtner, “Depletion layer photoeffects in semiconductors,” *Phyical Rev.*, vol. 116, no. 1, pp. 84–87, 1959.

[7] L. Peter and L. Peter, “Dynamic aspects of semiconductor photoelectrochemistry,” *Chem. Rev.*, vol. 90, no. 5, pp. 753–769, 1990.

[8] T. N. Rao, D. A. Tryk, K. Hashimoto, and A. Fujishima, "Band-Edge Movements of Semiconducting Diamond in Aqueous Electrolyte Induced by Anodic Surface Treatment," *J. Electrochem. Soc.* , vol. 146 , no. 2 , pp. 680–684, Feb. 1999.

[9] D. G. Hafeman, J. W. Parce, and H. M. Mcconnell, "Light-Addressable Potentiometric Sensor for Biochemical Systems," *Science (80-.).*, vol. 240, no. 4856, pp. 1182–1185, 1988.

[10] J. P. Goss, R. J. Eyre, and P. R. Briddon, "Theoretical models for doping diamond for semiconductor applications," *Phys. Status Solidi Basic Res.*, vol. 245, no. 9, pp. 1679–1700, 2008.

[11] W. Gajewski, P. Achatz, O. a. Williams, K. Haenen, E. Bustarret, M. Stutzmann, and J. a. Garrido, "Electronic and optical properties of boron-doped nanocrystalline diamond films," *Phys. Rev. B - Condens. Matter Mater. Phys.*, vol. 79, no. 4, pp. 1–14, 2009.

[12] D. S. Knight and W. B. White, "Characterization of diamond films by Raman spectroscopy," *J. Mater. Res.*, vol. 4, no. 02, pp. 385–393, 1989.

[13] K. O. (CEO D. D. Ltd), "Perconal communication."

[14] H. Kawarada, "Hydrogen-terminated diamond surfaces and interfaces," *Surf. Sci. Rep.*, vol. 26, no. 7, pp. 205–206, 1996.

[15] P. Salvador, "Subbandgap photoresponse of n-TiO2 electrodes: Transient photocurrent-time behaviour," *Surf. Sci.*, vol. 192, no. 1, pp. 36–46, 1987.

[16] S. Yoshihara, K. Shinozaki, T. Zenbayashi, S. Morino, T. Shirakashi, K. Hashimoto, D. a. Tryk, and a. Fujishima, "Nature of the photographic diamond surface phenomenon on boron-doped diamond," *Electrochim. Acta*, vol. 45, no. 20,

pp. 3375–3378, 2000.

Conclusion

Sepsis is a global issue that is often deadly. It is the result of the body's immune system attacking its own tissues following an infection. Being able to detect the development of a sepsis condition is essential to ensure a positive outcome for the patient. However, to date there is no fit-for-purpose quantitative point-of care assay for sepsis. Research today focuses on the detection of the biomarker procalcitonin.

In this thesis, a graphene based electrochemical immunoassay for the sepsis biomarker procalcitonin has been developed. Graphene was selected for its conductivity and transparency (possible combination with optical methods), and electrochemical methods were selected for their sensitivity, selectivity and low cost. The principle of this sensor relies on the formation of an ELISA sandwich on the surface of a graphene electrode, between an anti-procalcitonin antibody, procalcitonin and a horseradish peroxidase-labelled anti-procalcitonin antibody, the enzyme catalysing the redox reaction of o-phenylene diamine with H_2O_2 to produce an electrochemically detected product. Chapter 2 gives an introduction to the electrochemical behaviour of graphene as an electrode for a typical redox reactions. At typical CV sweep rates, $Ru(NH_3)_6^{3+/2+}$ approaches reversibility, whereas $Fe(CN)_6^{4-/3-}$ is extremely slow, presumably because it is an inner-sphere couple. Having demonstrated in Chapter 3 that the dimeric product of the horseradish peroxidase catalysed reaction of H_2O_2 and *o*-phenylene diamine can be detected using electrochemistry, a proof-of-concept sensor was developed for the detection of procalcitonin by square wave voltammetry on graphene, and is detailed in Chapter 4. However, the graphene electrodes could not be fabricated in a reproducible way and they could not be calibrated as sensors. Two methods were tested in order to circumvent this issue. First, arrays of graphene electrodes were produced from a single piece of graphene. Only half of the electrodes produced a suitable electrochemical signal in a typical redox couple solution, which is encouraging but not yet foolproof. Secondly, sodium dodecyl sulfate was used to renew the surface of a single electrode. This works by denaturing the structure of proteins and leaves only the first antibody attached to the graphene surface. Results showed that, by using this strategy, the electrochemical signal produced when the modified graphene electrode is exposed to procalcitonin, was recovered. While more progress is being made on the reproducibility of the graphene electrodes, Highly Oriented Pyrolitic Graphite (HOPG) was investigating

as a model for biosensing on graphene and the results are shown in Chapter 5. HOPG can be considered as a stack of graphene sheets and its surface is easily refreshed by peeling the surface using a scotch tape. The detection of PCT was measured using EIS, as it is a label-free method (there is only one antibody in this case) and therefore can help save time in the measurement of procalcitonin. The charge transfer resistance for $Ru(CN)_6^{3+/2+}$ was found to be linearly related to the concentration of procalcitonin in aqueous solution, in the clinically relevant concentration range (10 ng mL^{-1} to 100 nm L^{-1}) and with a suitable limit of detection (3.70 ng mL^{-1}).

As graphene is a good transparent conductor, optical methods could be combined with electrochemistry for the sensor readout. The results presented in Chapter 6 show that graphene can support localised surface plasmon resonance (LSPR), when metal nanoparticles are deposited on graphene either using electrochemistry or using electron beam lithography. In the former case, the particles are randomly dispersed over the graphene surface, whereas in the latter case, the particles form an array and the LSPR signal was better defined. When the graphene layer underneath the particles was modified with antibodies and procalcitonin, no obvious change in the LSPR absorption peak was observed. This was due to the proteins being outside the sensing volume of the particles. Therefore, another layer of graphene should be deposited on top of the array, then modified with proteins. It was also shown that two different metal nanoparticles (e.g. silver and gold) can be used simultaneously, in a graphene/ silver particles/graphene/gold particles sensor, giving two distinctive LSPR signals. One of these could be used as a reference in later experiments.

Future experiments will focus on the fabrication of a graphene/gold/graphene sensor for procalcitonin, possibly including a layer of silver nanoparticles to provide a reference signal. The optical detection will then be combined with electrochemical methods and eventually other biomarkers of sepsis such as C-reactive protein (CRP), tumor necrosis factor alpha (TNF α), and interleukines IL-6 and 10. Other work could include the fabrication of a graphene-based field effect transistor biosensor, where the graphene is used as the gate and subsequent modification with protein would induce a shift of the Dirac point.

Finally, boron doped diamond has been shown to give a photo-electrochemical response sensitive to solution pH and so presumably surface charge in general. This is another possible electrochemical/optical platform for biomarker detection.

List of publications

Papers

L. S. A. Mahe, S. J. Green, C. P. Winlove, and A. T. A. Jenkins, "Pyrene-wired antibodies on highly oriented pyrolytic graphite as a label-free impedance biosensor for the sepsis biomarker procalcitonin," J. Solid State Electrochem., vol. 18, no. 12, pp. 3245–3249, 2014.

S. J. Green, L. S. A. Mahe, D. R. Rosseinsky, and C. P. Winlove, "Potential and pH dependence of photocurrent transients for boron-doped diamond electrodes in aqueous electrolyte," *Electrochim. Acta*, vol. 107, pp. 111–119, 2013.

D. K. Polyushkin, J. Milton, S. Santandrea, S. Russo, M. F. Craciun, S. J. Green, L. Mahe, C. P. Winolve, and W. L. Barnes, "Graphene as a substrate for plasmonic nanoparticles," J. Opt., vol. 15, no. 11, p. 114001, 2013.

Conference Talks

L.S.A. Mahe, S. J. Green and C.P. Winlove, "Diagnosing Sepsis: A Graphene-Based Biosensor for Procalcitonin''
Great Western Electrochemistry Meeting 2012, University of Bath, UK
Electrochemical Horizons 2012, Trinity College Dublin, Ireland
Sartres Bio E Showcase 2013, Bristol, UK

Poster

L.S.A. Mahe, S. J. Green and C.P. Winlove, "A UV-Photoelectrochemical Study of Boron-Doped Diamond (BDD)''.